Universität der Bundeswehr München
Fakultät für Luft- und Raumfahrttechnik
Institut für Mechanik

Thermomechanical-chemically coupled Material Modelling and Computational Fluid Dynamics Simulation of Adhesives in Medicine

Dipl.-Ing. (FH) Sebastian Kolmeder

Vollständiger Abdruck der bei der Fakultät für Luft- und Raumfahrttechnik der Universität der Bundeswehr München zur Erlangung des akademischen Grades eines

Doktor-Ingenieurs (Dr.-Ing.)

eingereichten Dissertation

Promotionsausschuss:

Vorsitzender:	Prof. Dr. rer. nat. Michael Pfitzner
1. Berichterstatter:	Prof. Dr.-Ing. habil. Alexander Lion
2. Berichterstatter:	Prof. Dr.-Ing. habil. Jörn Ihlemann

Diese Dissertation wurde am 07. April 2016 bei der Universität der Bundeswehr München, 85577 Neubiberg eingereicht und durch die Fakultät für Luft- und Raumfahrttechnik am 18. Oktober 2016 angenommen.

Tag der Prüfung: 21. November 2016

Kurzfassung

Die vorliegende Arbeit beschäftigt sich mit der Materialcharakterisierung und der phänomenologischen Materialmodellierung von akrylischem Knochenzement während der Aushärtung sowie mit der Implementierung dieses Modells in einen numerischen Strömungsmechanik-Code mit dem Ziel der Anwendung auf die speziellen Fragestellungen der Vertebroplastie.
Ausgehend von der Analyse der Reaktionskinetik werden die thermodynamischen Eigenschaften von akrylischem Knochenzement im Hinblick auf ihre Abhängigkeit von der Temperatur und dem Fortschritt der Polymerisation untersucht. Die mechanischen Eigenschaften werden maßgeblich von zwei Prozessen beeinflusst, zum einen von der physikalischen Durchdringung der beiden Komponenten des akrylischen Knochenzements, dem Polymerpulver und der Monomerflüssigkeit, und zum anderen von der radikalischen Polymerisation. Dabei kann dieser maßgebliche Einfluss auf das mechanische Verhalten dieser beiden Prozesse zeitlich getrennt betrachtet werden. Die experimentellen Untersuchungen bilden die Grundlage für die Entwicklung eines thermomechanisch-chemisch gekoppelten Materialmodells, welches mit Hilfe von geeigneten Evolutionsgleichungen für die Durchdringung und die Polymerisation die beobachteten thermodynamischen und mechanischen Eigenschaften, wie Wärmefreisetzung und Volumenschrumpfung, beschreiben kann. Zusätzlich ist das Modell über geeignete Funktionale bzw. einen Potenzansatz in der Lage, das viskoelastische Materialverhalten und das scherverdünnende Fließverhalten wiederzugeben. Durch die Ableitung der konstitutiven Beziehungen unter Berücksichtigung des zweiten Hauptsatzes der Thermodynamik wird die thermodynamische Konsistenz des Materialmodells sicher gestellt. Weiterhin werden über geeignete Linearisierungen der Materialgleichungen und unter Einsatz gängiger numerischer Verfahren die Parameter des Materialmodells anhand der ermittelten experimentellen Daten bestimmt. Die numerische Implementierung des Materialmodells erfolgt in einem CFD-Code für Zweiphasenströmung, der die geometrischen und physikalischen Randbedingungen der porösen Knochenstruktur eines Wirbelkörpers, wie sie in der klinischen Anwendung der Vertebroplastie vorkommen, abbilden kann. Abschließende Beispielsimulationen sowie die Gegenüberstellung eines experimentellen und eines numerisch identisch abgebildeten Injektionsvorganges von akrylischem Knochenzement in eine poröse Struktur belegen die Möglichkeiten und die Leistungsfähigkeit der vorgestellten Methodik.

Abstract

This work is concerned with the material characterisation and the phenomenological modelling of acrylic bone cement during polymerisation as well as with the implementation of the model into a numerical CFD-code in order to apply it to the specific issues of vertebroplasty.
Based on the study of the reaction kinetics the thermodynamic properties of acrylic bone cement are analysed with respect to their dependence on temperature and the progress of polymerisation. The mechanical behaviour is significantly influenced by two processes, on the one hand by the dissolution of the two mixing components of acrylic cement, the polymer powder and the liquid monomer, and on the other hand by the radical polymerisation. Thereby the decisive influence of both processes on the mechanical behaviour can be considered chronologically separated. The experimental investigations provide a basis for developing a thermomechanical-chemically coupled material model which can describe the observed thermodynamic and mechanical behaviour, like heat release and shrinkage in volume by means of suitable evolution equations for the dissolution and polymerisation. In addition, appropriate functionals and a power law allow the model to represent the viscoelastic and shear-thinning characteristics. The thermodynamic consistency of the material model is provided by deriving the constitutive material equations in consideration of the second law of thermodynamics. Moreover, the parameters of the material model are determined on the basis of the obtained experimental data by linearising the material equations and applying established numerical methods. The model is implemented into a CFD-Code for two-phase flow which offers the possibility to include the geometrical and physical boundary conditions of a porous bone structure of a vertebral body as it is typical for the clinical application of vertebroplasty. Concluding example simulations as well as a comparison of an experimental and a numerical identically depicted injection process of acrylic bone cement into a porous structure prove the capabilities and the performance of the presented approach.

Contents

Notation

Abbreviations

Abbreviation	Denotation
ASTM	American Society for Testing and Materials
BPO	Dibenzoyl peroxide
CDI	Clausius-Duhem inequality
CFD	Computational fluid dynamics
CSF	Continuum-surface-force
CT	Computed tomography
μCT	Micro-computed tomography
CV	Control volume
DFG	German Research Foundation (Deutsche Forschungsgemeinschaft)
DICOM	Digital imaging and communications in medicine
DMA	Dynamical mechanical analysis
DMpT	Dimethyl-para-toluidine
DSC	Differential scanning calorimetry
EDMA	Ethylene-dimethacrylate
FEM	Finite element method
FV	Finite volume
FVM	Finite volume method
ISO	International Organization for Standardization
LBM	Lattice Boltzmann method
MMA	Methyl methacrylate
MULES	Multi-dimensional universal limiter with explicit solution
PISO	Pressure implicit with splitting of operator
PMMA	Polymethyl methacrylate
PVP	Percutaneous vertebroplasty
SIMPLE	Semi-implicit method for pressure-linked equations
STL	Stereo lithography
TFT-LCD	Thin-film-transistor liquid-crystal display
TMA	Thermal mechanical analysis
TMDSC	Temperature modulated differential scanning calorimetry
VoF	Volume-of-fluid

Abbreviation	Denotation
WHO	World Health Organization
WLF	Williams-Landel-Ferry
$Zr0_2$	Zirconium dioxide

Scalars

Symbol	Denotation
a	thermal diffusivity
c_d	specific heat capacity at constant deformation
c_p	specific heat capacity at constant pressure
d	progress of dissolution
e	specific internal energy
g	specific free enthalpy, Gibbs enthalpy
h	specific enthalpy
m	mass
p	hydrostatic pressure
q	degree of cure
r	heat supply per unit mass
t	physical time
v	specific volume
w_S	stress power
z	material-dependent intrinsic time
E	elasticity modulus
E_{kin}	kinetic energy
E_{in}	internal energy
E^*	complex elasticity modulus
G^*	complex shear modulus
G', G''	storage modulus, loss modulus
$\hat{G}$	absolute modulus
$G(t)$	relaxation function
H	released heat
J^*	complex compliance
$J(t)$	creep function
J	volume ratio, determinant of deformation gradient
L	mechanical power
M	shift function
Q	thermal power
R	ideal gas constant

Symbol	**Denotation**
V	absolute volume
α_1	phase fraction
γ	linear one-dimensional shear strain, shear strain components
$\dot{\gamma}$	linear one-dimensional shearrate
δ	loss angle
$\varepsilon, \varepsilon_e, \varepsilon_i$	linear one-dimensional normal strain, elastic, inelastic
ϵ_{vol}	volumetric strain
η	dynamic viscosity
θ	thermodynamic temperature
κ	curvature of free surface
λ	thermal conductivity
μ	elastic parameter
ν	kinematic viscosity
ν	Poisson's ratio
ϖ	incremental change in volume
ρ	mass density
σ	linear one-dimensional normal stress, stress components
σ	surface tension
τ	relaxation time
τ	linear one-dimensional shear stress
ϕ	flux
φ	volumetric change
ψ	specific free energy
ω	angular frequency
Ω	angular velocity
dv	scalar volume element (current configuration)
dV	scalar volume element (reference configuration)

First order tensors, vectors

Symbol	**Denotation**
$\mathbf{0}$	zero vector
$\mathbf{b}_{os}$	volume distributed surface tension force
$\mathbf{e}_1, \mathbf{e}_2, \mathbf{e}_3$	basis vectors (current configuration)
$\mathbf{e}_r, \mathbf{e}_\theta, \mathbf{e}_z$	basis vectors (cylindrical coordinates for capillary rheometer and parallel-plate rheometer)
$\mathbf{e}_r, \mathbf{e}_\phi, \mathbf{e}_\theta$	basis vectors (spherical coordinates, cone-plate rheometer)
$\mathbf{f}$	force vector
$\mathbf{f}_{os}$	surface tension force per unit area

Symbol	Denotation
$\mathbf{g}$	gravity acceleration vector
$\mathbf{k}$	volume force vector
$\mathbf{n}$	surface normal vector
$\mathbf{q}$	heat flux vector
$\mathbf{s}_f$	cell face area vector
$\mathbf{t}$	traction vector
$\mathbf{u}$	displacement vector
$\mathbf{v}$	velocity field
$\mathbf{x}$	position vector (current configuration)
$\mathbf{E}_1, \mathbf{E}_2, \mathbf{E}_3$	basis vectors (reference configuration)
$\mathbf{X}$	position vector (reference configuration)
$\mathrm{d}\mathbf{x}$	vector line element (current configuration)
$\mathrm{d}\mathbf{X}$	vector line element (reference configuration)
$\mathrm{d}\mathbf{a}$	vector area element (current configuration)
$\mathrm{d}\mathbf{A}$	vector area element (reference configuration)

Second order tensors

Symbol	Denotation
$\mathbf{1}$	unit tensor
$\mathbf{a}$	Finger deformation tensor
$\mathbf{e}$	Piola deformation tensor
$\mathbf{h}$	incremental displacement tensor
$\mathbf{A}$	Euler-Almansi strain tensor
$\mathbf{B}$	left Cauchy-Green tensor
$\mathbf{C}$	right Cauchy-Green tensor
$\mathbf{D}$	rate of deformation tensor
$\mathbf{E}$	Green-Lagrange strain tensor
$\mathbf{F}$	deformation gradient
$\mathbf{F}_t$	relative deformation gradient
$\mathbf{L}$	velocity gradient
$\mathbf{P}$	first Piola-Kirchhoff stress tensor
$\mathbf{R}$	rotation tensor
$\mathbf{T}$	Cauchy stress tensor
$\tilde{\mathbf{T}}$	second Piola-Kirchhoff stress tensor
$\mathbf{S}_E$	extra stress tensor of Cauchy-type
$\mathbf{U}, \mathbf{V}$	right and left stretch tensor
$\mathbf{W}$	spin tensor
$\mathbf{\Gamma}$	strain tensor on the intermediate configuration

Configurations

Symbol	**Denotation**
$\mathcal{B}$	material body
$\mathcal{C}$	current configuration
P	material point
$\mathcal{R}$	reference configuration
$\mathcal{Z}$	intermediate configuration
$\boldsymbol{\chi}_t$	function of motion

Operators and mathematical symbols

Symbol	**Denotation**
$\mathrm{grad}(\bullet)$	spatial gradient of $(\bullet)$
$\mathrm{Grad}(\bullet)$	material gradient of $(\bullet)$
$\mathrm{div}(\bullet)$	spatial divergence of $(\bullet)$
$\mathrm{Div}(\bullet)$	material divergence of $(\bullet)$
∇	Nabla-operator $\left(\frac{\partial}{\partial x_1}, ..., \frac{\partial}{\partial x_n}\right)$
$(\bullet)'\,(arg)$	derivative of $(\bullet)$ with respect to argument in brackets
$\dot{(\bullet)}$	material time derivative $\frac{d(\bullet)}{dt}$ of $(\bullet)$
$\exp(\bullet)$	exponential function of $(\bullet)$
$\max(\bullet)$	maximum of $(\bullet)$
$\max(\bullet)$	minimum of $(\bullet)$
$\lvert(\bullet)\rvert$	absolute value, norm of $(\bullet)$
$(\bullet)\cdot(\bullet)$	scalar product
$(\bullet)^{-T}$	transpose of $(\bullet)$
$(\bullet)^{-1}$	inverse of $(\bullet)$
$(\bullet)^{-T}$	inverse of the transpose of $(\bullet)$
$\mathrm{I}_{(\bullet)}, \mathrm{II}_{(\bullet)}, \mathrm{III}_{(\bullet)}$	invariants of $(\bullet)$
$\mathrm{tr}(\bullet)$	trace of $(\bullet)$
$\lVert(\bullet)\rVert$	norm of tensor $(\bullet)$
$\overset{\triangle}{(\bullet)}$	covariant Oldroyd derivative of $(\bullet)$
$\overset{\triangledown}{(\bullet)}$	contravariant Oldroyd derivative of $(\bullet)$
$\hat{(\bullet)}, \bar{(\bullet)}$	isochoric, volumetric part of $(\bullet)$
$(\bullet)_M$	mechanical part of $(\bullet)$
$(\bullet)_{\theta C}$	thermochemical part of $(\bullet)$, value of $(\bullet)$ on the thermochemical intermediate configuration
$(\bullet)_e, (\bullet)_v$	elastic and viscous part of a tensor
$(\bullet)_R$	quantity of the reference configuration

Symbol	**Denotation**
$(\bullet)_0$	amplitude or reference value of $(\bullet)$
$(\bullet)_F$	quantity in the liquid, uncured state
$(\bullet)_S$	quantity in the solid, completely cured state
$\mathfrak{F}[(\bullet)]$	functional of $(\bullet)$
$[[(\bullet)]]$	discretisation of $(\bullet)$
$\mathcal{A}$	set of linear equations
$\mathcal{A}_D, \mathcal{A}_H$	operators for set of linear equations
$[...]$	matrix, vector representiation in a set of linear equations
$(\bullet)_f$	$(\bullet)$ evaluated at the cell face

Products

Calculation specification	**Denotation**
$\mathbf{a} \cdot \mathbf{b} = a_i b_i$	scalar or inner product for vectors
$\mathbf{A} \cdot \mathbf{B} = A_{ij} Bij$	scalar or inner product for tensors
$\mathbf{Ab} = A_{ij} b_j \mathbf{E}_i$	linear transformation of a vector
$\mathbf{E}_i \otimes \mathbf{E}_k$	tensor basis
$\mathbf{AB} = A_{ij} B_{jk} \mathbf{E}_i \otimes \mathbf{E}_k$	tensor product of two tensors

1. Introduction

1.1. Polymethyl methacrylate in industry, technology and medicine

Polymethyl methacrylate (PMMA) is a thermoplastic material with a variety of industrial, technical and medical areas of application. It was developed independently by British, Spanish and German scientists in 1928, but Otto Röhm was the first to industrialise the manufacturing of acrylic glass plates out of PMMA. The established production method for PMMA is the radical polymerisation from methyl methacrylate (MMA). Depending on the production conditions, the length and entanglement of the polymer chains can vary and influence the material behaviour. PMMA is characterised by suitability for machining, welding, bonding, hot forming and laser cutting and offers a wide scope of design possibilities. Moreover, PMMA has favourable properties such as high light transmission, outstanding weather and ageing resistance as well as resistance to acids and lyes, high surface hardness, a variety of colouring options and a high recyclability. These properties make PMMA a popular material for transparent glass substitutes like rear lights, instrument clusters and lenses of exterior lights for automobiles, aircraft windows, walls for aquariums, bullet proof glasses and architectural applications like the Olympic facilities in Munich. It is further used for optical purposes like lenses, fibre optics and daylight redirection as well as in entertainment electronics, for example as cover for touch screens and as light guide for the backlight in TFT-LCDs. Beside the mentioned applications in industry and technology, the good compatibility of PMMA with human tissue was discovered in the late 1930s. Since then, PMMA has been employed for dentures, intraocular lenses and cosmetic surgery. In orthopaedic surgery, PMMA based acrylic bone cement, a two-component adhesive, serves to anchor prostheses in the remaining bone and to treat vertebral compression fractures by filling gaps and stabilising the affected vertebral body. The application of PMMA based bone cement in the associated spinal intervention is subject of this thesis and will be introduced in the following sections.

1.2. Medical background and motivation

Human bones are subject to continuous change. Special cells, osteoblasts and osteoclasts, are responsible for bone formation and bone resorption, respectively. Approximately until the age of 25, bone remodelling is dominated by bone formation. That means geometrical dimensions as well as bone mass increases. Thereafter, males' bone density declines slowly, whereas females'

bone density remains constant until the menopause only to decrease more rapidly afterwards. Osteoporosis is a disease that is closely related to bone resorption and is characterised by a comparatively rapid decrease in bone density [237]. One can distinguish between primary and secondary osteoporosis. Primary osteoporosis is mainly caused by lack of oestrogen, especially for females but also for males, by lack of physical exercise, old age and genetic predispositions [25]. In contrast, secondary osteoporosis is not age-related, but provoked by other underlying diseases. Examples are disturbances of hormonal balance and bone metabolism, tumours in the skeletal system and side effects of drugs among others [20, 163]. In the first stages, osteoporosis proceeds more or less unnoticed for the person concerned. Bone density measurements can give information on existence and severity of osteoporosis. However, with progress of the disease, low bone density and micro-architectural deterioration of bone tissue advance fractures within the complete human skeleton [2], especially within the hip, the wrist and the spinal column. Fractures and sintering within the spinal column lead to a decrease in body height and in most cases to severe back pain. According to the World Health Organization (WHO), more than 75 million people in Europe, Japan and the United States were affected by osteoporosis in 2003 [237] and therefore it is ranked among the ten most frequent and important diseases worldwide. In addition, the costs of osteoporosis, like hospital care, long term care, medication and loss of working days, also have an economic importance.

Besides proper nutrition and physical activity, different medical therapies are applied to prevent and treat osteoporosis [20]. However, if bone fractures appear, medical treatment and conservative pain therapies are frequently not sufficient and therefore surgical interventions become necessary. Particularly within the spinal column, the minimal invasive techniques vertebroplasty and kyphoplasty have proved to be successful [11, 71, 83, 104, 154, 186]. With both techniques, the surgery is performed under general anaesthesia with the patient lying on his stomach. This helps to align the spinal column in a straight position and to raise the affected vertebra. After locating the fracture by using computer tomography, the surgeon positions a biopsy needle through the patient's back, aligned in the direction of one of the transverse processes into the fractured vertebra. Only for kyphoplasty, a balloon is inflated inside the fracture to restore additional height of the vertebral body and to form a cavity for placing bone cement [63]. Thereafter the balloon is removed. In the meantime, the filling material, bone cement is prepared. Predominantly, acrylic based bone cements are applied, because of their convenient handling, their compatibility with the human body and long life cycles (cf. ch. 4). Recently, calcium phosphate cements and some other calcium based cements have become more and more popular [129, 182], as they feature biodegradability, which is desirable for young patients with high life expectancy, but more difficult processability and less mechanical strength. Acrylic bone cements are a mixture of two components, a liquid monomer and a polymer powder. A syringe is charged with the prepared cement and connected to the biopsy needle via a flexible tube. Right after mixing, the cement has a low viscosity, but due to the dissolution of the monomer into the polymer powder the viscosity rises continuously (cf. ch. 5). The cement viscosity is usually checked by a specimen of the cement that was not filled into the syringe. When the cement viscosity is estimated optimal, the physician injects the bone cement through the biopsy needle

into the vertebral body. The variation in viscosity offers the physician the possibility to take into account the individual characteristics of the vertebral fracture [100]. Generally, cement is injected at low viscosity for narrow gaps in the fracture and at higher viscosity, if greater cavities occurred [13]. Inside the human body the cement penetrates the affected vertebra and fills fractures and cavities. This process is monitored by X-ray or computer tomographic observation to visualise the cement distribution within the vertebral body and thus to minimise the risk of cement leakage into the surrounding tissue. Furthermore, the physician can influence the cement distribution by pulling out the needle while injecting. In some cases a bipedicular approach, that means using two needles, one at each transverse process, can lead to a better result than sticking to a unipedicular application [224]. Once the cement is placed inside the vertebra, the needle is removed. The body temperature of 37 °C accelerates the radical polymerisation, so that the cement cures within a period of ten minutes. With the aid of the solidified cement, the affected vertebra retrieves its mechanical strength and is stabilised within the vertebral column. The patient usually experiences immediate pain relief [210] and can be mobilised on the same day.

Although percutaneous vertebroplasty has now been performed for 25 years [64] and has become a standard surgical intervention in many hospitals around the world, there are frequent reports of complications that appear along with this minimal invasive operation technique. Cement leakage out of the vertebral body into unwanted regions is among the most common incidents [11, 23] and difficult to detect under X-ray observation [208]. The frequency of cement leakage does not differ significantly between vertebroplasty and kyphoplasty, but kyphoplasty is supposed to be the safer technique [180]. Generally, leakage is divided into three groups according to its location with respect to the vertebral body. Leaks via the basivertebral vein are classified as type B, via the segmental vein as type S and through a cortical defect as type C [246]. Depending on where the leakage occurs, different consequences can be expected. Leakage into the epidural space (type B) can lead to paralysis [219]. Furthermore, it has been reported that low viscosity cement can lead to migration of the cement into the inferior vena cava and the pulmonary arteries. Displaced bone cement thus leads to pulmonary embolism [174, 231], which can be asymptomatic, but also lethal [37, 38]. Another phenomenon coming along with vertebroplasty is the increased mechanical properties of the treated vertebra, since the mechanical strength and stiffness of acrylic cement exceeds that of bone material by at least one order of magnitude [14]. A load shift is the consequence, whereupon the adjacent vertebrae to the one treated experience significantly higher forces [14]. Several studies point out that this can be the reason for new fractures in adjacent vertebrae [17, 218, 228]. Especially, if cement leaks into the intervertebral disk, the risk is high for developing new subsequent fractures [135]. In this context the infiltrated volume of cement is discussed [83]. Injecting a high volume of cement is more likely to cause leakage and an increased stiffness of the treated vertebra and therefore it compromises adjacent vertebrae. In contrast, a small amount of cement is sufficient to restore the strength of a fractured vertebra [24, 160]. The danger of thermal necrosis due to exothermal polymerisation of acrylic bone cement is usually not addressed in corresponding articles. However, if bone cement leaks into the proximity of the spinal canal, high temperatures can lead

to neurological deterioration [241, 248]. Moreover it is not further scientifically investigated if elevated temperatures during polymerisation and the accompanied injury of intraspinal nervous tissue and nerve roots are the reason for pain relief or may even be crucial for rarely increased pain after a vertebroplasty [46, 83, 110, 233]. Additionally, the influence of residual monomer after polymerisation is not fully understood, but it is supposed to also damage surrounding tissue [6, 45, 134]. Beyond that, more seldom complications are existent that are not mentioned here explicitly [11, 186, 248].
The comprehensive list of complications indicates a lack of clarity about the complex material behaviour of acrylic bone cement as well as about the processes that take place inside the human body during and after minimal invasive interventions. To minimise or to avoid these potential complications, the objective of the presented work is to contribute to a better understanding of the flow and curing behaviour of acrylic bone cements used for vertebroplasty.
The presented work is part of a collaboration project together with the Chair of Solid Mechanics of the Chemnitz University of Technology and is funded by the German Research Foundation (DFG)[1]. Furthermore, this project was supported by the Heraeus Medical GmbH in terms of technical expertise and by providing acrylic bone cement material, by the Department for Trauma Surgery at the University Hospital in Innsbruck by providing μCT data of vertebral bodies and by the Faculty of Life Sciences at the Hamburg University of Applied Sciences by digital image processing of μCT data. Within this project a sophisticated computer simulation of the injection and the following curing of acrylic bone cement is developed, which provides insight into the thermomechanical processes inside the human body. The focus of the presented work is put on the detailed experimental characterisation of thermal and mechanical properties of a commercial acrylic bone cement during and after curing, as well as the modelling of the investigated material behaviour on the basis of continuum mechanics. Furthermore, the constitutive equations of the model were parametrised according to the experiments. For calculation of the injection of acrylic cement into the porous vertebral bone structure, initially filled with bone marrow, the adapted model was implemented in an open source computational fluid dynamics (CFD) code. As part of the collaboration project, but not as part of this thesis, the model was also implemented in a finite element code by the project partner from the Chemnitz University of Technology [119, 121]. Using the results of the CFD injection simulation as initial conditions, it is possible to simulate the curing phenomena of acrylic bone cements inside the human body.

1.3. Literature review

Vertebroplasty has been performed for more than 25 years, but the first application of acrylic bone cement in medicine dates from the early 1960s, when Sir John Charnley successfully anchored a hip prosthesis to the shaft of the femur [36]. Since then a lot of research was carried out on the investigation of acrylic bone cements, as well as on computer simulation of surgical

[1] DFG funded joint research project DFG-PAK 273 "Numerische Simulation komplexer Vorgänge bei Verfahren zur minimal invasiven Stabilisierung von osteoporotischen Wirbelkörpern".

interventions using acrylic bone cements. This section will give an overview of the research published in literature. The first part will concentrate on both the characterisation and modelling of thermal and mechanical properties of acrylic bone cement. Numerical simulations on bone cement material will be discussed afterwards. Since to the author's knowledge a comprehensive thermomechanical-chemically coupled material model has not yet been proposed for biomechanical simulations, an overview is going to be given on existing constitutive models for curing adhesives, designed for industry applications.

Mazzullo et al. were among the first to study the polymerisation kinetics of an acrylic bone cement for various temperatures by means of calorimetric measurements and to set up a kinetic model suitable to represent the temperature-dependent radical polymerisation [155]. Their approach is also able to account for uncomplete curing due to diffusion control. A similar model was introduced by Maffezzoli [150]. The reaction kinetics of a commercial bone cement was studied under isothermal and non-isothermal conditions. Typical effects like auto-acceleration and vitrification are included in their phenomenological model. Moreover, they suggested a characteristic induction time that considers the consumption of the inhibitor by free radicals in their kinetic model and delays the onset of the polymerisation reaction. Nearly identical, but slightly simpler models can be found in the works of Borzacchiello et al. and Nzihou et al. [29, 167] that exhibit the same key features. Vallo distinguished between a chemistry-controlled reaction and a diffusion-controlled reaction after the maximum rate of cure exceeded [229]. Each part of the reaction is described by a separate evolution equation. In contrast to the empirical models above, Hansen developed a kinetic approach taking explicitly into account the chemical reactions that govern the polymerisation process [77]. Stanczyk described the chain formation of polymerisation in a more mathematical way [214]. The creation of new polymer chains and the associated disappearing of relevant smaller chains as well as the activation by free radicals are explicitly modelled. This allows to calculate the current chemical composition of the polymerising bone cement. However, this model is difficult to identify on an experimental basis and is computationally more expensive. It should be noted that all mentioned models use Arrhenius behaviour to describe the temperature-dependent polymerisation process.

Regarding the specific heat capacity and the thermal conductivity of acrylic bone cements, it is common to use a fixed value measured by differential scanning calorimetry and literature values, respectively. In the work of Huiskes and Nzihou et al. the specific heat capacity is linearly dependent on temperature and progress of polymerisation, as proposed by Bailleul et al. for curing resins [10, 92, 167]. Accurate shrinkage and thermal expansion measurements during polymerisation are rarely found in literature, because of difficulties in capturing the density of a fluid and a solid with one device. Haas et al. and Gilbert et al. measured the volumetric shrinkage of commercial and self mixed bone cements in a mechanical unconstrained environment by a water displacement dilatometer [66, 74]. The Archimedes principle was employed by Muller et al. as well as by Rudolph et al. to detect volumetric changes during polymerisation [162, 198]. Most computational models in literature either neglect thermal expansion [136] or chemical shrinkage [179] or do not distinguish between them [33].

Since acrylic bone cements experience a phase transition from fluid to solid, the mechanical

behaviour can be divided into two areas. When the injection process of acrylic cement is considered, the fluid or rheological properties are important. Due to dissolution of the monomer into the polymer powder, the rheological behaviour of bone cement changes and is therefore difficult to capture experimentally. Farrar and Rose [56] and others [72, 112, 125, 202] preferred parallel-plate and cone-plate rheometers to determine the rheological characteristics of bone cement as it is possible to measure not only the viscous but also the viscoelastic properties. This type of rheometers can easily be temperature-controlled and thus give the possibility of thermomechanical investigations. In contrast to the device with parallel plates, the cone-plate rheometer features a constant shear rate across the radius. According to Lewis [125] and others [112, 207] capillary rheometry and coaxial Couette rheometry [72] are more suitable to analyse the flow conditions within the injection system and the porous bone structure. However, studying the process and temperature-dependent viscoelastic material properties is not possible. Carnelli et al. presented a self-construction rheometer specially designed to characterise bone cements [35]. All references above detected a shear thinning behaviour and the viscosity increasing with proceeding dissolution and polymerisation. For the purpose of modelling, power laws have been used to describe the shear thinning behaviour and the dependency on the process time [18, 112, 166, 220]. Neither the temperature dependency nor a consideration of the viscoelastic material behaviour can be found in material models representing the fluid behaviour of acrylic bone cements in literature.

If the curing or the mechanical long term behaviour of bone cement is of interest, the material is treated as a solid and different experimental and modelling approaches can be found in literature. An overview of mechanical cement properties, including creep measurement, was given by Lewis and others [125, 159, 201, 232]. Lion et al. measured the mechanical properties of acrylic bone cement by means of dynamical mechanical analysis and developed a constitutive model of finite linear viscoelasticity to represent the mechanical behaviour of polymethylmethacrylate-based bone cement [147]. The changing mechanical properties during curing were often considered as linear elastic, where the Young's modulus varies with proceeding polymerisation [33, 179]. A more advanced model for curing analysis by Lingois et al. takes the viscoelastic behaviour of bone cement into account [136].

Besides the experimental analysis and modelling of acrylic cements numerous computer simulations have been carried out to gather a deeper insight into the physical phenomena accompanied by the application of bone cement in the human body. Most of the numerical investigations apply to surgical interventions for anchoring prosthesis. However, the bone cements used for vertebroplasty and kyphoplasty are nearly identical to those utilised in joint replacement surgery. The flow behaviour and the distribution of the cement inside the vertebral body are essential for a successful vertebroplasty. For this reason, Beaudoin et al. studied the cement flow in spongy bone tissue [22]. In their work, the rheological behaviour of bone cement is represented by a power law and the porous bone structure is described in a simplified scheme, whereas different porosities were realised by elementary geometric modifications. In particular they focused on the influence of cement viscosity and bone porosity on the penetration depth into the bone tissue as well as on the pressure gradient within the porous structure. A similar power law

was used by Baroud et al., too [12, 13, 16, 19], to investigate the pressure conditions and flow in a cannula but not in a porous bone structure. Their model captures the pseudoplastic and rheopectic behaviour with proceeding time. Srimongkol et al. also reverted to the power law presented above [213]. They calculated the cement flow in the femoral canal and in the spongy tissue in a two-dimensional approach, using the Navier-Stokes-Brinkman equation. Bohner et al. examined the effect of cement viscosity, bone porosity and vertebral body dimensions on the extravasation risk of bone cement by means of the law of Hagen-Poiseuille and the law of Darcy [28]. The Lattice Boltzmann method (LBM) was pursued by Zeiser et al., to describe the flow in vertebral trabecular bones [247]. Moreover, the authors studied the anisotropic geometric and transport properties of vertebral trabecular bone. Teo et al. characterised the permeability of spongy tissue specimens using micro-computational fluid dynamics [221]. The interdependence between structural parameters of a morphological bone tissue model and its permeability was discussed by Widmer and Ferguson [238]. A patient specific simulation of a minimal invasive vertebroplasty was proposed by Teo [220, 222]. The variable porosity of the vertebral body scanned by computed tomography (CT) was determined by means of grey scale values of single voxels. For calculating the cement distribution inside the vertebra, Darcy's law, including the known power law for non-Newtonian fluid behaviour, was applied. The resulting cement distribution served as initial conditions for a structural analysis of the treated vertebra by means of finite element methods.

In addition to flow simulation, thermal simulations are of particular interest as acrylic bone cements show an exothermal curing behaviour. These thermal simulations give valuable information on the space- and time-dependent temperature distribution and can reveal areas that are at risk of thermal necrosis. Jefferiss was among the first to conduct a thermal analysis of curing cement to anchor an artificial hip prosthesis [99]. Starting with an initial temperature distribution, the author investigated the temperature evolution for a prosthesis-bone-cement-bone compound by means of a one-dimensional model. Huiskes introduced a time-dependent evolution of polymerisation as a heat source in his heat transfer equation for a two-dimensional analysis of a acetabular cup fixation [92]. His model also features a varying heat capacity and additional heat resistance at the prosthesis-cement and cement-bone interfaces. Mazzullo et al., Borzacchiello et al. and Maffezzoli et al. expanded the reaction kinetics for temperature dependency and studied the heat transfer with internal heat generation during a hip replacement for different cement layer thickness [29, 151, 155]. Moreover, they included the effect of vitrification in their models to demonstrate the relationship of final degree of reaction and maximum polymerisation temperature. In order to obtain more information about heat transfer at the bone-cement interface and therefore a more realistic temperature distribution, Stanczyk and van Rietbergen created a three-dimensional geometrical model obtained by micro-CT scanning [216]. The model at high resolution accounts for the trabecular bone-microstructure, filled with bone marrow and cement, in contrast to the continuous bulk material simulations above. An overview of modelling heat transfer for bone cement polymerisation can be found in a further paper by Stanczyk et al. [215].

The effects of polymerisation on the mechanical and thermal properties of acrylic cement as

well as the influence of chemical shrinkage on residual stresses have been rarely addressed in literature. Only a few studies exist that calculated the curing process of acrylic cement. Briscoe and New applied a finite element analysis, including material properties dependent on the local degree of cure, to predict the residual stresses in total hip replacement cement mantles [32, 33]. Perez et al. compared their numerical calculations of curing cement in a femoral implant with experimental measurements [179]. Residual stresses and chemical shrinkage for dental composites were computed under isothermal curing conditions by Lingois et al. [136]. Lennon and Prendergast developed a segregated approach [124]. Firstly, they performed a thermal analysis of curing cement in a physical model of femoral hip replacement and used the peak temperature distribution for a subsequent analysis of residual stress due to thermal shrinkage. Landgraf and coworkers introduce a thermomechanical-chemically coupled material model, based on detailed thermodynamic and mechanical experiments [109], to simulate the inner vertebral cement curing and examine the post operative deformation behaviour of a parametric vertebral body model [119, 120].

Beyond that a lot of computational studies engaged in analysing the postoperative problems and behaviour of acrylic bone cement. Here, the research of Rohlmann et al., Baroud et al., Liebschner et al., Jones et al. and Wilcox are mentioned as examples [14, 102, 120, 133, 193, 195, 196, 240]. All these studies focused on the altered stiffness of vertebral bodies due to augmentation with bone cement as well as the influence on adjacent vertebral discs and vertebral bones.

All approaches mentioned above enable only to model and numerically investigate part of the aspects concerning percutaneous vertebroplasty and kyphoplasty. Additionally, models that represent the curing behaviour of acrylic cements describe material properties simplified or neglect important phenomena, e.g. chemical shrinkage. More sophisticated modelling approaches that cover the behaviour of industrial curing adhesives have been developed recently. In principle, industrial curing adhesives show related characteristics like acrylic bone cements do, so that these modelling techniques can be adopted. The proposed phenomenological model is also based on an advanced approach, originally designed for curing adhesives. In the following, a literature overview is given for relevant modelling of curing adhesives.

White and Hahn were among the first to develop a linear viscoelastic model that accounts for mechanical properties depending on the degree of cure [236]. Including the calculation of cure kinetics this model is suitable to predict chemical and thermal strains. Kiasat suggested a model with cure-dependent elasticity parameters [106]. A particular feature of this model is that the evolution of the state of cure and therefore the cure-dependent stiffness does not influence the stress free configuration. It should be noted that this model is only applicable for small strains and not necessarily consistent with the second law of thermodynamics. Based on previous experimental and theoretical studies [4, 5], Adolf and coworkers introduced a thermomechanical consistent framework to describe non-linear viscoelastic behaviour of curing resins [3]. In their preliminary work they proposed a cure-dependent equilibrium modulus and a time-cure superposition [4]. Subsequently, they presented a linear viscoelastic model including temperature-dependent reaction kinetics to describe the curing process [5]. In a series of papers Hossain and

coworkers developed a material model for curing adhesives. Their first approach accounts for viscoelastic material behaviour and small strain deformation [89]. In continuing studies, they extended their model to finite strains, first for elastic material behaviour [88], followed by a finite strain viscoelastic model [90]. To ensure the thermomechanical consistency they formulate the free energy function. Although their model comprises shrinkage phenomena, it disregards heat generation due to exothermal reactions. A fairly comprehensive overview of existing approaches for modelling curing processes was also given by Hossain [87]. Mahnken developed a thermodynamic consistent model of polymer curing coupled to viscoelasticity at large strains on basis of the total Hencky strain tensor [152]. Lion and Höfer proposed a thermo-viscoelastic model for finite strains that is capable of representing the key phenomena accompanied by curing processes [141]. This model includes options for temperature-dependent reaction kinetics for the evolution of the degree of cure, varying viscoelastic properties depending on the curing process, chemical shrinkage and thermal expansion as well as exothermal heat generation due to curing. This model has also been subject to algorithmic formulations and finite element implementation in the work of Retka and Höfer [188]. Furthermore, experimental investigation and parameter identification of the model above relating to small strains has been performed by Yagimli and Lion [245]. Landgraf et al. [122] as well as Yagimli et al. [244] develop a constitutive modelling on the basis of the work of Lion and Höfer and apply it to bonded piezo metal composites and curing resins, respectively. Additionally, both illustrate the implementation of the model in commercial FE-codes. Recently, Liebl et al. expanded a viscoelastic model like that of Lion and Höfer by a viscoplastic part presented in the work of Schlimmer and Mahnken [153, 206] to account for plastic deformations as a measure of damage in curing adhesives [130, 131, 132].

1.4. Structure of thesis

The aim of this thesis is to establish a numerical framework in order to gain a deeper insight in and better understanding of the complex processes, that take place during the injection and curing of acrylic bone cement within a vertebroplastic surgery. In ch. 2, the fundamentals of continuum mechanics are briefly summarised as a common background for the following development of the material model. The next chapter, ch. 3, focuses on the theory of viscoelasticity, in which the material behaviour of acrylic bone cement can be classified. This theory of materials is necessary background knowledge for the interpretation of the results of the mechanical experiments and the formulation of the constitutive equations. In ch. 4 detailed information is given on the principal chemical and physical properties of acrylic bone cements. Furthermore, it is discussed how these properties influence the handling of acrylic cements for a vertebroplastic surgery. The thermodynamical and thermomechanical characterisation of a particular acrylic bone cement is presented in ch. 5. Thereby, all material properties which affect the behaviour of bone cement within a vertebroplastic surgery are examined in the relevant temperature range and mechanical load cases. On the basis of this material characterisation, as well as the theoretical background of chs. 2 and 3, a material model is developed in ch. 6, which is an extension

of the model proposed by Lion and Höfer [141]. In order to represent the particular material behaviour of the acrylic cement, examined in ch. 5, the parameters of the material functions of the model are adopted to the measurements in ch. 7 with the aid of numerical methods. In ch. 8, the implementation of the model, governing the injection process, into the open-source finite-volume toolbox OpenFOAM® is described. Finally, in ch. 9 some case studies demonstrate the capabilities of the computational framework with respect to the application in vertebroplasty. Moreover, a comparison of experiment and simulation for injecting bone cement into an artificial bone structure is given in this chapter. A summary of the presented work as well as a perspective on future enhancements conclude the thesis.

2. Fundamentals of continuum mechanics

The principles of continuum mechanics allow for the phenomenological description of the macroscopic deformation behaviour of material bodies. In this context a continuum represents a space of material points to which the local, homogenised material behaviour is assigned. Therefore, the knowledge of the underlying micro-structure of the material might be useful to develop constitutive material functions, but must not necessarily be understood. The continuum itself is rather characterised by field quantities, like stress, velocity or temperature, which are associated with the internal structure. However, it is important for this abstraction that length scales are small enough to capture high gradients of processes to be modelled.
Within the field of continuum mechanics one can distinguish between three basic types of equations with respect to their physical meaning:

- **Kinematics** describes the motion and deformation of a body, disregarding its causation.
- **Balance principles** form the material-independent mathematical description of fundamental laws of physics that govern the motion of a continuum.
- **Constitutive relations** describe the material itself and establish a relationship between kinematics and balance principles.

The constitutive relations are specific for the material described and will therefore be addressed extensively in ch. 6. Since the kinematics and the balance equations are material-independent, they will be discussed in the following, alongside stresses and stress power, as far as necessary for the presented work. For a deeper insight the interested reader is referred, amongst others, to the textbooks of Haupt [79], Altenbach and Altenbach [7] or Holzapfel [86].

2.1. Kinematics

2.1.1. Motion and deformation

In continuum theory, a material body $\mathcal{B}$ is considered to have a continuous distributed number of material points P. The motion and deformation of this body $\mathcal{B}$ is described by the motion of its points $\mathsf{P} \in \mathcal{B}$. At time t, the position of a specific point P is characterised by its position vector $\mathbf{x}(t)$. The assignment of position vectors to material points of a body at a certain time

t is called configuration (cf. fig. 2.1).

$$\boldsymbol{\chi}_t \,:\, \mathsf{P} \mapsto \mathbf{x} = \boldsymbol{\chi}\left(\mathsf{P}, t\right) \tag{2.1}$$

Two configurations play an important role. On the one hand, the reference configuration $\mathcal{R}$ is defined as configuration at time $t = t_0$, whose position vector is denoted as $\mathbf{x}\left(t_0\right) = \mathbf{X}$. In general, the reference configuration represents an undeformed configuration. On the other hand, the configuration at time t is marked as current configuration $\mathcal{C}$. Both configurations can be converted into each other by the displacement vector $\mathbf{u}$.

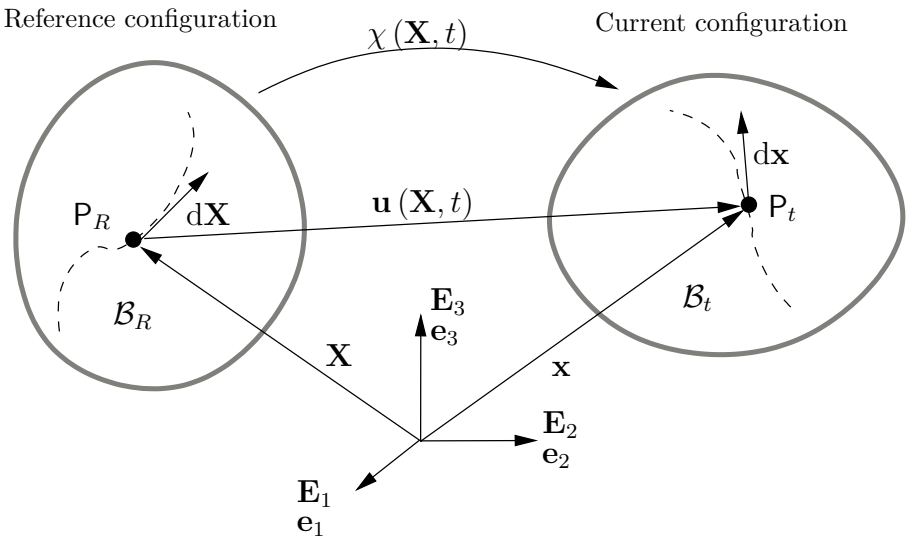

Figure 2.1.: Configuration, motion and deformation of a material body

$$\boldsymbol{\chi}\left(\mathsf{P}, t\right) = \mathbf{x}\left(\mathbf{X}, t\right) = \mathbf{X} + \mathbf{u}\left(\mathbf{X}, t\right) \tag{2.2}$$

$\boldsymbol{\chi}$ is denoted as motion and maps the material body from the reference configuration onto the current configuration in a bijective way, that means it is uniquely invertible. Thus it relates the position vectors of both configurations with each other.

If the motion or any other quantity is expressed as a function of the position vector $\mathbf{X}$ and time t, this description is called material (Lagrangian) description. It is particularly useful to track the motion of single material points. The spatial (Eulerian) description characterises the motion (or any other quantity) as function of the position vector $\mathbf{x}$. In the spatial description fixed points in space are focused and it is depicted how quantities change at these points in the course of time.

As a measure for local deformations in the vicinity of a material point the deformation gradient $\mathbf{F}$ is introduced as gradient of the motion $\boldsymbol{\chi}$.

$$\mathbf{F}\left(\mathbf{X}, t\right) = \frac{\partial \mathbf{x}}{\partial \mathbf{X}} = \frac{\partial \boldsymbol{\chi}\left(\mathbf{X}, t\right)}{\partial \mathbf{X}} \tag{2.3}$$

The deformation gradient maps the material tangent vector $\mathrm{d}\mathbf{X}$ into the spatial tangent vector $\mathrm{d}\mathbf{x}$. Since the deformation gradient defines a linear transformation, involving points in the

reference and the current configuration, it is invertible and denoted as two-point tensor.

$$\mathrm{d}\mathbf{x} = \mathbf{F}\left(\mathbf{X}, t\right)\,\mathrm{d}\mathbf{X} \quad \Leftrightarrow \quad \mathrm{d}\mathbf{X} = \mathbf{F}^{-1}\left(\mathbf{x}, t\right)\,\mathrm{d}\mathbf{x} \tag{2.4}$$

By means of the deformation gradient it is further possible to establish relations for local area and volume changes between the reference and the current configuration.

$$\mathrm{d}\mathbf{a} = \det\left(\mathbf{F}\right)\mathbf{F}^{-T}\,\mathrm{d}\mathbf{A} \tag{2.5}$$

$$\mathrm{dv} = \det\left(\mathbf{F}\right)\,\mathrm{dV} \tag{2.6}$$

It follows from the invertibility of the deformation gradient that $\det(\mathbf{F}) = J > 0$. This means that a material volume can never be compressed to a spatial volume equal to zero.

2.1.2. Strain tensors

The deformation from the reference configuration into the current configuration can be split into a pure rotation and a pure stretch by a polar decomposition of the deformation gradient.

$$\mathbf{F} = \mathbf{R}\mathbf{U} = \mathbf{V}\mathbf{R} \tag{2.7}$$

Therein, the rotation tensor $\mathbf{R}$ represents the rigid body rotations and the right and left stretch tensor $\mathbf{U}$ and $\mathbf{V}$, represent the local stretching, respectively. By means of the right and left stretch tensors it is possible to define the right ($\mathbf{C}$) and left Cauchy-Green tensor ($\mathbf{B}$). As local strain measures regarding the reference configuration and the current configuration, respectively, these strain tensors exclude any rigid body rotations.

$$\mathbf{C} = \mathbf{F}^T\mathbf{F} = \mathbf{U}^2 \quad \text{and} \quad \mathbf{B} = \mathbf{F}\mathbf{F}^T = \mathbf{V}^2 \tag{2.8}$$

For pure rotation ($\mathbf{F} = \mathbf{R}$) or no motion at all ($\mathbf{F} = \mathbf{1}$), the right and left Cauchy-Green tensor coincide with the identity tensor $\mathbf{1}$. Hence, the Green-Lagrange strain tensor $\mathbf{E}$, the Euler-Almansi strain tensor $\mathbf{A}$ (eq. (2.9)), the Piola tensor $\mathbf{e}$ and the Finger tensor $\mathbf{a}$ (eq. (2.10)) are introduced, in order to have a strain measure that coincides for pure rotation or no motion with the zero tensor $\mathbf{0}$.

$$\mathbf{E} = \frac{1}{2}\left(\mathbf{C} - \mathbf{1}\right) \qquad \text{and} \qquad \mathbf{A} = \frac{1}{2}\left(\mathbf{1} - \mathbf{B}^{-1}\right) \tag{2.9}$$

$$\mathbf{e} = \frac{1}{2}\left(\mathbf{C}^{-1} - \mathbf{1}\right) \qquad \text{and} \qquad \mathbf{a} = \frac{1}{2}\left(\mathbf{1} - \mathbf{B}\right) \tag{2.10}$$

Both, the Green-Lagrange strain tensor and the Piola tensor act on the reference configuration, whereas the Euler-Almansi strain tensor and the Finger tensor act on the current configuration. All four strain tensors are symmetric. Moreover, the Green-Lagrange strain tensor and the Euler-Almansi strain tensor as well as the Piola tensor and the Finger tensor can be transformed into each other by a push-forward operation (eq. (2.11)) and a pull back operation (eq. (2.12)),

respectively.

$$\mathbf{A} = \mathbf{F}^{-T}\mathbf{E}\mathbf{F}^{-1} \qquad \text{and} \qquad \mathbf{a} = \mathbf{F}\mathbf{e}\mathbf{F}^{T} \tag{2.11}$$

$$\mathbf{E} = \mathbf{F}^{T}\mathbf{A}\mathbf{F} \qquad \text{and} \qquad \mathbf{e} = \mathbf{F}^{-1}\mathbf{a}\mathbf{F}^{-T} \tag{2.12}$$

2.1.3. Rates of deformation tensors

Besides the deformation gradient and strain tensors, a detailed description of the material behaviour, especially the viscous deformation, requires the definition of the velocity gradient $\mathbf{L}$ with the aid of the material time derivative of the deformation gradient.

$$\dot{\mathbf{F}} = \frac{\partial}{\partial t}\left(\frac{\partial \mathbf{x}}{\partial \mathbf{X}}\right) = \frac{\partial \mathbf{v}}{\partial \mathbf{X}} = \frac{\partial \mathbf{v}}{\partial \mathbf{x}}\frac{\partial \mathbf{x}}{\partial \mathbf{X}} = \mathbf{L}\mathbf{F} \tag{2.13}$$

The velocity gradient can also be expressed as spatial gradient of the spatial velocity.

$$\mathbf{L} = \operatorname{grad}\mathbf{v}\left(\mathbf{x}, t\right) = \dot{\mathbf{F}}\mathbf{F}^{-1} \tag{2.14}$$

Additionally, the velocity gradient can be decomposed additively into the symmetric rate of deformation tensor ($\mathbf{D}$) and an anti-symmetric spin tensor ($\mathbf{W}$).

$$\mathbf{L} = \frac{1}{2}\left(\mathbf{L} + \mathbf{L}^{T}\right) + \frac{1}{2}\left(\mathbf{L} - \mathbf{L}^{T}\right) = \mathbf{D} + \mathbf{W} \tag{2.15}$$

Therein, the symmetric strain rate tensor $\mathbf{D}$ represents the rate of deformation of spatial tangent vectors. In contrast, the spin tensor $\mathbf{W}$ describes the angular velocity of spatial tangent vectors. The material time derivative of the Green-Lagrange strain tensor is given by

$$\dot{\mathbf{E}} = \frac{1}{2}\left(\dot{\mathbf{F}}^{T}\mathbf{F} + \mathbf{F}^{T}\dot{\mathbf{F}}\right) = \frac{1}{2}\dot{\mathbf{C}} \tag{2.16}$$

and a proportionality is existent to the material time derivative of the right Cauchy-Green tensor. Pushing this rate of the right Cauchy-Green tensor forward onto the current configuration yields the strain rate tensor.

$$\mathbf{F}^{-T}\dot{\mathbf{E}}\mathbf{F}^{-1} = \mathbf{D} = \overset{\triangle}{\mathbf{A}} = \dot{\mathbf{A}} + \mathbf{L}^{T}\mathbf{A} + \mathbf{A}\mathbf{L} \tag{2.17}$$

Herein, $\overset{\triangle}{\mathbf{A}}$ corresponds to the Oldroyd derivative of the Euler-Almansi strain tensor. In the textbook of Haupt, the different Oldroyd derivatives are defined [79].

2.1.4. Decomposition of deformation and intermediate configurations

For the description of specific material behaviours it can be advantageous to split the deformation gradient and to introduce one or more intermediate configurations $\mathcal{Z}$. These intermediate configurations do not have to be captured by the material itself, but rather serve to isolate different physical phenomena or special kinds of deformations within the complete deformation. This split leads to a multiplicative decomposition of the deformation gradient.
A volumetric-isochoric split was first introduced by Flory [59], where the motion is decomposed

into a change of shape (isochoric) and into a change of volume. For the isochoric part $\hat{\mathbf{F}}$ and for the volumetric part $\bar{\mathbf{F}}$ of the deformation gradient holds

$$\det(\hat{\mathbf{F}}) = \hat{J} = 1 \qquad \text{and} \qquad \bar{\mathbf{F}} = \bar{J}^{\frac{1}{3}}\mathbf{1} \quad . \tag{2.18}$$

It follows for the complete deformation gradient

$$\mathbf{F} = \bar{\mathbf{F}}\hat{\mathbf{F}} = \bar{J}^{\frac{1}{3}}\hat{\mathbf{F}} \quad . \tag{2.19}$$

The volumetric-isochoric split is used, when developing separate material functions for both parts. It is widely used in literature, especially for describing isotropic thermal expansions and chemical shrinkage phenomena, apart from the remaining incompressible mechanical behaviour [82, 138, 141]. It is important to notice that the sequence of decomposition does not matter.

A further kind of deformation split is the relative decomposition regarding the time domain.

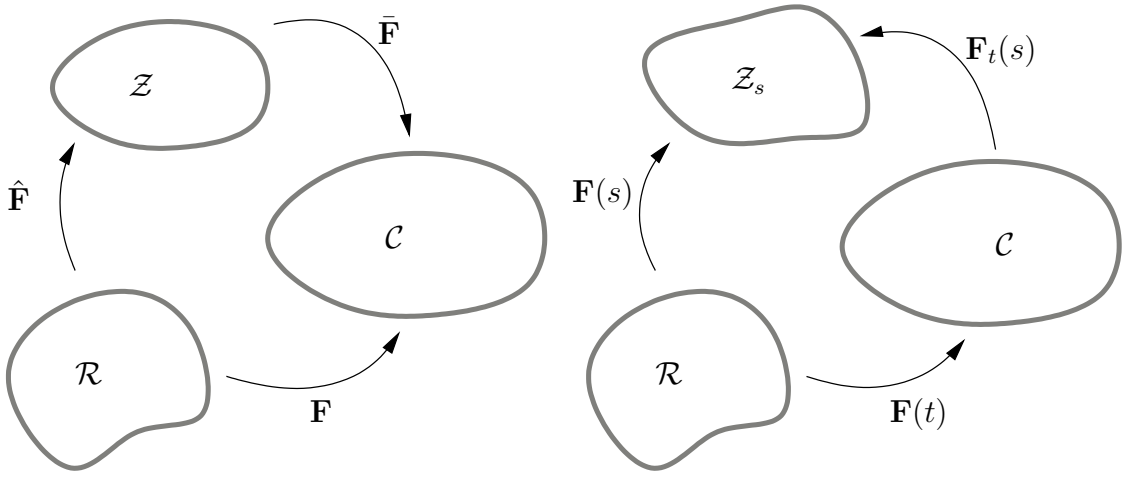

(a) Volumetric-isochoric decomposition (b) Relative decomposition

Figure 2.2.: Decomposition of motion

Therefore an intermediate configuration is introduced, which is occupied by the material body at time s, with $t_0 < s < t$ (cf. [80, 142]). However, this intermediate configuration is described from both, the reference configuration and the current configuration, as a current configuration (cf. fig. 2.2(a)). From the point of view of the intermediate configuration, the current configuration also acts as a reference configuration. In accordance with this mapping, the relative deformation gradient $\mathbf{F}_t(s)$ is defined as follows.

$$\mathbf{F}_t(s) = \mathbf{F}(s)\mathbf{F}^{-1}(t) \tag{2.20}$$

Hence, the relative deformation gradient maps from the present into the past.

Besides the volumetric-isochoric and the relative decomposition, further kinds of decompositions exist, for example into an elastic part and an inelastic part, in order to describe a special type of finite viscoelasticity [137]. This will be discussed briefly in sec. 3.5.

2.2. Stress and stress power

2.2.1. Stress measures

Kinetics describes the motion of a body disregarding its cause. Nonetheless, the material reacts to this motion by stresses. Similar to strain and strain rate measures, different stress tensors at finite deformation for both, the reference and the current configuration, exist. The symmetric

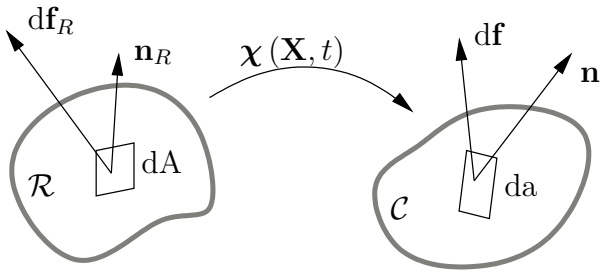

Figure 2.3.: Incremental forces acting on a hypothetical cut or actual surface of the reference and current configuration

Cauchy stress tensor $\mathbf{T}$ (also referred to as true stress) is defined on the current configuration and is a measure for the force $\mathrm{d}\mathbf{f}$ acting on a infinitesimal area da.

$$\mathrm{d}\mathbf{f} = \mathbf{t}\,\mathrm{da} = \mathbf{T}^T\,\mathbf{n}\,\mathrm{da} \tag{2.21}$$

Herein, $\mathbf{n}$ denotes the outward pointing surface normal vector, and $\mathbf{t}$ the traction vector. If the incremental force vector $\mathrm{d}\mathbf{f}$ is referred to the reference configuration, the first Piola-Kirchhoff stress tensor $\mathbf{P}$ is obtained.

$$\mathrm{d}\mathbf{f} = \mathbf{t}_R\,\mathrm{dA} = \mathbf{P}\,\mathbf{n}_R\,\mathrm{dA} \tag{2.22}$$

As the first Piola-Kirchhoff stress tensor relates the incremental force vector of the current configuration to oriented area vectors of the reference configuration, it is an unsymmetrical two-point tensor and states the so-called engineering stresses. Moreover, the second Piola-Kirchhoff-stress $\tilde{\mathbf{T}}$ is symmetric and defined as

$$\tilde{\mathbf{T}} = \mathbf{F}^{-1}\mathbf{P} \quad . \tag{2.23}$$

The above introduced stress measures can be converted into each other using the following relations.

$$\mathbf{T} = \frac{1}{J}\mathbf{P}\mathbf{F}^T \qquad = \frac{1}{J}\mathbf{F}\tilde{\mathbf{T}}\mathbf{F}^T \tag{2.24}$$

$$\mathbf{P} = J\mathbf{T}\mathbf{F}^{-T} \qquad = \mathbf{F}\tilde{\mathbf{T}} \tag{2.25}$$

$$\tilde{\mathbf{T}} = J\mathbf{F}^{-1}\mathbf{T}\mathbf{F}^{-T} = \mathbf{F}^{-1}\mathbf{P} \tag{2.26}$$

2.2.2. Stress power

An important quantity to formulate balance laws is the stress power, the product of a stress tensor and a strain rate. However, the stress power has to be identical regardless of the considered configuration. For this purpose conjugate variables, also referred to as dual variables, if the incremental stress power is considered [81], are introduced. Conjugate variables ensure that stress power is invariant to configurations. Within this work the stress power per unit volume in the reference configuration is formulated as scalar product of the second Piola-Kirchhoff stress tensor and the rate of the Green-Lagrange strain tensor,

$$\rho_R w_S = \tilde{\mathbf{T}} \cdot \dot{\mathbf{E}} \tag{2.27}$$

where ρ_R denotes the density in the reference configuration and w_S the stress power per unit mass. If the second Piola-Kirchhoff stress in eq. (2.27) is replaced with eq. (2.26) and taking into account eq. (2.17), the stress power with respect to the current configuration can be obtained.

$$\rho_R w_S = J\mathbf{F}^{-1}\mathbf{T}\mathbf{F}^{-T} \cdot \dot{\mathbf{E}} = J\mathbf{T} \cdot \mathbf{F}^{-T}\dot{\mathbf{E}}\mathbf{F}^{-1} = J\mathbf{T} \cdot \mathbf{D} \tag{2.28}$$

Consideration of the relationship (2.33) $\rho_R = J\rho$, which follows from eq. (2.6), yields

$$\rho w_S = \mathbf{T} \cdot \mathbf{D} \quad . \tag{2.29}$$

Furthermore, the stress power can be expressed in terms of the first Piola-Kirchhoff stress tensor, considering the symmetry of the Cauchy stress tensor.

$$\rho_R w_S = J\mathbf{T} \cdot \mathbf{D} = J\mathbf{T} \cdot \mathbf{L} = J\mathbf{T} \cdot \left(\dot{\mathbf{F}}\mathbf{F}^{-1}\right) = \mathbf{P} \cdot \dot{\mathbf{F}} \tag{2.30}$$

Eqs. (2.27) to (2.30) show that stress power can be equally expressed by the conjugate variables $\tilde{\mathbf{T}}$ and $\dot{\mathbf{E}}$, $\mathbf{T}$ and $\mathbf{D}$ as well as by $\mathbf{P}$ and $\dot{\mathbf{F}}$.

2.3. Balance equations

As mentioned in the beginning of this chapter, balance equations express fundamental laws of physics. They are independent of the material behaviour and have to be satisfied at any time. In the scope of classical mechanics the following principles are known:

- Conservation of mass
- Balance equation of linear momentum
- Balance equation of rotational momentum

In addition, the thermomechanical representation of material behaviour necessitates to include further thermodynamic principles:

- First law of thermodynamics

- Second law of thermodynamics

These thermodynamic principles relate the mechanical energy to thermal energy, and describe the conversion between both kinds of energy.
The above mentioned balance laws can be either expressed in a global (integral) or a local (differential) form, whereas the local form requires that the balanced quantities are continuously differentiable. Moreover, balance laws can be formulated with regard to both, the reference and the current configuration.

2.3.1. Conservation of mass

The conservation of mass indicates that the mass m of a material body is constant in the course of time, if no mass is added or removed.

$$m_R = \int_V \rho_R(\mathbf{X}, t)\, dV = \int_v \rho(\mathbf{x}, t)\, dv = \text{const.} \quad \Leftrightarrow \quad \frac{dm}{dt} = 0 \tag{2.31}$$

Assuming that this holds for arbitrary parts of the body, the local form of conservation of mass reveals the independence of density from time in material coordinates,

$$\frac{\partial}{\partial t}\rho_R(\mathbf{X}, t) = 0 \quad \Leftrightarrow \quad \rho_R = \rho_R(\mathbf{X}) \quad , \tag{2.32}$$

and leads to the following relation:

$$\rho_R = J\rho \tag{2.33}$$

If the conservation of mass is applied locally to the current configuration, the well known continuity equation is obtained (cf. [86]).

$$\frac{\partial \rho}{\partial t} + \operatorname{div}(\rho \mathbf{v}) = 0 \tag{2.34}$$

2.3.2. Balance of linear momentum

According to the balance of linear momentum, the change in linear momentum with respect to time of a body $\dot{\mathbf{I}}$ is equal to the sum of the surface ($\mathbf{t}$) and volume ($\mathbf{k}$) forces $\mathbf{f}$ acting on that body. In terms of the global material description the balance of momentum can be expressed as

$$\dot{\mathbf{I}} = \int_V \rho_R(\mathbf{X})\, \dot{\mathbf{v}}_R(\mathbf{X}, t)\, dV = \int_A \mathbf{t}_R(\mathbf{X}, \mathbf{n}_R, t)\, dA + \int_V \mathbf{k}_R(\mathbf{X}, t)\, \rho_R(\mathbf{X})\, dV = \sum \mathbf{f} \quad , \tag{2.35}$$

and corresponds in the current configuration to

$$\int_v \rho(\mathbf{x}, t)\, \dot{\mathbf{v}}(\mathbf{x}, t)\, dv = \int_a \mathbf{t}(\mathbf{x}, \mathbf{n}, t)\, da + \int_v \mathbf{k}(\mathbf{x}, t)\, \rho(\mathbf{x}, t)\, dv \quad . \tag{2.36}$$

Herein A and a denote the material and spatial surface respectively, and $\mathbf{v}$ denotes the spatial velocity. By means of eq. (2.21) and the divergence theorem, the spatial surface integral in eq.

(2.36) can be transformed into a volume integral.

$$\int_a \mathbf{t} da = \int_a \mathbf{T}\mathbf{n} da = \int_v \operatorname{div} \mathbf{T} dv \tag{2.37}$$

Hence, the local spatial description of the conservation of momentum states as

$$\operatorname{div} \mathbf{T} + \rho \mathbf{k} = \rho \frac{d\,\mathbf{v}}{dt} \quad . \tag{2.38}$$

Taking into consideration the relationship $\operatorname{div} \mathbf{T} = J^{-1} \operatorname{div} \mathbf{P}$ and eq. (2.33), the local material form of conservation of momentum can be derived.

$$\operatorname{div} \mathbf{P} + \rho_R \mathbf{k}_R = \rho_R \frac{d\,\mathbf{v}_R}{dt} \tag{2.39}$$

2.3.3. Balance of rotational momentum

The balance of rotational momentum is satisfied, if the temporal change in rotational momentum with respect to a certain point P is equal to the sum of all moments acting on the same point, resulting from both, surface and volume forces. Regarding the evaluation of conservation of rotational momentum within the current configuration yields the symmetry of the Cauchy stress tensor and, including eq. (2.26), the symmetry of the second Piola-Kirchhoff stress tensor.

$$\mathbf{T} = \mathbf{T}^T \quad \text{and} \quad \tilde{\mathbf{T}} = \tilde{\mathbf{T}}^T \tag{2.40}$$

However, as a two-point tensor the first Piola-Kirchhoff stress is not symmetric.

2.3.4. First law of thermodynamics

The first law of thermodynamics balances thermal and mechanical energies and therefore relates different kinds of energies in a system. The temporal change in internal (E_{in}) and kinetic (E_{kin}) energy, also referred to as total energy, has to be equal to the externally supplied mechanical (L) and thermal (Q) power.

$$\dot{E}_{kin} + \dot{E}_{in} = L + Q \tag{2.41}$$

Besides, the balance of mechanical energy (also called theorem of power expended) states that the externally supplied mechanical energy is equal to the sum of change in kinetic energy and stress power.

$$L = \dot{E}_{kin} + w_S \tag{2.42}$$

For proof of this relation the reader is referred to [79]. Using eq. (2.42) the first law of thermodynamics (eq. (2.41)) simplifies to

$$\dot{E}_{in} = w_S + Q \quad . \tag{2.43}$$

Expressed in words, eq. (2.43) states that the change in internal energy $\dot{E}_{in}$ is equal to the sum of stress power w_S and thermal power Q. From a physical point of view, the thermal power consists of a volume distributed heat source within the body and heat supply over the surfaces. In terms of the current configuration, the thermal power can be expressed as

$$Q = \int_v \rho r dv - \int_a \mathbf{n} \cdot \mathbf{q} da \quad , \tag{2.44}$$

where r denotes the local energy supply per unit mass and $\mathbf{q}$ is the heat flux vector. From eqs. (2.27), (2.29) and (2.30), the stress power is already known. Applying the divergence theorem and expressing the material time derivative of the internal energy $\dot{E}_{in}$ with aid of the specific internal energy e, eq. (2.43) can be written in the global spatial form

$$\int_v \rho \dot{e} dv = \int_v \left(\mathbf{T} \cdot \mathbf{D} - \operatorname{div} \mathbf{q} + \rho r \right) dv \quad , \tag{2.45}$$

and hence in the local spatial description

$$\rho \dot{e} = \mathbf{T} \cdot \mathbf{D} - \operatorname{div} \mathbf{q} + \rho r \quad . \tag{2.46}$$

The transformation into the reference configuration yields the local material description

$$\rho_R \dot{e} = \tilde{\mathbf{T}} \cdot \dot{\mathbf{E}} - \operatorname{Div} \mathbf{q}_R + \rho_R r \quad , \tag{2.47}$$

and the global material description

$$\int_V \rho_R \frac{\partial e}{\partial t} dV = \int_V \left(\tilde{\mathbf{T}} \cdot \dot{\mathbf{E}} - \operatorname{Div} \mathbf{q}_R + \rho_R r \right) dV \quad . \tag{2.48}$$

2.3.5. Second law of thermodynamics

The first law of thermodynamics states that the energy cannot be destroyed or generated, but can only be transformed form one kind of energy into another kind. However, it does not include any information about the direction of energy transformation. This information is provided by the second law of thermodynamics and introduces the concept of entropy. Entropy can be considered as a measure for the amount of energy that is irreversible transformed during a process and cannot be converted back to perform mechanical work [7]. An increase of entropy is associated with a transition from an ordered into a more disordered state within a system. In contrast, if a process is completely reversible, the entropy stays constant. Thus, according to the second law of thermodynamics, the rate of entropy has to be equal to or greater than the externally supplied entropy into the system (over surfaces and in the volume) and the generated entropy within a system. This leads to the following global spatial description of the second law of thermodynamics.

$$\frac{d}{dt} \int_v \rho s dv \geq \int_v \rho \frac{r}{\theta} dv - \int_a \frac{\mathbf{n} \cdot \mathbf{q}}{\theta} da \tag{2.49}$$

which is also known as the Clausius-Duhem inequality (C.D.I.). Therein, s denotes the specific entropy and θ the thermodynamic temperature. Using the divergence theorem, the local spatial form can be derived as

$$\rho\theta\dot{s} - \rho r + \operatorname{div}\mathbf{q} - \frac{1}{\theta}\mathbf{q}\cdot\operatorname{grad}\theta \geq 0 \quad . \tag{2.50}$$

The right hand side of eq. (2.50) is considered as dissipation in a spatial point. Similarly, the second law of thermodynamics can also be expressed in terms of the reference configuration, in a global

$$\frac{\partial}{\partial t}\int\limits_V \rho_R s dV \geq \int\limits_V \rho_R \frac{r}{\theta} dV - \int\limits_A \frac{\mathbf{n}_R\cdot\mathbf{q}_R}{\theta} dA \quad , \tag{2.51}$$

and a local form

$$\rho_R\theta\frac{\partial s}{\partial t} - \rho_R r + \operatorname{Div}\mathbf{q}_R - \frac{1}{\theta}\mathbf{q}_R\cdot\operatorname{Grad}\theta \geq 0 \quad . \tag{2.52}$$

The second law of thermodynamics is not a balance principle in the strict sense that governs mechanical and thermal processes. It rather makes demands on constitutive equations describing the thermal and mechanical material behaviour. These constitutive equations have to satisfy the second law of thermodynamics to show that they are consistent with the principle of irreversibility and cannot generate energy on their own. In order to evaluate the second law of thermodynamics, the application of thermodynamic potentials is quite common in continuum mechanics [93]. These potentials represent the thermodynamic state of the system or body in terms of natural or independent variables. Four kinds of thermodynamic potentials are well established for the mathematical description of material behaviours, namely the specific internal energy e, the specific free energy ψ, the specific enthalpy h and the specific free enthalpy g. They can be converted into each other by the following Legendre transformations:

$$\psi = e - \theta s \quad , \quad h = e - \frac{1}{\rho_R}\tilde{\mathbf{T}}\cdot\mathbf{E} \quad \text{and} \quad g = \psi - \frac{1}{\rho_R}\tilde{\mathbf{T}}\cdot\mathbf{E} \tag{2.53}$$

According to the particular thermodynamic potential chosen for modelling purposes and evaluation of the C.D.I., there exists a set of independent canonical variables (cf. [79, 140]). In general, the specific free energy is chosen as thermodynamic potential and formulated for thermomechanical material modelling, because deformation and temperature (as well as internal variables (cf. sec. 6.2)) are then defined as independent variables. This is especially useful for identifying the parameters of constitutive equations by experimental data, where deformation and temperature are controlled. However, it might be more convenient to use the spcific enthalpy or the specific free enthalpy as thermodynamic potentials, particularly, when considering calorimetric experiments under isobaric conditions [143, 144, 145, 146].

If the specific free energy is applied as thermodynamic potential, the local material form of the C.D.I. can be transformed for evaluation by taking into account eq. (2.47) and (2.53).

$$-\rho_R\dot{\psi} + \tilde{\mathbf{T}}\cdot\dot{\mathbf{E}} - \rho_R s\dot{\theta} - \frac{1}{\theta}\mathbf{q}_R\cdot\operatorname{Grad}\theta \geq 0 \tag{2.54}$$

This form of the C.D.I. will later be used to derive constraints for constitutive relations to guarantee thermomechanical consistency (cf. [39, 41]).

2.4. Constitutive equations

After kinematic relations and balance laws have been introduced in sec. 2.1 and 2.3, constitutive laws are required that describe the individual material properties of bone cement, e.g. in dependence on deformation and temperature. Constitutive laws link all phenomenological variables describing the macroscopic continuum behaviour, and therefore expand kinematic relations and balance laws to a solvable set of equations [7]. Process variables are stress, strain, temperature and heat flux etc., regarding mechanics and thermomechanics, but, depending on the continuum problem, this set of variables can be expanded further (e.g. internal variables, cf. ch. 6), if additional physical phenomena are considered (e.g. curing).
In general, the development of such constitutive equations has to account for the following constitutive principles in order to guarantee mathematical and physical consistency [7]:

- **Causality** - Dependent and independent variables have to be distinguished.
- **Determinism** - The present state of the continuum depends on the current loading and the load history.
- **Equipresence** - All independent variables have to appear initially in every constitutive equation, to identify possible interactions.
- **Material objectivity** - Constitutive relations have to be independent from the frame of reference (cf. [96]).
- **Local action** - The current state of a material point is only influenced by the immediate vicinity of the material point.
- **Fading memory** - Loading events in the far past have less influence on the current state of a continuum than loading events in the near past.
- **Physical consistency** - Constitutive equations have to be consistent with the balance laws and especially with the second law of thermodynamics.

These principles will be discussed in more detail together with the constitutive equations of viscoelasticity in chapter 3. Furthermore, one constitutive equation has to be developed for each dependent variable, whereas the choice of dependent variables is subjectively. In case of heat transfer, Fourier's law is commonly used (cf. sec. 6.6.5). However, for describing the mechanical behaviour, different material classes exist. In the solid domain the most established material classes are elasticity, plasticity, viscoplasticity and viscoelasticity and in the fluid domain, elasticity (perfect gas) and viscosity [79]. Materials are assigned to these material classes according to their mechanical behaviour. Since these material classes exhibit specific characteristics, they

differ in the form of their mathematical description (proportional, integral or differential). More complex material properties, e.g. the influence of ageing, glass transition, curing etc. (cf. ch. 6), require the extension of these basic material classes and the set of constitutive equations may get coupled more strongly.
The presence of material symmetries, like isotropy or orthotropy, and kinematic constraints, like incompressibility, usually simplify the constitutive equations.

3. Viscoelasticity

In literature, bone cement material is often assumed as a non Newtonian viscous fluid [18, 112, 220] in the liquid state or, after curing, as a linear elastic solid [33, 179]. However, the experimental mechanical analysis of acrylic bone cements shows more complex effects, such as die swelling, stress relaxation, creep and damping under cyclic loading (cf. ch. 5), which can not be captured by pure viscous or elastic constitutive equations respectively. These effects indicate clearly a viscoelastic material behaviour and therefore viscoelastic constitutive equations will be customised and used to model the material behaviour of bone cement (cf. ch. 6). This chapter will give an overview of viscoelastic constitutive equations in anticipation of ch. 6, where the material modelling of an acrylic bone cement will be presented in detail.
The first section deals with the basic principles of linear viscoelasticity based on rheological elements. A deeper insight into these topics is provided by the works of Lion [139] and Tschoegl [225]. Based on the special material behaviour of polymers, linear viscoelastic concepts are also discussed in the textbooks of Tobolsky [223], Ferry [57], Krawietz [113] and Schwarzl [209]. In the remaining section the theory will be extended to finite strains.

3.1. Principles of linear viscoelasticity

In linear viscoelasticity only small strains are considered. Furthermore, the material is supposed to behave linearly, so that the superposition principle according to Boltzmann is applicable. In general, linear viscoelastic material behaviour can be expressed as a functional relationship between stress and strain.

$$\sigma(t) = \int_0^t G(t-s)\,\varepsilon'(s)\,ds \quad \Leftrightarrow \quad \varepsilon(t) = \int_0^t J(t-s)\,\sigma'(s)\,ds \tag{3.1}$$

Within these two equivalent expressions, the current stress $\sigma(t)$ can be expressed as a linear functional of the deformation history $\varepsilon(t-s)$, with $0 \leq s \leq t$, or vice versa. The relaxation function $G(t)$ and accordingly the creep function $J(t)$ relate the dependent variable to the rate of the independent variable for strain-controlled processes and stress-controlled processes. Moreover, the relaxation function and the creep function can be transformed into each other.
In general, it is difficult to formulate material specific relaxation functions by means of experimental data. For this reason, the relaxation functions are derived with the aid of rheological elements. By combination of different rheological elements in parallel or in series, it is possible

to describe a wide range of mechanical material behaviours. For the purpose of modelling linear viscoelasticity, a combination of a spring and a damping element is used. In order to model other kinds of material behaviour, e.g. plasticity, other or additional element types, like friction elements are applied, but they are not considered more closely here.

3.2. Maxwell element

Regarding viscoelasticity, in the most basic case for strain space formulation, this combination of rheological elements equates to a connection in series of a spring and a damping element and is called Maxwell element. The material parameters in this model are the elasticity modulus E

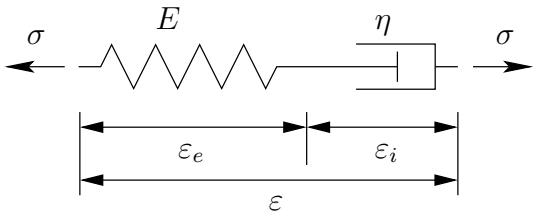

Figure 3.1.: Schematic representation of a Maxwell element

of the spring and the viscosity η of the dashpot. For describing the stress strain relation of a Maxwell element, the total deformation ε is split up into an elastic deformation of the spring ε_e and an inelastic deformation ε_i.

$$\varepsilon = \varepsilon_e + \varepsilon_i \tag{3.2}$$

For both elements, separate constitutive equations can be formulated.

$$\sigma = E\varepsilon_e \quad \text{and} \quad \sigma = \eta\dot{\varepsilon}_i \tag{3.3}$$

Taking into account eq. (3.2), the following constitutive equation can be derived for the Maxwell element:

$$\dot{\sigma} + \frac{1}{\tau}\sigma = E\dot{\varepsilon} \quad \text{with} \quad \tau = \frac{\eta}{E} \quad . \tag{3.4}$$

Herein, τ denotes the relaxation time. The solution in the sense of eq. (3.4) can be expressed in the familiar strain space and stress space formulation,

$$\sigma(t) = \int_0^t E \exp\left(-\frac{t-s}{\tau}\right) \varepsilon'(s)\, ds \quad \text{and} \quad \varepsilon(t) = \int_0^t \left(\frac{1}{E} - \frac{t-s}{\eta}\right) \sigma'(s)\, ds \quad , \tag{3.5}$$

and the relaxation function $G(t)$ as well as the creep function $J(t)$ according to eq. (3.1) can be identified as

$$G(t) = E \exp\left(-\frac{t}{\tau}\right) \quad \text{and} \quad J(t) = \frac{1}{E} - \frac{t}{\eta} \quad . \tag{3.6}$$

The relaxation function characterises the material response to spontaneous strain loading. Thereby, τ denotes the time when the stress response has decreased to 36.8% of the initial value. Accordingly, the creep function represents the material response to a spontaneous stress loading.
The Maxwell element is often extended to a three-parameter model by a single parallel spring [139, 225] to explain equilibrium phenomena of viscoelasticity, but this will not be discussed in more detail here.

3.2.1. Thermomechanical consistency

The thermodynamic consistency of the Maxwell element can be shown by evaluating the second law of thermodynamics in a one-dimensional, isothermal case considering small deformations [138].

$$\sigma\dot{\varepsilon} - \rho\dot{\psi} \geq 0 \tag{3.7}$$

Furthermore, the specific free energy of the Maxwell element is equivalent to the mechanical energy stored in the spring.

$$\rho\psi = \frac{1}{2}E\varepsilon_e^2 \tag{3.8}$$

Using eqs. (3.2), (3.3) together with the time derivative of the free energy, according to eq. (3.8) and inserting them into this form of the second law of thermodynamics, it yields the following inequality:

$$\sigma\dot{\varepsilon} - \rho\dot{\psi} = \sigma\dot{\varepsilon}_i = \frac{1}{\eta}\sigma^2 \geq 0 \quad . \tag{3.9}$$

As long as the viscosity η is greater than zero, the inelastic stress power is greater than or equal to zero and the constitutive equations (3.3) are conform with the Clausius-Duhem inequality. It has to be further notified that the viscosity must not be necessarily constant but can be a functional of the thermomechanical process history and the elasticity modulus E can be a function of the elastic strain ε_e [138]. This will be discussed in more detail in ch. 6.

3.2.2. Material response to harmonic loading

Aside from relaxation and creep, viscoelastic materials show a distinctive behaviour when loaded harmonically. The time-dependent harmonic excitation as well as the associated steady state material response can be expressed by complex representation as follows:

$$\varepsilon(t) = \varepsilon_0 \exp(i\omega t) \quad \text{and} \quad \sigma(t) = \sigma_0 \exp(i\omega t) \quad . \tag{3.10}$$

Inserting the harmonic strain excitation and stress response into eq. (3.4) yields the stress strain relation

$$\sigma_0(\omega) = \left(\underbrace{\frac{(\omega\tau)^2 E}{1+(\omega\tau)^2}}_{G'(\omega)} + i \underbrace{\frac{\omega\tau E}{1+(\omega\tau)^2}}_{G''(\omega)} \right) \varepsilon_0(\omega) = G^*(\omega)\,\varepsilon_0(\omega) \quad . \tag{3.11}$$

G^* is called the complex modulus and characterises the viscoelastic material behaviour under harmonic loading. The real part of the complex modulus G^* is denoted as storage modulus G' and is a measure for the reversible stored energy, that is in phase with the excitation. In contrast, the imaginary part of the complex modulus G^*, indicated as loss modulus G'', represents the irreversible, dissipative energy, that is out of phase. The quotient of loss modulus and storage modulus is referred to as loss tangent

$$\tan\delta = \frac{G''(\omega)}{G'(\omega)} \tag{3.12}$$

and contains the loss angle. The loss angle describes the angular phase shift between loading and response. In this context, the absolute value of the complex modulus is denominated as absolute modulus $\tilde{G}(\omega)$

$$\tilde{G}(\omega) = \sqrt{G'^2(\omega) + G''^2(\omega)} \tag{3.13}$$

For a sinusoidal excitation the stress response can expressed as

$$\sigma(t) = \varepsilon_0 \left(G'(\omega)\sin(\omega t) + G''(\omega)\cos(\omega t) \right) = \varepsilon_0 \tilde{G}(\omega)\sin(\omega t + \delta) \quad . \tag{3.14}$$

Moreover, the complex modulus can also be expressed in terms of the relaxation function

$$G^*(\omega) = i\omega \int_0^\infty G(t)\exp(-i\omega t)\,dt \quad . \tag{3.15}$$

If the harmonic loading is not strain-, but stress-controlled, a complex compliance J^* is introduced, whereat $G^*J^* = 1$ holds [57].

3.3. Generalised concepts for linear viscoelasticity

A single Maxwell element is appropriate to characterise the common phenomena of viscoelasticity in a qualitative way. However, in order to describe the mechanical behaviour of real viscoelastic materials quantitatively, its adaptability is not sufficient in most cases. To obtain more flexibility in the representation of a specific material behaviour a series of parallelly connected Maxwell elements can be employed. For a chain of n parallelised Maxwell elements, also referred to as generalised Maxwell model, the relaxation function can be expressed as a sum of exponential

functions, also known as Prony series.

$$G(t) = \sum_{k=1}^{n} E_k \exp\left(-\frac{t}{\tau_k}\right) \tag{3.16}$$

This representation is called discrete relaxation spectrum. Likewise, the storage and loss modulus can be written as

$$G'(\omega) = \sum_{k=1}^{n} E_k \frac{(\omega\tau_k)^2}{1+(\omega\tau_k)^2} \quad \text{and} \quad G''(\omega) = \sum_{k=1}^{n} E_k \frac{(\omega\tau_k)}{1+(\omega\tau_k)^2} \quad . \tag{3.17}$$

The stress response is now the sum of the stresses in every single branch (Maxwell elements).

$$\sigma(t) = \sum_{k=1}^{n} \sigma_k(t) = \int_0^t \left(\sum_{k=1}^{n} E_k \exp\left(-\frac{t-s}{\tau_k}\right)\right) \varepsilon'(s)\, ds \tag{3.18}$$

Altogether, the generalised Maxwell model has $2n$ parameters to be identified in order to represent the experimentally observed viscoelastic material behaviour. By increasing the number of Maxwell elements in the chain and reasonably choosing the parameters, the real material behaviour can be adapted with arbitrary accuracy. Fig. 3.2(a) and 3.2(b) illustrate that the generalised Maxwell model offers more freedom for fitting a specific viscoelastic behaviour. Furthermore, the storage moduli in fig. 3.2(a) show a distinctive dispersion area at the frequencies corresponding to the relaxation times specified in the models. In contrast, the loss moduli show maxima at the same frequencies.

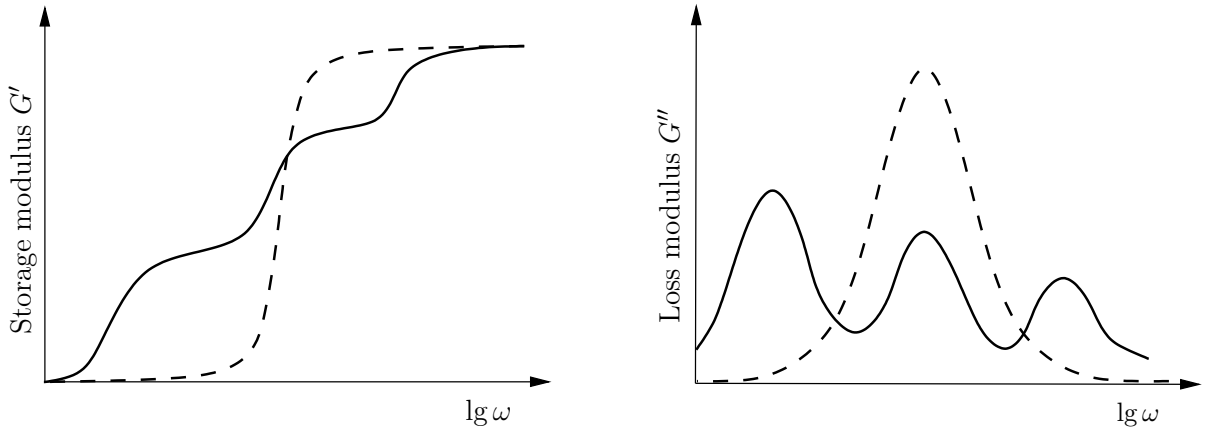

(a) Storage modulus (b) Loss modulus

Figure 3.2.: Comparison of spectra for Maxwell element (- -) and Maxwell chain (n=3)(—)

For determining the number of $2n$ parameters of the generalised Maxwell model there exist several strategies [225]. Using the discrete relaxation spectrum the viscoelastic material behaviour can be described by n ordinary differential equations.

To reduce the number of parameters the discrete relaxation spectrum can be replaced by a continuous relaxation spectrum, especially when the relaxation times are closely spaced [139, 225]. The relaxation function is thereby not given by a sum of exponential functions but by an integral

formulation.

$$G(t) = \int_0^\infty c(\tau) \exp\left(-\frac{t}{\tau}\right) d\tau \tag{3.19}$$

The distribution of moduli $c(\tau)$ can be specified in the crucial range of relaxation times and has to be non-negative. An interesting discussion and comparison of a viscoelastic material model for cured bone cement formulated with the aid of continuous and discrete relaxation spectra is given by Lion at al. [147]. Continuous relaxation spectra are convenient for analytical investigations, however, it is usually difficult to apply them for numerical simulations based on the finite element method. For this reason, they will not be studied any further within this framework. For further discussions on viscoelastic material models with continuous relaxation spectra the textbooks of Tobolsky and Tschoegl are suggested [223, 225].

3.4. Temperature and process-dependent viscosities

So far, only the time-dependent and accordingly the frequency-dependent behaviour of linear viscoelastic materials has been considered. However, acrylic bone cement is exposed to varying temperatures during a minimal invasive intervention and, in addition, undergoes a dissolution and a polymerisation process. Due to these temperature loadings and processes the viscoelastic material behaviour changes (cf. sec. 5.7). For example, both, the storage and loss modulus increase with proceeding polymerisation. To incorporate these phenomena into the rheological model presented above, the viscosities are supposed to change with temperature and/or other processes. The elastic moduli remain constant in order to preserve thermodynamic consistency. This leads to the concept of process-dependent viscosities.
Using the example of temperature, variable viscosities are typically described by the subsequent expression:

$$\eta(\theta) = \eta(\theta_0)\, a(\theta) \quad , \quad a(\theta) > 0 \quad \text{and} \quad a(\theta_0) = 1 \quad . \tag{3.20}$$

Therein θ_0 is an arbitrary reference temperature. For most polymers relaxation and creep processes are faster at high temperatures and slower at low temperatures [209] so that $\partial a / \partial \theta \leq 0$ holds. To satisfy the second law of thermodynamics, the viscosities have to be non-negative at any time and therefore, a has to be non-negative. Furthermore, a new temperature-dependent time scale $z(t)$ can be introduced.

$$\dot{z} = \frac{1}{a(\theta(t))} \quad \Rightarrow \quad z(t) = \int_0^t \frac{ds}{a(\theta(s))} \tag{3.21}$$

Considering eq. (3.21), it is obvious that the temperature-dependent time scale $z(t)$, also referred to as material time,

- is equal to the physical t time, if $\theta(t) = \theta_0$ and $a(\theta) = 1$

- runs faster than the physical time t, if $\theta(t) > \theta_0$ and $a(\theta) < 1$
- runs slower than the physical time t, if $\theta(t) < \theta_0$ and $a(\theta) > 1$

Now it is possible that stress and strain are specified as a function of the material time z instead of the physical time t. Taking also into account the temperature-dependent viscosity in eq. (3.20) and the rate of the material time z in eq. (3.21), the differential equation (3.4) can be rewritten as

$$\frac{d\sigma}{dz}\dot{z} + \frac{1}{a(\theta(t))}\frac{1}{\tau}\sigma = E\frac{d\varepsilon}{dz}\dot{z} \quad \Leftrightarrow \quad \dot{\sigma} + \frac{\dot{z}}{\tau}\sigma = E\dot{\varepsilon} \quad , \tag{3.22}$$

whereat

$$\dot{\sigma}(z(t)) = \sigma'(z)\,\dot{z} \quad \text{and} \quad \dot{\varepsilon}(z(t)) = \varepsilon'(z)\,\dot{z} \tag{3.23}$$

holds. The differential equation (3.22b) is identical to eq. (3.4a), but it refers to the material time z and hence the solution can be written as

$$\sigma(t) = \int_0^{z(t)} E\exp\left(-\frac{z(t)-w}{\tau}\right)\varepsilon'(w)\,dw \quad , \quad z(t) = \int_0^t \frac{ds}{a(\theta(s))} \quad \text{and} \quad w(u) = \int_0^u \frac{ds}{a(\theta(s))} \quad . \tag{3.24}$$

By substituting the physical time t by a material time z, it is not only possible to consider temperature-dependent viscosities, but also any other dependence of viscoelasticity material [139], for example on humidity [183] or on the amplitude of strain [185]. Accordingly, the material time z is not a functional of the temperature history, but of the corresponding parameter.

3.4.1. Superposition principle

A thermorheologically simple material is characterised by the fact that its mechanical behaviour can be described by a Maxwell chain, where all viscosities depend on temperature, and only on temperature, in the same manner. Otherwise the material is referred to as thermorheologically complex. In case of thermorheologically simple materials the time-temperature- and the frequency-temperature-superposition can be applied, which are very helpful for the experimental characterisation of the material and the parameter identification of the model. In the following these superposition principles will be explained in more detail. Aside from temperature, these superposition principles can also be transferred to other parameters, like humidity, stress, strain rate etc. [139].

The superposition principle states that, when experimentally analysing thermorheologically simple materials, time and temperature and, accordingly, frequency and temperature are equivalent. Descriptively, this means at higher temperatures than the reference temperature, the dispersion areas (cf. fig. 3.2) shift to shorter times and higher frequencies and at lower temperatures the dispersion areas shift to longer times and lower frequencies (cf. fig. 3.3) [209]. It is obvious that either increasing the time / decreasing the frequency or decreasing the temperature has the same effect on the relaxation function / storage modulus.

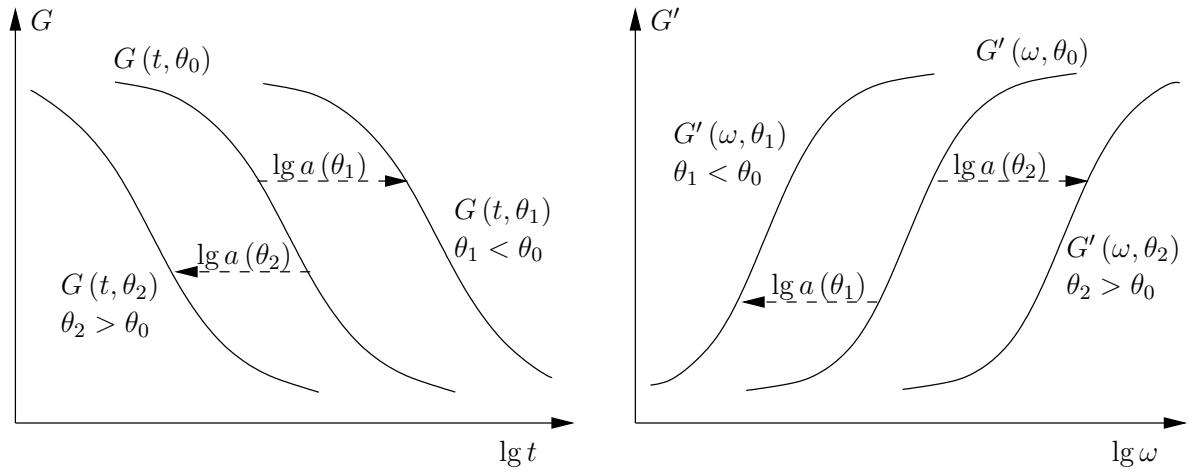

Figure 3.3.: Time-temperature superposition for relaxation function and frequency-temperature superposition for storage modulus

Mathematically, this relationship can be expressed for the relaxation function

$$G\left(t,\theta\right)=G_{\theta_0}\left(t/a\left(\theta\right)\right)=G_{\theta_0}\left(10^{lg(t)-lg(a(\theta))}\right) \tag{3.25}$$

and for the storage modulus

$$G'\left(\omega,\theta\right)=G'_{\theta_0}\left(\omega a\left(\theta\right)\right)=G'_{\theta_0}\left(10^{lg(\omega)+lg(a(\theta))}\right) \quad , \tag{3.26}$$

whereat the function $a\left(\theta\right)$, known from above, is called time-temperature-superposition factor or simply shift function and satisfies the requirements given in eq. (3.20).
Thus the superposition principle offers further possibilities when experimentally characterising thermorheologically simple materials. By varying the temperature, the frequency range for a reference temperature can be extended to regions that are usually experimentally not accessible, either due to the very long duration of the experiment or due to limitations of the testing equipment [94, 185, 187].

3.5. Concepts for finite viscoelasticity

The previous considerations are only valid for small, one-dimensional deformations. During the polymerisation of bone cement a volume shrinkage of 6-8 % (cf. sec. 5.4) occurs which can lead to deformations, where the assumption of small strains is not admissible any longer. For this reason, the model presented in ch. 6 is based on finite strain viscoelasticity. Coleman and Noll [40] were among the first to transfer the linear theories of viscoelasticity, presented above, into the framework of finite strains, explained in chapter 2. In the past, two main concepts have been established to describe finite viscoelasticity on a phenomenological basis, namely multiplicative viscoelasticity and functional viscoelasticity. Both concepts will be outlined shortly.

3.5.1. Multiplicative viscoelasticity

Multiplicative viscoelasticity is based on a split of the deformation gradient into an elastic part and a viscous part, as mentioned in sec. 2.1.4 and was first proposed by Lubliner [149].

$$\mathbf{F} = \mathbf{F}_e \mathbf{F}_v \tag{3.27}$$

Taking into account the definition of the Green-Langrange strain tensor, given by eqs. (2.8a) and (2.9a), the multiplicative split leads to an additive decomposition of the strain tensor on the intermediate configuration.

$$\boldsymbol{\Gamma} = \mathbf{F}_v^{-T} \mathbf{E} \mathbf{F}_v^{-1} = \frac{1}{2}\left(\mathbf{F}_e^T \mathbf{F}_e - \mathbf{1}\right) + \frac{1}{2}\left(\mathbf{1} - \mathbf{F}_v^{-T} \mathbf{F}_v^{-1}\right) = \boldsymbol{\Gamma}_e + \boldsymbol{\Gamma}_v \tag{3.28}$$

This can be considered in analogy to the one-dimensional case, where the overall deformation is also split into an elastic and an inelastic part (cf. eq. (3.2)). Similarly, the strain rate on the intermediate configuration, using eq. (2.17), is also split into an elastic and a viscous part.

$$\overset{\triangle}{\boldsymbol{\Gamma}} = \mathbf{F}_v^{-T} \dot{\mathbf{E}} \mathbf{F}_v^{-1} = \left(\boldsymbol{\Gamma}_e + \boldsymbol{\Gamma}_v\right)^{\bullet} + \mathbf{L}_v^T \left(\boldsymbol{\Gamma}_e + \boldsymbol{\Gamma}_v\right) + \left(\boldsymbol{\Gamma}_e + \boldsymbol{\Gamma}_v\right) \mathbf{L}_v = \overset{\triangle}{\boldsymbol{\Gamma}}_e + \overset{\triangle}{\boldsymbol{\Gamma}}_v = \mathbf{D}_e + \mathbf{D}_v \tag{3.29}$$

The evaluation of the resulting stress and the elastic strain tensor is carried out with the aid of further constitutive equations:

$$\mathbf{T} = \frac{\partial \psi\left(\boldsymbol{\Gamma}_e\right)}{\partial \boldsymbol{\Gamma}_e} \quad \text{and} \quad \mathbf{T} = \eta\, f\left(\mathbf{D}_v\right) \quad . \tag{3.30}$$

The analogy to eqs. (3.3a) and (3.3b) is obvious. For eq. (3.30a) a specific free energy has to be formulated, depending on the elastic strain tensor. Due to the structure of the constitutive equations this kind of finite viscoelasticity is based on internal variables of strain type. Examples for multiplicative viscoelasticity can be found in Reese and Govindjee [184] and Johlitz [101].

3.5.2. Functional viscoelasticity

Contrary to multiplicative viscoelasticity, there is no need for introducing an intermediate configuration in functional viscoelasticity. In fact, stress is regarded in the most general case as a functional of the deformation history here.

$$\tilde{\mathbf{T}} = \underset{s \leq t}{\mathfrak{F}} \left[\mathbf{E}\left(s\right)\right] \tag{3.31}$$

However, the formulation of a functional only based on experiments is difficult, as stated in sec. 3.1. For this reason, the concept of rheological elements is also regarded in finite viscoelasticity. Reflecting the differential equation (3.4), a similar expression can be formulated in terms of the reference configuration for the case of finite strains:

$$\dot{\tilde{\mathbf{T}}} + \frac{1}{\tau}\tilde{\mathbf{T}} = -2\rho_R \mu \dot{\mathbf{e}} \quad . \tag{3.32}$$

Herein μ is an elasticity parameter. The solution to eq. (3.32) can be obtained by expanding with $\exp\left(\frac{t}{\tau}\right)$

$$\exp\left(-\frac{t}{\tau}\right)\left(\exp\left(\frac{t}{\tau}\right)\tilde{\mathbf{T}}\right)^{\bullet} = -2\rho_R\mu\dot{\mathbf{e}} \tag{3.33}$$

and integrating

$$\tilde{\mathbf{T}} = -\int_{-\infty}^{t} 2\rho_R\mu\exp\left(-\frac{t-s}{\tau}\right)\mathbf{e}'(s)\,ds \quad . \tag{3.34}$$

Again, the analogy to the infinitesimal theory is clearly visible. Further details to the above mentioned concept can be found in Haupt and Lion [80] and Haupt [79]. Similar approaches are discussed by Simo [211] and Kaliske and Rothert [103] where internal variables of stress type are introduced.
Chapter 6 will address the concept of functional viscoelasticity in the framework of the proposed material model in more detail.

4. Acrylic bone cement

In 1928, the German chemist Otto Röhm, as well as British and Spanish scientists, succeeded independently of each other in polymerising methyl methacrylate to polymethyl methacrylate. The first application of PMMA, also known as Plexiglas®, was in the paint and coating industries. But rapidly new areas of application of PMMA appeared due to its break-proof, glass-like and weather-resistant character and so it became indispensable in the aerospace, automotive, construction and optical industries, to name just a few. The most important material properties of PMMA at 20 °C are listed in tab. 4.1.

Table 4.1.: Properties of polymethyl methacrylate at 20 °C

Parameter	Value
Density	$1.19\,\mathrm{g\,cm^{-3}}$
Glass temperature	105 °C
Coefficient of thermal expansion	$80 \times 10^{-6}\,\mathrm{K^{-1}}$
Thermal conductivity	$0.19\,\mathrm{W\,(m\,K)^{-1}}$
Specific heat capacity	$1.47\,\mathrm{kJ\,(kg\,K)^{-1}}$
Young's modulus	$2700 - 3200\,\mathrm{N\,mm^{-2}}$
Tensile strength	$70\,\mathrm{N\,mm^{-2}}$
Water absorption	$< 1\,\%$

A few years after the first successful polymerisation of PMMA, the excellent biocompatibility of PMMA was noticed. Human tissue tolerates PMMA and is not resorbed, once implanted in the human body. In 1935, the first dental prostheses were produced and 4 years later the first contact lenses made of PMMA were manufactured. Furthermore, the companies *Degussa* and *Kulzer* developed the first cold-curing PMMA system in 1943, so there was no need of external heat to start the polymerisation. These quick developing polymerisation techniques led to new possibilities in the medical sector. Defects in the skeleton were filled up and cranial plates were produced with the aid of the new material [114]. The anchoring of femoral head prostheses in the femur with the aid of a PMMA-based two-component adhesive, being one of the most frequent orthopaedic procedures today, was first performed by Charnly in 1958 [36]. As the main functions of these PMMA-based adhesives within such an anchoring match with the functions of construction cement, the expression "acrylic bone cement" has been established for medical PMMA. Closely following, other prostheses were also anchored by means of bone cement. For treating vertebral bodies that have come down with osteoporosis, i.e. vertebroplasty, acrylic bone cement was first used by Galibert in 1987, as mentioned in the beginning [64]. Since then,

attempts have been made to replace PMMA-based cement by other, more biodegradable materials, especially calcium phosphate cements [8]. These bioactive cements allow for resorption and bone regeneration due to their osteoconductive properties [129]. Moreover, the curing reaction of calcium phosphate cements is less exothermal than the polymerisation of PMMA and does not cause high temperatures in the surrounding tissue. However, the mechanical properties can not compete with those of acrylic cements. Its thixotropic rheological behaviour and the risk of phase separation involve a poor injectability of this kind of cement [75, 76]. In the cured solid state, they are weaker and more brittle, which is insufficient for some loading situations within the spinal column. Rapid resorption of calcium phosphate cements and slow bone remodelling can further result in recurrence of back pain. These reasons make acrylic bone cement still the favourite cement used in orthopaedics and especially in vertebroplasty. Over the years PMMA cements have been proved save and efficient due to their flexibility and well balanced physical properties [165, 234], although there are still possibilities for improvement [52].
The following sections will give a general overview of the behaviour and properties of acrylic bone cement, in particular during the dissolution and curing process, in order to facilitate a better understanding of the experiments, presented in ch. 5. Quantitative descriptions refer to the commercial acrylic bone cement *Osteopal® V* manufactured by *Heraeus Medical GmbH*, which has been analysed within this study. All the other information applies for acrylic bone cements in general.

4.1. Composition and mixing of acrylic bone cement

In contrast to industrial produced PMMA, acrylic bone cement is not polymerised from the pure monomer MMA, but is rather a two-component adhesive system to ease the handling during the clinical application. Usually, the two components are a polymer in powder form and a liquid monomer. Acrylic bone cements belong to the group of cold polymerising systems.
The polymer powder consists of spherical PMMA and/or different MMA copolymers in the range of 50 μm and contains an initiator dibenzoyl peroxide (BPO), a radio-pacifier, usually zirconium dioxide or barium sulphate, for visibility under X-ray observation and sometimes a dye for colouring. The latter two ingredients do not contribute to the curing process [114]. Cements used in endoprosthetics contain antibiotics to avoid infections at the prosthesis interface, but cements designed for vertebroplasty do not include any antibiotics. The differences in the composition of the polymer, i.e. the mass fraction of PMMA, different MMA copolymers, radiopacifier and BPO, as well as the molecular-mass distribution of PMMA and MMA copolymers, significantly influence the physical properties of the cement. Acrylic cements of different manufacturers exhibit therefore different physical properties and differ in their performance during vertebroplasty [31, 49].
MMA is the main ingredient of the liquid monomer and includes dimethyl-para-toluidine (DMpT) as an activator and also a dye, e.g. chlorophyll. Small amounts of hydroquinone are added to avoid polymerisation of the liquid while stored.

Table 4.2.: Composition of the acrylic bone cement *Osteopal® V*

Powder		Liquid	
MMA/MA copolymers	84 %	MMA monomers	97.5 %
Benzoyl peroxide	14.8 %	Dimethyl-para-toluidine	2 %
Radio-pacifier ZrO_2	< 0.1 %	Hydroquinone	$\sim$ 50ppm
Chlorophyll	< 0.001 %	Chlorophyll	< 0.0001 %

Both, the liquid and the powder are typically sterilised by ultra-filtration and gamma irradiation or ethylene oxide gas and packaged individually [49, 127].
For *Osteopal® V*, the polymer powder and the monomer liquid are mixed at a mass ratio of 2.76 : 1. Most commonly the two components are stirred together in a bowl by means of a spatula to produce a viscous dough. This mixing technique was also followed up in this study, as recommended by *Heraeus Medical GmbH*, and provided reproducible results. However, different commercial mixing systems have been developed in the past, some of them using vacuum technique, to improve the strength as well as to reduce the porosity of bone cement [15, 128, 242].

4.2. Dissolution and radical polymerisation of acrylic bone cement

Immediately after the two components are mixed together, two processes start. On the one hand, a physical dissolution process begins, also referred to as swelling process, during which the monomer penetrates the polymer powder, which leads to a persistent increase in viscosity. This enables the physician to find the optimal consistency for the particular clinical case. In literature, the dissolution process is rarely discussed and often not clearly distinguished from the chemical polymerisation that causes the final hardening of the bone cement.
On the other hand, a chemical polymerisation process is initiated with the aid of free radicals. These free radicals are formed within the so-called initiation reaction, when initiator and activator interfere with each other. BPO gets decomposed by DMpT and the free radicals toluidine and benzoyloxy are produced (cf. fig. 4.1). The benzoyloxy free radical decays further in carbon dioxide and a phenyl free radical, which actually triggers the polymerisation of MMA. This initiation reaction is necessary because pure radicals can not be added to the powder due to their volatile nature.
The polymerisation is usually delayed, because hydroquinone is oxidised first by the free radicals. After the complete amount of hydroquinone is consumed, phenyl radicals attack the polymerisable double bond of the MMA monomer. The product itself is a radical, too, and is able to attach to further MMA monomers (cf. fig. 4.2). Thus the polymer chain keeps growing by adding up monomer molecules to polymer macromolecules. The high number of free radicals generated produces many fast growing polymer chains and leads to a rapid conversion of MMA to PMMA [114]. With proceeding polymerisation the initially liquid dough transforms to a viscoelastic solid. The reaction rate is influenced amongst others by the number of free radicals produced.

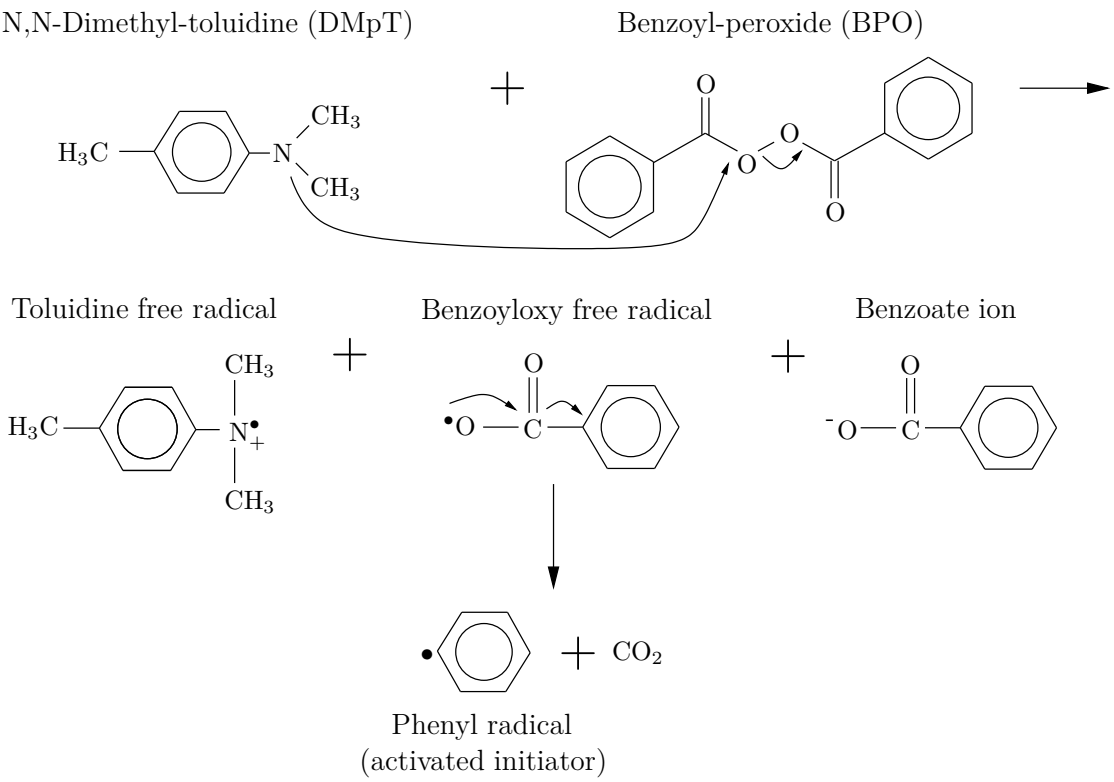

Figure 4.1.: Forming of free radicals by the reaction of BPO and DMpT

Furthermore, the spherical MMA copolymers are encapsulated by the growing chains into a solid matrix [51, 227]. To a certain extent, chain outgrowth of the pre-polymerised MMA beads also occurs [165]. Unless a crosslinker is added, like ethylene dimethacrylate (EDMA), the chains do not develop a network, i.e. they are not linked with each other. Chain growth is terminated by two different reasons. Most likely, two reactive chain ends meet and build a non-reactive polymer molecule or all of the monomer is consumed in the vicinity of the reactive chain end. The molar mass of the polymer chains varies between $100,000\,\mathrm{g/mol}$ and $1,000,000\,\mathrm{g/mol}$, whereat the molar mass of MMA monomer is 100 g/mol [31]. The other components, like radio-pacifier or dye, do not take part in the chemical reaction, but are uniformly spread in the cured cement. The description above suggests different possibilities to influence the progress of the polymerisation. By changing the amount of initiator and activator, the number of growing chains is affected. A smaller amount of initiator and activator would result in an extended duration of the polymerisation, longer chains and therefore enhanced mechanical properties [49]. In addition, the liquid to powder ratio impacts the progress and the mechanical properties as well. According to this ratio shorter or longer chains are developed and more or less pre-polymerised material gets encapsulated. Usually, the pre-polymerised MMA has a greater average molecular weight than the final product. Furthermore, the liquid to powder ratio affects also the dissolution process and therefore the time-dependent increase of viscosity.
The heat generation during the exothermal polymerisation is 57 kJ per mole MMA. Thus the temperature evolution depends predominantly on the amount of monomer used, but it can also

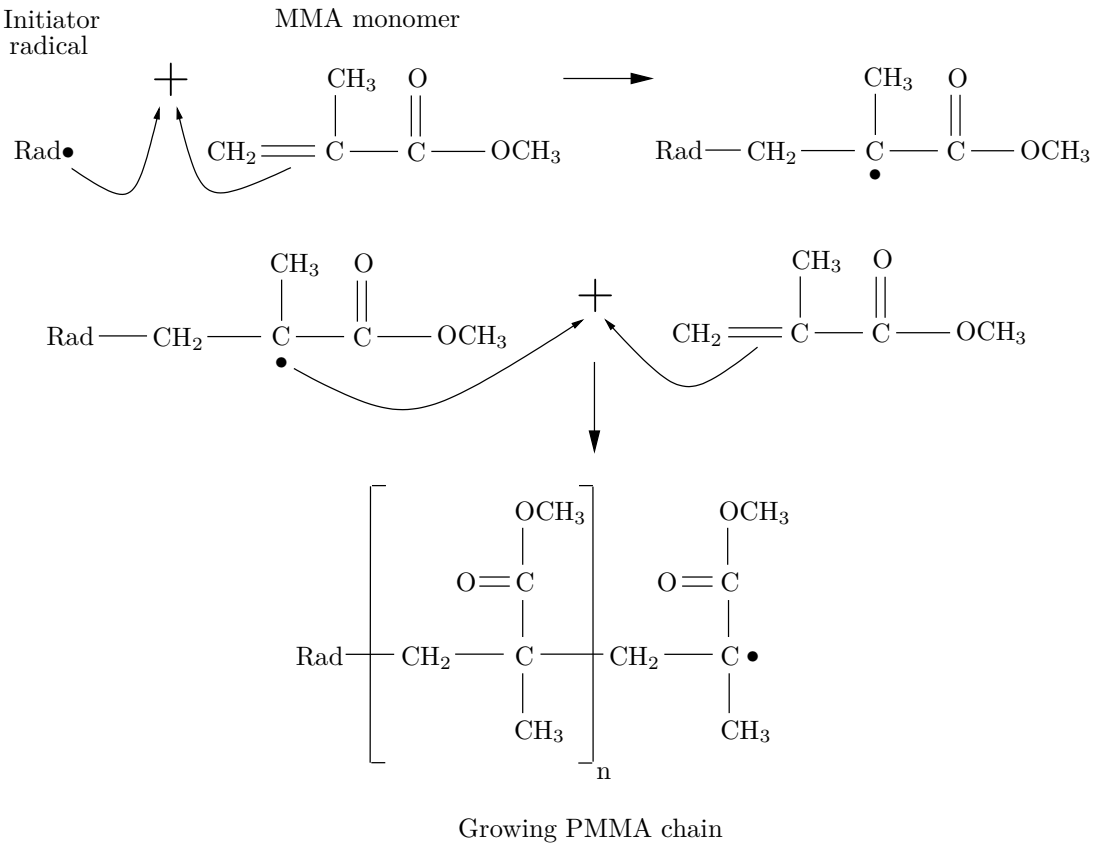

Figure 4.2.: Radical polymerisation of MMA monomer to PMMA polymer

be influenced by the liquid to powder ratio, since the co-polymerised MMA and the radio-pacifier act as heat sinks. As the number of molecules and therefore the molecular distance (between the MMA monomers before polymerisation and the molecules bonded in the polymer chain) decreases severely during polymerisation, the density of the cement increases. Polymerisation of pure MMA to PMMA shows a relative large shrinkage in volume of 21 %. Depending on the liquid to powder ratio, commercial bone cements show a volume shrinkage of approximately 7 % [114]. Air inclusions, possibly caused by handmixing or decanting, can reduce the volume shrinkage.

Radio-pacifier is essential for the fluoroscopic visibility during the injection. However, it tends to increase porosity [165] and alters the mechanical properties. Thereby it seems that zirconium dioxide increases tensile strength, fracture toughness and crack propagation resistance and barium sulphate reduces tensile strength and improves crack propagation resistance [67].

Under in-vivo conditions the MMA monomer will never be converted completely to polymer chains due to a vitrification effect. That means by proceeding polymerisation and increasing solidification, the mobility of monomers reduces and they are not added to chains any further. The polymerised bone cement exhibits a residual monomer content of about 2-6 % [31]. Within the following 2-3 weeks after the main polymerisation the monomer content reduces further to approximately 0.5 %, mainly because of a slow post-polymerisation, but also because of the

diffusion into the blood circuit and subsequent breathing out or metabolism within the Krebs cycle[1].

4.3. Viscosity and handling properties

The cement viscosity is the most important parameter in the application in vertebroplasty. As mentioned earlier, the dissolution and the polymerisation, and therefore the evolution of the increasing viscosity, is determined mainly by the chemical composition of the powder and the liquid. Moreover, both processes also depend on temperature: The lower the chosen temperature, the slower the process of dissolution and polymerisation.
From a physical point of view, both, dissolution and polymerisation start simultaneously right after mixing. However, polymerisation is delayed due to hydroquinone consumption and thereafter starts very slowly, because of the relative small mobility of activator and initiator at room temperature. At this stage, the material behaviour and increase of viscosity is dominated by the effects of the dissolution process. Once the bone cement enters the human body, the temperature change from room temperature to the body temperature of about 37 °C leads to an acceleration of the polymerisation and material properties are mainly influenced by chain growth. At the same time, the dissolution process decelerates and comes to halt as the solidification of bone cement starts. This behaviour is illustrated in fig. 4.3. In addition, measurements show that the polymerisation has a negligible influence on the mechanical behaviour of the cement directly after mixing (cf. sec. 5.5.1).

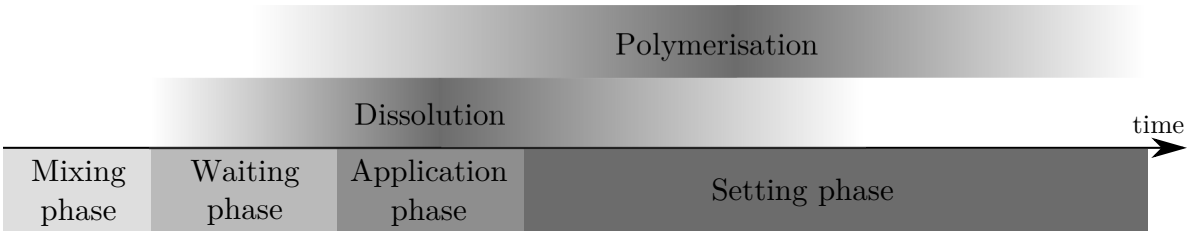

Figure 4.3.: Dissolution and polymerisation compared to clinical cement process phases

In the clinical field, the processing of bone cement is divided into four different steps:

1. During the **mixing phase**, both components are homogenised thoroughly into a viscous fluid. The recommended time for mixing varies between 1 and 2 minutes.

2. The **waiting phase** is characterised as the period between mixing and the time the cement reaches a sufficiently high viscosity to be applied. Depending on the cement, this period lasts up to several minutes.

3. Usually 2-4 minutes remain in the **application phase**. The cement passes through a

[1] The Krebs cycle is a cycle of different biochemical reactions in living organisms and plays an important role in the metabolism of aerobic cells. Amongst others MMA can also be degraded in this cycle.

viscosity range, where it offers favourable properties to guarantee a successful intervention. However, the surgeon has to decide when the optimal conditions of the cement are reached for his particular case.

4. After the cement has been injected, the **setting phase** starts. The polymerisation is accelerated due to the elevated temperature within the human body.

These four phases are opposed to the dissolution and the polymerisation in fig. 4.3. The clinician is not supposed to alter the liquid to powder ratio. So the only possibility to influence the duration of the latter three phases is to vary the temperature of the mixed dough by pre-chilling both components. By lowering the temperature, a reduced initial viscosity of the cement is obtained. Dissolution and polymerisation run off more slowly and waiting phase, application phase and setting phase are extended [114]. Corresponding to the standards ISO 5833 and ASTM F 451, two characteristic times exist that can be determined on every cement under standardised conditions at 23 °C:

- The time from the beginning of mixing until the time, when the cement mixture separates cleanly from a gloved finger, is called **doughing time**. The doughing time represents also the start of the application phase.
- The **setting time** is elapsed from the start of mixing, just until the arithmetic average of the ambient temperature and the peak temperature of polymerisation is reached. It is a measure for the final hardening of the cement.

Within acrylic bone cements the categories of low and high viscosity cements can be distinguished. High viscosity cements already have an increased viscosity during and after mixing, so that there is a potential risk for entrapping of air. The waiting phase is accordingly short and the application phase is extended. In contrast, low viscosity cements exhibit a longer waiting phase with a low initial viscosity. The increase in viscosity during the application phase is more distinctive compared to high viscosity cements. Low viscosity cements, such as *Osteopal® V*, are usually applied in vertebroplasty, because they guarantee a proper distribution within the vertebral body as well as a good interlock with bone tissue, however the risk of leakage remains. High viscosity cements are preferred in kyphoplasty to adequately fill the balloon-created cavity. Due to the difference in composition, commercial cements show a more or less great variation in the time scale of waiting, application and setting phase and therefore in the evolution of viscosity. Moreover, viscosity is the most important handling parameter for the surgeon to time the injection and determines the success of the operation. In order to ensure an effective intervention, a broad knowledge and experience of the surgeon is necessary to choose the right time to inject and to select the appropriate kind of cement for the specific case.

4.4. Mechanical properties and long-term behaviour

Once the bone cement has been injected, has filled out the fractures and cavities and has polymerised to a solid, it has to perform mechanical tasks within the treated vertebra and the spinal column. Bone cement has to stick together the fractured parts of the vertebra, to relieve the weak bone tissue and to transfer forces, mainly in the direction of the spinal column. The exact loading situation depends on the individual case, is complex and difficult to determine. But predominantly, bone cements used in vertebroplasty experience a compressive loading. Beyond that, considerable stresses appear in the spinal column for different activities [194], thus, adequate mechanical strength is one of the key demands for bone cements to ensure long-term stability of the treated vertebra [115].
In literature, a great variety of mechanical testing data on acrylic bone cements can be found. However, the results are difficult to compare, because the mixing processes, sample preparation, storage and testing methods are different or are not specified in the publications [49]. For this reason only two testing methods according to the standard specification ISO 5833 are quoted briefly.

- A compression test is executed with a cylindrical specimen of 6 mm in diameter and 12 mm in height at a temperature of 23 °C ± 1 °C. The specimen should be prepared 24 hours before testing and be compressed between two parallel plates with a speed of 19.8-25.4 mm/min. This test provides the compressive strength as characteristic value, which is the nominal stress the material can sustain before compressive failure. The minimum requirement for acrylic cements according to ISO 5833 is 70 MPa. *Osteopal*® *V* achieves 87 MPa [1].

- The other mechanical testing method specified by ISO 5833 is a four point bending test. Specimens have a rectangular shape with the dimensions 75.0 mm × 10.0 mm × 3.3 mm. The supporting bearings have a distance of 60 mm and the loading bearings have a distance of 20 mm and are displacement-controlled with a speed of 5 mm/min. Preparation and ambient temperature correspond to the compression test. Values obtained from this method are the bending strength (stress before specimen fails) and the bending modulus. To this end, deflections at the loading forces 15 N and 50 N are evaluated. The standard specification ISO 5833 requires for bending strength a minimum value of 50 MPa and for the bending modulus a value of 1800 MPa, respectively, whereat the values for *Osteopal*® *V* amount for the bending strength 58 MPa and for the bending modulus 3100 MPa [1].

Since these tests are performed at a temperature of 23 °C ± 1 °C, they are not very significant for the behaviour of the cement inside the human body. In general, mechanical properties of amorphous thermoplastics, like PMMA, vary with temperature, resulting in a lower modulus for higher temperatures. Moreover, the specification ISO 5833 was originally designed for acrylic cements used in joint replacement, where other requirements are necessary than for cements used for vertebroplasty and kyphoplasty. The high demanded values for the bending values might

be inappropriate for this purpose and probably cause the load-shifting and failures of adjacent vertebrae mentioned in sec. 1.2. Beyond that, these characteristic values might be suitable to compare bone cements, but they contain no information about the more complex viscoelastic behaviour of acrylic bone cement.
A further fact that has to be taken into account when interpreting the above mechanical properties is the long-term behaviour of acrylic cement inside the human body. Two effects mainly influence this long-term behaviour

- Post-curing due to residual monomer
- Water uptake in in the body fluid environment

Post-curing has already been addressed above and increases the stiffness of the cement during the first 2-3 weeks after application by approximately 10-30 %. The water uptake of bone cement is 1-2 % within 4-8 weeks after incubation and an especially high rate of uptake in the first few days [115]. Even these relatively small amounts of water can already influence the glass transition temperature of bone cement. Similar to pure PMMA, acrylic bone cement exhibits a glass transition at 105 °C, when completely cured. In the saturated state glass transition is lowered by approximately 20-30 °C, and therefore the bone cement is still in a glassy state at body temperature, but stiffness decreases compared to the dry state. Post-curing and water uptake are adverse effects.
According to its viscoelastic behaviour, acrylic bone cement is able to creep. Thereby, stresses that have occurred during polymerisation or otherwise can be reduced over time. In addition bone cement has to sustain quite a lot loading cycles without fatigue with regard to human movements in different physiological activities. Tests for this purpose are conducted following the standard specification ISO 5833 described above, but loaded dynamically at a certain frequency (e.g. 5 Hz) and in a saline bath at 37 °C. The number of load cycles before fatigue can give valuable information whether a certain acrylic bone cement is appropriate for application in minimal invasive spine surgery. For further information the reader is referred to Kühn et al. [115].

5. Experimental investigations

Extended continuum mechanic models that are able to describe the injection and exothermic curing behaviour of adhesives, such as bone cement, require a detailed experimental investigation of the considered material. On the one hand this investigation gives valuable information on how to structure the model, on the other hand, these experiments are necessary to parametrise the model, so that it is able to represent the material behaviour in the desired range of temperature and other boundary conditions. Experiments which focus only on the mechanical behaviour and on characteristic values, like e.g. compressive strength (cf. sec. 4.4), of bone cement are not sufficient. In addition, calorimetric and thermodynamic measurements are necessary in order to gather valuable information about the chemical and thermodynamic processes that take place during dissolution and curing. As dissolution and curing definitely influence the mechanical (and curing additionally the thermodynamic) behaviour, it is also the aim of these experimental investigations to identify the dependencies and interrelations of dissolution, polymerisation and mechanical and thermodynamical behaviour among each other. This will become clearer during the discussion of the specific experimental results in this chapter.
The listing below itemises the different experiments that have been carried out for material characterisation within the scope of this thesis:

- Reaction kinetics and released heat of reaction
- Specific heat capacity
- Thermal conduction
- Chemical shrinkage
- Thermal expansion
- Rheological properties during dissolution
- Mechanical properties during curing
- Mechanical properties after curing

It is reasonable to start with the calorimetric measurements, as the progress of polymerisation will influence the mechanical and thermodynamic behaviour significantly. Vice versa, the effect of stress on the curing behaviour and dissolution is disregarded in this study, as it is difficult to measure and is likely to have minor influence on both processes [69]. After that, the thermodynamic properties specific heat and thermal conductivity are examined with respect to

temperature and progress of dissolution and polymerisation. Furthermore, a special focus will be laid on the effect of dissolution, polymerisation and temperature on the density of acrylic cement as this may cause severe residual stresses after a vertebroplasty. The major part will be the investigation of rheological and mechanical properties during and after the two different processes, dissolution and polymerisation. Here, it is important to discover how the mechanical behaviour is affected by each process and how both processes interact with each other. At the end, mechanical properties after curing will be observed and will yield useful information for the modelling structure.

5.1. Specimen preparation

In this study, the bone cement *Osteopal® V* has been analysed as a representative for other acrylic bone cements. Both components, powder and liquid were provided by *Heraeus Medical GmbH* as non sterilised bulk material in contrast to the sterile clinical packages. It is important to notice here that acrylic bone cements differ widely in their characteristic effects, but the basic behaviour is common for all acrylic cements.

As dissolution and polymerisation are irreversible and strongly temperature-dependent processes, particular attention has to be paid when preparing samples in order to get reproducible specimens in high quality. This implies working under the same temporal and thermal conditions during sample preparation [15, 116]. In order to have identical initial conditions, the powder and liquid component were stored at 5 °C and taken out of the refrigerator directly before mixing. The pre-chilling has further advantageous effects. On the one hand, it guarantees a minimal progress of polymerisation during the handling time before starting the measurement, e.g. a DSC-experiment. On the other hand, the mixed bone cement has a low viscosity at low temperatures, so that air inclusions can be avoided almost completely and narrow corners of moulding forms are reliably filled. The additional cooling of the ceramic bowls for mixing was omitted.

Both components were weighed in separate bowls at a liquid-to-powder ratio of 2.76 : 1 and merged together in the bowl of the powder at room temperature of 20 °C. A spatula was used to mix the powder and liquid to a dough for 30 seconds. Special care was taken not to heat up the bowl by the palm of the hand. Subsequently, the cement was stirred on an orbital shaker for 60 seconds. The further handling is specific for the experiment and will be explained in the corresponding following sections.

In order to distinguish the effects of dissolution and polymerisation, some experiments were conducted with a modified cement mixture. To this end, a pure monomer liquid without activator and dye was used, so that no free radicals were formed and polymerisation was avoided. Thereby, the physical properties changed only marginally and the pure effects of dissolution could be observed. The mixing procedure was identical to that described above. In the following, this mixture will be also referred to as non-polymerising cement.

5.2. Calorimetric measurements

During the exothermic polymerisation of MMA to PMMA-chains, a specific amount of heat is released by the MMA molecule that is added to a chain (cf. sec. 4.2). This fact can be used to measure the progress of polymerisation simply by recording the amount of heat being released. By means of differential scanning calorimetry (DSC) the released heat can be quantified.

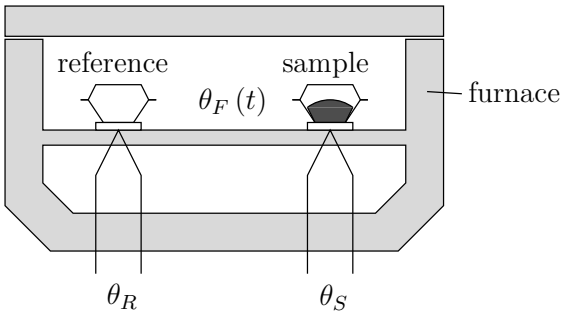

Figure 5.1.: Schematic of heat flux differential scanning calorimetry

Therefore two crucibles, one of them containing a sample, the other one being empty (reference), are submitted to a temperature programm $\theta_F\,(t)$ in a common furnace (cf. fig. 5.1). Due to the specific heat capacity of the sample as well as exothermic or endothermic processes (e.g. curing, melting evaporating and phase changes) the heat flux from the furnace to the sample crucible and to the reference crucible is different and results in a temperature difference between the sample crucible and the reference crucible. This temperature difference can be detected by thermocouples below both crucibles. In a heat flux differential scanning calorimeter, this temperature difference is proportional to the difference between the heat flux into or out of the sample and the heat flux into or out of the reference and can be quantified by careful calibration. Thus differential scanning calorimetry enables the measurement of the heat of reaction of acrylic bone cement during polymerisation. For a detailed insight into the theory of differential scanning calorimetry the textbook of Höhne et al. [95] is a good choice.

5.2.1. Reaction kinetics and enthalpy of reaction

The polymerisation of acrylic bone cement is strongly dependent on temperature because of the mobility of activator, initiator and MMA molecules. Thus the polymerisation is accelerated when the bone cement enters the human body and is exposed to the altered temperature of 37 °C. Moreover, the curing itself releases heat and thus, the bone cement experiences even higher temperatures. The exothermic polymerisation leads to a kind of self-accelerating process. In order to quantify the reaction kinetics, isothermal calorimetric measurements were performed on a heat flux DSC of the type *DSC* 204 *F*1 *Phoenix* from *Netzsch*. A reasonable temperature range from 15 °C to 65 °C with a step size of 5 °C was chosen for isothermal experiments. In

general, reaction kinetics can also be studied by non-isothermal experiments [197]. But here, isothermal experiments are preferred, like in many other studies [150, 167, 229], to emphasise the temperature dependency and omit baseline measurements.
For the sample preparation, acrylic bone cement was mixed according to the description in sec. 5.1. Subsequently, a droplet with a mass of 5-8 mg was put into the aluminium crucible of the DSC-device. The sample crucible was weighed before and after sample insertion, as well as after the experiment. Moreover, the lid of the crucible was pierced with a hole, in order to avoid a pressure increase due to evaporation. Pre-chilling showed here a further advantage, namely the droplet was distributed smoothly on the bottom of the crucible due to low viscosity, guaranteeing an enhanced heat conduction towards the thermocouple of the DSC-apparatus. After the sample crucible was positioned within the furnace, measurements were started $220\,\mathrm{s} \pm 10\,\mathrm{s}$ after the first contact between both components. The temperature was kept constant for one hour and the released heat flux dH/dt per unit mass, also referred to as DSC-signal, was recorded. Fig. 5.2 shows the result of these isothermal measurements.

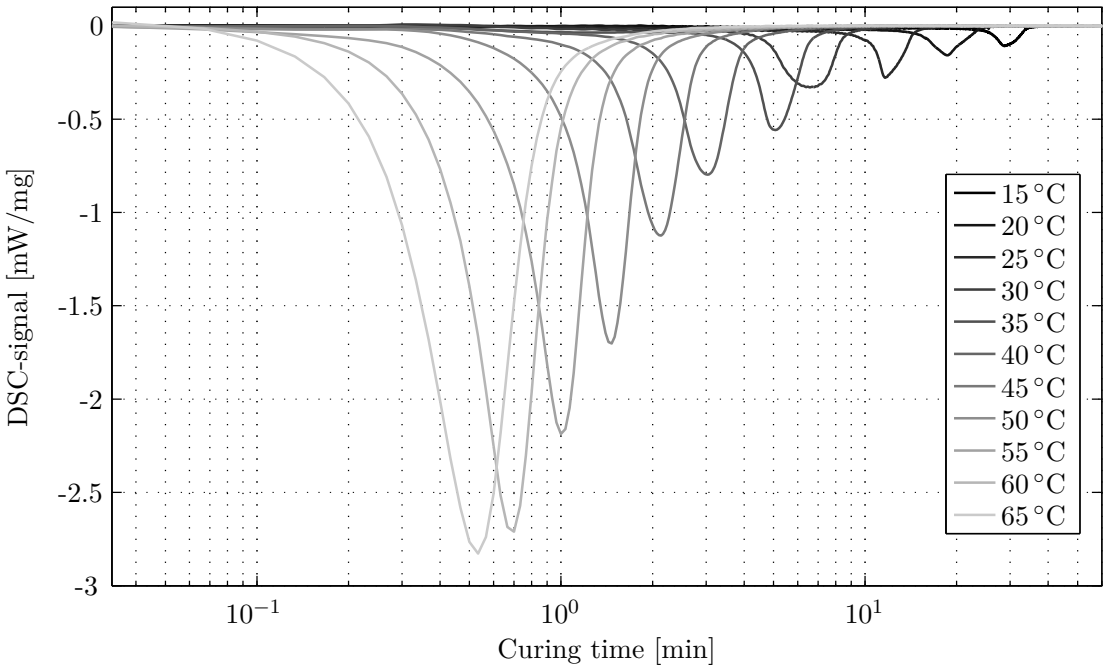

Figure 5.2.: Released heat power of acrylic bone cement during curing at different temperatures

It is obvious that the kinetics of polymerisation strongly depends on temperature. In contrast to a temperature of 65 °C, where the main part of the polymerisation is finished within less than 5 minutes, the polymerisation at a temperature of 15 °C takes more than 30 minutes. Nevertheless, all curves in fig. 5.2 exhibit the same shape. At lower temperatures, a phase, where almost no energy is released due to immobility of the molecules, is more distinctive. Subsequently, more and more heat is released per unit time until a peak is reached. This peak indicates the maximum conversion rate of MMA to PMMA. After this peak the heat power decreases steadily towards zero. The area enclosed between the curve and the zero axis is a measure for the released

heat during curing. The semi-logarithmic scale distorts these areas indeed, however, the released heat is still not identical for isothermal polymerisation at different temperatures. In sec. 4.2 it is stated that MMA will usually not be converted completely to polymer chains due to vitrification. This vitrification effect can be interpreted as a glass transition. At the beginning of polymerisation, the glass transition of the mixture itself is far below room temperature and rises with proceeding polymerisation [27, 205, 235]. When the increasing glass temperature of the mixture reaches the isothermal curing temperature, the curing cement changes into the glassy state and the mobility of initiator, activator and MMA molecules reduces severely. In this case not the temperature changes, which is done when the glass transition of polymers is studied, but the glass transition of the mixture itself changes. This implies that, as long as the isothermal curing temperature is below the glass transition of the fully cured cement, namely 105 °C, conversion of MMA to PMMA will never be complete. Furthermore, it explains the greater amount of heat released at higher curing temperatures, because more MMA is polymerised. In the glassy state, the polymerisation is said to be diffusion-controlled compared to concentration-controlled below the glass transition temperature. The diffusion-controlled polymerisation exhibits a conversion rate that is diminished by several orders of magnitude, compared to concentration-controlled polymerisation.

To further examine and quantify these circumstances, the experiments discussed above were extended. After one hour of isothermal curing, the furnace was cooled down by 15 °C and afterwards heated up three times to 150 °C and cooled down to 15 °C below the corresponding isothermal curing temperature. In between, heating and cooling phases with a temperature rate of 10 °C/min and isothermal phases with a duration of 5 minutes were inserted (cf. fig. 5.3)

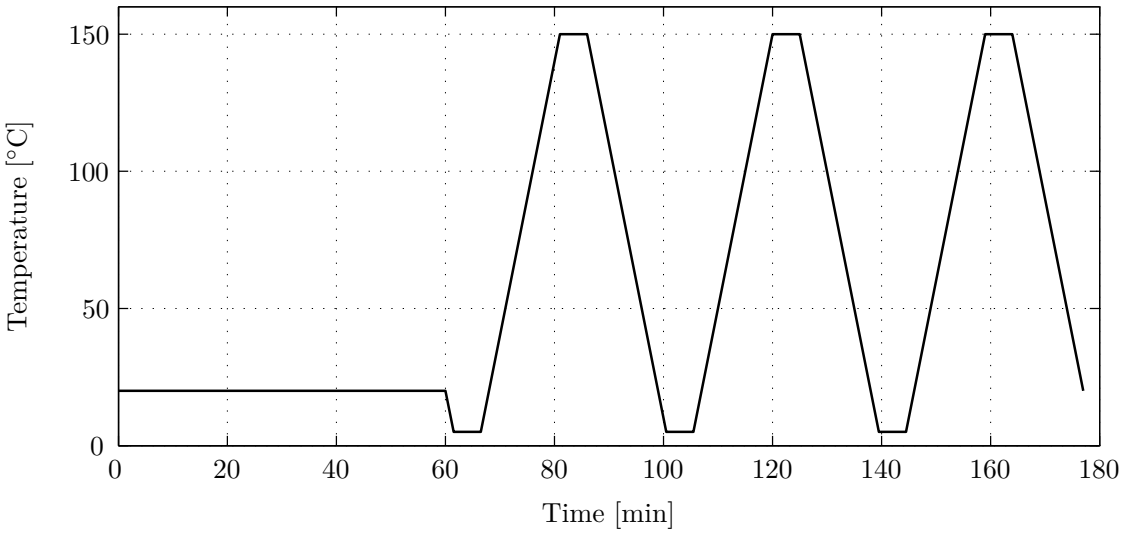

Figure 5.3.: Temperature profile for calorimetric experiments

This extension of the isothermal calorimetric measurement helps to determine the residual heat of reaction of non-converted MMA due to vitrification. By heating up the vitrified bone cement the temperature rises above the glass transition temperature of the partially cured cement, and

hence, the reaction becomes again concentration-controlled and accelerated. Due to the fact that the temperature is further elevated above the glass transition temperature of the fully polymerised material, it can be assumed that all MMA molecules are consumed. Fig. 5.4 shows the heat flux power of the sample for the 1st, 2nd and 3rd heating ramp (exemplarily for a foregoing isothermal curing at 50 °C). The overshooting at the beginning of the temperature ramps is caused by the spontaneous transition from the isothermal phase into a temperature ramp. By the agreement of the 2nd and 3rd ramp, it is indicated that the polymerisation is completely finished at the end of the first ramp where all three ramps coincide. The heat power of the first ramp is composed of the released heat power of the polymerisation, the power needed to heat up the sample and the heat power to overcome the glass transition in the vicinity of 105 °C. In contrast, the heat power of the second and third ramp are only composed of the latter two parts. Assuming that the specific heat capacity for the partially cured cement (1st ramp) and for the fully cured cement (2nd and 3rd ramp) are nearly identical, the area between the first and second/third curve can be interpreted as residual heat of reaction in a good approximation. The assumption is justified because almost three quarters of the initial mixture is co-polymerised MMA and more than 50 % MMA monomer has already been converted during the isothermal phase.

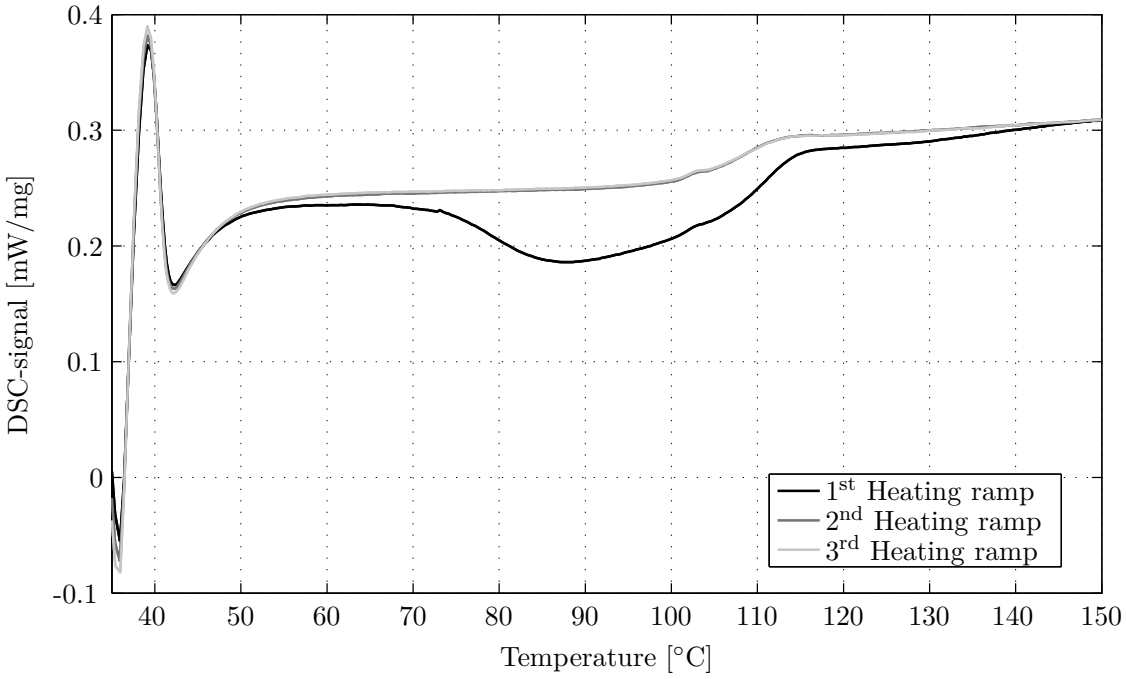

Figure 5.4.: DSC-signal for heating ramps in the non-isothermal part of the calorimetric measurements (exemplary for a foregoing isothermal curing at 50 °C)

It is also remarkable, that all three DSC-signals overlap at the very beginning and deviate after two minutes. This can be ascribed to the glass transition temperature of the partially cured cement, which lies 10 °C to 20 °C above the isothermal curing temperature. Aside, the overlap is also an evidence that the heat capacity of the partially and the fully cured bone cement are

almost consistent.
By weighing the sample crucibles after the experiments, a small loss of mass of approximately 0.1 mg can be detected. The volatile monomer might be responsible for this, however this mass loss is less than 2 % and was disregarded for the following considerations.
Isothermal experiments are also conducted with a non-polymerising mixture (cf. sec. 5.1). During the isothermal part, no heat flux was detected at all. This means that dissolution is neither exothermic nor endothermic. Only above 80 °C, polymerisation is induced thermally. With the aid of this experimental data the temperature-dependent reaction kinetics, including the phenomena of vitrification, can be quantified [107] (cf. sec. 7.1). As indicated, the enthalpy of reaction can be determined from the experiments described above as well. Integrating the DSC-signal over the isothermal polymerisation time yields the cumulative enthalpy of reaction. For non-isothermal experiments, the energy needed to heat up or being released by cooling down has to be taken into account additionally. Due to uncomplete curing in the investigated range, both parts, the released heat during the isothermal phase and during the first temperature ramp, have to be added up to obtain the total enthalpy of reaction.
The progress of the cumulative enthalpy of reaction during a one hour lasting isothermal polymerisation phase and a following temperature ramp (as described in sec. 5.2.1) is illustrated in fig. 5.5 for different constant temperatures.

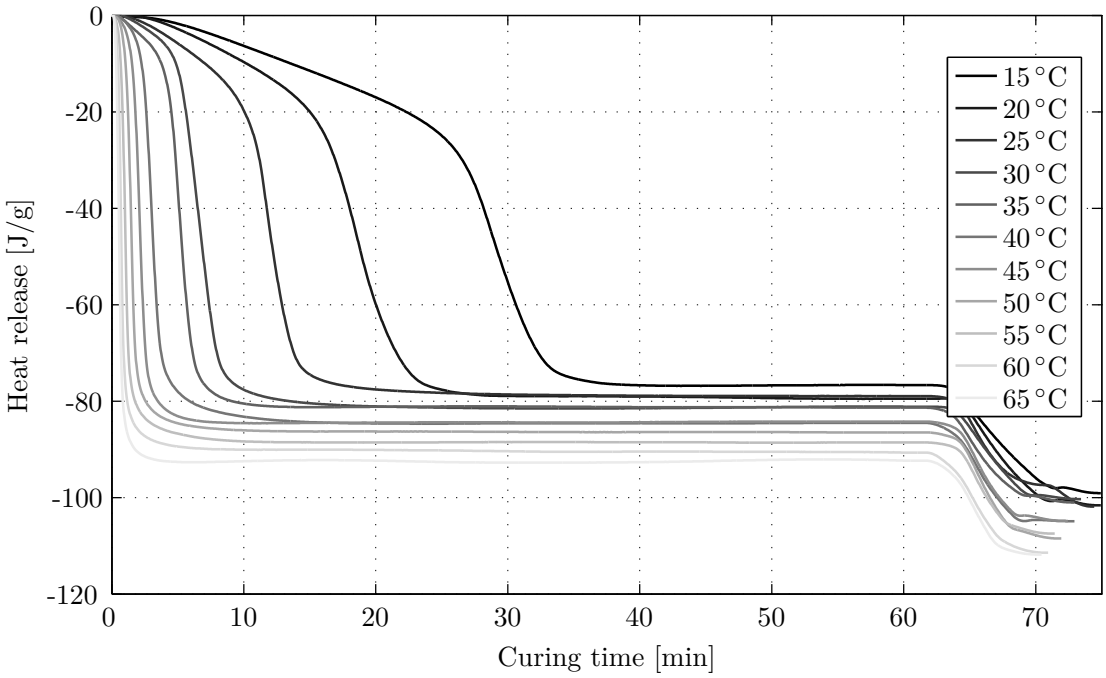

Figure 5.5.: Cumulative heat released during isothermal polymerisation and following temperature ramp

Three important facts have to be deduced from fig. 5.5. First, the temperature dependence of the reaction kinetics is emphasised by the cumulative heat release. Second, the higher the temperature during the isothermal phase, the lower is the cumulative heat release during the

temperature ramp. And third, the total heat of reaction depends on the temperature of the isothermal polymerisation phase, namely the higher the temperature during the isothermal phase, the higher the total heat of reaction. This will be discussed in more detail in sec. 6.5.1. Compared to the theoretical value of 148 J/g, the measured value for the total enthalpy of reaction is quite low with approximately 105 J/g. Part of the difference can be assigned to the convection by the purging gas nitrogen which is used in the DSC-apparatus. This heat loss by convection is not captured by the DSC-sensors and increases with an advanced rate of reaction. Further measurements with non-isothermal temperature profiles should be conducted to clarify the discrepancy.

5.2.2. Specific heat capacity

The specific heat capacity is an essential parameter, if non-isothermal processes, like the in-vivo polymerisation of acrylic bone cement, are considered. In the most simple case, the specific heat capacity is a function of temperature. Furthermore, the temperature-dependent enthalpy of reaction (cf. sec. 5.2.1) implies that the specific heat capacity changes with proceeding polymerisation, namely in a descending manner (cf. sec. 6.5.1). Other dependencies, like on pressure, were disregarded, due to their expected minor influence.
For solids and liquids, the specific heat capacity is generally determined at constant pressure. This characteristic value c_p exceeds the specific heat capacity at constant volume c_v by the additional amount of energy necessary for thermal expansion. The specific heat capacity c_p is therefore the amount of energy needed to heat up a certain material by 1 °C per unit mass at constant pressure. Differential scanning calorimetry is also suitable to determine the isobaric specific heat capacity [170]. For this purpose, a sample is heated up and the required heat flux is measured. However, with conventional methods, a characterisation of the specific heat capacity is only possible for temperature ranges where no additional enthalpy changes, like polymerisation, occur. Thus, the specific heat capacity is first determined for the uncured and the completely cured material. Moreover, the measurement is carried out within a so-called comparative methodology. That means that the DSC-signal of bone cement is compared to a standard material, usually sapphire, where the specific heat capacity over temperature is well known. In order to guarantee results of high quality, further points have to be considered. Crucibles with a high thermal conductivity, e.g. aluminium crucibles, are the first choice to detect the heat flux exactly. Standard and sample specimen should have about the same mass. The starting temperature is stabilised by a 10 minute lasting isothermal phase and 10 °C below the desired temperature range to prevent overshooting within the evaluation interval. Two baseline measurements with an empty crucible, one standard measurement, using a sapphire sample, as well as a sample measurement are conducted under identical conditions and with the same crucible. The baseline measurements serve to eliminate the influence of the crucible. If two consecutive baseline measurements coincide, the conditions in the furnace are sufficiently constant.
The specific heat capacity of the sample c_p can be evaluated in the appropriate temperature

range by the following formula

$$c_{p,sample} = \frac{(P_{DSC,sample} - P_{DSC,baseline})\ m_{standard}\ c_{p,standard}}{(P_{DSC,standard} - P_{DSC,baseline})\ m_{sample}} \quad . \tag{5.1}$$

Herein P_{DSC} corresponds to the DSC-signal of the particular measurement and m is the mass in the crucible. For the purpose of measuring uncured bone cement, a sample was prepared, using the MMA liquid without activator (as described in sec. 5.2.1) after having recorded baseline and standard measurements. For the sample measurement of fully cured cement, a flat, already completely cured piece of bone cement was chosen, to enhance heat transfer within the crucible. The relevant temperature range was scanned with a constant heating rate of 10 °C/min for all four measurements.

Fig. 5.6 displays the results for the temperature-dependent specific heat capacity of uncured and completely cured acrylic bone cement. The specific heat capacity of uncured bone cement shows

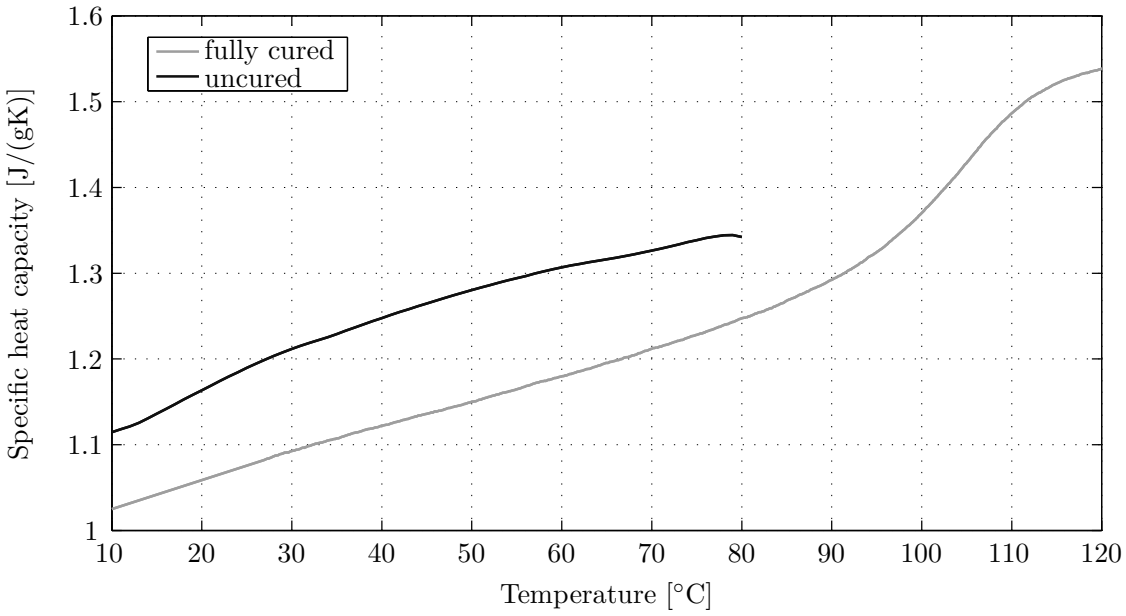

Figure 5.6.: Specific heat capacity of uncured and completely cured acrylic bone cement at constant pressure

an almost linear increase in the range of 10 °C to 80 °C by 20 %. Measurements beyond the temperature of 80 °C were not possible because polymerisation is induced thermally, although an activator is missing. The completely cured cement shows also a linear temperature dependency between 10 °C and 90 °C. Above 90 °C, acrylic bone cement shows, analogue to commercial PMMA, a distinctive glass transition, where the inflexion point can be identified at 105 °C. The glass transition temperature at approx. 105 °C, however, is not relevant for the application of acrylic bone cement. The fact that the specific heat capacity of cured bone cement is approximately $0,1\,\mathrm{J/(g\,K)}$ lower than the specific heat capacity of uncured bone cement is in agreement with the dependency of total enthalpy of reaction on temperature (cf. sec. 6.5.1).

Besides the knowledge of the specific heat capacity in the uncured and cured state it is also

desirable to characterise the behaviour of the specific heat during polymerisation in the context of material modelling [203, 204, 243]. As mentioned, this is not possible with the standard method described above. Instead, temperature modulated DSC (TMDSC) offers possibilities to separate the heat flux of reversible processes (e.g. heating, cooling, glass transition) from irreversible processes (e.g. polymerisation). Therefore a harmonic temperature oscillation with a given frequency and a small amplitude of 0.5 °C to 2 °C is superimposed on the actual temperature program. The reaction kinetics for isothermal phases has already been known from sec. 5.2. Therefore this temperature program is appropriate to superimpose harmonic temperature oscillations according to

$$\theta = \theta_0 + \theta_A \sin(\omega t) \qquad \text{with} \qquad \dot{\theta} = \theta_A \omega \cos(\omega t) \quad . \tag{5.2}$$

Herein θ_0 denotes the constant component of the temperature program, θ_A the amplitude of the superimposed oscillation and ω the angular frequency of the oscillation. The specimen responses also with a harmonic oscillation in heat flux, however, phase shifted.

$$\frac{P_{DSC}}{\Delta m} = A + B \sin(\omega t) + C \cos(\omega t) \tag{5.3}$$

Taking into account the fundamental equation for DSC investigations (cf. sec. 6.5.1)

$$\frac{P_{DSC}}{\Delta m} = \dot{h}(q,\theta) = \frac{\partial h}{\partial q}\dot{q} + \frac{\partial h}{\partial \theta}\dot{\theta} \quad , \tag{5.4}$$

with h being the specific enthalpy per unit mass and q being the progress of polymerisation, as well as the finding from the previous section, that the reaction rate of polymerisation is dependent on temperature and the progress of polymerisation itself (cf. sec. 6.2.2),

$$\dot{q} = f(q,\theta) \approx f(q,\theta_0) + \left.\frac{\partial f}{\partial \theta}\right|_{\theta_0} \theta_A \sin(\omega t) \quad , \tag{5.5}$$

the specimen's response in heat flux can be written as

$$\frac{P_{DSC}}{\Delta m} = \frac{\partial h}{\partial q} f(q,\theta_0) + \frac{\partial h}{\partial q}\left.\frac{\partial f}{\partial \theta}\right|_{\theta_0} \theta_A \sin(\omega t) + \frac{\partial h}{\partial \theta}\theta_A \omega \cos(\omega t) \quad . \tag{5.6}$$

The parameters A, B and C from eq. (5.3) can be identified in eq. (5.6) as

$$A = \frac{\partial h}{\partial q} f(q,\theta_0) \tag{5.7}$$

$$B = \frac{\partial h}{\partial q}\left.\frac{\partial f}{\partial \theta}\right|_{\theta_0} \theta_A \tag{5.8}$$

$$C = \frac{\partial h}{\partial \theta}\theta_A \omega = c_p(t)\,\theta_A\,\omega \quad . \tag{5.9}$$

Thereby A is the temporal average of the DSC-signal P_{DSC} and B is the amplitude of the DSC-signal, caused by the reaction kinetic response to the temperature oscillation and is in phase with the excitation. The parameter C is proportional to the product of the angular frequency of the temperature oscillation and the amplitude of the superimposed oscillation. The proportionality factor can be identified as the specific heat capacity c_p [145, 230]. In order that these relations are valid, the response function is only allowed to deviate slightly from an ideal

harmonic oscillation with constant amplitude. This requires the changes due to the proceeding polymerisation to be small within one period. The parameters A, B and C can be determined by a Fourier transformation of the DSC-signal.
Similarly to the measurement of the specific heat capacity in the uncured and cured state, the recording of a baseline, a standard measurement as well as a specimen measurement is necessary. Specimen preparation of acrylic bone cement was carried out analogous to the measurement of reaction kinetics. Again, the standard DSC-signal and the specimen DSC-signal are corrected by the reproducible baseline. After the determination of the parameters A, B and C, the specific heat capacity can be evaluated from the following relation.

$$c_{p,sample}(t) = c_{p,standard}\frac{C_{sample}(t)}{C_{standard}(t)} \tag{5.10}$$

The best results were obtained with an oscillation period of 50 seconds and an amplitude of 1 °C. For larger oscillation periods, not enough cycles fell on the accelerated part of the polymerisation. Shorter oscillation cycles could not be realised to be ideally harmonical due to controlling capabilities of the DSC-apparatus. The amplitude of 1 °C was best for the resolution achieved by the Fourier transformation. Measurements and evaluations were conducted for mean temperatures of 15 °C and 20 °C and the results are displayed in fig. 5.7. At higher temperatures, polymerisation induced a pronounced influence on the heat flux, so that the requirement of small deviations from an ideal oscillation was not fulfilled any longer and a reasonable evaluation within the accelerated phase of polymerisation was not possible.

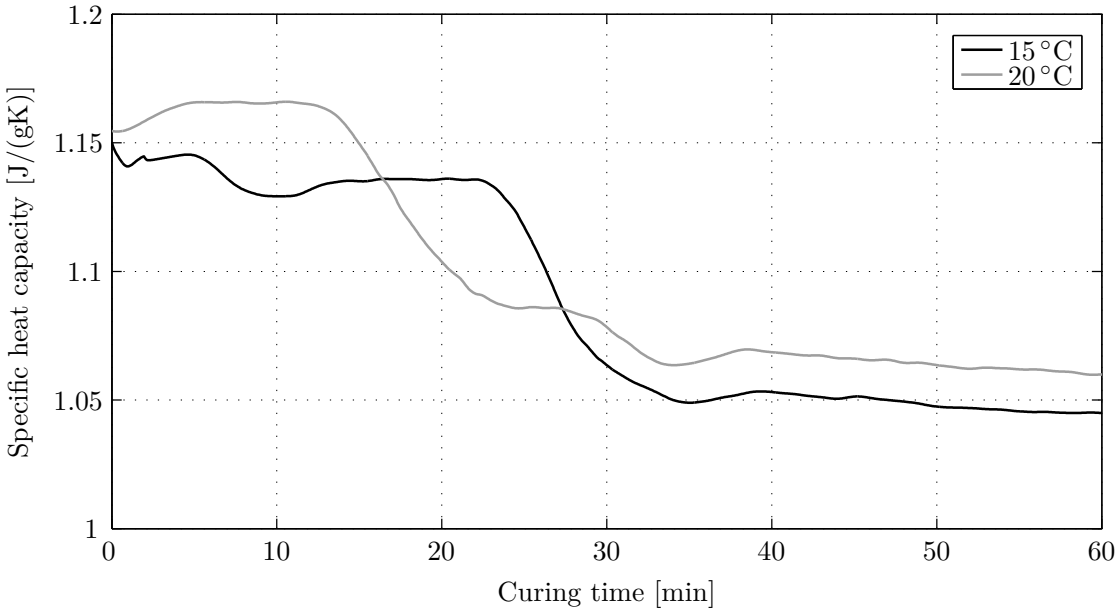

Figure 5.7.: Specific heat capacity of polymerising acrylic bone cement under constant pressure and at temperatures of 15 °C and 20 °C

For both mean temperatures, the specific heat capacity changes its value from the uncured to the cured material with proceeding polymerisation. The growing chains seem to decrease the

mobility of the molecules and thus reduce the ability to store thermal energy. As expected, the course of the specific heat capacity in fig. 5.7 reveals the different temporal progress in polymerisation for 15 °C and 20 °C isothermal polymerisation temperature.

5.3. Thermal conductivity

Thermal conductivity is a further important material property needed to solve thermomechanically coupled problems, especially when heat is released inside the material, like it is the case for bone cement. Generally, thermal conductivity is difficult to measure. For plastic materials, the laser flash application has been widely established to determine the thermal diffusivity: One side of a disc-shaped specimen is charged with a laser impulse, while the time-dependent temperature rise on the other side of the specimen is recorded by infra-red measurement technology. By comparison with mathematical models and data fitting, the recorded time-dependent temperature can be correlated to a value for thermal diffusivity [34, 177]. Moreover, the knowledge of density (cf. sec. 5.4) and specific heat capacity is used to calculate the thermal conductivity by the following relationship.

$$\lambda = \rho \, c_p \, a \tag{5.11}$$

Therein λ denotes the thermal conductivity, ρ the density and a the thermal diffusivity of the specimen. In addition, the whole apparatus can be installed within a furnace to take into account the temperature dependency of the thermal conductivity.
For measuring the thermal conductivity in the cured state, disc-shaped specimens with a diameter of 12.7 mm and a height of 2 mm were prepared. A two-piece mould was used, consisting of two parallel aluminium plates, with the upper plate having bores of 12.7 mm in diameter and a height of 2 mm. Both plates were separated by a foil to ensure a plane surface and simple de-moulding. Bone cement was prepared according to sec. 5.1 and filled into the bores with the plates firmly attached to each other. The mould was slightly overfilled. After curing, the elevation was ground off to produce coplanar surfaces.
The specimens were analysed in a laser flash apparatus *LFA 427* from *Netzsch* within a temperature range from 20 °C to 120 °C. Fig. 5.8 illustrates the computed thermal conductivity of cured bone cement.
In the range from 20 °C to 80 °C, the thermal conductivity of bone cement exhibits a decreasing trend which can be roughly approximated by a linear dependency on temperature. This is also the region relevant for the application of bone cement. The relative change of thermal conductivity in this range is below 10 %. Towards higher temperatures, the thermal conductivity decreases rapidly, due to glass transition of thermal conductivity from 80 °C to 100 °C. Although the specific heat capacity rises continuously and the density decreases slightly in this region (cf. figs. 5.6 and 5.10), the decisive factor for the sudden decrease of the thermal conductivity is the change in the phonon mean speed at the glass transition [68, 50]. The phonon mean speed is again proportional to the root of the storage modulus, which exhibits a sudden drop at the

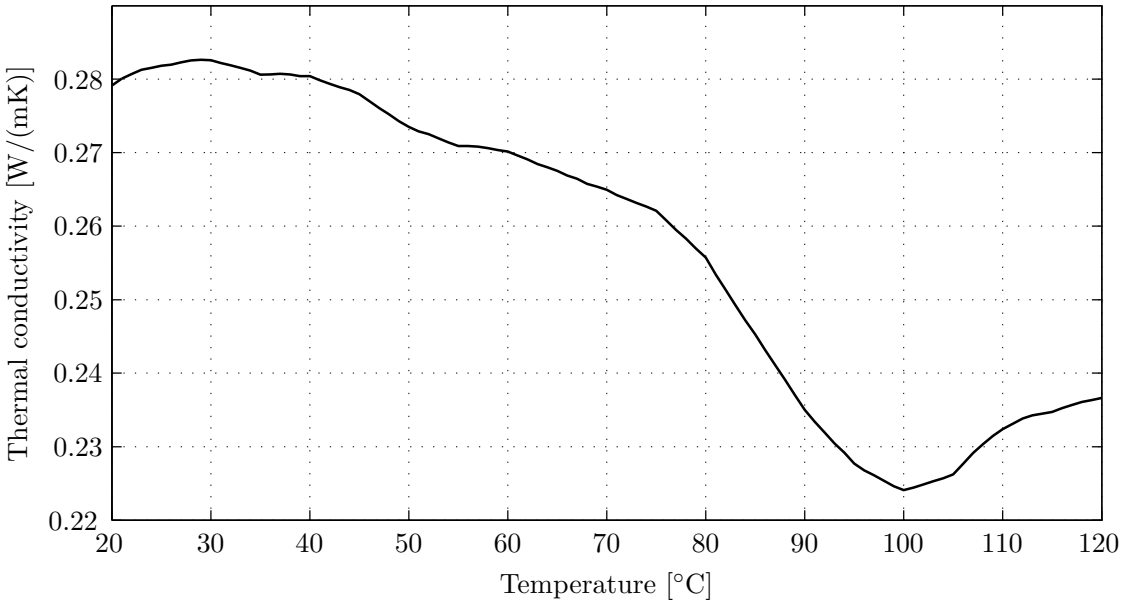

Figure 5.8.: Thermal conductivity of cured bone cement in the temperature range from 20 °C to 120 °C

glass transition (cf. fig. 5.27). In a more descriptively way, the increased polymer chain mobility above the glass transition temperature decelerates the transport of heat. The subsequent increase above 100 °C can be explained by the glass transition of specific heat capacity and thermal expansion at about 105 °C, which also affect the thermal conductivity as stated in eq. (5.11). According to Risen and Schawe [190, 191], the determination of the glass transition by different thermal analysis techniques leads to different temperature values because the glass transition is a rate-dependent thermo-viscoelastic phenomenon [143].

The investigation of the thermal diffusivity of bone cement in the uncured state is more complicated, because the dough-like specimen can not be positioned in the apparatus without changing its shape. Metallic specimen pans, where bone cement is encapsulated, would be necessary and mathematical models would have to be adopted in expensive preliminary experiments.

Polymerisation also influences the thermal conductivity. Measurement techniques that rely on a local application of energy, like the laser flash principle, are therefore not suitable. A local acceleration of polymerisation due to the laser flash would cause inhomogeneous curing conditions. Moreover, heat is released by the polymerisation and would disturb the heat transfer of the laser impulse. Within the scope of this thesis, Faller tried to identify the temperature- and cure-dependent thermal conductivity of acrylic bone cement with the aid of inverse methods [54]. A disc-shaped specimen of curing acrylic cement was isolated at the bottom and circumference and observed from the top. The temperature profile over time on distinctive points of the top surface were recorded. This data was used to fit the temperature- and cure-dependent thermal conductivity of a comprehensive model, similar to the one introduced in ch. 6. However, the temperature profile on the top surface exhibited no distinctive dependency on the value of thermal conductivity, to accurately determine model parameters.

Due to the complexity to access the value of thermal conductivity for the uncured and polymerising acrylic cement, as well as the non-distinctive dependency of the temperature field on this value, further measurements on thermal conductivity were omitted. However, the analysis of variable thermal conductivity for curing materials should be part of future research.

5.4. Density

By linking MMA molecules with the PMMA-chains, they need less space, and thus acrylic bone cements show a shrinkage in volume during polymerisation. Supplementary, the cement is exposed to temperature alterations because of the elevated body temperature and the heat generation of the cement itself. The additional thermal energy is responsible for an expansion of the acrylic cement. Both effects, chemical shrinkage and thermal expansion are superposed in the clinical application. Compared to epoxy systems (cf. [66, 85, 235]), acrylic bone cements show a larger shrinkage, up to 10 % in volume. The consequence is the appearance of residual stresses if the material is mechanically constrained while polymerising. Therefore, these effects should also be considered in modelling the polymerisation of acrylic cements.
Investigating the change in density due to polymerisation and thermal expansion for polymerising acrylic bone cement is particularly challenging because the measurement principle must be applicable for high-viscous liquids and solids at the same time. As there is a lack of commercial devices for this task, a self-built-up volumetric dilatometer, based on the Archimedes principle, was developed [107]. For this purpose, a precision balance of the type *ME235P* from *Sartorius* was mounted over a cooling thermostat (*Lauda RE207*) as sketched in fig. 5.9.

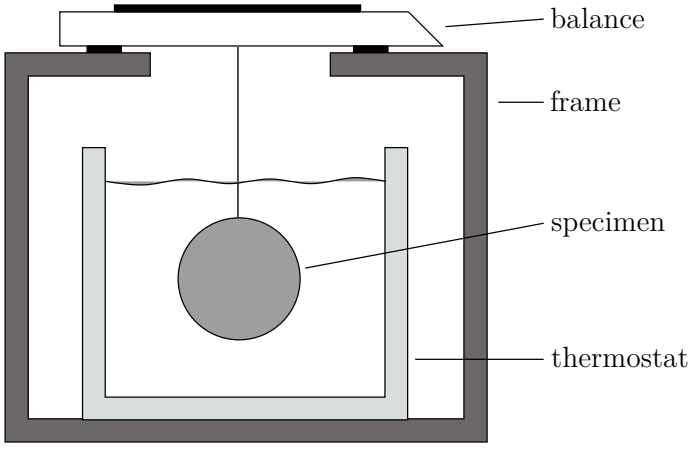

Figure 5.9.: Schematic of self-built-up volumetric dilatometry

Both devices were connected to a computer, that ran a control routine. The thermostat bath was filled with 5 litres of silicone oil which can be tempered from −40 °C up to 200 °C. Further thermocouples, also connected to the computer, were placed in the vicinity of the specimen in the thermostat bath to record the temperature during the experiment. The specimen was connected

via a nylon cord to the underfloor weighing system of the balance and dipped completely into the silicone oil in the thermostat bath. Subsequently, the specimen's weight in silicone oil as well as the temperature were recorded. According to Archimedes principle the specimen's density ρ_{sp} can be derived as follows:

$$\rho_{sp} = \rho_{fl}(\theta)\frac{m_{sp}}{m_{sp} - F_{g,fl}/g} \quad . \tag{5.12}$$

Herein, $\rho_{fl}(\theta)$ denotes the density of the silicone oil, depending on temperature, m_{sp} is the mass of the specimen, weighed before dipping into the bath, $F_{g,fl}$ is the weight of the specimen in silicone oil and g denotes the gravitational acceleration.

For the specimen preparation, the bone cement was mixed according to the description in sec. 5.1. Subsequently, the cement was poured on a thin-walled polyethylene foil. Another piece of foil was placed on top of the cement without any air inclusions. With the aid of a small glass, that was put upside down over the foil-cement-foil sandwich, a circular area was separated. At the edge of the glass, the bone cement was squeezed away and the upper and lower foil were pressed onto each other, thus forming a seal. A cutter knife was used to cut both foils on the outer circumference of the glass. The result was a disc shaped, sealed specimen of bone cement weighing about 4 g, having 1-3 mm in thickness and 35mm in diameter. The special shape of the specimen accounts for an effective heat convection and guarantees an almost isothermal temperature distribution in the specimen. Moreover, the sealing of the specimen enables to measure the density of liquid and solid bone cement. The weight of the foils is approximately 0.015 g and hence can be neglected. After weighing the uncured sealed specimen, it was spiked on a little hook at the end of the nylon cord. Thereafter the specimen was dipped in the preconditioned silicone oil (cf. fig. 5.9). At first, the thermal expansion behaviour of bone cement was investigated in the uncured and the fully cured state, also to get an overview of the total chemical shrinkage during polymerisation. Therefore, the bone cement was mixed using the monomer liquid without activator to avoid polymerisation and the uncured specimen was prepared as described above. The fully polymerised specimen had been cured at 110 °C (above glass transition) to ensure a complete conversion of MMA. In both experiments, the temperature was increased in steps of 5 °C from 10 °C up to 80 °C and was kept constant for 3 minutes to achieve a constant temperature in the bath and in the specimen. Fig. 5.10 illustrates the density of uncured and completely cured bone cement in the investigated range.

For both conditions, uncured and polymerised, the dependency of density on temperature is almost linear, but the coefficient of thermal expansion, represented by the slope of the curves, is approximately twice as high for the uncured cement. Above 60 °C, the thermal expansion of uncured cement increases more intensely. Based on temperature, the density values for uncured and cured bone cement vary between 8.6 % at 10 °C and 12.5 % at 60 °C, which represents the overall shrinkage due to polymerisation. Compared to literature values, this seems to be quite high, however, the values above are for a complete conversion of the monomer. The fact that the curve is reproducible for the uncured cement proves that the process of dissolution has no influence on density.

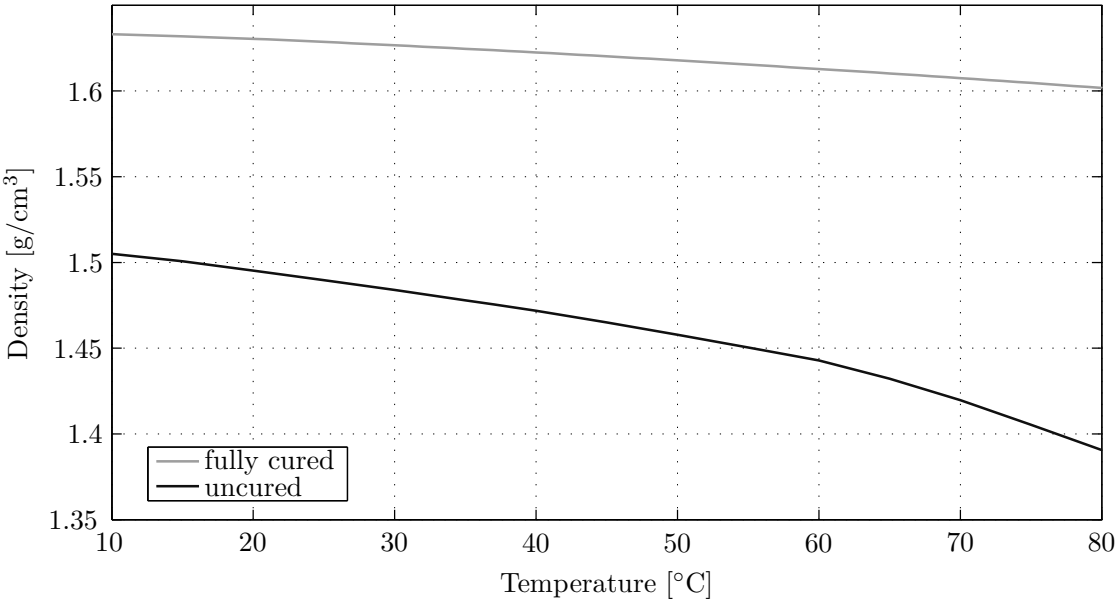

Figure 5.10.: Density of uncured and completely cured acrylic bone cement in the range from 10 °C to 80 °C

For analysing the chemical shrinkage during polymerisation, specimens were prepared as described above, using monomer including the activator. Similar to the DSC experiments, the first value was recorded after approximately 220 seconds had elapsed from the start of mixing. Measurements were performed with this set up in the range from 12 °C to 62 °C and a duration of one hour to capture the entire polymerisation, even at low temperatures. Fig. 5.11 presents the evolution of density during isothermal curing for acrylic bone cement.

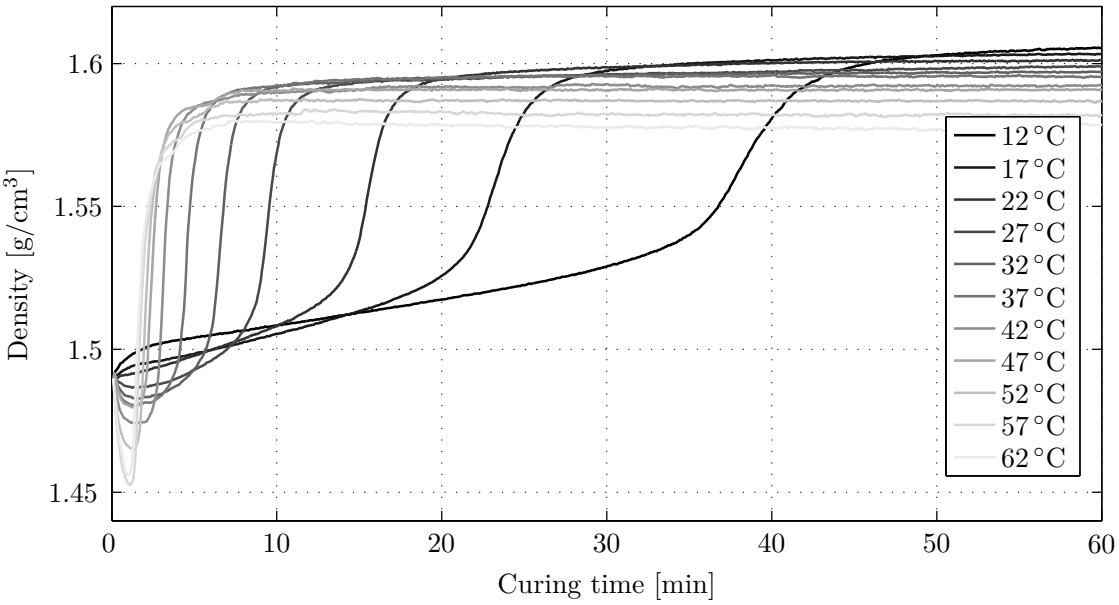

Figure 5.11.: Evolution of density for acrylic bone cement during isothermal curing

In general, the course of polymerisation shrinkage follows clearly the characteristics of the accumulated heat released (cf. sec. 5.2.1). All specimens start at approximately $1.49\,\mathrm{g/cm^3}$, the density of uncured acrylic cement at room temperature. Thereafter, i.e. in the first four minutes, some overshooting can be detected. This is the case because the specimen is prepared at room temperature of 20 °C whereas the thermostat bath is already preconditioned according to the desired experiment temperature. The temperature difference leads to corresponding thermal expansion or shrinkage. Especially at high bath temperatures, thermal expansion and chemical shrinkage of the accelerated polymerisation overlap. For example, the specimen at 57 °C test temperature reaches a lower density than the specimen at 62 °C test temperature. This indicates that, at high temperatures, the reaction, and hence the chemical shrinkage, is faster than temperature compensation and thermal expansion. After the main polymerisation the specimens exhibit different densities. One reason is of course due to the different test temperatures, and therefore thermal expansion. But also a different amount of monomer was converted, related to the diffusion-controlled reaction. Hence a different degree of polymerisation and a different amount of chemical shrinkage are the results. Though, the thermal expansion has a greater effect than the different degree of polymerisation for each temperature, resulting in the curves for lower temperatures lying over the curves for higher temperatures. On closer examination of fig. 5.11, the curves for lower temperatures still show a small slope after the main polymerisation, being an evidence for the post polymerisation mentioned in sec. 4.2.
Beyond that, the dissolution process has no influence on either of the above investigated material parameters (released heat, specific heat capacity and density). The effect of dissolution on the thermal conductivity was not proved in this work, but from a physical point of view it is supposed to be negligible.

5.5. Preliminary mechanical investigations

The analysis of the thermomechanical behaviour of acrylic bone cement is a major challenge. As a result of dissolution and polymerisation, the mechanical material properties vary within several orders of magnitude. Especially the transition from a liquid to a solid has particular demands on the testing facility because mechanical properties of a liquid and a solid have to be captured simultaneously with the same device.
Aside from technical difficulties in measuring the mechanical properties of acrylic bone cement during dissolution and curing, these properties are also dependent on temperature, shear rate and frequency [107, 108, 125, 126, 147] and it would be desirable to study the influence of these parameters on the mechanical behaviour during dissolution and curing as well.
Before focusing systematically on the dependencies of the rheological and mechanical behaviour of acrylic bone cement in the remaining sections of this chapter, the following subsections shall provide a fundamental understanding of the influence of dissolution and polymerisation on the mechanical behaviour to the reader.

5.5.1. Rheometry

With the aid of parallel-plate rheometry, the difference between the dissolution process and the polymerisation process and the effect of these processes on the mechanical behaviour of bone cement should be found out. For these experiments, a parallel-plate rheometer *AR G2* from *TA Instruments* was employed. Consecutively, polymerising and non-polymerising bone cement, prepared according to sec. 5.1, was positioned between two parallel plates of 8 mm in diameter and with a gap of 1 mm (cf. fig. 5.25 and sec. 5.7). The experiments were started 220 seconds after the start of mixing. An oscillatory shear loading of 0.1 % and 10 Hz at a temperature of 20 °C was applied to both disc-shaped specimens. Due to the viscoelastic material behaviour, the specimen responds harmonically as well, but phase-shifted. With the aid of eqs. (5.21) to (5.25) the storage modulus G' and loss modulus G'' can be gained, which are presented in fig. 5.12.

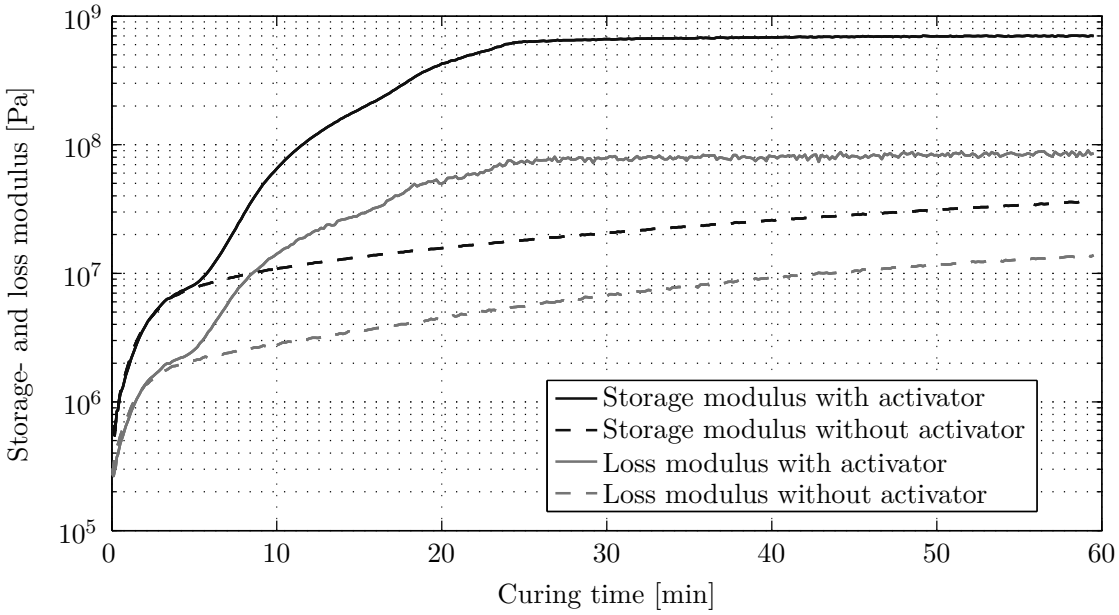

Figure 5.12.: Storage and loss modulus of polymerising and non-polymerising bone cement for an oscillatory loading of 0.1 % at a frequency of 10 Hz and at a temperature of 20 °C

In both cases depicted in fig. 5.12, the storage and loss modulus rise continuously across several orders of magnitude. After a steep increase at the beginning the curves of both moduli flatten for non-polymerising and polymerising cement. Until then, the behaviour of non-polymerising and polymerising acrylic cement is identical, but they deviate after approximately 6 minutes from the start of the experiments. For polymerising cement, the storage and loss modulus experience another sharp increase. Compared to the enthalpy of reaction, illustrated in fig. 5.5, this is also the point where polymerisation begins to accelerate. Contrary, the storage and loss modulus of non-polymerising cement is only slightly rising. Fig. 5.12 clearly points out that the first increase in both moduli is only due to the process of dissolution. Hence, the mechanical

behaviour is identical for non-polymerising and polymerising cement during the first minutes of processing. Only after polymerisation gets accelerated, the dissolution plays a minor role and comes to a halt. The advanced chain growth is responsible for the second sharp increase of storage and loss modulus and, therefore, the final hardening.
A closer look at fig. 5.12 reveals that the storage modulus is always greater than the loss modulus. Thus, elastic effects are evident and dominant throughout the processing of acrylic bone cement. A so called gel point, where storage and loss modulus cross each other [26, 91], or a maximum in the loss modulus as an indication for vitrification [235], like it is typical for curing resins, can not be observed.
As an indicator for the dissipative part of the mechanical work applied, the loss factor is commonly used and is expressed as

$$\tan\delta = \frac{G''}{G'} \quad . \tag{5.13}$$

Fig. 5.13 displays the loss factor for both experiments, polymerising and non-polymerising cement. Starting at approximately 0.45, the loss factor decreases with proceeding dissolution. The peaks at the very beginning are likely to be caused by lining-up the experiment. Polymerising bone cement exhibits a local maximum at the beginning of accelerated polymerisation, but continues to decrease for advanced polymerisation. For cured bone cement, elastic effects exceed the dissipative material behaviour by almost one order of magnitude. By chain growth, the material behaviour gets more elastic. In contrast, non-polymerising bone cement shows a local minimum in the loss factor after ten minutes. A slight increase is visible afterwards, ending at a value of 0.38. The development of the loss factor, as displayed in fig. 5.13, is not typical for

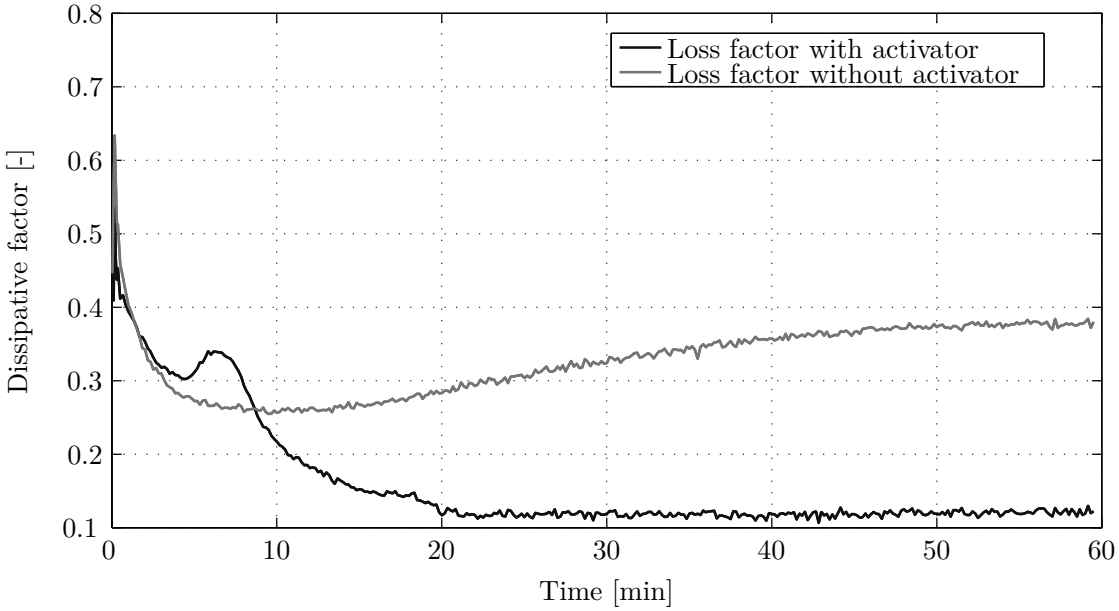

Figure 5.13.: Dissipation factor of polymerising and non-polymerising bone cement for an oscillatory loading of 0.1 % at a frequency of 10 Hz and at a temperature of 20 °C

curing materials. Usually the loss factor takes values above 1 before curing. However, the local maximum at the beginning of accelerated polymerisation tends to be a characteristic behaviour for acrylic bone cement.

5.5.2. Pan-indenter experiment

To acquire further information on the changing mechanical properties of bone cement due to dissolution and curing, a special tool for a universal testing machine (*Zwick & Roell* type *ZN 20*) was designed. It consists of a cylindrical pan which is 20 mm in diameter D and 30 mm in height H inside, and a cylindrical indenter with a diameter d of 8 mm (cf. fig 5.14). The indenter features a hemispherical tip, which is equipped with a thermocouple. The wiring of the thermocouple is achieved by a small concentric bore within the indenter. Further thermocouples are placed near the inner side wall of the pan, at the pan bottom, as well as 14 mm and 28 mm above the bottom (cf. fig 5.14). Therefore, small bores were installed in the side wall of the pan. Attached to the traverse of the universal testing machine, the indenter can be moved in the vertical direction. The initial distance Δl between the indenter and the bottom of the pan is 15 mm. Pan and indenter were manufactured out of aluminium.

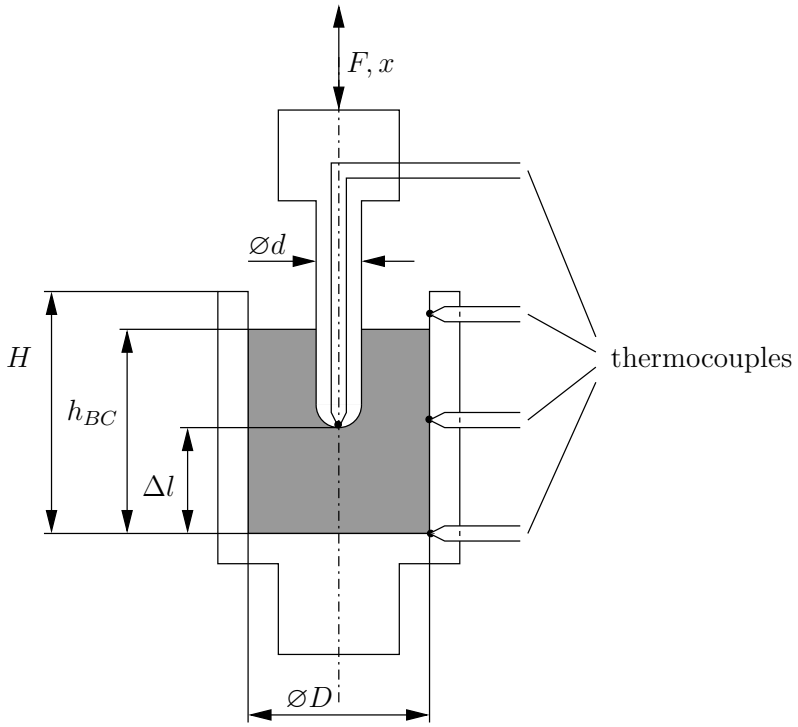

Figure 5.14.: Indenter-pan-equipment for a universal testing machine to determine viscoelastic properties during curing

For the experiments, the bone cement was mixed according to the description in sec. 5.1 and filled into the pan up to a height h_{BC} of approximately 25 mm with the indenter being arranged in the initial position. After mechanical equilibrium was reached, the indenter could be

moved with different force- and displacement-controlled programs to examine the mechanical behaviour of bone cement during polymerisation. A temperature control was not possible, so that the experiments were run at a room temperature of approx. 20 °C. Displacement-controlled programs are particularly difficult to design because a too large displacement leads immediately to a contact loss between cement and indenter and, therefore, distort the measuring results. Additionally, the polymerisation induced shrinkage causes a loading that drags the indenter towards the bottom of the pan (cf. fig. 5.15) and has to be taken into account as well. In contrast to displacement-controlled experiments, force-controlled experiments compensate the shrinkage induced displacement automatically. For both types of experiments an iterative process is necessary to determine the admissible displacements and forces, respectively. A good starting point is an experiment with the indenter force adjusted at zero over the entire experiment duration. Due to the cement shrinkage, the indenter will be dragged towards the pan bottom when polymerisation gets accelerated. The recorded indenter displacement over time is a particularly useful piece of information as it indicates the course of the polymerisation, facing the given boundary conditions. Consequently, a time based rise in displacement- or force-controlled loading can be designed that is adapted to the increasing cohesiveness of the polymerising cement. Additionally, for displacement-controlled experiments, this indenter displacement has to be superposed to the further indenter movement to avoid contact loss between cement and indenter. In the following, harmonically force-controlled experiments are considered more closely.

Exemplarily, fig. 5.15 shows a force-controlled experiment. Similar to the experiments mentioned before, 220 seconds elapsed from the beginning of mixing until the experiment was started. The first subfigure plot indicates the temperature profiles at the positions of the thermocouples displayed in fig. 5.14. Within the first 1000 seconds of the experiment a slight rise in temperature of 2 °C can be observed. Initial polymerisation and temperature compensation between the initial cement temperature of 18 °C and room temperature are responsible for this ascent. Subsequently, when the polymerisation gets accelerated, heat is released more quickly and the temperature reaches a peak value. It is not surprising that the thermocouple at the indenter tip experiences a more spontaneous temperature rise than the thermocouples at the wall do, as it is closer to the geometrical centre of the cement bulk, where the polymerisation gets accelerated first. Moreover, the poor thermal conductivity of bone cement augments this effect. This poor thermal conductivity is also responsible for the peak temperature value at the indenter tip being higher than at the pan wall. In contrast, aluminium is an excellent thermal conductor and explains that the three wall temperatures are almost equal. A further interesting observation is the rapid temperature decline at the indenter tip after the peak value has been reached and the fact that this decline is faster than at the pan wall. Therefore, heat has to be discharged by the indenter more quickly than by the pan, which is not obvious regarding both geometries. Moreover, this effect can also be generated by a separation between indenter and cement due to chemical shrinkage. A detailed numerical investigation can lead to a closer insight into these phenomena, being apparent in all conducted experiments.

The last subplot in fig. 5.15 shows the resulting displacement of the indenter due to the force excitation, chemical shrinkage and thermal expansion. Subtracting the absolute displacement at

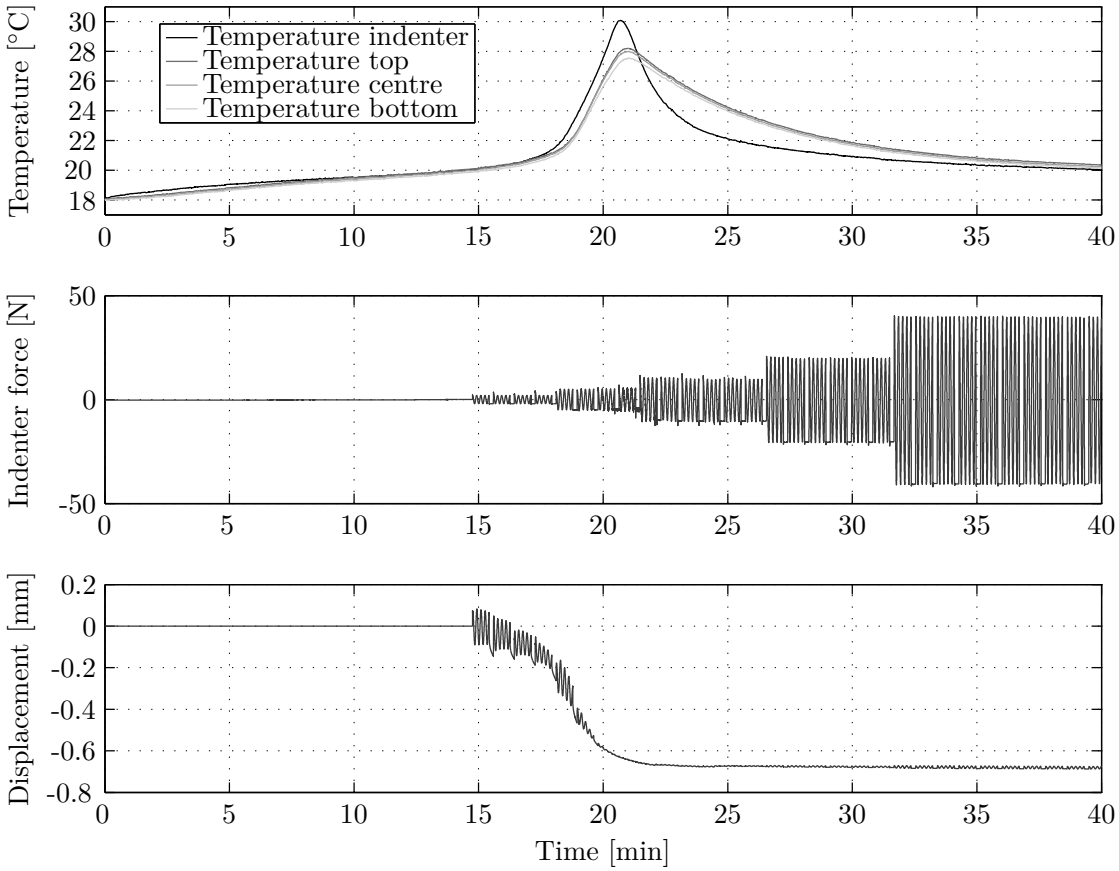

Figure 5.15.: Temperatures, force and displacement for a force-controlled experiment

the end from the displacement at the experiment start yields a displacement of 0.6 mm, which is ascribed solely to chemical shrinkage. A comparison of the temperature and displacement profile reveals that the main heat release and the highest rate of shrinkage coincide. This behaviour is expected, having in mind the characteristics of polymerisation (cf. ch. 4). It is remarkable that this displacement is much higher than the sustainable force induced displacement. Even at the beginning of the accelerated polymerisation (i.e. at approx. 1000 seconds) a displacement peak-to-peak value of more than 0.4 mm would lead to an immediate contact loss between cement and indenter. Displacement-controlled experiments, where the indenter is kept fixed in the initial position (i.e. does not move for the entire experiment duration), have showed that the force rises continuously between pan and indenter as soon as chemical shrinkage starts. At about 160 N to 180 N the chemical shrinkage advanced in such a way that the compound fails adhesively.

There are two additional circumstances that give valuable information about the mechanical behaviour of bone cement and its change by polymerisation. The first circumstance, namely that the cement bulk can sustain increased force loading provoked by chain growth, is quite obvious. At the beginning, only a small force amplitude causes a quite large displacement response. Although the loading increases with progressing polymerisation, the displacement amplitude diminishes continuously. The second observation is based on the viscoelastic nature of bone

cement and can be detected as hysteresis in a force-displacement-diagram. Such a diagram is showed in fig. 5.16. Thereby, it has to be remarked that the displacement due to shrinkage was subtracted from the overall displacement, like it is displayed in fig. 5.15. This displacement due to shrinkage has been gained by low-pass-filtering, so that in fig. 5.16 only the displacement due to the application of force is visible. In addition, the force-displacement curve is only plotted in the range of accelerated polymerisation, i.e. from 880 s to 1500 s, representing the starting in dark black colour and turning into grey in the course of time. Clearly, the slope of the hystereses decreases with increasing degree of cure and vanishes almost completely as polymerisation is finished. The area within the hysteresis can be interpreted as a measure for the viscous losses. Unfortunately, the amplitude of the loading force is not constant, however, one can identify a decreasing area of the hystereses taking into account the changing amplitude. This observation coincides with the progress of the loss factor (cf. fig. 5.13), discussed earlier, although the local maximum in the loss factor is difficult to identify in the changing areas of the hystereses. At the end of the main polymerisation process, the hysteresis diminished extremely. Although the loading force was increased again, less mechanical work is done and less energy is lost by dissipation.

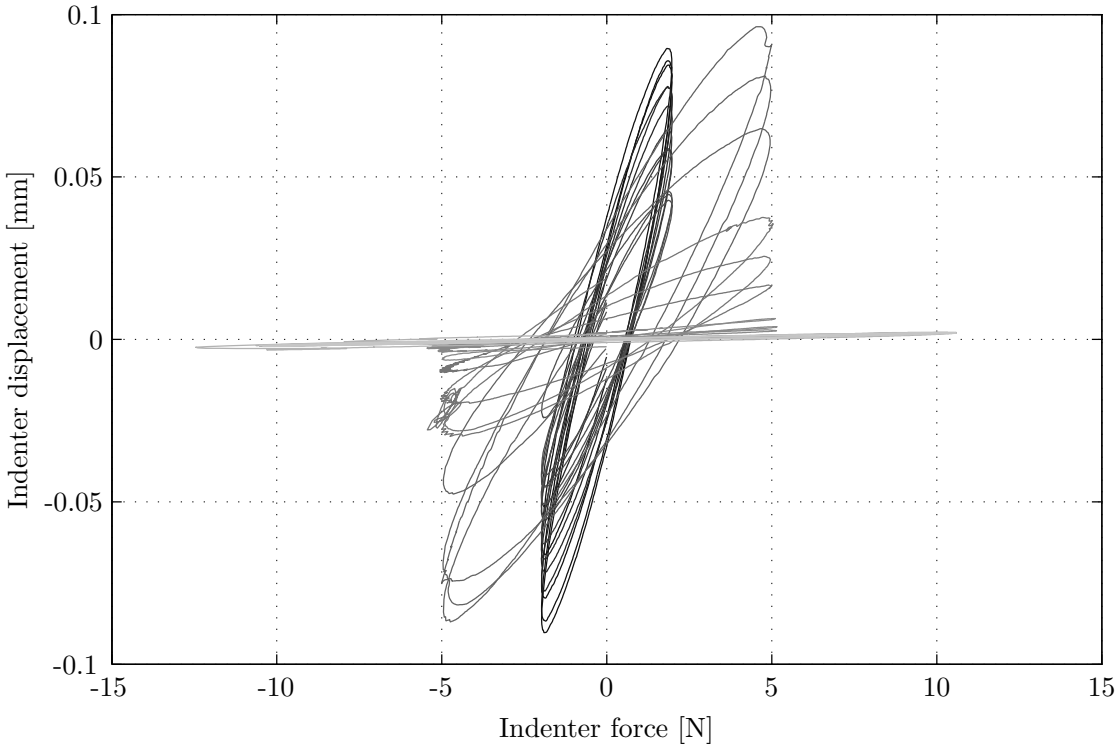

Figure 5.16.: Indenter displacement vs. indenter force for a force-controlled experiment

With the aid of the experiments presented above, a diverse overview of the thermomechanical behaviour of acrylic bone cement was gained and conclusions for the performance inside the human body can be drawn. The trabecular structure of a vertebra, for example, is additionally loaded by the relatively large amount of chemical shrinkage and may even be partially destroyed. However, for developing and parametrising continuum mechanical models for acrylic bone ce-

ment, these experiments are not sufficient. For this purpose, a detailed experimental investigation on a broader basis is necessary. The mechanical material behaviour has to be studied with respect to those parameters that influence the behaviour of bone cement in the vertebroplastic application and are desired to be covered by the material model. Parametrisation of the model demands also that characteristic values, like storage and loss modulus, are easily gained by the experiments. Unfortunately, this is not true for the pan-indenter test, but the previous presented measurements provide valuable information on how to design the experimental setup and parameter studies, which will be discussed in the following.

5.6. Rheological investigations

The pan-indenter experiment has showed that acrylic cement cannot sustain tensional loadings during the mixing, waiting and application phase, because it has fluid character. Since the injection of acrylic bone cement plays a key role in the vertebroplastic surgery process and decides highly upon its success, it is inevitable to study the mechanical behaviour in this state. Moreover, it was reported throughout the literature that bone cement exhibits a shear-thinning behaviour and the viscosity increases with proceeding dissolution [56, 72, 112, 125, 202]. The science of rheology offers different techniques to describe bone cement in the fluid phase by measurable quantities [44]. Out of these techniques, a cone-plate and a capillary rheometer were chosen in this study to analyse the rheological properties of bone cement during time scales which are relevant for injection. Their advantages will be discussed alongside the explanations to the measurement setup and results.

5.6.1. Cone-plate rheometer

A plate and a cone were designed to fit on the previously mentioned *AR G2* rheometer from *TA Instruments*. For controlling temperature, the rheometer is equipped with a hinged oven including nitrogen cooling. The diameters of cone and plate are 15 mm for experiments at 15 °C and 20 °*C* and 10 mm for experiments at 25 °C and 30 °C, respectively, to fully use the torque range of the rheometer. Preliminary experiments have showed that a cone angle of 5 ° is most appropriate for the task [169]. In addition, the tip of the cone was flattened in order to account for the particle size of the polymer powder [158, 176]. The following fig. 5.17 shows a schematic diagram with all necessary parameters. An advantage of cone-plate rheometry is that the dynamic viscosity η is easily accessible by measuring the torque M_d and knowing the geometric dimensions R and α [158], while operated at constant angular velocity Ω between cone and plate (cf. fig. 5.17).

$$\eta = \rho\nu = \frac{3M_d}{2\pi R^3}\frac{\tan\alpha}{\Omega} \approx \frac{3M_d}{2\pi R^3}\frac{\alpha}{\Omega} \tag{5.14}$$

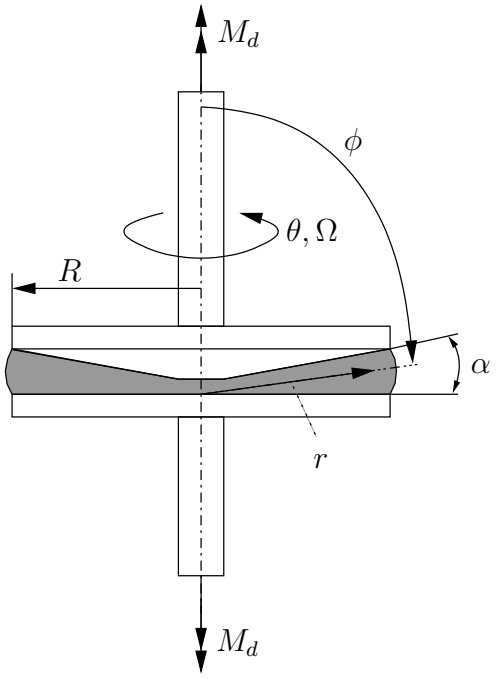

Figure 5.17.: Cone-plate rheometer

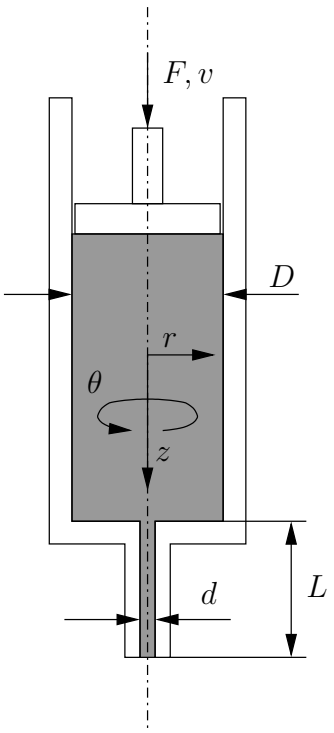

Figure 5.18.: Capillary rheometer

Furthermore, this type of rheometer exhibits a constant shear rate $\dot{\gamma}$ across the radius and can easily be temperature-controlled by a surrounding oven. The shear rate is given by

$$\dot{\gamma} = \frac{\Omega}{\tan \alpha} \approx \frac{\Omega}{\alpha} \quad . \tag{5.15}$$

Rotational rheometers, such as used in this study, are suitable to establish a precise overview of the material behaviour and are able to measure shear rates up to $10\,\mathrm{s}^{-1}$. However, shear rates of bone cement flow in vertebroplasty can reach up to values of $100\,\mathrm{s}^{-1}$.

5.6.2. Capillary rheometer

For the purpose of considering higher shear rates, capillary rheometer experiments were performed as well. In contrast to cone and plate rheometers, capillary rheometers are more application-oriented with respect to vertebroplasty and are able to generate shear rates up to $200\,\mathrm{s}^{-1}$ and beyond. Within this study, a capillary rheometer was designed to fit into a universal testing machine (*Zwick & Roell* type *ZN 20*). The schematic setup of this type of rheometer is illustrated in fig. 5.18. The diameter D of the reservoir is 15 mm. It is equipped with exchangeable capillaries, specified by the parameters L and d. Three different slenderness ratios $\lambda = L/d = 6.7$, 10 and 13.7 were realised, whereat the diameter $d = 3\,\mathrm{mm}$ remained constant. All surfaces having contact with the cement were reamed. Temperature control is resigned in this device because the large sample mass complicates adjusting uniform temperatures within

short time.
The viscosity for a fully developed pipe flow can be calculated as follows [123, 176]:

$$\eta = \frac{\tau_w}{\dot{\gamma}_w} \tag{5.16}$$

$$\tau_w = \frac{\Delta p d}{4L} \tag{5.17}$$

$$\dot{\gamma}_w = \frac{32\dot{V}}{\pi d^3} \quad . \tag{5.18}$$

Herein, τ_w and $\dot{\gamma}_w$ are the shear stress and the shear rate at the wall, and $\dot{V}$ is the volumetric flow rate. The pressure drop Δp can be calculated knowing the force F acting on the plunger and the cross section of the plunger. However, this determination of the viscosity η is only valid for a Newtonian fluid within a fully developed pipe flow. As stated earlier, bone cement exhibits a non-Newtonian, shear-thinning fluid behaviour. Thus the shear stress τ_w and the shear rate $\dot{\gamma}_w$ are only apparent, but do actually not appear at the wall. In addition, the velocity profile across the radius is not shaped parabolically, but flattened in the centre. To account for the non-Newtonian behaviour of bone cement and the pressure drop at the entrance, where the flowing material goes from a wide reservoir to a narrow capillary, correction procedures have to be applied [44, 123, 176].

5.6.2.1. Bagley correction

The Bagley correction considers the pressure drop at the capillary entrance and exit, that is not due to viscous, but elastic forces. It yields the true shear stress at the wall. Therefore, experiments with capillaries of different length L, but with the same diameter d are necessary, while all other parameters, e.g. the shear rate $\dot{\gamma}_w$, remain constant. Assuming that the same inlet pressure drop p_{corr} occurs for these different capillaries, it is possible to correct this pressure drop. According to fig. 5.19 the overall pressure drop Δp is plotted over the slenderness ratio L/d. The pressure drop Δp for a slenderness ratio equal to 0 can be determined by cubic extrapolation. This pressure drop p_{corr} is due to entrance losses and has to be subtracted from the overall pressure drop Δp to get the true pressure drop due to the viscous flow within the capillary. Using eq. (5.17), the true shear stress at the wall $\tau_{w,corr}$ can be calculated.

5.6.2.2. Rabinowitsch-Weissenberg correction

Eq. (5.18) is only valid for a fully developed flow profile of a viscous fluid. However, bone cement shows clearly viscoelastic properties, for example visible in effects like a non-zero storage modulus, die swelling (cf. ch. 3), and therefore, the flow profile and the shear rate deviate from those of a pure viscous fluid [164]. Near the wall, shear-thinning fluids exhibit a significantly larger velocity gradient than Newtonian fluids do. Thus the shear rate of a shear-thinning fluid

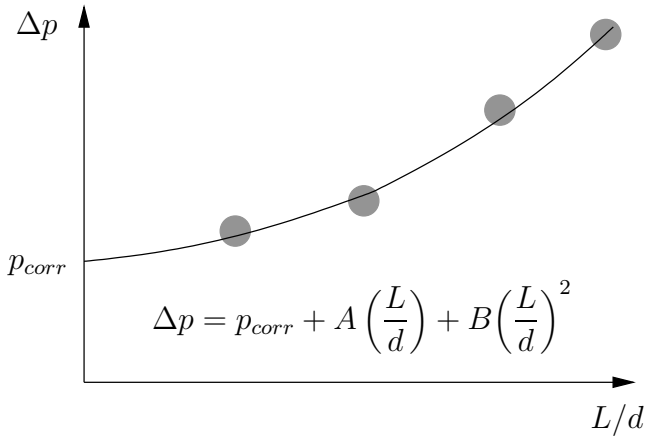

Figure 5.19.: Bagley correction

at the wall is larger compared to a Newtonian fluid. To compensate this phenomena within the data evaluation (eq. 5.18) the Rabinowitsch-Weissenberg correction is applied. Thereby, the true shear stress $\tau_{w,corr}$ (already corrected (see sec. 5.6.2.1)) is plotted over the shear rate $\dot{\gamma}_w$ (calculated by eq. (5.18)) on a double-logarithmic scale. This implies the conducting of experiments with varying shear rates [164]. A straight line is fitted to the related data points and the slope n is identified according to fig. 5.20.

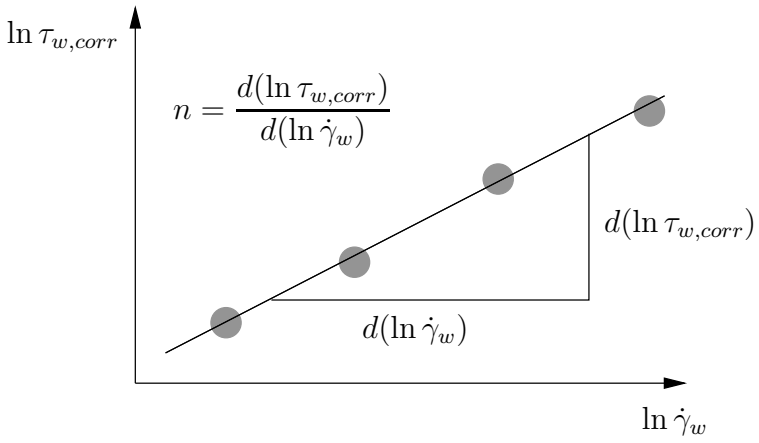

Figure 5.20.: Rabinowitsch-Weissenberg correction

The true shear rate is calculated as follows:

$$\dot{\gamma}_{w,corr} = \frac{1}{4}\dot{\gamma}_w \left[3 + \frac{1}{n}\right] = \frac{8\dot{V}}{\pi d^3}\left[3 + \frac{d(\ln \dot{\gamma}_w)}{d(\ln \tau_{w,corr})}\right] \quad . \tag{5.19}$$

Subsequently, the true viscosity can now be calculated as

$$\eta_{corr} = \frac{\tau_{w,corr}}{\dot{\gamma}_{w,corr}} \quad . \tag{5.20}$$

Without this Rabinowitsch-Weissenberg correction the shear rate would be underestimated and hence, the dynamic viscosity would be overestimated (cf. [123, 176]).
In addition, it is possible that non-Newtonian fluids may also show some gliding on the wall. The assumption of zero tangential velocity at the wall is violated and the motion of the fluid is a superposition of gliding and flowing. The viscosity can be corrected for these phenomena by the Mooney correction [164]. Therefore, measurements with constant shear stress and hence capillaries with a constant slenderness ratio L/d are required. Such an analysis was not handled in this study, but should be addressed in further investigations.

5.6.3. Experimental results

The previous measurements in sec. 5.5.1 have showed that polymerisation has a negligible influence on the mechanical behaviour of the cement directly after mixing. For this reason and the facilitation of cleaning the instruments, non-polymerising acrylic cement was used for these experiments. The mixing procedure was again conform with the explanations in sec. 5.1. For cone-plate rheometry, bone cement was placed on the plate and subsequently, the distance between cone and plate was adjusted. Excessive cement was then removed. The capillary rheometer has a modular design and was filled bottom up, with the plunger already installed, to avoid air inclusions. Afterwards, the nozzle was screwed on and the complete capillary was mounted onto the universal testing machine. Approximately, $220\,\mathrm{s} \pm 10\,\mathrm{s}$ after the first contact of both components, the data recording was started for both rheological techniques.

5.6.3.1. Cone-plate rheometer

On the cone and plate rheometer, experiments were carried out for four different temperatures of 15, 20, 25 and 30 °C, and three different shear rates of 1, 5 and $10\,\mathrm{s}^{-1}$. The maximum shear rate was limited by the rotating speed of the rheometer and the maximum temperature was limited by the fact that the bone cement specimen immediately formed a film at temperatures above 30 °C so that adhesion between cone and cement could not be guaranteed. The following fig. 5.21 displays the results of the cone and plate rheometer experiment, evaluated according to sec. 5.6.1. In summary, three facts are important to notice. First, the dynamic viscosity of acrylic bone cement increases with increasing time, that means with proceeding dissolution. Second, at higher temperatures the dissolution progresses faster. And third, bone cement shows a shear-thinning behaviour. That means the dynamic viscosity of bone cement decreases with increasing shear rate. During the analysis of all temperatures and shear rates, acrylic bone cement shows a uniform behaviour.

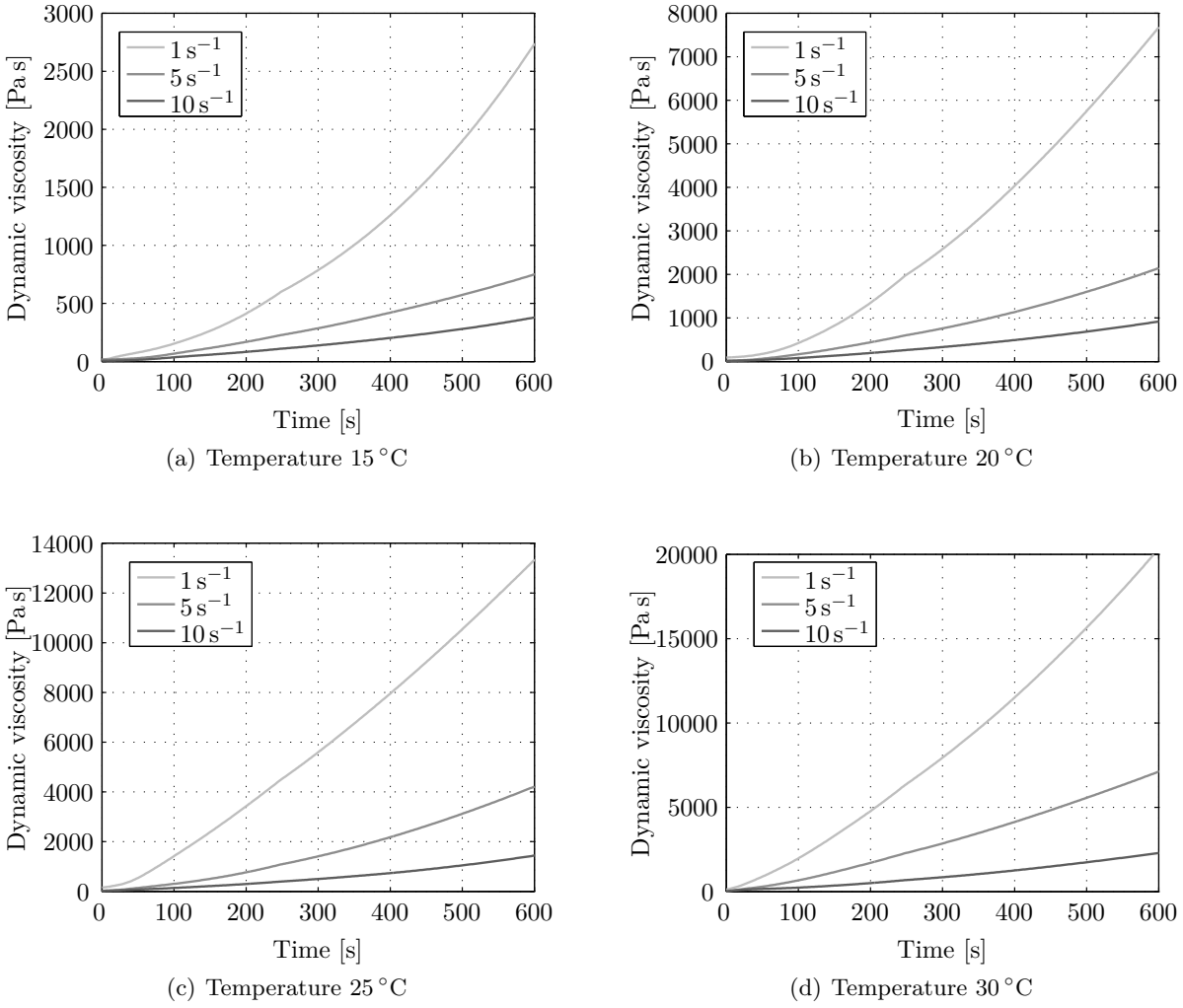

(a) Temperature 15 °C

(b) Temperature 20 °C

(c) Temperature 25 °C

(d) Temperature 30 °C

Figure 5.21.: Cone-plate rheometer results

5.6.3.2. Capillary rheometer

All measurements with the capillary rheometer were carried out at a room temperature of 20 °C. Three different apparent shear rates were chosen, namely 10, 50 and 100 s^{-1}. The experiment had to be interrupted several times for apparent shear rates of 50 and 100 s^{-1}, otherwise the plunger would have reached the bottom within a shorter time range than 10 minutes. The force F was interpolated at periods, when the plunger was resting. As friction was unavoidable, blind curves were recorded for each shear rate and the result was subtracted from the experimental force curves. Fig. 5.22 displays the total pressure drop measured at the capillary rheometer. Throughout all measurements, the total pressure drop increased with higher apparent shear rates and increasing capillary length. According to sec. 5.6.2, the Bagley correction and the Rabinowitsch-Weissenberg correction were applied in order to obtain the true viscosity at the true shear rate.

Fig. 5.23(a) shows that the correction pressure p_{corr} is in the range of the total pressure drop Δp.

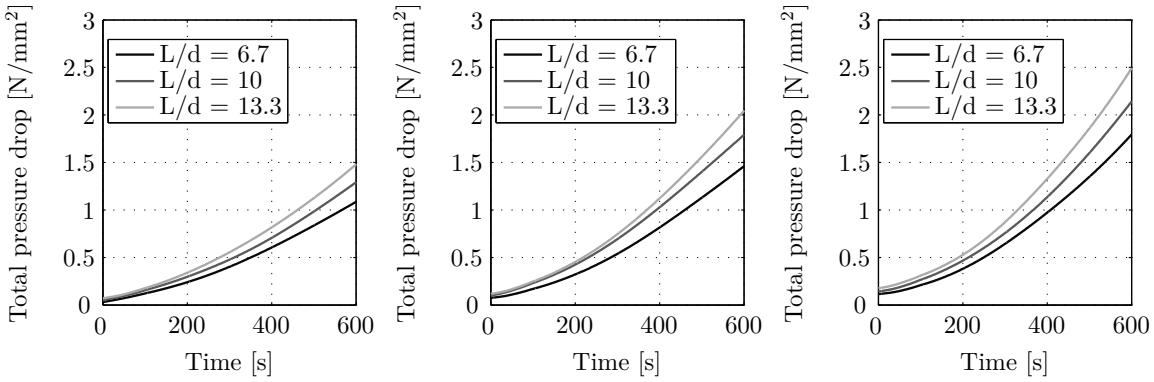

(a) $\dot{\gamma}_w = 10\,\mathrm{s}^{-1}$ (b) $\dot{\gamma}_w = 50\,\mathrm{s}^{-1}$ (c) $\dot{\gamma}_w = 100\,\mathrm{s}^{-1}$

Figure 5.22.: Total pressure drop measured with capillary rheometer

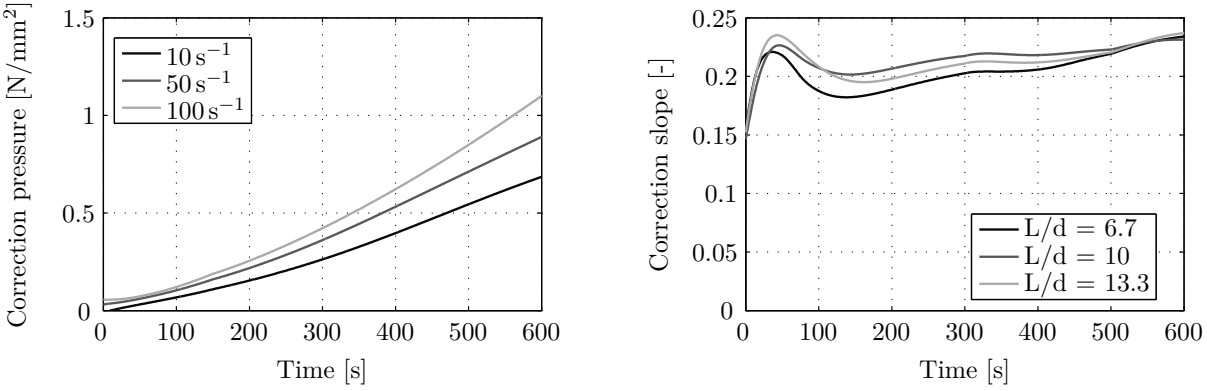

(a) Bagley correction (b) Rabinowitsch-Weissenberg correction

Figure 5.23.: Result of Bagley correction and Rabinowitsch-Weissenberg correction

That means that without the Bagley correction, the viscosity, according to eq. (5.16) and (5.17) would be significantly overestimated. The correction slope in fig. 5.23(b) in combination with eq. (5.19) show that the true shear rate is approximately twice as high as the shear rate predicted by eq. (5.18). Instead of the apparent shear rates 10, 50 and $100\,\mathrm{s}^{-1}$, the Rabinowitsch-Weissenberg correction states the true shear rate as 19, 95 and $191\,\mathrm{s}^{-1}$ (see also fig. 5.24). Evaluating eq. (5.18) leads to the following corrected progress of dynamic viscosity in fig. 5.24. In addition, fig. 5.24 shows the measurement of cone-plate rheometry for 20 °C and $10\,\mathrm{s}^{-1}$ (dashed line). Although the measurement technique is completely different, a good agreement between cone-plate and capillary rheometry can be noticed. Moreover, the shear-thinning behaviour is continued at higher shear rates.

Most fluids show a decrease in viscosity with increasing temperature. Unfortunately, this phenomenon cannot be observed in the experiments showed above because the effect of dissolution on viscosity is much more distinctive. Further experiments, including temperature modulation, would be necessary to distinguish between reversible (temperature dependence of viscosity) and non-reversible (temperature dependence of dissolution) effects on the viscosity of acrylic cement

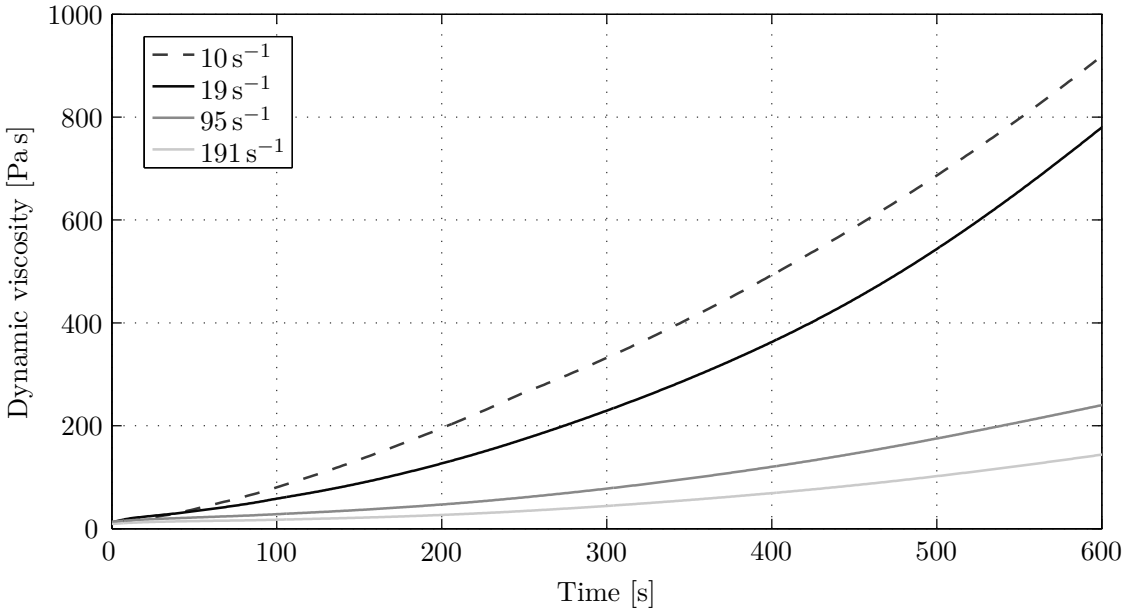

Figure 5.24.: Capillary rheometer results (—) compared to cone-plate rheometer results (- -)

[108]. However, the experimental techniques described above are to inert for a fast temperature control.

Although extending the experimental temperature range would be favourable, the rheological experiments provide an accurate overview of the flow behaviour of bone cement under varying parameters as they may appear for a spinal surgery in the context of vertebroplasty. It is important to notice that these results are only valid as long as the dissolution process dominates the mechanical behaviour of bone cement, which is true for the waiting and application phase (cf. sec. 4.3). However, further experiments are necessary to analyse the behaviour of acrylic bone cement in the polymerisation-controlled phase.

5.7. Mechanical behaviour during polymerisation

In contrast to the application phase, where acrylic bone cement is treated like a fluid from a physical point of view, cement does not flow during the setting phase, but undergoes a transition from a fluid to a solid. As there is no movement besides shrinkage and thermal expansion, it is reasonable to treat acrylic cement as a solid, rather than a fluid, while polymerising. The preliminary experiments in sec. 5.5.1 have showed that mechanical parameters change within several orders of magnitude during this transition. To experimentally cover this range, a rotational rheometer equipped with parallel plates and operated with a harmonic excitation is an appropriate measuring technique (cf. sec. 5.5.1) [56, 168] and is chosen to analyse the mechanical behaviour of an acrylic cement on a broader basis.

Fig. 5.25 shows the schematic parameters of a parallel-plate rheometer. Compared to a cone and plate rheometer the cone is replaced with a second plate. As an operating unit, an *AR G2*

rheometer from *TA Instruments* was used again. In order to exploit the torque range of the rheometer, a plate radius R of 4 mm and a initial gap distance d of 1 mm is chosen. As bone cement exhibits chemical shrinkage while polymerising, the plate distance will also decrease during the experiment. To allow such a shrinkage, the gap distance is normal-force-controlled. Moreover, the measurement alignment, as showed in fig. 5.25, is surrounded by a hinged oven, including the possibility of nitrogen cooling for temperature controlling. The experiments are

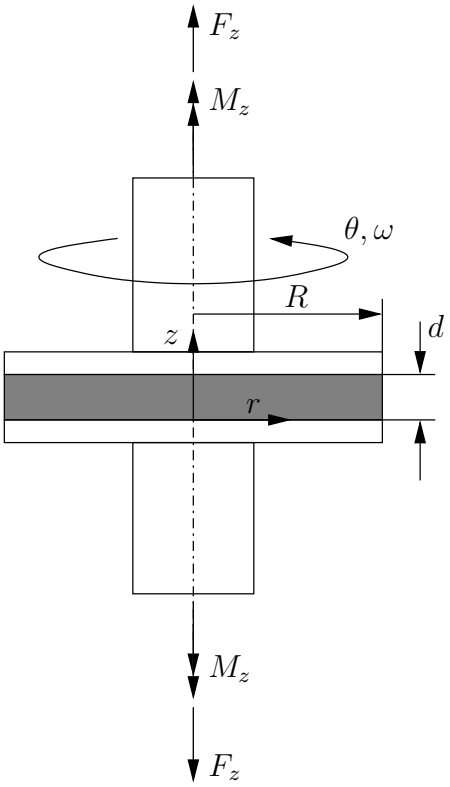

Figure 5.25.: Schematic of parallel-plate rheometer

designed in a way that it is easy to gain mechanical properties that are typical in solid mechanics. Therefore, a mono frequent, harmonic, angular excitation is applied to the top plate (while the lower plate remains fixed), which can be expressed as

$$\gamma(t,r) = \frac{r\theta(t)}{d} = \gamma_0(r)\sin(\omega t) \quad \text{with} \quad \omega = \frac{2\pi}{T} = 2\pi f \quad . \tag{5.21}$$

Herein, γ is the shear strain (for small twist), R the plate radius, θ the twist, γ_0 the shear strain amplitude and ω the angular frequency. As the acrylic cement material behaves viscoelasticly and the shear amplitudes are not too large, the stress response to this excitation is also harmonic, but phase shifted with respect to the excitation and can be measured as torque:

$$M(t) = M_0 \sin(\omega t + \delta) \quad . \tag{5.22}$$

Taking into account the geometrical dimensions and small twist, the maximum shear stress τ at the plate edge ($r = R$) can be derived as [44, 158]

$$\tau(t) = \frac{2M(t)}{\pi R^3} = \tau_0 \sin(\omega t + \delta) \quad . \tag{5.23}$$

The maximum shear stress τ_0 is generally used for the evaluation of further characteristic values (cf. [44, 158]).
In analogy to sec. 3.2.2, the shear stress can also be expressed in terms of the shear storage modulus and shear loss modulus or complex shear modulus, whereat

$$\tau(t, R) = \gamma_0 \left(G'(\omega) \sin(\omega t) + G''(\omega) \cos(\omega t) \right) = \gamma_0 \tilde{G}(\omega) \sin(\omega t + \delta) \quad , \tag{5.24}$$

and

$$G'(\omega) = \frac{\tau_0}{\gamma_0} \cos\delta \qquad G''(\omega) = \frac{\tau_0}{\gamma_0} \sin\delta \tag{5.25}$$

holds. For this analysis, it is required that the change in influencing material properties (i.e. the degree of cure) is small within one evaluation cycle. Compared to a cone-plate rheometer, the shear strain and the shear rate are not constant across the radius for a parallel-plate rheometer (cf. eq. (5.21)). However, the experiments were only executed at small angles within the linear range as greater shear strains would have damaged the specimen as soon as the cement solidifies (cf. sec. 5.5.2). Preliminary experiments proofed also the independence of the complex modulus on the shear strain at small excitation angles [53].
For the specimen preparation, polymerising bone cement was mixed according to sec. 5.1 and placed on the preconditioned bottom plate. Subsequently, the gap distance was reduced to 1 mm and excessive cement was removed in order to guarantee a well shaped cylindrical specimen. The torsional loading and data recording were started approximately 220 seconds after both components were stirred together.
Isothermal experiments were performed at a temperature range from 15 °C to 40 °C, in a frequency band from 1 Hz to 40 Hz and with a shear strain amplitude of 0.1 %. The temperature range was limited to 40 °C, because the sample starts to polymerise during the preparation on the preconditioned plate at higher temperatures so that an adhesive contact between cement and the top plate cannot be established. The limiting factors for the frequency band are not getting enough data points at low frequencies (one data point per period only). At higher frequencies (> 40 Hz), the torque induced by the moment of inertia of the rheometer clearly exceeds the torque generated by the material response. Therefore, measurements at frequencies higher than 40 Hz are imprecise. The shear amplitude is limited by the maximum detectable torque of the rheometer when the cement is fully polymerised.
Fig. 5.26 shows the results of the isothermal parallel-plate rheometer experiments expressed in shear storage modulus (left diagram) and shear loss modulus (right diagram). The experiments for different frequencies but for a specific temperature are combined in a single diagram. With increasing temperature from fig. 5.26(a) to fig. 5.26(k), the influence of the temperature-dependent reaction kinetics on chain growth and hence on mechanical strength is evident. Comparing the

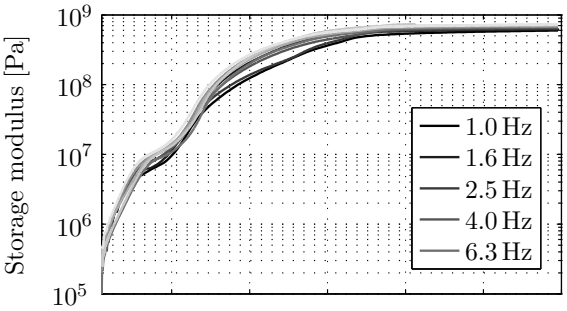

(a) Storage modulus at 15 °C

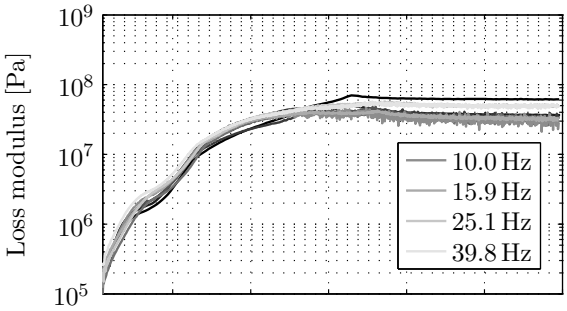

(b) Loss modulus at 15 °C

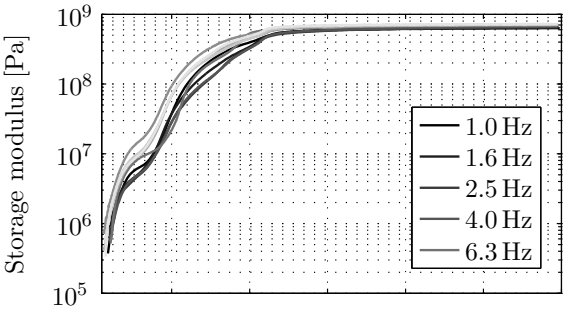

(c) Storage modulus at 20 °C

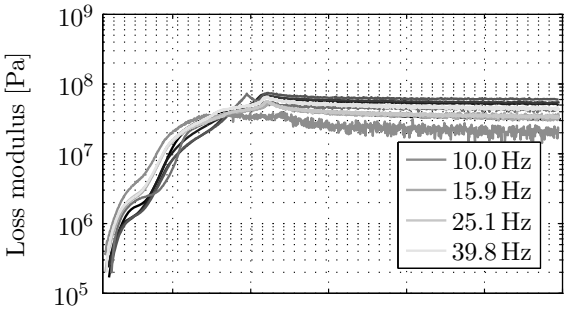

(d) Loss modulus at 20 °C

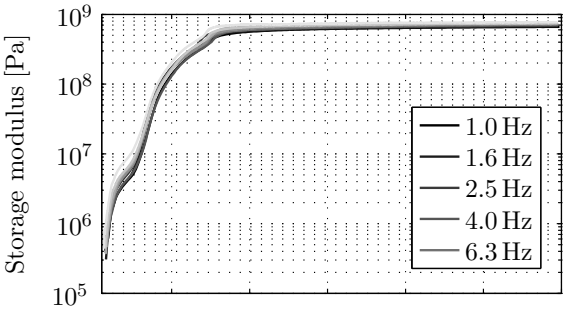

(e) Storage modulus at 25 °C

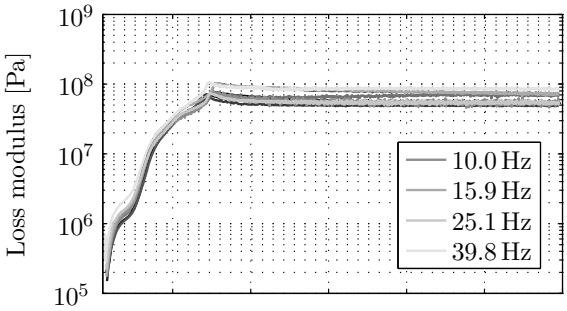

(f) Loss modulus at 25 °C

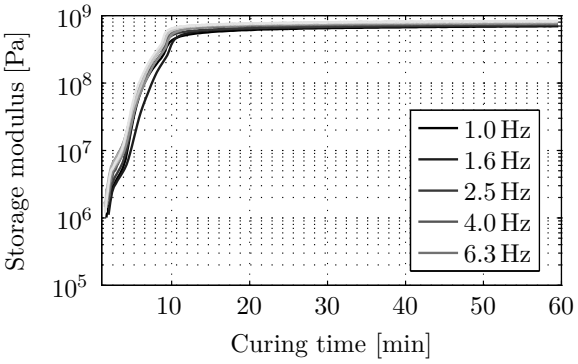

(g) Storage modulus at 30 °C

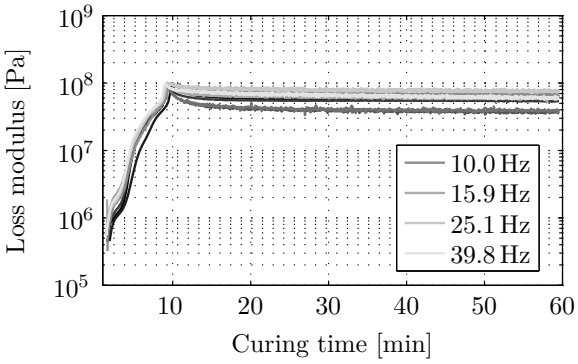

(h) Loss modulus at 30 °C

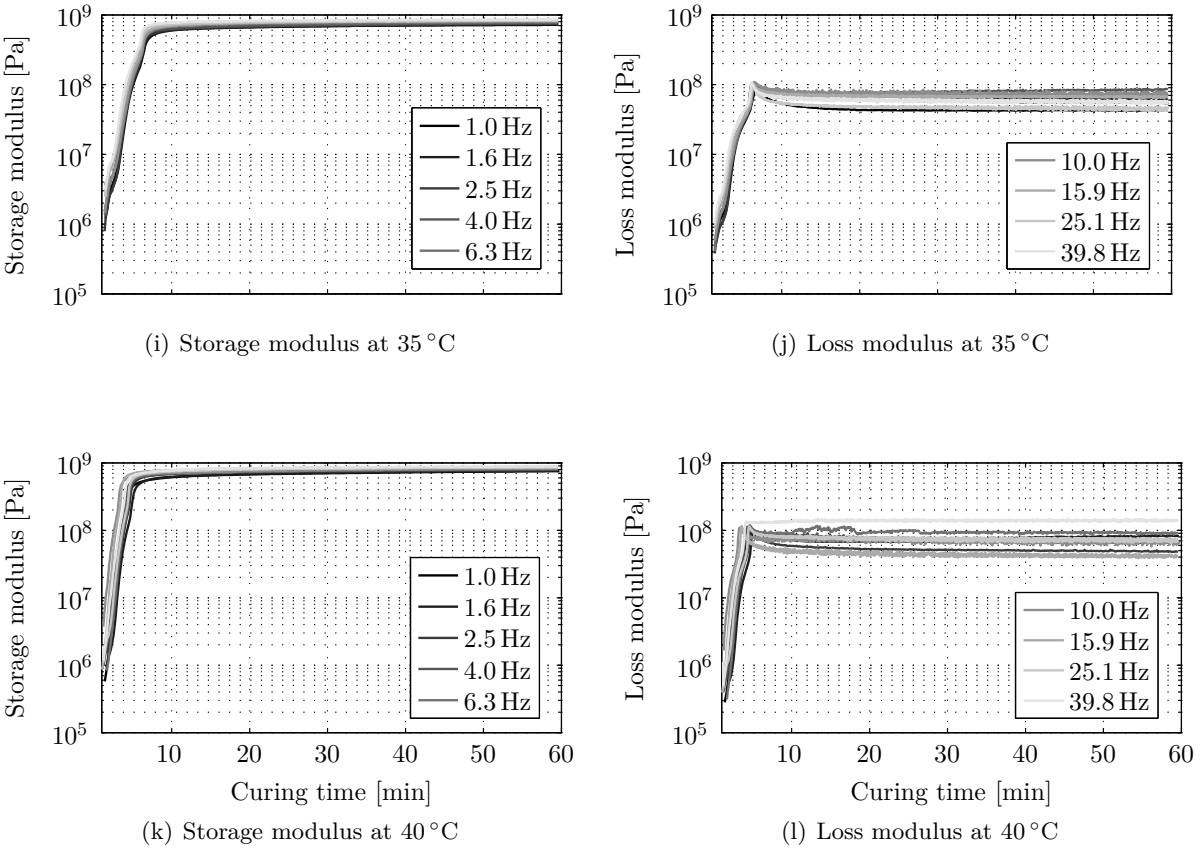

(i) Storage modulus at 35 °C

(j) Loss modulus at 35 °C

(k) Storage modulus at 40 °C

(l) Loss modulus at 40 °C

Figure 5.26.: Parallel-plate rheometer results at different temperatures and frequencies

storage modulus for different isothermal experiments with the cumulative heat released during isothermal polymerisation (cf. fig. 5.5), a good correspondence can be observed. The elapsed times when storage and loss modulus start to increase, coincide with those when heat is released in the calorimetric tests. Moreover, the maximum storage modulus is reached at the same time the heat release has finished. For temperatures up to 30 °C the main dissolution process (first steep increase in storage and loss modulus) can be distinguished from the accelerated polymerisation (second steep increase in storage and loss modulus). The change from dissolution to polymerisation becoming the dominating process always occurs in the range of approximately $5 \cdot 10^6$ Pa to $1 \cdot 10^7$ Pa for the storage modulus. In contrast, experiment temperatures above 30 °C cause the accelerated polymerisation to start so early that dissolution and polymerisation overlap. Focusing on the final value for the storage modulus, higher temperatures seem to cause a higher value in the final storage modulus. On the one hand, higher temperatures lead to a higher final degree of cure, but on the other hand, higher temperatures also lead to a softening of thermoplastic polymers. In this case, the advanced chain growth seems to have a greater impact on the final storage modulus than softening has. The loss modulus exhibits a similar course during dissolution and polymerisation as the storage modulus does. However, a peak is visible at the point of time when the storage modulus has almost reached its final value. This peak indicates the transition into the glassy state, where polymerisation gets diffusion-controlled (cf.

fig. 5.27). After this peak, the loss modulus decreases slightly and ends up with a final value that is approximately one magnitude lower than the final value of the storage modulus.
With regard to the loading frequency, dependencies are not as obvious at first glance as they are for the temperature. On a closer look, the material is slightly stiffer at higher frequencies which can be explained by its viscoelastic nature. In general, this holds for both, the cured and the uncured cement and is even more distinctive during polymerisation. However, this frequency-dependence is not easily dissolvable in the experiments, since the frequency span is quite narrow and small variations occur in sample preparation and geometry. In the diagrams for the loss modulus (cf. fig. 5.26(b) to fig. 5.26(l)) , the same dependence on the frequency can be noticed, although not as clearly as for the storage modulus. Experiments with a single specimen but different frequencies confirm the increase of storage and loss modulus with increasing frequency (cf. sec. 5.8.1).
The calorimetric measurements in sec. 5.2.1 reveal an uncomplete curing for isothermal experiments below the glass temperature of the solidified material. In order to identify possible effects of post-curing or uncomplete curing on the mechanical behaviour, a temperature ramp with 5 °C/min up to 150 °C was added, supplementary to the measuring process described above. This peak temperature was held for 5 minutes to ensure a complete conversion of the monomer. Subsequently, the temperature was lowered to the body temperature of 37 °C with a temperature rate of −5 °C/min. Fig. 5.27 exemplarily shows the course of temperature, storage and

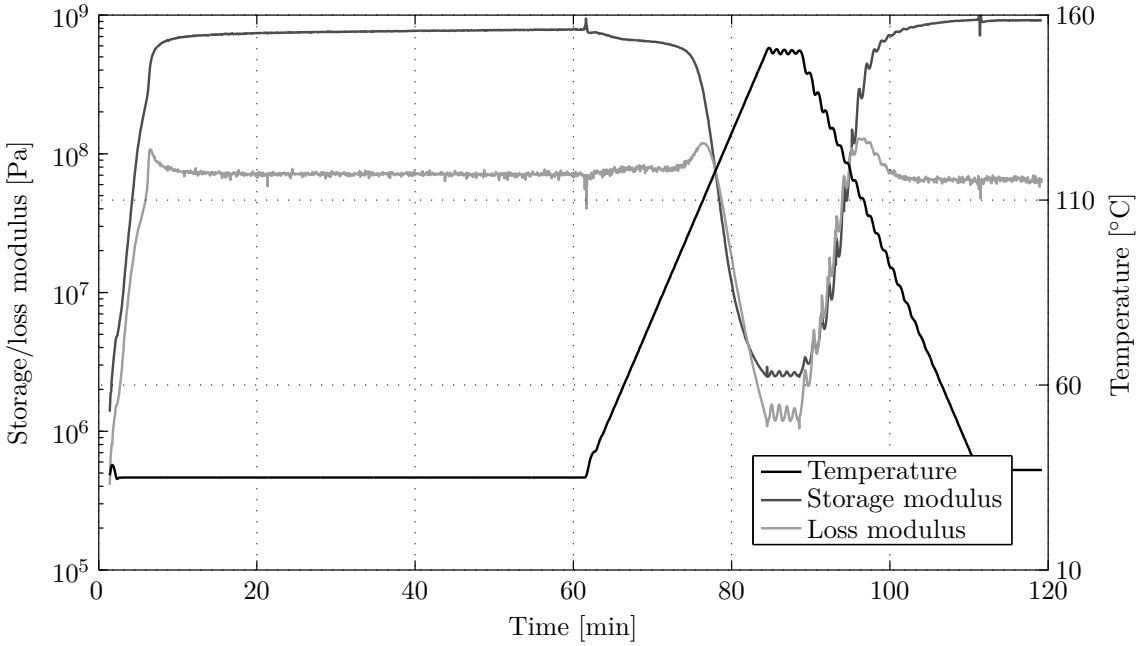

Figure 5.27.: Progress of temperature, storage and loss modulus for post-curing at 35 °C and 6, 3 Hz

loss modulus at 35 °C and 6, 3 Hz for the post-curing procedure described above. As soon as the temperature is increased, the storage modulus decreases and contrarily the loss modulus rises slightly. Two effects influence the mechanical behaviour of acrylic cement here, namely

softening due to the temperature increase and further hardening due to post-curing, whereat the softening has a greater impact. As soon as the temperature reaches the glass transition, both, storage and loss modulus decrease severely. Throughout the experiments, it is noticeable that the glass transition is marked by a peak of the loss modulus. At the end of the experiment, when a temperature of 37 °C is maintained, a distinct increase in the storage modulus (from $7.8 \cdot 10^8$ Pa to $9.1 \cdot 10^8$ Pa) and a decrease in the loss modulus (from $7.2 \cdot 10^7$ Pa to $6.7 \cdot 10^7$ Pa) is recognisable. Thus, a further post-polymerisation after glass transition (diffusion-controlled) is likely to be accompanied with a relevant increase in storage modulus and a decrease in loss modulus (cf. sec. 5.8.1). The other measurements exhibited the same effect, whereas the change in the moduli was also superposed by an additional softening and hardening due to lower and higher curing temperatures compared to the final temperature of 37 °C.

5.8. Mechanical behaviour after polymerisation

5.8.1. Dynamic-mechanical analysis

In addition to the rheometer experiments, the mechanical behaviour of polymerised bone cement was also investigated by means of dynamic-mechanical analysis (DMA). The aim of these experiments was to examine the mechanical long term behaviour, especially the diffusion-controlled curing within the human body. As mentioned in sec. 4.4, the mechanical properties of acrylic bone cements in the human body are influenced by post-curing and water uptake. However, a complete conversion of the monomer is not likely to be attained, because the monomer will also diffuse out of the cement bulk.
The DMA-experiments were performed using prismatic specimens with a rectangular edge dimensions $b \times h$, which are clamped at a fixed length l and exposed to a constant preload. Subsequently, a dynamic harmonic load is superposed to the preload in such a way that the specimen is only subjected to tensile loading. Similar to the rheometer experiment, the response of the specimen is a phase-shifted harmonic force or displacement. This data can be used to calculate the frequency- and temperature-dependent storage modulus E' and loss modulus E'' [157]

$$E'(\omega) = \frac{\sigma_0}{\varepsilon_0} \cos\delta \qquad E''(\omega) = \frac{\sigma_0}{\varepsilon_0} \sin\delta \quad , \tag{5.26}$$

whereas

$$\sigma_0 = \frac{F_0}{bh} \qquad \varepsilon_0 = \frac{l_0}{l + l_p} \tag{5.27}$$

holds. Herein, F_0 denotes the force amplitude and l_0 the displacement, both only due to dynamic loading. l_p is the displacement due to preloading and δ is the phase angle between mechanical loading and material response.
For DMA-experiments, the prismatic specimens are moulded in a casting mould. A base area of

$2 \times 5\,\text{mm}$ and a clamped length of 40 mm leads to an efficient resolution of the machine setup. Bone cement is therefore mixed according to sec. 5.1 and filled into the mould, similar to the procedure described in sec. 5.3. Afterwards, the test samples are allowed to polymerise at room temperature for 30 minutes. After removing from the mould, all but three specimens are stored in Ringer's solution[1] at 37 °C over a different period to simulate the environment of the human body. These three other specimens are treated differently. One of the remaining three samples is analysed by means of DMA directly after demoulding and acts as a reference. It is likely that quite an amount of residual monomer will remain inside the specimen. The degree of cure should be around 80 %, but of course is not homogeneous within the specimen due to the different evolution of temperature across the specimen. Another sample is stored at 120 °C for one hour after demoulding to ensure an almost complete conversion of the monomer. This specimen should be the stiffest one of all because of the increased polymer chain length. Back at room temperature, this sample is also DMA analysed without any further treatment. A third specimen is stored at room temperature in ambient air for two weeks (340 h) and is analysed afterwards. Some of the residual monomer will diffuse out of the specimen, another part will polymerise and some residual monomer will remain inside the specimen. With the aid of these three specimens, it is easier to evaluate how acrylic bone cement behaves mechanically after being stored in Ringer's solution. The dynamic-mechanical analysis was performed on an electrodynamic oscillating system *Eplexor* 500 manufactured by *Gabo*. In the depicted experiments in fig. 5.28 and 5.29, the preload displacement was chosen as 0.5 % of the clamped length l, the harmonic displacement was set to 0.1 % and the frequency was driven from 0.5 Hz to 80 Hz. Moreover, the temperature was set to 37 °C, equal to the body temperature.

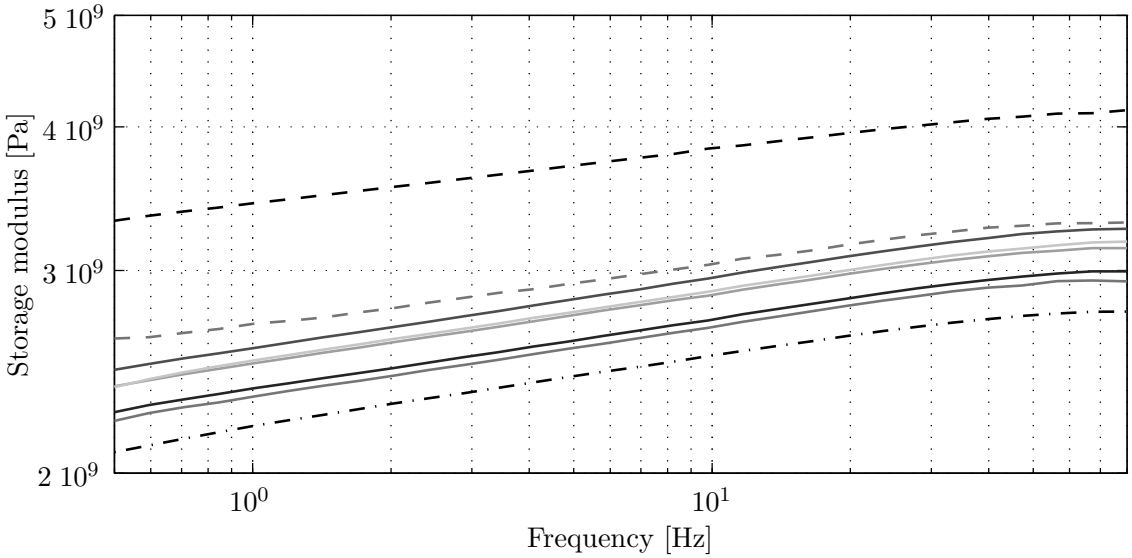

Figure 5.28.: Storage modulus of cured bone cement for different treatment and ageing at 37 °C, loaded with 0.5 % static preload and a harmonic excitation with 0.1 % amplitude

Fig. 5.28 and 5.29 represent the storage and loss modulus for the measurement procedure de-

[1] Ringer's solution is produced by solving sodium chloride, potassium chloride and calcium chloride in water. It is commonly used to simulate the body fluid for investigating ageing effects on biomaterials.

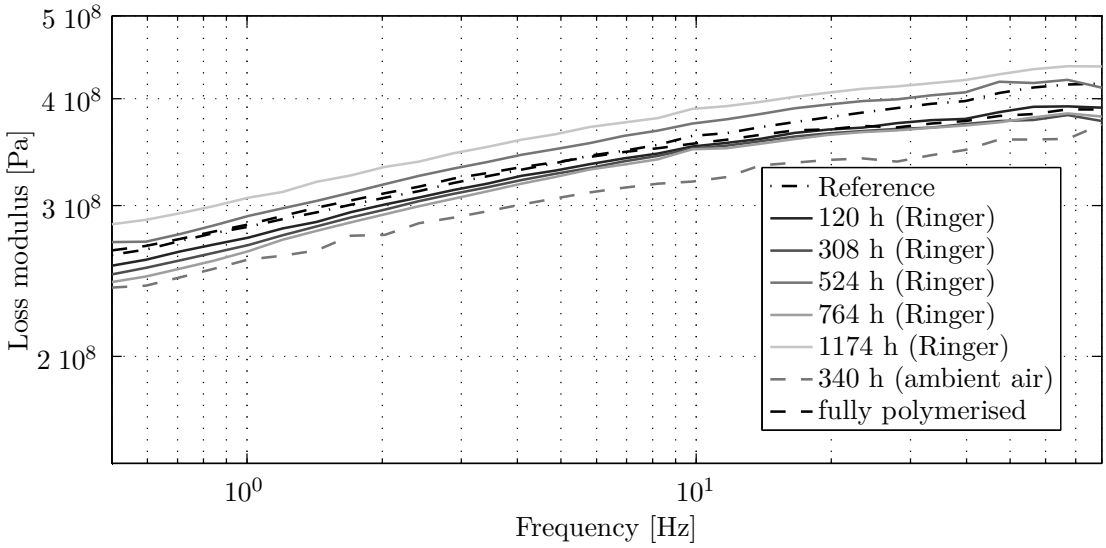

Figure 5.29.: Loss modulus of cured bone cement for different treatment and ageing at 37 °C, loaded with 0.5 % static preload and a harmonic excitation with 0.1 % amplitude

scribed above. Both, the storage and loss modulus exhibit a distinctive frequency-dependence and confirm the results of the parallel-plate rheometer experiment (cf. sec. 5.7). According to the viscoelastic behaviour, the stiffness increases with increasing frequency and the same applies to the loss modulus. It is remarkable that, independent of the ageing duration or the medium, the frequency-dependency of storage and loss modulus is preserved, resulting in a parallel shift of the curves. Regarding the specimens that were not exposed to the Ringer's solution, a clear difference is evident. The specimen that is analysed directly after demoulding is the least stiffest, followed by the specimen stored at ambient air and the post-cured specimen. The increase in stiffness (i.e. the storage modulus) due to post-curing heat treatment is almost half the stiffness value of the reference sample. However, the loss modulus is about equal for the reference and the post-cured specimen with heat treatment. The loss modulus of the specimen stored at ambient air is even lower. Looking at the results of the specimens stored in Ringer's solution, the storage modulus lies above the value for untreated specimen and below the value for the specimen stored at ambient air. Among the specimens stored in Ringer's solution, there is no clear tendency visible that the moduli increase or decrease with increasing storage period. The values for the storage modulus do not deviate much at all. The weight increase, measured with a precision balance *ME235P* from *Sartorius*, yields a value of 0.7 % for the specimen stored in Ringer's solution for 120 h and rises only slightly to 0.8 % for the specimen stored for 1174 h. Apparently, the long-time water uptake in acrylic bone cement is a very slow process and this might explain small deviations of the moduli. However, the water uptake seems to decrease the stiffness, since the values for the storage modulus of the specimens stored in Ringer's solution lie below the values of the specimen stored at ambient air, whereas the post-curing effect in Ringer's solution at 37 °C should be higher than in ambient air at 22 °C. A precise statement on the effect of water uptake on the damping behaviour cannot be made upon the conducted experiments. Therefore, continuing experiments are necessary, where the effects of water uptake

and post-curing can be separated.
By comparing the dynamic-mechanical analysis results, where the dynamic Young moduli are determined, with the results of the parallel-plate rheometer experiments (cf. sec. 5.7), where the dynamic shear moduli are measured, a conclusion on the Poisson's ratio can be drawn. Assuming that

$$E^* = 2G^*(1+\nu) \tag{5.28}$$

holds, Poisson's ratio can be calculated. On a closer examination of the parallel-plate rheometer results and DMA experimental results, the complex shear modulus in the fully cured state can be identified as about one third of the value of the complex elasticity modulus. This yields a Poisson's ratio of approximately 0.5 (values above 0.5 are not admissible for solids) and suggests the incompressibility of acrylic cement material. In literature, Poisson's ratio of solid PMMA in the glassy state is indicated from 0.35 to 0.4 and rises up to 0.5 for temperatures beyond the glass transition [111]. Furthermore, advanced experimental investigations have showed that Poisson's ratio for viscoelastic material behaviour is also time- and frequency-dependent [70, 118, 148]. In the frequency domain, Poisson's ratio is complex like the dynamic Young and shear modulus. However, it is particularly difficult to determine the time- or frequency-dependent Poisson's ratio, as a simultaneous measurement of two viscoelastic response functions (i.e $E^*(\omega)$ and $G^*(\omega)$ or $E(t)$ and $G(t)$) with a unique measurement is inevitable [226]. O'Brien et al. [173] proofed experimentally that Poisson's ratio of epoxy resins is also dependent on the degree of cure and temperature, tending to a value of 0.5 in the rubbery regions. Unfortunately, no measurement device was available in the scope of this study, where two viscoelastic response function could have been detected simultaneously. Although the determined value seems to be quite high, it confirms that the dynamic Young moduli (measured by DMA) and the dynamic shear moduli (measured by rheometer) are still comparable, while measured with two different techniques.

5.8.2. Quasi-static analysis

The previously presented dynamic-mechanical analysis is suitable to identify the viscoelastic properties of solid materials. In order to analyse whether the material reaches an equilibrium state or yields when loaded constantly, a dynamic-mechanical analysis is inapplicable, as excitation frequencies (or temperatures, cf. sec. 3.4.1) have to be very low. For modelling issues, yet, the fact of yielding is important to know. An easier access to identify the yielding behaviour is offered by a quasi-static analysis on a universal testing machine.
For this purpose, dumb-bell specimens are moulded in a process similar to the specimens used in the dynamic-mechanical analysis (cf. sec. 5.8.1). These specimens have a rectangular cross section of 4 mm × 3 mm over a length of 30 mm. After demoulding, the specimens are stored in ambient air for two weeks prior to testing, so that post-curing and monomer diffusion related effects can take place. A temperature of 37 °C is chosen to mimic the human body environment. In order to study the quasi-static material behaviour, the known universal testing machine from

Zwick & Roell was equipped with appropriate specimen holders, a temperature chamber and and a precise axial extensometer of the type *EXA 25-10* manufactured by *Sandner*.
Fig. 5.30 shows the resulting strain for different loading levels, whereas the load was applied with a velocity of 50 N/s. At the beginning of the experiment an instantaneous strain is visible,

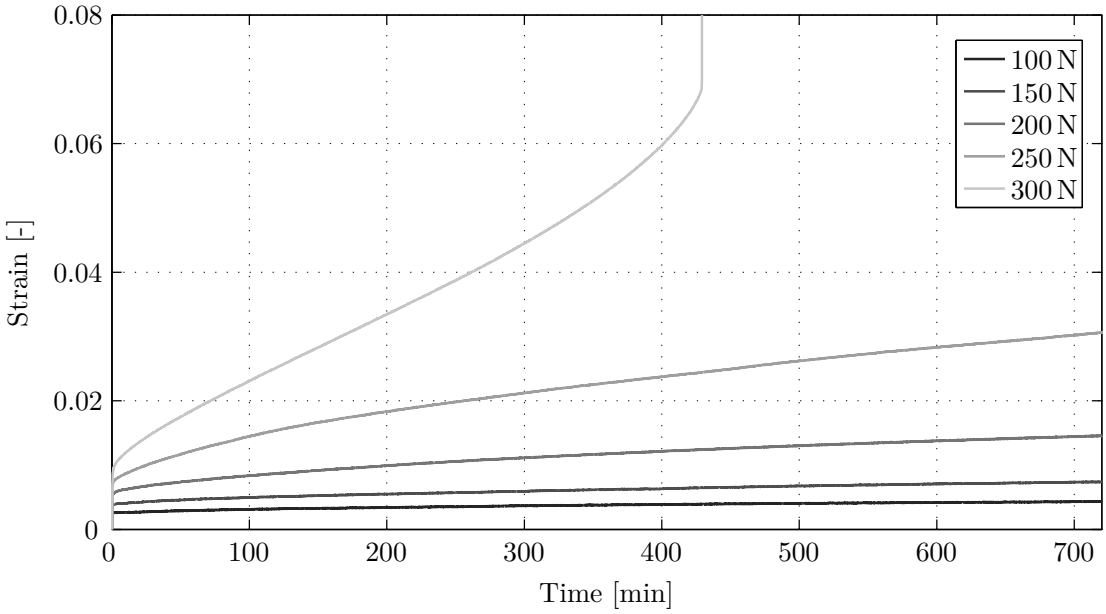

Figure 5.30.: Quasi-static tensile testing of bone cement under constant load at 37 °C

resulting from the elastic response of acrylic cement. Throughout the different loading levels, an equilibrium condition cannot be observed. This is a clear indicator for yielding and the increase in strain is more distinctive for higher loading. For a loading of 300 N the strain rises up to approx. 6.8 % after 400 minutes and the material starts to fail. Assuming a homogeneous distribution the stress at a load level of 300 N is 25 N/mm^2. Compared to specimens that were post-cured for one hour at 120 °C (experiments also conducted in the scope of this thesis, but no additional fig.) the stress level of 35 N/mm^2 at failure is significantly higher, but the failure strain decreases to approx. 5 %. Thus, post-curing embrittles the bone cement.
The conducted experiments in this chapter offer a detailed insight into the complex behaviour of acrylic bone cements during the processes of dissolution and polymerisation. The main influences of temperature, dissolution and polymerisation on the thermodynamic and mechanical behaviour have been worked out and serve as a basis for developing the material model and constitutive material functions. Of course, some side effects like post-curing, water uptake and the possible interrelation of dissolution and polymerisation are not fully covered, as this was not possible within the scope of this work. However, the related experiments clearly indicate the limitations for the developed model in ch. 6 and where to focus future research activities.

6. Material modelling

Based on the information of the previous chapter on the kinetic, thermodynamic and mechanical behaviour of acrylic bone cement during the different phases of vertebroplasty, this chapter will present and explain the material modelling. This modelling will focus on the dissolution and the main polymerisation process. The long-term behaviour will not be subject to modelling within this thesis.

As a necessary third part of equations within continuum mechanics, in addition to the kinematics and balance equations (cf. ch. 2), the material functions will be able to reflect the individual thermomechanical behaviour of bone cement and interrelate deformation and stress including the dependency on the dissolution and polymerisation process. The following part will illustrate some basic considerations on how to structure the experimental investigations in order to obtain a feasible modelling scope.

The experiments in ch. 5 have shown that dissolution and accelerated polymerisation coincide with one or more clinical cement process phases (cf. fig. 4.3). Of course, polymerisation starts also right after mixing both cement components together, however, rheological and mechanical behaviour of acrylic cement are predominantly influenced by only one of these two processes, not by both at the same time. For example, dissolution reigns during the waiting and application phase and significantly determines the rheological properties of acrylic cement, while polymerisation is accelerated and drastically changes the mechanical parameters within the setting phase (cf. sec. 5.5.1). Certainly, the time during the waiting and the application phase cannot be neglected for initial polymerisation, but a significant influence on the rheological properties of the cement due to initial polymerisation can not be discovered at room temperature (cf. sec. 5.5.1). Vice versa, when polymerisation gets accelerated within the setting phase, the increase of stiffness by dissolution can be neglected as dissolution itself comes to a stop anyway. Especially when dissolution progresses at room temperature and polymerisation gets accelerated by a temperature elevation inside the human body, as it is the case for vertebroplasty, the period of main influence on the rheological and mechanical behaviour of bone cement can be separated between dissolution and polymerisation, whereat the transition range diminishes.

These considerations do not suggest to use only one single material model to describe the thermomechanical behaviour of bone cement throughout the whole vertebroplastic process, including dissolution and polymerisation, but instead to develop two separate, but closely related models. The first model should cover the main dissolution process during the waiting and application phase and of course, include initial polymerisation. The second model should be capable to represent the thermo-mechanical material behaviour during the setting phase, while the main

polymerisation is going on. These stand-alone models can be tailored according to the needs to describe separately the material properties for dissolution and polymerisation. Another fact that suggests the application of two models is the common use of two different numerical techniques for injecting bone cement into the vertebra, a fluid dynamics problem, and curing of acrylic cement inside the vertebra, a solid mechanics problem. Usually, the finite volume method (FVM) is used for fluid dynamics problems and the finite element method (FEM) is used for solid mechanics problems, although both techniques can also be used vice versa.
Having outlined the model partitioning, the following chapter will present the structure of both models based on the physical process dissolution and chemical process polymerisation and will carve out the thermomechanical coupling.

6.1. Basic interrelationship

In order to gain a comprehensive overview of the basic thermomechanical interrelationships for dissolution and polymerisation of acrylic cement, fig. 6.1 illustrates the main dependencies discovered in ch. 5 for each of the two processes. During the waiting and application phase, there are four different physical domains, dissolution, polymerisation, thermodynamics and fluid mechanics that interact with each other (cf. fig 6.1(a)). The rheometer experiments (cf. sec. 5.6) demonstrate that the dissolution process influences the rheological behaviour (fluid mechanics) of the mixed cement, while dissolution itself is strongly affected by temperature (thermodynamics). A higher ambient temperature facilitates dissolution. Furthermore, heat is generated by viscous losses when the material experiences shear forces. The other way round, a temperature change will cause a change in density. The superposed direct dependence of viscosity on temperature, as discussed in sec. 5.6, is disregarded here, as its influence is difficult to capture. Although, initial polymerisation does not influence the rheological behaviour of bone cement, it has to be considered within the first model stage. On the one hand, there has already been a minor heat release (cf. sec. 5.2.1 and 5.5.2), which will influence the temperature. On the other hand, the actual degree of cure at the beginning of the setting phase will depend on the temperature history during the waiting and application phase and directly affects the beginning of the accelerated polymerisation. In other words, the degree of cure at the beginning of the setting phase is an initial condition for calculating the curing of bone cement in this phase.
In contrast to the first model stage, dissolution can be neglected in the second stage. Here the three domains, polymerisation, thermodynamics and mechanics, interact with each other (cf. fig. 6.1(b)). The proceeding polymerisation causes changes in the specific heat capacity and generates heat. Vice versa, polymerisation itself is strongly temperature driven. The mechanical behaviour is affected by polymerisation through chain growth, which increases the mechanical strength and the density. Moreover, the thermodynamic and mechanical properties are coupled by dissipative losses caused by deformation and the temperature-dependent material behaviour. Changes in temperature can also invoke thermal strains due to the temperature-dependent density.

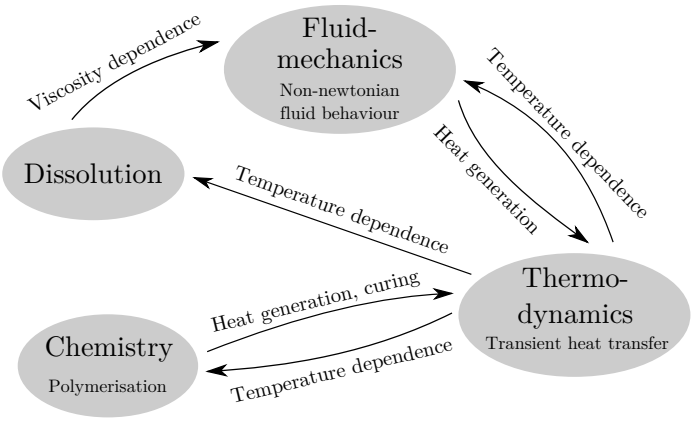

(a) Dissolution

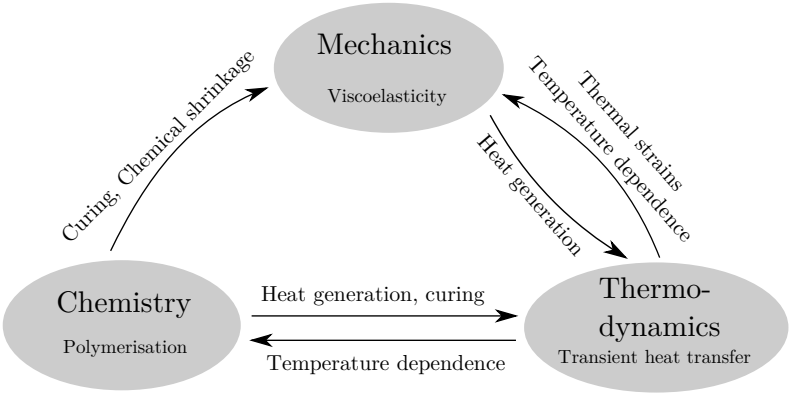

(b) Polymerisation

Figure 6.1.: Interaction of mechanics, thermodynamics, dissolution and polymerisation for the two model stages during vertebroplasty

The depiction of these interrelations for both model stages will be useful for the setup of the constitutive equations. During the different steps, it will be referred to these interactions so that the model structure becomes clearer.
As the structure of both model stages is similar, the modelling for dissolution and polymerisation will be described in parallel and the particular differences will be indicated. Where it makes sense, the specific features of each model will be explained in subsections. At the end of this chapter, the constitutive equations will be summarised for both model stages.
The following phenomenological modelling is based on the work of Lion and Höfer [141]. Some modifications are made to adopt it for describing curing phenomena of acrylic bone cements.

6.2. Evolution equations

Both, dissolution and polymerisation are irreversible processes that are a kind of driving force for the change in material properties of bone cement during vertebroplasty and determine the mechanical and thermodynamic behaviour. If their actual progress is known, the behaviour of

acrylic cement can be indicated. To this end, the modelling of these processes will be discussed first.
For modelling purposes, the evolution of both processes has to be expressed in a mathematical formulation that can predict, dependent on initial and boundary conditions, the actual progress of the particular process. Evolution equations are such adequate equations that describe the internal state of the material in a directly or indirectly measurable quantity. In case of bone cement application, separate evolution equations have to be set up for both processes, dissolution and polymerisation, because they appear to progress independently, as explained above.

6.2.1. Progress of dissolution

Dissolution affects only the rheological behaviour (cf. fig. 6.1(a)) of bone cement and can only be measured indirectly by rheological quantities. In order to characterise the internal state of dissolution in the material model, an internal variable d is introduced. Thereby, small values of d shall represent an initial state of dissolution and d shall increase with proceeding dissolution. This is achieved by formulating a rate equation for the evolution of d

$$\frac{dd}{dt} = \begin{cases} (K_{d1} + K_{d2} d^m)\,, & \text{if } d < d_{max} \\ 0, & \text{if } d \geq d_{max} \end{cases} \tag{6.1}$$

The rate of d is distinguished by cases to stop the evolution, once a maximum possible value for d is reached. For $d < d_{max}$, the progress of dissolution is determined by the sum of the initial rate of change K_{d1} and the progress-dependent rate $K_{d2} d^m$. m is a material specific parameter to describe the influence of the progress of dissolution itself on the progress-dependent rate. In order to consider the dependence on temperature of the dissolution process (as depicted in fig 6.1(a)), an Arrhenius behaviour is imposed on the parameters K_{d1} and K_{d2}:

$$K_{di} = A_{di} \exp\left(\frac{E_{di}}{R\theta}\right) \qquad i = 1, 2 \tag{6.2}$$

Herein, A_{di} are material specific parameters, E_{di} are the material specific activation energies, $R = 8.314\,\mathrm{J/(molK)}$ is the universal gas constant and θ the thermodynamic temperature. This evolution equation for the dissolution process is sufficient for representing all effects described in sec. 5.6. Additionally, sec. 7.4 will illustrate how eq. (6.1) in combination with eq. (6.2) is parametrised by using the experimental data since there is no simple physical interpretation of the value of d.

6.2.2. Progress of polymerisation

As dissolution and polymerisation are considered to be independent within the scope of this thesis, a further internal variable q is introduced to represent the progress of the polymerisation process. In contrast to dissolution, polymerisation affects not only the mechanical properties, including density, but also the specific heat capacity and the release of heat. Moreover, a

physical meaning can be assigned to the value of the internal variable q. For curing polymers and adhesives, it has been common practise to define this internal variable q as the relation of the cumulative released heat of the polymerisation $H(t)$ with respect to the total reaction enthalpy H_u according to

$$q(t) = \frac{H(t)}{H_u} \qquad \text{with} \qquad H(t) = \int_0^t Q_p\left(\overline{t}\right) d\overline{t} \quad . \tag{6.3}$$

Herein $Q_p\left(\overline{t}\right)$ denotes the heat power by the chemical reaction at time $\overline{t}$. Thus, the internal variable q represents the progress of reaction measured in converted energy. When describing the kinetics of chemical reactions, the internal variable is also referred to as degree of cure or chemical coordinate.

Among the numerous phenomenological models that exist in literature to mathematically describe the kinetics for exothermal polymerisation and curing of adhesives, Kamal and Sourour [105, 212] were the first to propose a rate-dependent equation for an adequate modelling of reaction kinetics. However, the original evolution equation by Kamal and Sourour does not account for vitrification effects (cf. sec. 5.2.1), as it will always end up with a final degree of cure of 1.0 after a sufficiently long period. The fact that acrylic cement will experience an uncomplete polymerisation as long as the curing temperature remains below the glass transition temperature can be accounted for by a diffusion factor f_D proposed by Fournier et al. [62]. For describing the curing process of acrylic cement the following evolution equation results:

$$\frac{dq}{dt} = (K_{q1} + K_{q2} q^k)(1-q)^l f_D(q) \qquad \text{with} \qquad f_D(q) = \left[\frac{2}{1+\exp(\frac{q-q_{end}}{b})} - 1\right] \quad . \tag{6.4}$$

Herein k and l are interdependent material parameters (e.g. $k + l = 3$) and generally do not depend on temperature. Both parameters control the influence of the degree of cure on its rate. K_{q1} and K_{q2} exhibit again an Arrhenius behaviour and are responsible for the temperature-dependent behaviour:

$$K_{qi} = A_{qi} \exp\left(\frac{E_{qi}}{R\theta}\right) \qquad i = 1, 2 \tag{6.5}$$

Analogical to eq. (6.2), A_{qi} are material specific parameters and E_{qi} are the activation energies. The diffusion factor f_D in eq. (6.4), which determines the barrier from a concentration- to a diffusion-controlled reaction, has to be specified further. Therein, b is an empirical material constant and q_{end} is the maximum attainable degree of cure at a certain curing temperature. For $q << q_{end}$ the diffusion factor has a value of almost 1 and does not influence the behaviour of the remaining evolution equation. As $q \to q_{end}$, the diffusion factor tends towards 0. Hence the rate $\frac{dq}{dt}$ converges towards 0 and the reaction comes to a stop. The correlation between q_{end} and the actual curing temperature is often described by a non-linear approach of DiBenedetto [48]. In the case of acrylic cement, a modified linear approach is more suitable.

$$\frac{T_g(q) - T_{g,0}}{T_{g,1} - T_{g,0}} = \kappa q + \xi \tag{6.6}$$

In eq. (6.6), $T_g(q)$ is the glass transition temperature of curing cement at the specific degree of cure q, $T_{g,0}$ is the glass transition temperature at $q = 0$, $T_{g,1}$ is the glass transition temperature at $q = 1$ and κ and ξ are additional material parameters. In order to obtain the maximum attainable degree of cure q_{end} at a certain curing temperature T_{iso}, eq. (6.6) has to be rearranged.

$$q_{end} = \frac{f(T) - \xi}{\kappa} \qquad \text{with} \qquad f(T) = \frac{T_{iso} + \Delta T - T_{g,0}}{T_{g,1} - T_{g,0}} \qquad \text{and} \qquad T_g(q_{end}) = T_{iso} + \Delta T \quad (6.7)$$

Due to the vitrification effect, the attainable glass transition temperature $T_g(q_{end})$ exceeds the actual curing temperature T_{iso} by ΔT [205, 235]. Eqs. (6.6) and (6.7) are only valid if the curing temperature is at least by ΔT below the final glass transition temperature $T_{g,1}$ of the fully cured material, otherwise the result for q_{end} is incorrect and non-physical. This is fulfilled for the curing temperature range from 15 °C to maximum 80 °C, which is typical for vertebroplasty. By combining the evolution equation by Kamal and Sourour, which is able to represent the accelerated polymerisation behaviour accurately, with the additional diffusion factor, the observed effects in sec. 5.2.1, including uncomplete polymerisation, are now mathematically captured.
With both evolution equations the internal state of acrylic bone cement can be described along the three clinical cement process phases: waiting phase, application phase and setting phase. In both evolution equations, the influence of temperature on the progress of the internal variables is obvious. As mentioned before, this necessitates the calculation of eq. (6.4) in the waiting and application phase to include the initial polymerisation. The knowledge of the internal state of the material, i.e. the actual progress of dissolution and polymerisation, is the basis for the further modelling.

6.3. Decomposition of deformation

A basic idea of the proposed material model is to distinguish between strains that are only induced by mechanical loads, i.e. body forces, surface forces or external forces, and strains that are induced by a change in the specific volume due to temperature variations or polymerisation shrinkage. This differentiation is achieved by a multiplicative split of the deformation gradient (as introduced in sec. 2.1.4) into a mechanical part and a thermochemical part:

$$\mathbf{F} = \mathbf{F}_M \mathbf{F}_{\theta C} \quad . \tag{6.8}$$

This decomposition results in a thermochemical intermediate configuration which represents the fictive deformations only due to temperature change and polymerisation shrinkage (cf. fig. 6.2). These deformations are attributed to the thermochemical deformation gradient $\mathbf{F}_{\theta C}$ and are assumed to be isotropic, since acrylic bone cement exhibits no directional structure.
According to these constraints, the thermochemical deformation gradient $\mathbf{F}_{\theta C}$ can be written as

$$\mathbf{F}_{\theta C} = \varphi(\theta, q)^{1/3} \mathbf{1} \qquad \text{with} \qquad \det(\mathbf{F}_{\theta C}) = J_{\theta C} = \varphi(\theta, q) \quad . \tag{6.9}$$

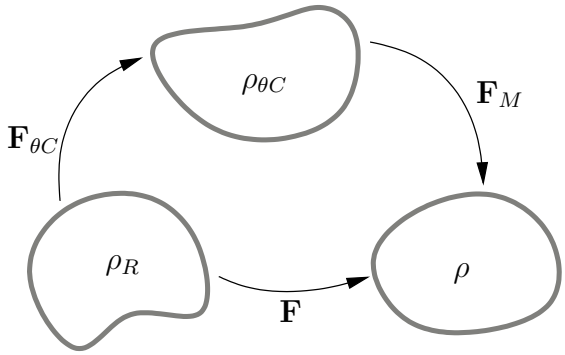

Figure 6.2.: Decomposition of deformation gradient and thermochemical intermediate configuration

The function $\varphi(\theta, q)$ in eq. (6.9) specifies the volumetric strains with respect to temperature θ and degree of cure q. However, according to the principle of equipresence (cf. sec. 2.4 and [79]), the function φ could depend on all internal and external variables. In order to keep the modelling simple, only these variables will be included in the function φ from the start, whose influence has been obviously discovered in the experiments. Having in mind the results of sec. 5.4, the function $\varphi(\theta, q)$ can be modelled more precisely. As already discussed, the experiments propose the change in density to be linear in temperature and degree of cure. Moreover, the varying thermal expansion behaviour with respect to the progress in polymerisation should also be taken into account. These conclusions end up in the expression

$$\varphi(\theta, q) = 1 + (\alpha + \Delta\alpha q(t))(\theta - \theta_0) + \beta q(t) \quad . \tag{6.10}$$

Herein, α is the coefficient of linear thermal expansion with respect to the reference temperature θ_0 in the uncured state, $\Delta\alpha$ is the change of the coefficient of linear thermal expansion due to proceeding polymerisation and β is the chemical shrinkage. The reference temperature θ_0 has been chosen to be equal to the body temperature of 37 °C.
The change in volume can also be deduced by relating the density of the reference configuration ρ_R with the density of the thermochemical intermediate configuration $\rho_{\theta C}$, following eq. (2.6):

$$\rho_{\theta C} = \frac{\rho_R}{\det(\mathbf{F}_{\theta C})} = \frac{\rho_R}{\varphi(\theta, q)} \quad . \tag{6.11}$$

Mechanical stresses are attributed to the mechanical part of the deformation gradient $\mathbf{F}_M$, which can be expressed in terms of the overall deformation and the thermochemical change in volume

$$\mathbf{F}_M = \frac{1}{\varphi(\theta, q)^{1/3}}\mathbf{F} \quad . \tag{6.12}$$

The literature review in sec. 5.8.1 indicates a Poisson's ratio smaller than 0.5 for PMMA in the glassy state. However, for simplicity and due to the lack of data, acrylic bone cement is assumed to be mechanically incompressible for the scope of both model stages. Therewith the determinant of the mechanical deformation gradient reads as

$$det(\mathbf{F}_M) = J_M = 1 \quad . \tag{6.13}$$

The deformation split explained above applies for both model stages, although, the thermochemical deformation will be rather small during the dissolution process.

6.4. Stress power

The evaluation of the Clausius-Duhem inequality requires the calculation of the stress power. In order to obtain the stress power under consideration of the split of the deformation gradient mentioned above, a few considerations are necessary (cf. [141]).
Starting from the definition of the second Piola-Kirchhoff stress tensor in eq. (2.26) and combining this definition with the split of the deformation gradient in eq. (6.8) yields

$$\tilde{\mathbf{T}} = J\mathbf{F}^{-1}\mathbf{T}\mathbf{F}^{-T} = J_M J_{\theta C}\mathbf{F}_{\theta C}^{-1}\mathbf{F}_M^{-1}\mathbf{T}\mathbf{F}_M^{-T}\mathbf{F}_{\theta C}^{-T} \quad . \tag{6.14}$$

Therein, the expression

$$\tilde{\mathbf{T}}_M = J_M\mathbf{F}_M^{-1}\mathbf{T}\mathbf{F}_M^{-T} \tag{6.15}$$

defines the so-called mechanical second Piola-Kirchhoff stress tensor. Furthermore, the Green strain tensor can be written as

$$\mathbf{E} = \frac{1}{2}\left(\mathbf{F}^T\mathbf{F} - \mathbf{1}\right) = \frac{1}{2}\left(\mathbf{F}_{\theta C}^T\mathbf{F}_M^T\mathbf{F}_M\mathbf{F}_{\theta C} - \mathbf{1}\right) \quad , \tag{6.16}$$

taking into account the multiplicative split of the deformation gradient. According to eq. (6.15) the mechanical right Cauchy–Green tensor $\mathbf{C}_M$ and the corresponding Green strain tensor $\mathbf{E}_M$ can be defined as

$$\mathbf{C}_M = \mathbf{F}_M^T\mathbf{F}_M \quad \text{and} \quad \mathbf{E}_M = \frac{1}{2}\left(\mathbf{C}_M - \mathbf{1}\right) \quad . \tag{6.17}$$

Based on eqs. (6.16) and (6.17), the material time derivative of the Green strain tensor is derived as

$$\dot{\mathbf{E}} = \frac{1}{2}\left(\dot{\mathbf{F}}_{\theta C}^T\mathbf{C}_M\mathbf{F}_{\theta C} + \mathbf{F}_{\theta C}^T\dot{\mathbf{C}}_M\mathbf{F}_{\theta C} + \mathbf{F}_{\theta C}^T\mathbf{C}_M\dot{\mathbf{F}}_{\theta C}\right) \quad . \tag{6.18}$$

Referring to eq. (2.27), including eqs. (6.14), (6.15) and (6.18) and considering $\mathbf{A}\cdot\mathbf{B} = \left(\mathbf{A}^T\mathbf{B}\right)\cdot\mathbf{1}$, the stress power per unit mass can now be specified further as

$$\rho_R w_S = \tilde{\mathbf{T}}\cdot\dot{\mathbf{E}} = \frac{J_{\theta C}}{2}\left(\mathbf{F}_{\theta C}^{-1}\tilde{\mathbf{T}}_M\mathbf{F}_{\theta C}^{-T}\left(\dot{\mathbf{F}}_{\theta C}^T\mathbf{C}_M\mathbf{F}_{\theta C} + \mathbf{F}_{\theta C}^T\dot{\mathbf{C}}_M\mathbf{F}_{\theta C} + \mathbf{F}_{\theta C}^T\mathbf{C}_M\dot{\mathbf{F}}_{\theta C}\right)\right)\cdot\mathbf{1} \quad . \tag{6.19}$$

In order to simplify this expression, a thermochemical velocity gradient $\mathbf{L}_{\theta C}$ is introduced according to

$$\mathbf{L}_{\theta C} = \dot{\mathbf{F}}_{\theta C}\mathbf{F}_{\theta C}^{-1} = \frac{1}{3\varphi}\left(\frac{\partial\varphi}{\partial\theta}\dot{\theta} + \frac{\partial\varphi}{\partial q}\dot{q}\right)\mathbf{1} \quad . \tag{6.20}$$

Including this thermochemical velocity gradient and using eq. (6.11) the stress power can be formulated as

$$w_S = \frac{1}{\rho_R}\tilde{\mathbf{T}} \cdot \dot{\mathbf{E}} = \frac{1}{2\rho_{\theta C}} \left(\tilde{\mathbf{T}}_M \dot{\mathbf{C}}_M + \tilde{\mathbf{T}}_M \mathbf{C}_M \mathbf{L}_{\theta C} + \tilde{\mathbf{T}}_M \mathbf{C}_M \mathbf{L}_{\theta C}^T \right) \cdot \mathbf{1} \quad . \tag{6.21}$$

As the thermochemical deformation gradient is a diagonal tensor (according to eq. (6.9)), the thermochemical velocity gradient is also diagonal and $\mathbf{L}_{\theta C} = \mathbf{L}_{\theta C}^T$ holds. Moreover, taking into account the relationship between the material time derivative of the mechanical right Cauchy–Green tensor and the corresponding mechanical Green strain tensor $\dot{\mathbf{E}}_M = \frac{1}{2}\dot{\mathbf{C}}_M$, the final form of the stress power reads as

$$w_S = \frac{1}{\rho_R}\tilde{\mathbf{T}} \cdot \dot{\mathbf{E}} = \frac{1}{\rho_{\theta C}} \left(\tilde{\mathbf{T}}_M \cdot \dot{\mathbf{E}}_M + \mathbf{C}_M \tilde{\mathbf{T}}_M \cdot \mathbf{L}_{\theta C} \right) \quad . \tag{6.22}$$

The second term of the right hand side of eq. (6.22) can be further evaluated under consideration of the relations (6.13), (6.15), (6.17) and (6.20):

$$\begin{aligned} \tilde{\mathbf{C}}_M \tilde{\mathbf{T}}_M \cdot \mathbf{L}_{\theta C} &= tr \left(\mathbf{F}_M^T \mathbf{F}_M \left(J_M \mathbf{F}_M^{-1} \mathbf{T} \mathbf{F}_M^{-T} \right) \frac{1}{3\varphi} \left(\frac{\partial \varphi}{\partial \theta}\dot{\theta} + \frac{\partial \varphi}{\partial q}\dot{q} \right) \mathbf{1} \right) \\ &= \frac{\mathrm{tr}(\mathbf{T})}{3\varphi} \left(\frac{\partial \varphi}{\partial \theta}\dot{\theta} + \frac{\partial \varphi}{\partial q}\dot{q} \right) \quad . \end{aligned} \tag{6.23}$$

In eq. (6.22), two additive parts of the stress power can be distinguished. The expression $\tilde{\mathbf{T}}_M \cdot \dot{\mathbf{E}}_M$ identifies the mechanically induced stress power and the remaining term $\mathbf{C}_M \tilde{\mathbf{T}}_M \cdot \mathbf{L}_{\theta C}$ represents the thermochemically induced stress power.
The thermochemically induced stress power will play a significant role during accelerated polymerisation, as chemical shrinkage and thermal expansion will cause remarkable thermochemical velocity gradients. However, during dissolution this part of the stress power will make a minor contribution to the overall stress power.

6.5. Specific free energy

Alongside the stress power, the evaluation of the Clausius-Duhem inequality requires the definition of a thermodynamic potential as explained in sec. 2.3.5. In this context, the specific Helmholtz free energy is chosen as thermodynamic potential and can be additively split into a mechanical and a thermochemical part.

$$\psi = \psi_M + \psi_{\theta C} \tag{6.24}$$

The mechanical part ψ_M is attributed to the energy stored by deformation, regardless its causation due to internal and external forces, chemical shrinkage or thermal expansion. The thermochemical part ψ_{θ_C} represents the energy that is stored or released by chemical or thermodynamic processes, like polymerisation or altering temperature. Recently, Lion et al. proposed a hybrid free energy density as thermodynamic potential for thermomechanical material modelling [140]. This approach is based on an additive decomposition of the stress power into an isochoric and a

volumetric part and offers particular advantages for identifying material parameters by isobaric experiments.
In order to gain a better understanding of this additive split of the free energy as thermodynamic potential, both parts will be explained more precisely in the following sections.

6.5.1. Thermochemical free energy

For measuring and describing the level of the energy potential of chemical reactions or thermodynamic processes, not the specific Helmholtz free energy, but the specific enthalpy is the standard physical quantity, which can be determined in calorimetric experiments. In contrast, the thermochemical free energy cannot be characterised straightforward in these experiments. In order to describe the thermochemical free energy of bone cement for the processes typical for vertebroplasty, a detour via the enthalpy has to be made. Therefore, an expression for the thermochemical enthalpy is developed on the basis of the first law of thermodynamics and afterwards the interrelation with the thermochemical free energy will be derived. This will be demonstrated more clearly in the following explanations.
Taking the time-derivative of the definition of the enthalpy (cf. eq. (2.53))

$$\dot{e} = \dot{h} + \frac{1}{\rho_R}\left(\dot{\tilde{\mathbf{T}}} \cdot \mathbf{E} + \tilde{\mathbf{T}} \cdot \dot{\mathbf{E}}\right) \quad , \tag{6.25}$$

and combining it with the first law of thermodynamics in eq. (2.47) leads to the first law of thermodynamics using the enthalpy as thermodynamic potential:

$$\rho_R \dot{h} = -\dot{\tilde{\mathbf{T}}} \cdot \mathbf{E} - \operatorname{Div} \mathbf{q}_R + \rho_R r \quad . \tag{6.26}$$

Regarding differential scanning calorimetry experiments, the specimen is usually investigated under constant pressure, if the lid is pierced (cf. sec. 5.2). In this case, the temporal change in the stress is zero and therefore $\dot{\tilde{\mathbf{T}}} = \mathbf{0}$. Furthermore, the local energy supply r is equal to zero. Therewith, for DSC experiments eq. (6.26) reads as

$$\rho_R \dot{h} = -\operatorname{Div} \mathbf{q}_R \quad \text{and} \quad \rho \dot{h} = -\operatorname{div} \mathbf{q} \tag{6.27}$$

in the local material and spatial form, respectively. Transferring it to the global form an applying the divergence theorem yields

$$\int_V \rho_R \dot{h} dV = -\int_V \operatorname{Div} \mathbf{q}_R dV = -\int_A \mathbf{q}_R \cdot \mathbf{n}_R dA \quad . \tag{6.28}$$

The right hand side of eq. (6.28) denotes the thermal energy per unit time that is transferred to the specimen via its surface, and thus is equal to the DSC-power P_{DSC}. Assuming homogeneous conditions within a DSC-sample, the left hand side of eq. (6.28) can also be written as

$$\int_V \rho_R \dot{h} dV = \dot{h} \Delta m \quad . \tag{6.29}$$

This leads to the fundamental equation for DSC investigations,

$$\dot{h} = \frac{P_{DSC}}{\Delta m} \quad , \tag{6.30}$$

and states that the temporal change in the specific enthalpy is equal to the DSC-Power per unit mass.

According to the principle of equipresence, the specific enthalpy can depend on all internal and external variables. However, it is reasonable to suppose that the enthalpy is only a function of stress $\tilde{\mathbf{T}}$, temperature θ and degree of cure q, as these quantities bear the greatest influence on it. With the assumption $h = h(\tilde{\mathbf{T}}, \theta, q)$ the rate of enthalpy reads as

$$\dot{h} = \frac{\partial h}{\partial \tilde{\mathbf{T}}} \cdot \dot{\tilde{\mathbf{T}}} + \frac{\partial h}{\partial \theta}\dot{\theta} + \frac{\partial h}{\partial q}\dot{q} \quad . \tag{6.31}$$

For DSC experiments under constant pressure, the temporal change in stress is zero ($\dot{\tilde{\mathbf{T}}} = \mathbf{0}$), and therefore only the thermochemical part of the enthalpy is considered. The first summand on the right hand side of eq. (6.31) vanishes and inserting the result in eq. (6.30) yields

$$\frac{\partial h}{\partial \theta}\dot{\theta} + \frac{\partial h}{\partial q}\dot{q} = \frac{P_{DSC}}{\Delta m} \quad . \tag{6.32}$$

The first term on the left hand side of eq. (6.32) can be identified as the definition of the specific heat under constant pressure:

$$\frac{\partial h}{\partial \theta} = c_p \quad . \tag{6.33}$$

Eq. (6.32) points out that the thermochemical rate of enthalpy can be accessed straightforward in DSC experiments as performed in sec. 5.2. On the basis of these measurements, the modelling dependencies for the specific enthalpy can be motivated as follows:

$$h(\theta, q) = h_F(\theta)(1-q) + h_S(\theta)q \quad \forall\, 0 \leq q \leq 1 \tag{6.34}$$

$$h_F(\theta) = h_{F0} + a_F(\theta - \theta_0) + \frac{1}{2}b_F(\theta - \theta_0)^2 \tag{6.35}$$

$$h_S(\theta) = h_{S0} + a_S(\theta - \theta_0) + \frac{1}{2}b_S(\theta - \theta_0)^2 \quad . \tag{6.36}$$

Herein, h_F denotes the enthalpy of the uncured, h_S the enthalpy of the fully cured material and θ_0 is an arbitrary reference temperature. h_{F0}, h_{S0}, a_F, a_S, b_F and b_S are material parameters to be identified. Both, the enthalpy of the uncured h_F and the enthalpy of the fully cured material h_S can be interpreted as Taylor series expansions (second-order approximation) in the vicinity of the reference temperature θ_0. The reason for choosing such a formulation becomes clearer if the definition of the specific heat (eq. (6.33)) is taken into account. Applying this definition to

eqs. (6.34) to (6.36) yields

$$\begin{aligned} c_p(\theta, q) &= \frac{\partial h_F}{\partial \theta}(1-q) + \frac{\partial h_S}{\partial \theta} q \\ &= c_{p,F}(\theta)(1-q) + c_{p,S}(\theta) q \qquad (6.37) \\ c_{p,F}(\theta) &= \frac{\partial h_F}{\partial \theta} = a_F + b_F(\theta - \theta_0) \qquad (6.38) \\ c_{p,S}(\theta) &= \frac{\partial h_S}{\partial \theta} = a_S + b_S(\theta - \theta_0) \quad . \qquad (6.39) \end{aligned}$$

According to eqs. (6.37) to (6.39), a linear dependence of the specific heat on temperature at a constant degree of cure, as observed in sec. 5.2.2, by definition leads to a quadratic dependence of the specific enthalpy on temperature. Moreover, the further modelling of the specific heat and the specific enthalpy for $0 < q < 1$ with a simple rule of mixtures of the fluid and solid component (e.g. $c_{p,F}$, $c_{p,S}$, h_F and h_S) is in good agreement with the TMDSC experiments in sec. 5.2.2.

With this kind of modelling, the specific enthalpy also results in a temperature-dependent total enthalpy of reaction, which is gained by taking the derivative of the specific enthalpy h with respect to the degree of cure q:

$$\begin{aligned} -h_u(\theta) &= \frac{\partial h}{\partial q} = h_S(\theta) - h_F(\theta) \qquad (6.40) \\ &= h_{S0} - h_{F0} + (a_S - a_F)(\theta - \theta_0) + \frac{1}{2}(b_S - b_F)(\theta - \theta_0)^2 \quad . \end{aligned}$$

$\frac{\partial h}{\partial q}$ is negative because the specific enthalpy decreases during polymerisation from $h_F(\theta)$ to $h_S(\theta)$. In addition, eqs. (6.37) and (6.40) indicate that a dependency of the specific heat on the degree of cure (i.e. $c_{p,F} \neq c_{p,S}$) by definition involves a dependency of the total enthalpy of reaction on temperature. This interrelation is also visible in the fundamental equation for DSC investigations if the results of eqs. (6.37) and (6.40) are taken into account to reformulate eq. (6.32) as

$$c_p(\theta, q)\dot{\theta} - h_u(\theta)\dot{q} = \frac{P_{DSC}}{\Delta m} \quad . \qquad (6.41)$$

The two terms on the left hand side, that make up the specific DSC power $\frac{P_{DSC}}{\Delta m}$, now have a clear physical meaning. According to eq. (6.41), the DSC power is non zero if the temperature changes (which is related to the specific heat capacity) or if the degree of cure changes (which is related to the total enthalpy of reaction) with time.

Having gained a detailed insight into the modelling of the thermochemical potential in terms of the specific enthalpy, now the relations to the thermochemical free energy have to be established. Therefore the additive split of the free energy (cf. eq. (6.24)) has to be further investigated. In general, the mechanical part of the free energy is a function of stress producing mechanical deformations $\mathbf{E}_M$, the dissolution d, the degree of cure q and of course the temperature θ

$$\psi_M = \psi_M\left(\mathbf{E}_M, d, q, \theta\right) \quad . \qquad (6.42)$$

Depending on which application phase of vertebroplasty is observed, either the dissolution d or the degree of cure q might vanish as an independent variable of the mechanical free energy function (cf. sec. 6.1). This will become clearer with the further development of the model. In contrast, the thermochemical part of the free energy $\psi_{\theta C}$ is a function of the degree of cure q and temperature θ, but not of the dissolution d as it shows no influence on the corresponding measurements.

$$\psi_{\theta C} = \psi_{\theta C}\left(q, \theta\right) \quad . \tag{6.43}$$

For DSC investigations with pierced lids, stresses will only arise due to the ambient pressure and are therefore very small (in the range of 0.1 MPa). These stresses cause negligible mechanical deformations and will therefore be assumed to be zero for DSC investigations. In conclusion, the mechanical part of the free energy is also zero, regarding DSC experiments, and only the thermochemical free energy is addressed in the following considerations.
In order to obtain a relation between the specific enthalpy and the free energy, the Legendre transformations from sec. 2.3.5 are evaluated in the following manner:

$$h = e - \theta s - \frac{1}{\rho_R}\tilde{\mathbf{T}} \cdot \mathbf{E} + \theta s \quad . \tag{6.44}$$

The term $e - \theta s$ can be identified as free energy (cf. eq. (2.53)). As mechanical stresses, stress induced deformations and hence the mechanical free energy are assumed to be zero, the term $\frac{1}{\rho_R}\tilde{\mathbf{T}} \cdot \mathbf{E}$ vanishes. From eq. (2.53), it follows that

$$\dot{\psi}_{\theta C} = \dot{e} - \dot{\theta} s - \theta \dot{s} \quad . \tag{6.45}$$

In addition, the first law of thermodynamics states a relation between the time derivative of the internal energy and entropy

$$\dot{e} = \theta \dot{s} - p\dot{v} \quad . \tag{6.46}$$

Under the constraint of $p = 0$ eq. (6.46) simplifies to $\dot{e} = \theta \dot{s}$ and inserting into eq. (6.45) and rearranging yields

$$s = -\frac{\partial \psi_{\theta C}}{\partial \theta} \quad . \tag{6.47}$$

By application of the transformation $y - xy' = -x^2(y/x)'$ and under the given constraints, eq. (6.44) reduces to

$$h = \psi_{\theta C} - \theta \frac{\partial \psi_{\theta C}}{\partial \theta} = -\theta^2 \frac{\partial}{\partial \theta}\left(\frac{\psi_{\theta C}}{\theta}\right) \quad . \tag{6.48}$$

Rearranging eq. (6.48) and subsequent integration results in

$$\frac{\psi_{\theta C}\left(\theta, q\right)}{\theta} - \frac{\psi_{\theta_0 C}\left(\theta_0, q\right)}{\theta_0} = -\int_{\theta_0}^{\theta} \frac{h(\vartheta, q)}{\vartheta^2} d\vartheta \quad . \tag{6.49}$$

By a further conversion of eq. (6.49), the expression,

$$\psi_{\theta C}(\theta, q) = \frac{\theta}{\theta_0}\psi_{\theta_0 C}(\theta_0, q) - \theta \int_{\theta_0}^{\theta} \frac{h_F(\vartheta)(1-q) + h_S(\vartheta)q}{\vartheta^2} d\vartheta \tag{6.50}$$

is obtained and hence, by considering the relationship $s = -\frac{\partial \psi_{\theta C}}{\partial \theta}$ the specific enthalpy s can be written as

$$s = -\frac{\psi_{\theta_0 C}(\theta_0, q)}{\theta_0} + \int_{\theta_0}^{\theta} \frac{h_F(\vartheta)(1-q) + h_S(\vartheta)q}{\vartheta^2} d\vartheta + \frac{h_F(\theta)(1-q) + h_S(\theta)q}{\theta} \quad . \tag{6.51}$$

Consequently, the following relations between enthalpy, entropy and free energy can be established for the reference temperature θ_0

$$\theta_0 s(\theta_0, q) = -\psi_{\theta C}(\theta_0, q) + h_F(\theta_0)(1-q) + h_S(\theta_0) q \tag{6.52}$$

$$\theta_0 s(\theta_0, 0) = -\psi_{\theta C}(\theta_0, 0) + h_F(\theta_0) \tag{6.53}$$

$$\theta_0 s(\theta_0, 1) = -\psi_{\theta C}(\theta_0, 1) + h_S(\theta_0) \quad . \tag{6.54}$$

In eq. (6.53), $\psi_{\theta C}(\theta_0, 0)$ denotes the specific free energy of the uncured liquid state $\psi_{\theta C,F}(\theta_0)$ and in eq. (6.54), $\psi_{\theta C}(\theta_0, 1)$ denotes the specific free energy of the completely cured solid state $\psi_{\theta C,S}(\theta_0)$ at the reference temperature. A simple mixture rule is assumed for the free energy for an arbitrary degree of cure $0 \leq q \leq 1$ so that the free energy at the reference temperature reads as

$$\psi_{\theta C}(\theta_0, q) = \psi_{\theta C,F}(\theta_0)(1-q) + \psi_{\theta C,S}(\theta_0)(q) \quad . \tag{6.55}$$

In analogy, this is carried out for the specific entropy s (i.e $s(\theta_0, 0) = s_F(\theta_0)$ and $s(\theta_0, 1) = s_S(\theta_0)$) and hence the specific entropy for an arbitrary degree of cure $0 \leq q \leq 1$ at the reference temperature is obtained:

$$s(\theta_0, q) = s_F(\theta_0)(1-q) + s_S(\theta_0)(q) \quad . \tag{6.56}$$

Combining eqs. (6.55) and (6.56) with eq. (6.52) and rearranging terms results in

$$\psi_{\theta C}(\theta_0, q) = (h_F(\theta_0) - \theta_0 s_F(\theta_0))(1-q) + (h_s(\theta_0) - \theta_0 s_S(\theta_0))\, q \quad . \tag{6.57}$$

This expression for the specific free energy at the reference temperature can now be inserted in eq. (6.50):

$$\begin{aligned} \psi_{\theta C}(\theta, q) = {} & \frac{\theta}{\theta_0}\left[(h_F(\theta_0) - \theta_0 s_F(\theta_0))(1-q) + (h_s(\theta_0) - \theta_0 s_S(\theta_0))\, q\right] \\ & -\theta \int_{\theta_0}^{\theta} \frac{h_F(\vartheta)(1-q) + h_S(\vartheta)q}{\vartheta^2} d\vartheta \quad . \end{aligned} \tag{6.58}$$

With the aid of partial integration

$$\begin{aligned}
-\theta \int_{\theta_0}^{\theta} \frac{h_F(\vartheta)(1-q)+h_S(\vartheta)q}{\vartheta^2} d\vartheta &= \theta\left[\frac{h_F(\theta)(1-q)}{\theta}+\frac{h_S(\theta)q}{\theta}\right] \\
&\quad -\theta\left[\frac{h_F(\theta_0)(1-q)}{\theta_0}+\frac{h_S(\theta_0)q}{\theta_0}\right] \\
&\quad -\theta \int_{\theta_0}^{\theta} \frac{h'_F(\vartheta)(1-q)+h'_S(\vartheta)q}{\vartheta} d\vartheta \\
&= h_F(\theta)(1-q)+h_S(\theta)q \\
&\quad -\frac{\theta}{\theta_0}\left(h_F(\theta_0)(1-q)+h_S(\theta_0)q\right) \\
&\quad -\theta \int_{\theta_0}^{\theta} \frac{c_{p,F}(\vartheta)(1-q)+c_{p,S}(\vartheta)q}{\vartheta} d\vartheta \quad , \qquad (6.59)
\end{aligned}$$

the integral in eq. (6.58) can be replaced and the thermochemical free energy is expressed as

$$\begin{aligned}
\psi_{\theta C}(\theta,q) &= h_F(\theta)(1-q)+h_S(\theta)q \\
&\quad -\theta[(s_F(\theta_0)+\int_{\theta_0}^{\theta} \frac{c_{p,F}(\vartheta)}{\vartheta} d\vartheta)(1-q)+(s_S(\theta_0)+\int_{\theta_0}^{\theta} \frac{c_{p,S}(\vartheta)}{\vartheta} d\vartheta)q] \quad . \qquad (6.60)
\end{aligned}$$

Taking into account the thermodynamic relation

$$\frac{c_p}{\theta} = \frac{\partial s}{\partial \theta} \quad , \qquad (6.61)$$

the term inside the squared brackets in eq. (6.60) can be identified as specific entropy s and hence the final expression for the thermochemical free energy is obtained:

$$\psi_{\theta C}(\theta,q) = h(\theta,q) - \theta s(\theta,q) \quad . \qquad (6.62)$$

The relation above is particularly valid for the process of polymerisation. During the dissolution process eq. (6.60) simplifies under the assumption $q \approx 0$ to

$$\psi_{\theta C}(\theta) = h_F(\theta) - \theta(s_F(\theta_0)+\int_{\theta_0}^{\theta} \frac{c_{p,F}(\vartheta)}{\vartheta} d\vartheta) \quad . \qquad (6.63)$$

6.5.2. Mechanical free energy

The previous section disregarded the internal energy that is stored or released by mechanical deformations. However, during the deformations that bone cement experiences during a vertebroplastic surgery, a significant amount of internal energy is transferred. This amount of energy in terms of the free energy as thermodynamic potential is the topic of this section.
The creep experiments in sec. 5.8.2 have shown that bone cement does not reach an equilibrium state during the time scales relevant for a vertebroplastic surgery (i.e. 2-3 hours). Therefore

no equilibrium stress and hence no associated mechanical free energy will be considered in the presented model. Due to the constraint of mechanical incompressibility (i.e. $det\,(\mathbf{F}_M) = 1$), a volumetric part of the mechanical free energy can be omitted. On the basis of this discussion, the following expression for the mechanical free energy is proposed (cf. [80, 142]):

$$\psi_M = -\int_{-\infty}^{t} G_k(t-s)\frac{d}{ds}\,\mathrm{tr}(\mathbf{e}_M(s))ds \quad . \tag{6.64}$$

Therein G_k describes an arbitrary relaxation function and $\mathbf{e}_M$ is the mechanical Piola strain tensor, which is given by $\mathbf{e}_M = \frac{1}{2}(\mathbf{C}_M^{-1} - \mathbf{1})$.
The proposed relaxation function G_k above only accounts for the time- and frequency-dependent viscoelastic behaviour. In order to include the degree of cure- and temperature-dependent viscoelastic material properties of acrylic bone cement, a material-dependent intrinsic time scale $z(t)$ is introduced, similarly to sec. 3.4 and the work of Haupt and Lion [80].

$$\dot{z}(t) = M(q(\theta,t),\theta(t)) \geq 0, \quad z(t) = \int_{-\infty}^{t} M(q(\theta,\tau),\theta(\tau))d\tau, \quad \zeta(s) = \int_{-\infty}^{s} M(q(\theta,\tau),\theta(\tau))d\tau \tag{6.65}$$

Herein, M is denoted as shift function and is dependent on the progress of polymerisation q and the temperature θ. This substitution by an intrinsic time scale $z(t)$ leads to a relative decomposition of the the mechanical deformation gradient on the thermochemical intermediate configuration in the z-domain (cf. sec. 2.1.4 and fig. 6.3).

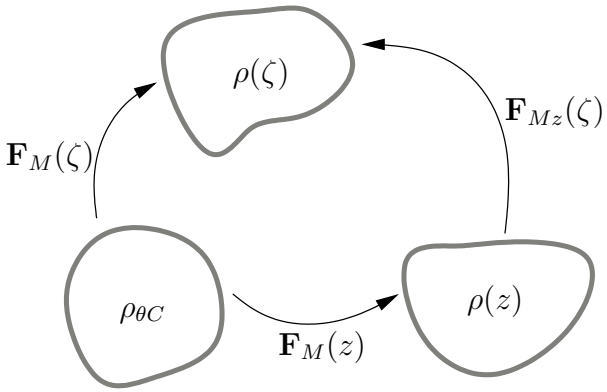

Figure 6.3.: Relative decomposition of the mechanical deformation gradient in the z-domain

The resulting relative mechanical deformation gradient can be expressed as

$$\mathbf{F}_{Mz}(\zeta) = \mathbf{F}_M(\zeta)\mathbf{F}_M^{-1}(z) \quad \text{whereas} \quad \mathbf{F}_{Mz}(z) = \mathbf{1} \quad \text{holds.} \tag{6.66}$$

In analogy to sec. 6.4, the relative Cauchy Green and Piola strain tensors can be defined as follows:

$$\mathbf{C}_{Mz}(\zeta) = \mathbf{F}_{Mz}^T(\zeta)\mathbf{F}_{Mz}(\zeta) = \mathbf{F}_M^{T-1}(z)\mathbf{C}_M(\zeta)\mathbf{F}_M^{-1}(z) \tag{6.67}$$

$$\mathbf{e}_{Mz}(\zeta) = \frac{1}{2}(\mathbf{C}_{Mz}^{-1} - \mathbf{1}) = \mathbf{F}_M(z)(\mathbf{e}_M(\zeta) - \mathbf{e}_M(z))\mathbf{F}_M^T(z) \quad . \tag{6.68}$$

Including the intrinsic time scale, and therewith the dependency of the viscoelastic behaviour on temperature and degree of cure, instead of the physical time t, the expression (6.64) for the mechanical free energy is replaced by the following relation:

$$\psi_M = -\int_{-\infty}^{z} G_k(z-\zeta)\frac{d}{d\zeta}\operatorname{tr}(\mathbf{e}_{Mz}(\zeta))d\zeta \quad . \tag{6.69}$$

The evolution of the free energy now depends on the degree of cure, temperature and the history of the relative Piola strain tensor.

6.6. Evaluation of the Clausius-Duhem inequality

The evaluation of the Clausius-Duhem inequality yields constitutive relations for stress and entropy that guarantee thermomechanical consistency.
Some further calculations are necessary to conveniently insert the different parts into the expression given by eq. (2.54). First the temporal derivative of the thermochemical and mechanical free energy is required. Considering eqs. (6.33) and (6.61) the temporal derivative of the thermochemical free energy yields:

$$\begin{aligned}
\dot{\psi}_{\theta C} &= \frac{d}{dt}\left(h\left(\theta,q\right)-\theta s\left(\theta,q\right)\right) \\
&= \frac{\partial h}{\partial\theta}\dot{\theta}+\frac{\partial h}{\partial q}\dot{q}-\theta\left[\frac{\partial s}{\partial\theta}\dot{\theta}+\frac{\partial s}{\partial q}\dot{q}\right]-\dot{\theta}s\left(\theta,q\right) \\
&= \left[\left(h_S(\theta)-h_F(\theta)\right)-\theta\left(s_S(\theta_0)-s_F(\theta_0)+\int_{\theta_0}^{\theta}\frac{c_{p,S}(\vartheta)-c_{p,F}(\vartheta)}{\vartheta}d\vartheta\right)\right]\dot{q} \\
&\quad -\left[\left(s_F\left(\theta_0\right)+\int_{\theta_0}^{\theta}\frac{c_{p,F}\left(\vartheta\right)}{\vartheta}d\vartheta\right)\left(1-q\right)+\left(s_S\left(\theta_0\right)+\int_{\theta_0}^{\theta}\frac{c_{p,S}\left(\vartheta\right)}{\vartheta}d\vartheta\right)q\right]\dot{\theta} \\
&= \frac{\partial\psi_{\theta C}}{\partial q}\dot{q}+\frac{\partial\psi_{\theta C}}{\partial\theta}\dot{\theta} \quad .
\end{aligned} \tag{6.70}$$

The material time rate of the thermochemical free energy is equal to the partial derivative of the free energy with respect to the degree of cure multiplied by the temporal derivative of the degree of cure and the related terms with regard to temperature.
The material time derivative of the mechanical free energy function, as stated in eq. (6.69), can be obtained by applying the Leibniz rule for parameter integrals (cf. (A.1)) and the chain rule $\frac{d}{dt}=\frac{d}{dz}\dot{z}(t)$ and thus reads as

$$\dot{\psi}_M = -\int_{-\infty}^{z}\frac{\partial}{\partial z}G_k(z-\zeta)\frac{\partial}{\partial\zeta}\operatorname{tr}(\mathbf{e}_{Mz}(\zeta))d\zeta\dot{z}(t)-G_k(0)\left.\frac{\partial}{\partial\zeta}\operatorname{tr}(\mathbf{e}_{Mz}(\zeta))\right|_{\zeta=z}\dot{z}(t) \quad . \tag{6.71}$$

Taking into account the relations (2.16), (6.68) and the mechanical incompressibility

$$\frac{d}{dt}\left(J_M\right)=J_M\operatorname{tr}(\mathbf{F}_M^{-1}\dot{\mathbf{F}}_M)=\operatorname{tr}(\mathbf{L}_M)=\operatorname{tr}(\mathbf{D}_M)=0 \quad , \tag{6.72}$$

the second term on the right hand side turns out to be zero because of (cf. [142])

$$\begin{aligned}\frac{\partial}{\partial\zeta}\operatorname{tr}(\mathbf{e}_{Mz}(\zeta))\Big|_{\zeta=z} &= \left(\mathbf{F}_M(z)\mathbf{e}'_M(z)\mathbf{F}_M^T(z)\right)\cdot\mathbf{1} = \mathbf{e}'_M(z)\cdot\mathbf{C}_M(z)\\ &= \frac{1}{2}\left(\dot{\mathbf{C}}_M^{-1}(z)\right)\cdot\mathbf{C}_M(z) = -\frac{1}{2}\mathbf{C}_M^{-1}(z)\mathbf{C}'_M(z)\mathbf{C}_M^{-1}(z)\cdot\mathbf{C}_M(z)\\ &= -\frac{1}{2}\operatorname{tr}(\mathbf{C}'_M(z)\mathbf{C}_M^{-1}(z)) = -\frac{1}{2}\operatorname{tr}(\mathbf{F}_M^{T-1}(z)\mathbf{F}_M'^{T}(z)+\mathbf{F}'_M(z)\mathbf{F}_M^{-1}(z))\\ &= -\frac{1}{2}\operatorname{tr}(\mathbf{D}_M(z)) = 0 \quad . \end{aligned} \tag{6.73}$$

Herein $'$ represents the derivative with respect to the argument of the particular tensor (i.e. $\mathbf{e}'_M(z) = \frac{d\,\mathbf{e}_M(z)}{dz}$ and $\mathbf{C}'_M(z) = \frac{d\,\mathbf{C}_M(z)}{dz}$). In addition, the partial derivative $\frac{\partial^2}{\partial z\partial\zeta}\operatorname{tr}\mathbf{e}'_{Mz}$ can be converted using eq. (6.68) and (2.16):

$$\begin{aligned}\frac{\partial^2}{\partial z\partial\zeta}\operatorname{tr}(\mathbf{e}_{Mz}(\zeta)) &= \frac{\partial^2}{\partial z\partial\zeta}\left[\mathbf{F}_M(z)(\mathbf{e}_M(\zeta)-\mathbf{e}_M(z))\mathbf{F}_M^T(z)\cdot\mathbf{1}\right]\\ &= \mathbf{e}'_M(\zeta)\cdot\mathbf{C}'_M(z) = 2\mathbf{e}'_M(\zeta)\cdot\mathbf{E}'_M(z) \quad . \end{aligned} \tag{6.74}$$

Inserting eq. (6.74) and (6.73) into eq. (6.71) yields

$$\begin{aligned}\dot{\psi}_M &= -\int_{-\infty}^{z} G'_k(z-\zeta)\frac{d}{d\zeta}\operatorname{tr}(\mathbf{e}_{Mz}(\zeta))d\zeta\dot{z}(t)\\ &\quad -2\int_{-\infty}^{z} G_k(z-\zeta)\mathbf{e}'_M(\zeta)d\zeta\cdot\dot{\mathbf{E}}_M(t)\end{aligned} \tag{6.75}$$

for the material time derivative of the mechanical free energy function. Inserting the derived expressions for stress power (eq. (6.22)), as well as the material time rates for the thermochemical and mechanical free energy functions (eqs. (6.70) and (6.75)) into the Clausius-Duhem inequality in the form of eq. (2.54) results in

$$\begin{aligned}\theta\gamma &= +\int_{-\infty}^{z} G'_k(z-\zeta)\frac{d}{d\zeta}\operatorname{tr}(\mathbf{e}_{Mz}(\zeta))d\zeta\dot{z}(t)\\ &\quad +2\int_{-\infty}^{z} G_k(z-\zeta)\mathbf{e}'_M(\zeta)d\zeta\cdot\dot{\mathbf{E}}_M - \frac{\partial\,\psi_{\theta C}}{\partial q}\dot{q} - \frac{\partial\,\psi_{\theta C}}{\partial\theta}\dot{\theta}\\ &\quad +\frac{1}{\rho_{\theta C}}\left(\tilde{\mathbf{T}}_M\cdot\dot{\mathbf{E}}_M + \mathbf{C}_M\tilde{\mathbf{T}}_M\cdot\mathbf{L}_{\theta C}\right)\\ &\quad -s\dot{\theta} - \frac{1}{\theta\rho_R}\mathbf{q}_R\cdot\operatorname{Grad}\theta \geq 0 \quad .\end{aligned} \tag{6.76}$$

Here, γ is the local entropy production. By rearranging terms and including the relation (6.23) the CDI can be written as

$$\begin{aligned}\theta\gamma \;=\; & \left(\frac{1}{\rho_{\theta C}}\tilde{\mathbf{T}}_M + 2\int_{-\infty}^{z} G_k(z-\zeta)\mathbf{e}'_M(\zeta)d\zeta\right)\cdot\dot{\mathbf{E}}_M \\ & + \int_{-\infty}^{z} G'_k(z-\zeta)\frac{d}{d\zeta}\,\mathrm{tr}(\mathbf{e}_{Mz}(\zeta))d\zeta\dot{z}(t) \\ & + \left(\frac{\mathrm{tr}(\mathbf{T})}{3\rho_{\theta C}\varphi}\frac{\partial\,\varphi}{\partial\theta} - \frac{\partial\,\psi_{\theta C}}{\partial\theta} - s\right)\dot{\theta} \\ & + \left(\frac{\mathrm{tr}(\mathbf{T})}{3\rho_{\theta C}\varphi}\frac{\partial\,\varphi}{\partial q} - \frac{\partial\,\psi_{\theta C}}{\partial q}\right)\dot{q} \\ & - \frac{1}{\theta\rho_R}\mathbf{q}_R\cdot\mathrm{Grad}\,\theta \geq 0 \quad . \end{aligned} \tag{6.77}$$

In order to ensure thermodynamic consistency for arbitrary temperature processes and mechanical loadings the CDI has to be fulfilled at any time. Therewith, constitutive equations for stress and entropy can be obtained by claiming the expressions in brackets in front of the material time rate of the mechanical Green-Lagrange strain tensor and the temperature to be equal to zero. Hence, the following relations for the mechanical second Piola-Kirchhoff stress tensor

$$\tilde{\mathbf{T}}_M = -2\rho_{\theta C}\int_{-\infty}^{z} G_k(z-\zeta)\mathbf{e}'_M(\zeta)d\zeta \quad , \tag{6.78}$$

and for the specific entropy

$$s = \frac{\mathrm{tr}(\mathbf{T})}{3\rho_{\theta C}\varphi}\frac{\partial\,\varphi}{\partial\theta} - \frac{\partial\,\psi_{\theta C}}{\partial\theta} \quad , \tag{6.79}$$

are gained. Moreover, the following term, including the partial derivative of the thermochemical free energy with respect to the degree of cure,

$$\left[\frac{\mathrm{tr}(\mathbf{T})}{3\rho_{\theta C}\varphi}\frac{\partial\,\varphi}{\partial q} - \frac{\partial\,\psi_{\theta C}}{\partial q}\right]\dot{q} \geq 0 \tag{6.80}$$

has to be equal to or greater than zero for thermodynamic consistency. The residual inequality reads as

$$\theta\gamma = \int_{-\infty}^{z} G'_k(z-\zeta)\frac{d}{d\zeta}\,\mathrm{tr}(\mathbf{e}_{Mz}(\zeta))d\zeta\dot{z}(t) - \frac{1}{\theta\rho_R}\mathbf{q}_R\cdot\mathrm{Grad}\,\theta \geq 0 \quad . \tag{6.81}$$

In the subsequent sections, the particular terms will be evaluated and discussed in more detail.

6.6.1. Constitutive equations for stress

Due to the constraint of incompressibility, the derived stress-strain-relation in eq. (6.78) has to be extended by the constitutively undetermined reaction stress $-p\mathbf{C_M}^{-1}$ (cf. [141]) and states

as

$$\tilde{\mathbf{T}}_M = -p\mathbf{C}_M^{-1} - 2\rho_{\theta C} \int_{-\infty}^{z} G_k(z-\zeta)\mathbf{e}'_M(\zeta)d\zeta \quad . \tag{6.82}$$

The mechanical incompressibility yields $\det(\mathbf{C}_M) = 1$ and $\frac{d}{dt}\det(\mathbf{C}_M) = \det(\mathbf{C}_M)\,\mathbf{C}_M^{-1}\cdot\dot{\mathbf{C}}_M = 0$. Thus the work that is done by the reaction stress $-p\mathbf{C}_M^{-1}$ along the mechanical deformation $\mathbf{E}_M$, $-p\mathbf{C}_M^{-1}\cdot\dot{\mathbf{E}}_M = -1/2p\mathbf{C}_M^{-1}\cdot\dot{\mathbf{C}}_M$ is zero, vanishes within the stress power and does not appear in the CDI [142]. This reaction stress due to the pressure p leads to an additive split of the second Piola-Kirchhoff stress into a volumetric part $\bar{\tilde{\mathbf{T}}}_M = -p\mathbf{C}_M^{-1}$ and an isochoric extra stress $\hat{\tilde{\mathbf{T}}}_E$ with

$$\hat{\tilde{\mathbf{T}}}_E = -2\rho_{\theta C} \int_{-\infty}^{z} G_k(z-\zeta)\mathbf{e}'_M(\zeta)d\zeta \quad . \tag{6.83}$$

For a further evaluation of eq. (6.83), the relaxation function G_k has to be specified in more detail. According to sec. 3.3, the relaxation function G_k can be represented by a Prony series of the form

$$G_k(z-\zeta) = \sum_{k=1}^{n} \mu_k \mathrm{e}^{-\frac{z-\zeta}{\tau_k}} \quad . \tag{6.84}$$

Incorporating the Prony series into eq. (6.83) leads to

$$\hat{\tilde{\mathbf{T}}}_E = \sum_{k=1}^{n} \hat{\tilde{\mathbf{T}}}_{E,k} = -2\rho_{\theta C} \int_{-\infty}^{z} \sum_{k=1}^{n} \mu_k \mathrm{e}^{-\frac{z-\zeta}{\tau_k}} \mathbf{e}'_M(\zeta)d\zeta \quad , \tag{6.85}$$

whereas the extra stress $\hat{\tilde{\mathbf{T}}}_E$ is additively split into several parts $\hat{\tilde{\mathbf{T}}}_{E,k}$ according to the Prony series. This three-dimensional stress functional corresponds to a chain of n Maxwell elements in the one-dimensional case. The stress-strain-relation for a single extra stress $\hat{\tilde{\mathbf{T}}}_{E,k}$ is conform with eq. (3.34). Differentiation and extracting the term e^{z/τ_k}, corresponding to eq. (3.33), yields the ordinary differential equations

$$\dot{\hat{\tilde{\mathbf{T}}}}_{E,k} + \frac{\dot{z}(t)}{\tau_k}\hat{\tilde{\mathbf{T}}}_{E,k} = -2\rho_{\theta C}\mu_k\mathbf{e}'_M \qquad \text{with} \qquad k = 1,..,n \quad . \tag{6.86}$$

Eq. (6.86) can be pushed forward to the current configuration by the transformation $\mathbf{S}_{E,k} = 1/J\mathbf{F}_M\hat{\tilde{\mathbf{T}}}_{E,k}\mathbf{F}_M^T$ and results in

$$\overset{\triangledown}{\mathbf{S}}_{E,k} + \frac{\dot{z}(t)}{\tau_k}\mathbf{S}_{E,k} = 2\rho_{\theta C}\mu_k\mathbf{D}_M \quad , \tag{6.87}$$

taking into account the relation $\mathbf{e}'_M(z) = 1/2(\mathbf{C}_M^{-1})' = -\mathbf{F}_M^T\mathbf{D}_M\mathbf{F}_M^{T-1}$ according to eqs. (2.17) and (6.68) and

$$\overset{\triangledown}{\mathbf{S}}_{E,k} = \dot{\mathbf{S}}_{E,k} - \mathbf{L}_M\mathbf{S}_{E,k} - \mathbf{S}_{E,k}\mathbf{L}_M^T \tag{6.88}$$

which is the contravariant Oldroyd derivative. The extra stress tensor $\mathbf{S}_{E,k}$ is of Cauchy-type with respect to the current configuration. The mechanical strain rate tensor $\mathbf{D}_M$ is given by

$$\mathbf{D}_M = \frac{1}{2}(\dot{\mathbf{F}}_M \mathbf{F}_M^{-1} + \mathbf{F}_M^{T-1} \dot{\mathbf{F}}_M^T) \quad . \tag{6.89}$$

The combination of eqs. (2.24), (6.82), (6.85) and the push forward transformation results in the overall Cauchy stress tensor $\mathbf{T}$

$$\mathbf{T} = -p\mathbf{1} + \sum_{k=1}^{n} \mathbf{S}_{E,k} \quad . \tag{6.90}$$

In case of uncured bone cement, it is difficult to experimentally identify the elastic properties. Therefore the elastic properties are assumed to be infinitely stiff in good approximation. Considering $\eta_k = \mu_k \tau_k$ and $\mu_k \to \infty$ eq. (6.87) reduces to

$$\mathbf{S}_{E,k} = 2\eta_k \mathbf{D}_M \quad . \tag{6.91}$$

Moreover, the mechanical free energy vanishes in accordance with eq. (6.84) and (6.69). In this special case the mechanical free energy is not a function of the dissolution d as stated earlier (cf. eq. (6.42)).

6.6.2. Constitutive equations for entropy

The potential relation for entropy in eq. (6.79) can be rewritten as

$$s = \frac{-p}{\rho_R} \frac{\partial \varphi}{\partial \theta} - \frac{\partial \psi_{\theta C}}{\partial \theta} \quad , \tag{6.92}$$

by using the relation (6.11) and for the trace of the Cauchy stress

$$tr(\mathbf{T}) = -3p \quad . \tag{6.93}$$

In contrast to eq. (6.47), eq. (6.92) now also takes into account conditions for $p \neq 0$. Entropy rises with decreasing pressure because a more disordered state is attained. An additional dependence of entropy on the degree of cure comes with the term $\frac{\partial \varphi}{\partial \theta}$ because $\frac{\partial \varphi}{\partial \theta} = f(q)$ (cf. eq. (6.10)) and reduces the decrease of entropy with proceeding polymerisation.
Furthermore, the potential relation for entropy leads to the definition of the specific heat capacity at constant mechanical deformation

$$\frac{\partial s}{\partial \theta} = -\frac{1}{\rho_R} \frac{\partial p}{\partial \varphi} \left(\frac{\partial \varphi}{\partial \theta} \right)^2 - \frac{\partial^2 \psi_{\theta C}}{\partial \theta^2} = \frac{c_d}{\theta} \quad , \tag{6.94}$$

whereat $\frac{\partial^2 \varphi}{\partial \theta^2} = 0$ (cf. eq. (6.10)). However, the specific heat capacity at constant deformation is not applicable for mechanically incompressible materials, and hence, under the assumption of $p = const.$, eq. (6.94) can be interpreted as specific heat at constant pressure

$$\frac{\partial s}{\partial \theta} = -\frac{\partial^2 \psi_{\theta C}}{\partial \theta^2} = \frac{c_p}{\theta} \quad , \tag{6.95}$$

which is in accordance with eq. (6.62) and (6.37).
For evaluating the first law of thermodynamics (cf. sec. 6.6.5) the material time rate of the entropy is required:

$$\begin{aligned} \dot{s} &= \frac{-\dot{p}}{\rho_R}\frac{\partial\,\varphi}{\partial\theta} + \frac{-p}{\rho_R}\frac{\partial^2\varphi}{\partial\theta\partial q}\dot{q} - \frac{\partial\psi_{\theta C}}{\partial\theta\partial q}\dot{q} - \frac{\partial^2\psi_{\theta C}}{\partial\theta^2}\dot{\theta} \\ &= \frac{-\dot{p}}{\rho_R}\frac{\partial\,\varphi}{\partial\theta} - \left(\frac{p}{\rho_R}\frac{\partial^2\varphi}{\partial\theta\partial q} + \frac{\partial\psi_{\theta C}}{\partial\theta\partial q}\right)\dot{q} - \left(\frac{\partial^2\psi_{\theta C}}{\partial\theta^2}\right)\dot{\theta} \quad . \end{aligned} \tag{6.96}$$

6.6.3. Further requirements from the Clausius-Duhem inequality

Within the scope of this work only the forward reaction of polymerisation is considered. Therefore the temporal derivative of the degree of cure, i.e. the reaction rate is always non-negative ($\dot{q} \geq 0$). Hence, the remaining factor of eq. (6.80) also has to be non-negative and, in combination with eq. (6.11) and (6.93), reads as:

$$\frac{-p}{\rho_R}\frac{\partial\,\varphi}{\partial q} - \frac{\partial\,\psi_{\theta C}}{\partial q} \geq 0 \quad . \tag{6.97}$$

The hydrostatic pressure p is commonly very small and positive, while the partial derivative

$$\frac{\partial\,\varphi}{\partial q} = \Delta\alpha(\theta - \theta_0) + \beta \tag{6.98}$$

is negative, unless very low temperatures are regarded (cf. sec. 7.3). In this context it should be mentioned, that the linear thermal expansion model (cf. eq. (6.10)) is only applicable in a certain neighbourhood of the reference temperature θ_0. Therewith, in total, the first term in eq. (6.97) is usually positive. The second term on the left hand side of eq. (6.97) can be written as (according to eq. (6.70))

$$\frac{\partial\,\psi_{\theta C}}{\partial q} = (h_S(\theta) - h_F(\theta)) - \theta\left(s_S(\theta_0) - s_F(\theta_0) + \int_{\theta_0}^{\theta}\frac{c_{p,S}(\vartheta) - c_{p,F}(\vartheta)}{\vartheta}d\vartheta\right) \quad . \tag{6.99}$$

Expressed in words, the total heat of reaction at a certain temperature θ has to be greater than the corresponding decrease in enthalpy times the temperature θ. Using the Legendre transformations specified in eq. (2.53), this term can be further interpreted as the change in the free enthalpy or Gibbs energy Δg for the polymerisation reaction. For exergonic reactions, i.e. reactions that are favourable or spontaneous, such as the radical polymerisation within the considered temperature range, the change in the free enthalpy is negative [117]. In sum, the whole expression in eq. (6.97) is non-negative for ordinary loading processes.

6.6.4. Dissipation

The term

$$\int_{-\infty}^{z} G_k'(z-\zeta)\frac{d}{d\zeta}\operatorname{tr}(\mathbf{e}_{Mz}(\zeta))d\zeta\dot{z}(t) \geq 0 \tag{6.100}$$

has to be non-negative and describes the dissipative energy, generated by mechanical deformations of external and internal forces and has to be non-negative as well. Integration by parts yields

$$\begin{aligned}\int_{-\infty}^{z} G_k'(z-\zeta)\frac{d}{d\zeta}\operatorname{tr}(\mathbf{e}_M(\zeta))d\zeta\dot{z}(t) &= [G_k'(z-\zeta)\operatorname{tr}(\mathbf{e}_M(\zeta))]_{-\infty}^{z} \\ &\quad + \int_{-\infty}^{z} G_k''(z-\zeta)\operatorname{tr}(\mathbf{e}_M(\zeta))d\zeta\dot{z}(t) \geq 0\end{aligned} \tag{6.101}$$

whereas

$$\frac{\partial}{\partial\zeta}G_k'(z-\zeta) = -G_k''(z-\zeta) \tag{6.102}$$

and

$$\operatorname{tr}(\mathbf{e}_M(z)) = \operatorname{tr}(\mathbf{F}_M(z)(\mathbf{e}_M(z)-\mathbf{e}_M(z))\mathbf{F}_M^T(z)) = 0 \tag{6.103}$$

holds. With the assumption of asymptotic relaxation functions exhibiting the following property

$$\lim_{z\to\infty} G_k'(z) = 0 \quad , \tag{6.104}$$

the first term on the right hand side in eq. (6.101) vanishes and eq. (6.100) can also be written as

$$\int_{-\infty}^{z} G_k''(z-\zeta)\operatorname{tr}(\mathbf{e}_{Mz}(\zeta))d\zeta\dot{z}(t) \geq 0 \quad . \tag{6.105}$$

By definition, the intrinsic time z proceeds only forward and hence the temporal derivative $\dot{z}$ is non-negative. Moreover, the trace $\operatorname{tr}(\mathbf{e}_{Mz}(\zeta))$ of the relative mechanical Piola strain tensor can be expressed in terms of the inverse relative mechanical Cauchy Green tensor by means of eq. (6.68) and reads as:

$$\operatorname{tr}(\mathbf{e}_{Mz}(\zeta)) = \operatorname{tr}(\frac{1}{2}(\mathbf{C}_{Mz}^{-1}(\zeta)-\mathbf{1})) = \frac{1}{2}(\operatorname{tr}(\mathbf{C}_{Mz}^{-1}(\zeta))-3) \quad . \tag{6.106}$$

Since the mechanical Cauchy Green tensor $\mathbf{C}_M$ and also the inverse relative mechanical Cauchy Green tensor $\mathbf{C}_{Mz}$ are unimodular, positive definite, symmetric tensors under the constraint of mechanical incompressibility,

$$\operatorname{tr}(\mathbf{C}_{Mz}^{-1}(\zeta)) \geq 3 \tag{6.107}$$

holds (cf. [80]) and the non-negativity of $\mathrm{tr}(\mathbf{e}_{Mz}(\zeta))$ is proven. In order to obtain an overall non-negative dissipation, the resulting requirement is to have a positive second derivative of the relaxation function

$$G_k''(z-\zeta) = \sum_{k=1}^{n} \frac{\mu_k}{\tau_k^2} \mathrm{e}^{-\frac{z-\zeta}{\tau_k}} \geq 0 \quad . \tag{6.108}$$

In addition to the above criteria, Haupt and Lion [80] as well as Lion and Kardelky [142] present further requirements to the relaxation function for a thermodynamically consistent modelling. For preserving a positive free energy function and a meaningful stress functional, the additional requirements $G_k \geq 0$ and $G_k' \leq 0$ are claimed. This correlates to a positive relaxation function with negative slope and positive curvature.
As mentioned in sec. 6.6.1, the mechanical part of the free energy vanishes if a pure viscous material behaviour is assumed during the dissolution process of acrylic bone cement. In this case, the Clausius-Duhem inequality reads as

$$\begin{aligned} \theta\gamma \;=\; & \frac{1}{\rho_{\theta C}} \mathbf{T}_M \cdot \mathbf{D}_M \\ & + \left(\frac{\mathrm{tr}(\mathbf{T})}{3\rho_{\theta C}\varphi} \frac{\partial \varphi}{\partial \theta} - \frac{\partial \psi_{\theta C}}{\partial \theta} - s \right) \dot{\theta} \\ & + \left(\frac{\mathrm{tr}(\mathbf{T})}{3\rho_{\theta C}\varphi} \frac{\partial \varphi}{\partial q} - \frac{\partial \psi_{\theta C}}{\partial q} \right) \dot{q} \\ & - \frac{1}{\theta \rho_R} \mathbf{q}_R \cdot \mathrm{Grad}\, \theta \geq 0 \quad . \end{aligned} \tag{6.109}$$

In contrast to the viscoelastic behaviour described above, not only a certain part of the stress power, but the total stress power is dissipated due to the viscous behaviour during dissolution. In this case, the stress power is given by

$$w_S = \frac{1}{\rho_{\theta C}} \mathbf{T}_M \cdot \mathbf{D}_M = \frac{1}{\rho_{\theta C}} \mathbf{T}_M \cdot \mathrm{grad}\, \mathbf{v}\,(\mathbf{x}, t) \quad , \tag{6.110}$$

and a potential relation can not be derived by means of a formulation for the free energy and the Clausius-Duhem inequality. A viscous material cannot store mechanical energy.

6.6.5. Equation of heat conduction

The last term within the Clausius-Duhem inequality in form of eq. (6.77) is attributed to heat conduction. The non-negativity of this term

$$-\frac{1}{\theta \rho_R} \mathbf{q}_R \cdot \mathrm{Grad}\, \theta \geq 0 \tag{6.111}$$

ensures that heat is always conducted from areas with higher temperatures to areas with lower temperatures including the temperature gradient as driving factor. In this work, Fourier's law of heat conduction serves as constitutive relation for the heat flux vector and reads as

$$\mathbf{q}_R = -\lambda\, \mathrm{Grad}\, \theta \quad , \tag{6.112}$$

whereas λ is the coefficient of heat conduction and is always positive. According to the measurements in sec. 5.3, this coefficient can be modelled to depend linearly on temperature within the range from 20 °C to 80 °C:

$$\lambda(\theta) = \lambda_0 + c_\lambda(\theta - \theta_0) \quad . \tag{6.113}$$

λ_0 and c_λ are material parameters to be identified. The modelling of the thermal conductivity can be extended similarly to the characterisation of the specific heat in eqs. (6.37) to (6.39) when the influence of the degree of cure on the thermal conductivity is known. Although, widely used in literature, it should be mentioned that there exist, alongside Fourier's law of heat conduction, more sophisticated approaches as constitutive relation for the heat flux vector. For example the constitutive equation by Cattaneo, which includes an additional time constant to realise a phase shift between temperature gradient and heat flux and therewith a finite transport velocity of information (cf. [189, 239]). The constitutive equation by Cattaneo for heat conduction can be interpreted as equivalent to viscoelasticity in solid mechanics and Fourier's law is the counterpart to Hooke's law. However, for macroscopic scales and still moderate heat generation by exothermal polymerisation, Fourier's law is sufficient to describe the temperature distribution within curing bone cement (cf. [54]).

After the constitutive relations for entropy and the heat flux vector are established, the equation of heat conduction can be derived form the first law of thermodynamics. Starting from eq. (2.47) in combination with the Legendre transformation $\psi = e - \theta s$ yields

$$(\dot{\psi} + \theta\dot{s} + \dot{\theta}s) = \frac{1}{\rho_R}\tilde{\mathbf{T}} \cdot \dot{\mathbf{E}} - \frac{1}{\rho_R}\operatorname{Div}\mathbf{q}_R + r \quad . \tag{6.114}$$

The insertion of eqs. (6.22), (6.23), (6.70), (6.75), (6.92) and (6.96) into eq. (6.114) and the consideration of the relation $-p\mathbf{C}_M^{-1} \cdot \dot{\mathbf{E}}_M = 0$ as well as the absence of volume distributed heat sources ($r = 0$) results in

$$\begin{aligned} & -\int_{-\infty}^{z} G_k''(z-\zeta)\,\operatorname{tr}(\mathbf{e}_{Mz}(\zeta))d\zeta\dot{z}(t) + \left(\frac{p}{\rho_R}\frac{\partial\,\varphi}{\partial q} + \frac{\partial\,\psi_{\theta C}}{\partial q}\right)\dot{q} \\ & +\theta\left(\frac{-\dot{p}}{\rho_R}\frac{\partial\,\varphi}{\partial\theta} - \left(\frac{p}{\rho_R}\frac{\partial^2\varphi}{\partial\theta\partial q} + \frac{\partial\psi_{\theta C}}{\partial\theta\partial q}\right)\dot{q} - \left(\frac{\partial^2\psi_{\theta C}}{\partial\theta^2}\right)\dot{\theta}\right) \\ = \; & -\frac{1}{\rho_R}\operatorname{Div}\mathbf{q}_R \quad . \end{aligned} \tag{6.115}$$

By rearranging the terms and using eqs. (6.33), (6.47), (6.48) and (6.61), eq. (6.115) can be converted into

$$\begin{aligned} c_p\dot{\theta} \;=\; & -\frac{\partial\,h}{\partial q}\dot{q} + \int_{-\infty}^{z} G_k''(z-\zeta)\,\operatorname{tr}(\mathbf{e}_{Mz}(\zeta))d\zeta\dot{z}(t) \\ & -\frac{1}{\rho_R}\operatorname{Div}\mathbf{q}_R - \theta\left(\frac{-\dot{p}}{\rho_R}\frac{\partial\,\varphi}{\partial\theta} - \frac{p}{\rho_R}\frac{\partial^2\varphi}{\partial\theta\partial q}\dot{q}\right) \quad . \end{aligned} \tag{6.116}$$

In this form, a physical meaning can be attributed to each term. The whole specific heating power $c_p\dot{\theta}$, is the sum of the heat power $-\frac{\partial\,h}{\partial q}\dot{q}$, generated by the polymerisation heat power, the

mechanical dissipation power, the heat power that is supplied or discharged by heat conduction and the heat power that is generated by thermal expansion under varying pressure and varying thermal expansion with the rate of reaction. For the dissolution process the mechanical dissipation is not given by eq. (6.105) but has to be replaced by $\mathbf{T}_M \cdot \mathbf{D}_M$ in eq. (6.116).
Tab. 6.1 summarises the constitutive equations that have been derived and developed in the previous sections for both parts of the model, dissolution and polymerisation.

Table 6.1.: Constitutive equations for bone cement during dissolution

Evolution of dissolution	$\frac{dd}{dt} = \begin{cases} (K_{d1} + K_{d2} d^m), & \text{if } d < d_{max} \\ 0, & \text{if } d \geq d_{max} \end{cases}$
	$K_{di} = A_{di} \exp\left(\frac{E_{di}}{R\theta}\right) \qquad i = 1, 2$
Evolution of polymerisation	$\frac{dq}{dt} = (K_{q1} + K_{q2} q^k)(1-q)^l f_D(q)$
	$f_D(q) = \left[\frac{2}{1 + \exp(\frac{q - q_{end}}{b})} - 1\right]$
	$K_{qi} = A_{qi} \exp\left(\frac{E_{qi}}{R\theta}\right) \qquad i = 1, 2$
	$q_{end} = \frac{f(T) - \xi}{\kappa}$
	$f(T) = \frac{T_{iso} + \Delta T - T_{g,0}}{T_{g,1} - T_{g,0}} \quad \text{with} \quad T_g(q_{end}) = T_{iso} + \Delta T$
Deformation	$\mathbf{F} = \mathbf{F}_M \mathbf{F}_{\theta C} \qquad det\,(\mathbf{F}_M) = 1$
Thermal deformations	$\mathbf{F}_{\theta C} = \varphi(\theta, q)^{1/3} \mathbf{1}$
	$\varphi(\theta, q) = 1 + (\alpha + \Delta\alpha q(t))(\theta - \theta_0) + \beta q(t)$
Free energy	$\psi = \psi_M + \psi_{\theta C}$
	$\psi_{\theta C}(\theta, q) = h(\theta, q) - \theta s(\theta, q)$
	$\psi_M = \begin{cases} 0, & \text{dissolution} \\ -\int_{-\infty}^{z} G_k(z-\zeta) \frac{d}{d\zeta} \operatorname{tr}(\mathbf{e}_{Mz}(\zeta)) d\zeta, & \text{polymerisation} \end{cases}$
	$G_k(z-\zeta) = \sum_{k=1}^{n} \mu_k \mathrm{e}^{-\frac{z-\zeta}{\tau_k}}$
	$\dot{z}(t) = M(...) \geq 0, \quad z(t) = \int_{-\infty}^{t} M(...) d\tau, \quad \zeta(s) = \int_{-\infty}^{s} M(...) d\tau$

Enthalpy	$h(\theta, q) = h_F(\theta)(1-q) + h_S(\theta)q \quad \forall\, 0 \le q \le 1$
	$h_F(\theta) = h_{F0} + a_F(\theta - \theta_0) + \frac{1}{2} b_F (\theta - \theta_0)^2$
	$h_S(\theta) = h_{S0} + a_S(\theta - \theta_0) + \frac{1}{2} b_S (\theta - \theta_0)^2$
Entropy	$s = \frac{-p}{\rho_R} \frac{\partial \varphi}{\partial \theta} - \frac{\partial \psi_{\theta C}}{\partial \theta}$
Stress	$\mathbf{T} = -p\mathbf{1} + \sum_{k=1}^{n} \mathbf{S}_{E,k}$
	$\sum_{k=1}^{n} \mathbf{S}_{E,k} = \mathbf{S}_E = 2\eta \mathbf{D}_M,$ dissolution
	$\overset{\triangledown}{\mathbf{S}}_{E,k} + \frac{\dot{z}(t)}{\tau_k} \mathbf{S}_{E,k} = 2\rho_{\theta C} \mu_k \mathbf{D}_M,$ polymerisation
Dissipation	$D = \begin{cases} \mathbf{T}_M \cdot \mathbf{D}_M, & \text{dissolution} \\ \int_{-\infty}^{z} G_k''(z-\zeta) \operatorname{tr}(\mathbf{e}_{Mz}(\zeta)) d\zeta \dot{z}(t), & \text{polymerisation} \end{cases}$
Heat flux	$\mathbf{q}_R = -\lambda \operatorname{Grad} \theta$
	$\lambda(\theta) = \lambda_0 + c_\lambda(\theta - \theta_0)$

What is still missing are the constitutive functions for the viscosity in the dissolution-driven part and an explicit expression for the shift function M for the polymerisation-dominated part of the model. Both constitutive equations will be addressed more precisely in ch. 7 as they are closely linked to the parameter identification procedure.

7. Parameter identification

In the previous chapter, the material specific constitutive equations, which complement the kinematic relations and balance laws, have been developed, mainly motivated by the experimental investigations in ch. 5. Therewith, the material model is able to represent the thermodynamic and mechanical behaviour of bone cement qualitatively and quantitatively. However, in order to match the constitutive equations to the experimental findings, the parameters within these constitutive equations have to be adjusted by means of analytical and numerical methods. The analytical methods serve to obtain appropriate initial values and boundaries for the numerical methods and are specific for kinetic, thermodynamic and mechanical constitutive equations. Therefore these methods will be addressed in the particular sections following. Once suitable initial values are available, the constitutive parameters can be fitted to the experimental data in a least-squares sense. For this purpose, the software package MATLAB® was employed, which offers built-in routines for the non-linear least-squares method that uses either the 'trust-region-reflective' [43, 42] or the Levenberg-Marquardt algorithm [161].
Furthermore, the parameter identification of the presented model makes it reasonable to follow up a specific strategy or sequence regarding the constitutive equations. Since the modelling assumes that, on the one hand, the reaction kinetics for polymerisation only depends on temperature and the reaction process itself, and on the other hand, most other material properties depend amongst others on the reaction progress, the parameters for reaction kinetics of polymerisation can be identified first, without any knowledge of mechanical and thermal properties. Consecutively, the parameters within the other constitutive equations, such as the specific heat, the chemical and thermal volume changes and the relaxation function can be determined with the knowledge of the actual progress of polymerisation. The evolution of dissolution is supposed to influence only the mechanical behaviour during the setting phase, and therefore the parameters for the evolution equation of dissolution can only be identified on the basis of the rheological behaviour. In this context, dissolution can be regarded as a mechanical internal variable. The following sections will explain the parameter identification strategy of the related constitutive equations in more detail and show the quality and ability of the model to represent the experimentally determined behaviour of acrylic bone cement.

7.1. Reaction kinetics

In order to determine the material parameters of the constitutive equations describing the polymerisation progress of bone cement, the experimental data from sec. 5.2.1 has to be evaluated further. According to eq. (6.3), the course of the degree of cure q can be calculated for each isothermal experiment, including the temperature ramps after the isothermal phase. As a result, the final degree of cure at the end of the isothermal phase for the different experimental temperatures can be determined. Fig. 7.1 shows the experimentally determined values as well as the representation of this uncompleted curing by the model. For an adequate parametrisa-

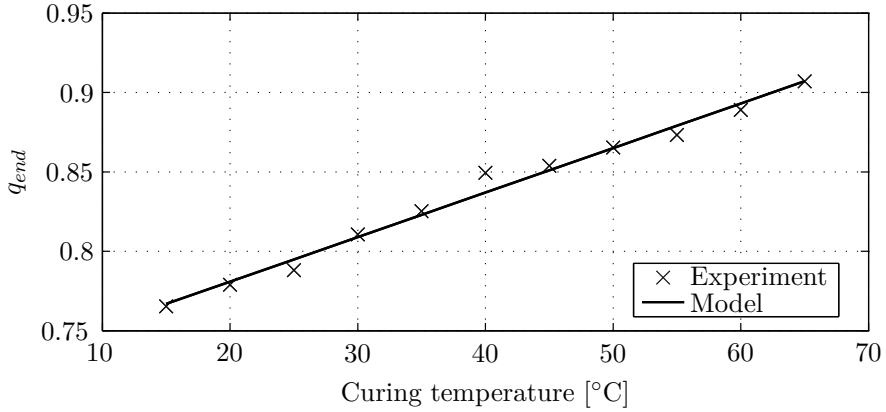

Figure 7.1.: Maximum attainable degree of cure for specific isothermal curing processes

tion of eqs. (6.6) and (6.7) the glass transition temperature of the uncured and the fully cured material has to be identified. Due to the fact that uncured bone cement does not really exhibit a glass transition temperature $T_{g,0}$, the melting temperature of MMA of approx. $-50\,°\mathrm{C}$ is used instead. From the experiments in ch. 5, the glass transition temperature of fully cured bone cement $T_{g,1}$ is known as $105\,°\mathrm{C}$. Moreover, the temperature ramps following the isothermal curing phase (cf. sec. 5.2.1) indicate that polymerisation restarts at a temperature ΔT of $20\,°\mathrm{C}$ above the isothermal curing temperature. This temperature also represents the glass transition temperature of the uncompletely cured material at a certain curing temperature below the glass transition temperature $T_{g,1}$ of the completely cured material. With the aid of this information suitable start parameters can be calculated for a least-squares optimisation. The finally identified parameters are summarised in table 7.1. For determining the parameters of the evolution

Table 7.1.: Material parameters for maximum attainable degree of cure

$T_{g,0}$	$T_{g,1}$	ΔT	ξ	κ
K	K	K	-	-
223	378	20	-1.2159	2.3007

equation (6.4) in combination with the Arrhenius behaviour in eq. (6.5) by non-linear least-square algorithms, a good choice of initial values is essential. Otherwise the algorithm will not

converge to a solution. In the case of dynamic DSC experiments, i.e. with different constant heating rates, there exist various procedures to estimate the kinetic parameters, and therewith to gain reliable initial values [60, 65, 175, 200]. However, for isothermal experiments, these techniques are not applicable and the following approach is applied to obtain an appropriate set of starting parameters. At first, it is reasonable to identify the parameters for each experiment temperature separately. Thereby values for K_{q1} and K_{q2} can be determined directly at first, without expressing them by an Arrhenius behaviour. Starting at the lowest curing temperature, the obtained parameters serve as the starting parameter set for the next temperature, The initial values for K_{q1} and K_{q2} can be added with a small offset, as the initial reaction rate (represented by K_{q1}) and the overall reaction rate increase with rising curing temperature. This procedure yields a set of four parameters belonging to the specific curing temperatures. Now the resulting parameters K_{q1} and K_{q2} can be used to fit the Arrhenius behaviour according to eq. (6.5), which provides suitable initial values for the activation energies E_{q1} and E_{q2}, as well as for the material specific parameters A_{q1} and A_{q2}. The gained parameters for k and b should not vary much across the different curing temperatures and the arithmetic mean of each parameter can be calculated. Subsequently, a non-linear optimisation routine can be set up, now taking into account all curing temperatures within the least square algorithm at once, using the initial parameters discussed previously. The following fig. 7.2 shows both, the calculated degree of cure from the measurements and the reaction progress predicted by the evolution equation.

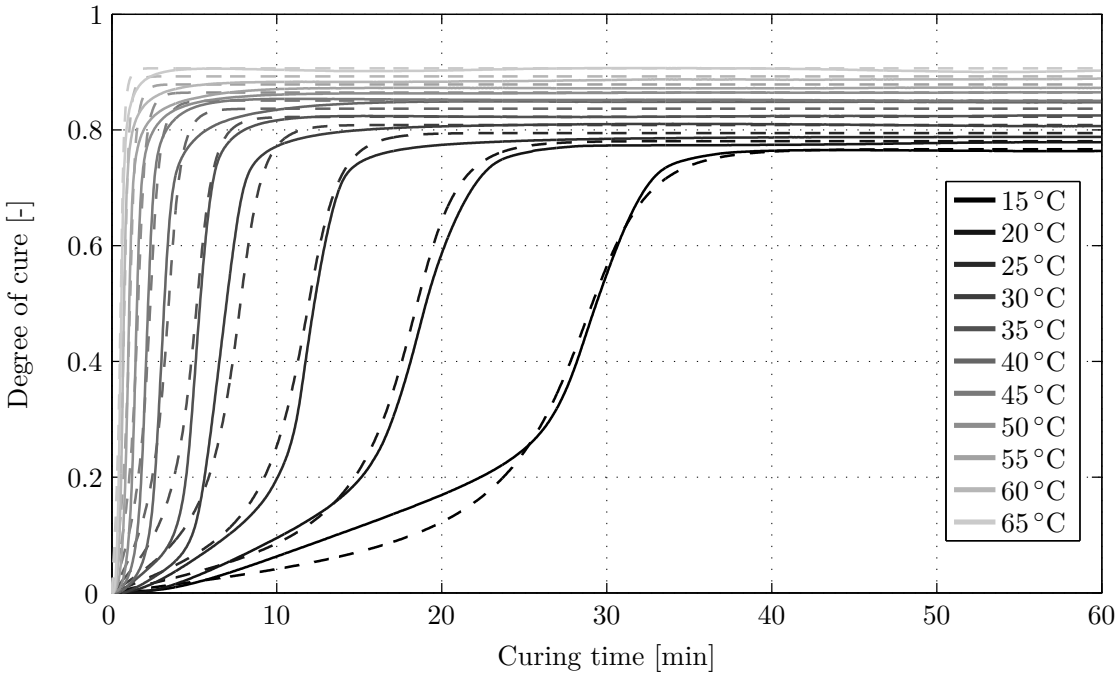

Figure 7.2.: Comparison of the progress of the degree of cure of acrylic bone cement; Measurement (—) and simulation (- -) with identified parameters

Generally, the evolution equation is able to represent the temperature-dependent curing behaviour of acrylic bone cement very well. Even the vitrification effect is captured accurately.

In the transition region to the maximum reaction rate and into the vitrification region, some improvement is still possible, maybe by choosing a different structure of the evolution equation. Tab. 7.2 lists the overall identified parameters for the reaction kinetics of bone cement.

Table 7.2.: Material parameters for the reaction kinetics of the polymerisation process

A_{q1}	E_{q1}	A_{q2}	E_{q1}	k	l	b
s^{-1}	J/mol	s^{-1}	J/mol	-	-	-
$1.792 \cdot 10^{10}$	$7.964 \cdot 10^4$	$3.234 \cdot 10^6$	$4.571 \cdot 10^4$	2.05	0.95	0.1917

The total heat of reaction can also be gained from DSC-measurements. Since the model takes into account a temperature-dependent specific heat capacity, the enthalpy of reaction is also temperature-dependent. Therefore, the total heat of reaction will be considered in combination with the identification of the specific heat capacity.

7.2. Specific heat capacity, enthalpy of reaction and thermal conductivity

The constitutive equations for the specific heat (cf. eqs. (6.37) to (6.39)) consider different linear dependencies on temperature for uncured and fully cured bone cement. With the measurements of the specific heat capacity for uncured and fully cured bone cement in sec. 5.2.2, it is convenient to identify the parameters a_F, b_F, a_S and b_S of the linear equations, which govern the temperature-dependent behaviour of the specific heat capacity. Tab. 7.3 summarises the parameter values identified with least-squares methods.

Table 7.3.: Material parameters for specific heat capacity

a_F	b_F	a_S	b_S
J/(gK)	$J/(gK^2)$	J/(gK)	$J/(gK^2)$
1.226	0.003288	1.112	0.003011

Moreover, fig. 7.3 compares the measurements with the simulation based on the parametrised constitutive model of the specific heat capacity. The linear relationship of temperature in the constitutive equations is adequate to represent the measured course.
Aside from the temperature-dependency, the modelling accounts further for a changing heat capacity with respect to the progress of polymerisation. This is illustrated in fig. 7.4 and obviously the modelled specific heat capacity fits the measurements for an isothermal polymerisation quite well. In particular, the decrease in the specific heat at high reactions rates is covered by the constitutive equations. The deviations between modelling and measurement apparent in fig. 7.4 might arise from both, lack of measuring precision with TMDSC (cf. sec. 5.2.2) and modelling accuracy.
The parameters a_F, b_F, a_S and b_S affect not only the specific heat capacity, but also the reaction enthalpy according to the relation $\frac{\partial h}{\partial \theta} = c_p$. However, with the aid of measurements of the

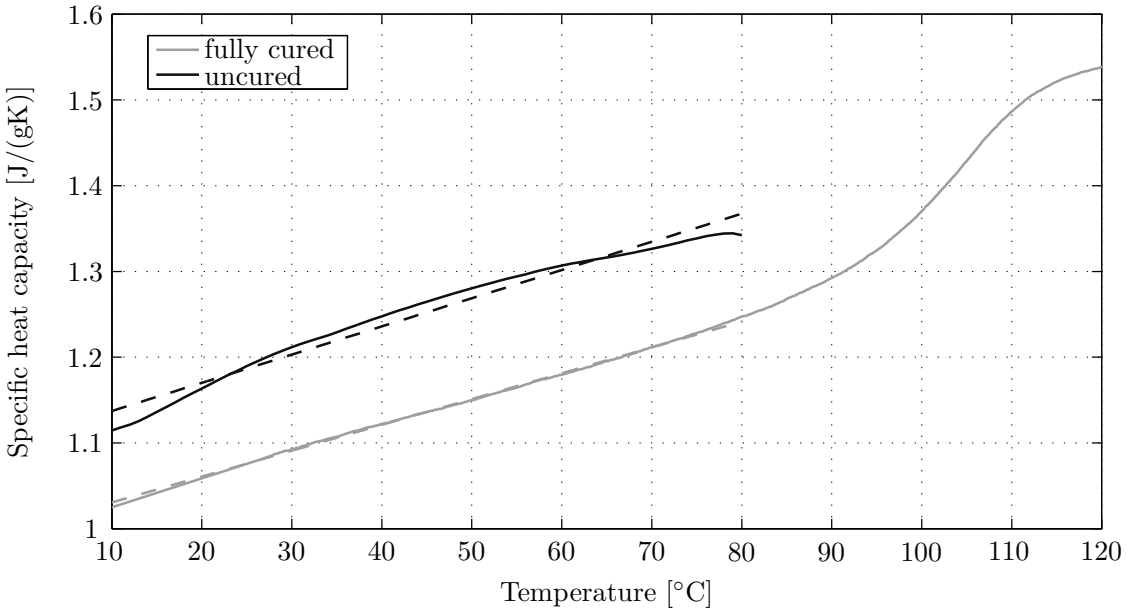

Figure 7.3.: Specific heat capacity of uncured and fully cured bone cement; Measurement (—) and simulation (- -) with identified parameters

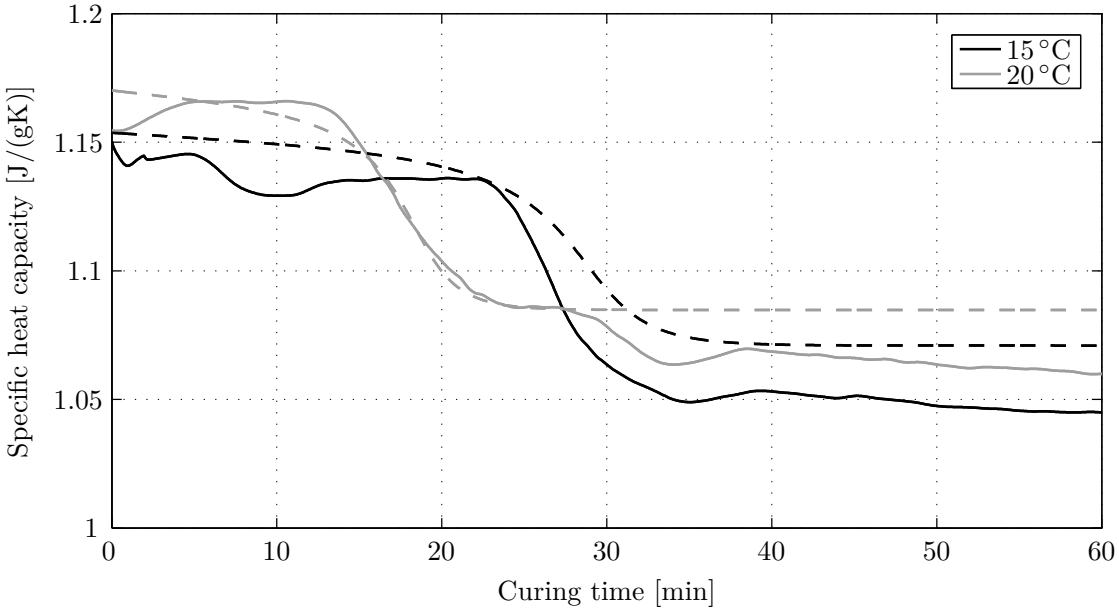

Figure 7.4.: Change of the specific heat capacity of bone cement during polymerisation; Measurement (—) and simulation (- -) with identified parameters

specific heat capacity, these parameters can be accessed more easily, than it would be possible by measurements of the enthalpy of reaction (cf. sec. 5.2.1). On the one hand, this is due to the fact that measurements of the specific heat are more sensible to these parameters than measurements of the enthalpy of reaction are. On the other hand, the parameters can be determined by

one single experiment for specific heat measurements, whereas for the reaction enthalpy at least a few measurements would be necessary. In addition, the comparative method with sapphire yields more accurate results than standard DSC experiments do.
Nonetheless, the absolute value of the enthalpy of reaction at the reference temperature $h_{S0}-h_{F0}$ has to be determined from measurements of the reaction kinetics, as the parameters a_F, b_F, a_S and b_S only specify the change in the enthalpy of reaction with respect to temperature. Adapting this enthalpy of reaction at the reference temperature in eq. (6.40) to the final values from sec. 5.2.1 with the aid of fitting methods available in MATLAB® and using the parameter values in tab. 7.3 yields the value presented in tab. 7.4.

Table 7.4.: Enthalpy of reaction at the reference temperature of 37 °C

$h_{S0} - h_{F0}$
J/g
-99.93

Basically, it would also be possible to identify the enthalpy of reaction at the reference temperature in combination with the reaction kinetics, assuming the values for a_F, b_F, a_S and b_S are already known. However, with a separate identification, a further degree of freedom is avoided in the identification routine of the reaction kinetics, and, as fig. 7.5 shows, the model parametrisation with respect to the experiments is quite accurate.

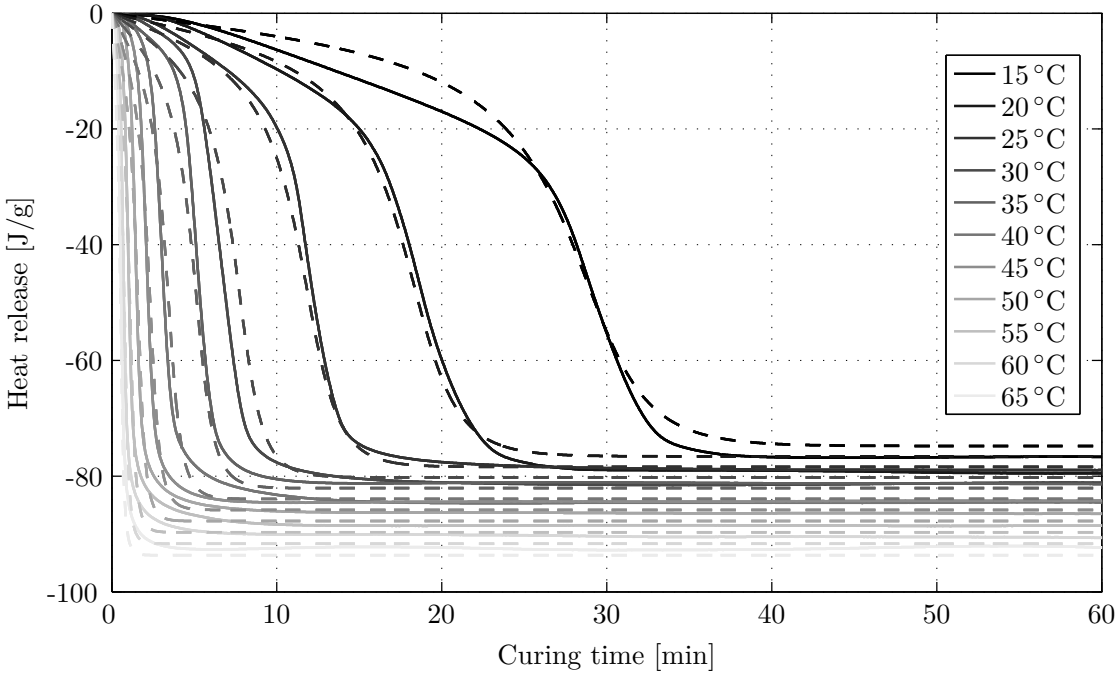

Figure 7.5.: Overall enthalpy of reaction for acrylic bone cement; Measurement (—) and simulation (- -) with identified parameters

The thermal conductivity as further important thermodynamic material property is difficult to capture experimentally (cf. sec. 5.3), especially in case of varying temperature and degree of

cure. For this reason, the model only takes into account a basic temperature-dependent thermal conductivity. Within the relevant temperature range from 10 °C to 80 °C, the experimentally obtained course (cf. fig. 5.8) can be approximated by a linear relationship. The identified parameters, according to eq. (6.113) are summarised in tab. 7.5.

Table 7.5.: Material parameters for thermal conductivity

λ_0	c_λ
W/(mK)	W/(mK^2)
0.2788	−0.000423

7.3. Density

After the reaction kinetics and the thermodynamic material parameters have been identified, the equation for volumetric strain due to thermal expansion and chemical shrinkage as mechanical material property can be adjusted. Therefore the density, experimentally investigated in sec. 5.4, can be converted into volumetric strain ϵ_{vol} or the corresponding function φ, respectively. On the basis of eq. (6.10) and eq. (6.11), the following relation can be established:

$$\varphi = 1 + \epsilon_{vol} = \frac{\rho_{ref}}{\rho} \quad . \tag{7.1}$$

Herein, ρ_{ref} denotes the reference density at 37 °C of uncured bone cement with the value 1.4697 g/cm^3.

Appropriate starting parameters for a parameter optimisation method that uses the data in fig. 5.11, can be obtained by fitting eq. (6.10) to the density course in the uncured and completely cured condition, as illustrated in fig. 5.10. With the aid of the modelled reaction kinetics the optimisation routine can include every single density course at constant temperature in fig. 5.11 into the least square criteria. However, absolute care is necessary when the first 4 to 5 minutes of the data in fig. 5.11 within the optimisation routine are omitted, as a time-dependent temperature change inside the specimen from room temperature towards the bath temperature takes place.

The parameter optimisation leads to the values listed in tab. 7.6. Comparing the values for thermal expansion α and chemical shrinkage β confirms, that both phenomena are in the same order of magnitude for temperature changes of more than 10 °C. Furthermore, the negative value of $\Delta\alpha$ proves the observation in fig. 5.10 of less thermal expansion in the solid state, but induces also higher chemical shrinkage for temperatures above the reference temperature and less chemical shrinkage for temperatures below the reference temperature.

Fig. 7.6 shows the measured and simulated density ratio φ, using the density at 37 °C of the uncured bone cement as reference. Therein a good agreement in the temporal course of chemical shrinkage between experimental and simulated values is obvious. Greater deviations for high curing temperatures at the very beginning in fig. 7.6 arise from the temperature change within

Table 7.6.: Material parameters for thermal expansion and chemical shrinkage

α	$\Delta\alpha$	β
1/K	1/K	-
0.000928	−0.000367	−0.090602

the thermal bath as mentioned above. In addition, the variation in the density after the main polymerisation process, which is not only due to thermal expansion but also due to a different degree of cure (caused by vitrification effects), is also represented precisely by the constitutive equation.

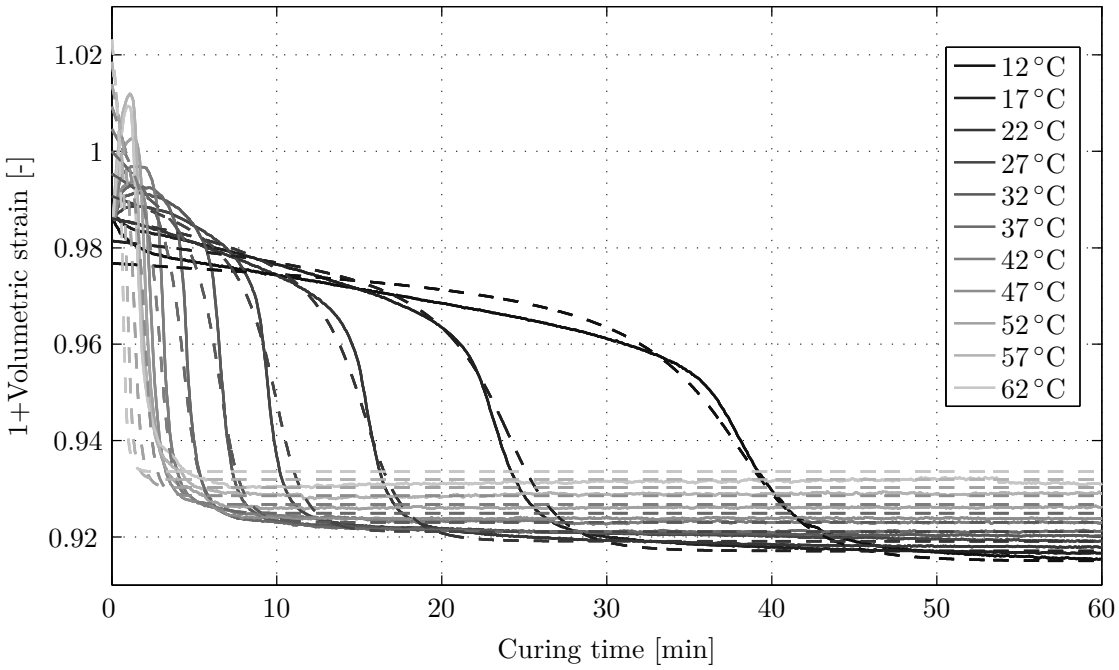

Figure 7.6.: Density ratio due to chemical shrinkage and thermal expansion; Measurement (—) and simulation (- -) with identified parameters

7.4. Progress of dissolution and rheological behaviour

The identification of the evolution equation for dissolution has been left open until now because the dissolution process effects only the rheological behaviour. This section will focus on the identification of the material parameters for the evolution equation for dissolution, as well as on the specification and parametrisation of the equation for describing the dependency of the viscosity on the current state of the dissolution and the shear rate (cf. sec. 5.6.3).
In order to set up the constitutive equation for the viscosity dependency, it is reasonable to recall the three major phenomena of the rheological behaviour of acrylic cement during dissolution (cf. sec 5.6). Firstly, the proceeding dissolution causes the viscosity to rise and secondly, a higher

temperature will accelerate the dissolution process. These two phenomena will be covered by the internal variable for the dissolution process. As a third phenomenon, the shear thinning behaviour of the liquid bone cement was detected, which is independent from the progress of dissolution. This shear thinning behaviour can be represented by using a power law fluid model in the form of

$$\mathbf{T} = -p\mathbf{1} + 2g\left(|4\mathrm{II}_{\mathbf{D}_M}|\right)^{(h-1)/2}\mathbf{D}_M \quad . \tag{7.2}$$

Herein, g and h are additional material constants and II_{D_M} is the second principal invariant of the mechanical rate-of-deformation tensor, which is given by

$$\mathrm{II}_{\mathbf{D}_M} = \frac{1}{2}\left(\mathrm{tr}^2\left(\mathbf{D}_M\right) - \mathrm{tr}\left(\mathbf{D}_M^2\right)\right) \quad . \tag{7.3}$$

In contrast to the first and third principal invariants, the second principal invariant is calculated only on the basis of off-diagonal elements of $\mathbf{D}_M$. Considering the physical significance of the diagonal and off-diagonal elements of $\mathbf{D}_M$, namely that the diagonal elements represent the rate of change of a material line element, currently aligned in the direction of the corresponding base vector, divided by the length of this line element and that the off-diagonal elements represent the rate of change of the angle between two line elements currently aligned in the directions of the corresponding base vectors, the second principal invariant is a measure of the overall pure shear rate of a material volume element and hence suitable to be applied in the constitutive law. In order to consider all three phenomena in the constitutive equation for stress (i.e. eq. (6.91)), the dynamic viscosity is a function of both, the internal variable for dissolution d and the second invariant of the mechanical rate-of-deformation tensor:

$$\eta = f(d, \mathrm{II}_{\mathbf{D}_M}) = \eta_0(d)g\left(|4\mathrm{II}_{\mathbf{D}_M}|\right)^{(h-1)/2} \quad . \tag{7.4}$$

In principal, eq. 7.4 is able to represent all three phenomena mentioned above. To identify the parameters in eq. (7.4) in combination with the evolution equation for dissolution (cf. sec. 6.2.1), it is necessary to know the rate-of-deformation tensor for both experimental applications, the cone-plate rheometer and the capillary rheometer. Using the spherical coordinates r, ϕ, θ for the cone-plate rheometer (cf. fig. 5.17) and the cylindrical coordinates r, θ, z in case of the capillary rheometer (cf. fig. 5.18), the velocity field can be specified for both applications as:

Cone-plate rheometer		Capillary rheometer	
$\mathbf{v}_r = \mathbf{v}_\phi$	$= \mathbf{0}$	$\mathbf{v}_r = \mathbf{v}_\theta$	$= \mathbf{0}$
$\mathbf{v}_\theta$	$= r\omega(\phi)\mathbf{e}_\theta$	$\mathbf{v}_z$	$= w(r)\mathbf{e}_z$

Following eqs. (2.14) as well as (2.15), the velocity gradients for each application can be expressed as:

$$\mathbf{D}_M = -\frac{\dot{\gamma}}{2}\begin{bmatrix}0 & 0 & 0\\ 0 & 0 & 1\\ 0 & 1 & 0\end{bmatrix} \tag{7.5}$$

$$\mathbf{D}_M = -\frac{\dot{\gamma}}{2}\begin{bmatrix}0 & 0 & 1\\ 0 & 0 & 0\\ 1 & 0 & 0\end{bmatrix} \tag{7.7}$$

with

$$\dot{\gamma} = \sin\phi\frac{\partial}{\partial\phi}\left(\frac{\omega(\phi)}{\sin\phi}\right) \tag{7.6}$$

with

$$\dot{\gamma} = \frac{\dot{V}}{\pi R^3}\frac{3h+1}{h+1}\left(\left(1+\frac{1}{h}\right)\left(\frac{r}{R}\right)^{\frac{1}{h}}\right) \tag{7.8}$$

A detailed derivation of expression (7.8) is given in app. A. In case of small cone angles the shear rate in eq. (7.6) can be written in a simplified form (cf. app. A). Regarding the capillary rheometer, the shear rate at the capillary wall $\dot{\gamma}|_{r=R} = \dot{\gamma}_w$ is of interest:

$$\dot{\gamma} = \frac{\Omega}{\alpha} \tag{7.9}$$

$$\dot{\gamma}_w = \frac{\dot{V}}{\pi R^3}\frac{3h+1}{h} \tag{7.10}$$

On closer inspection, it is obvious that both expressions for the shear rate $\dot{\gamma}$ in eqs. (7.9) and (7.10) correspond to the particular expressions for the shear rate in eqs. (5.15) and (5.20) in the experimental section. Thereby, the power law coefficient h is conform with the slope n within the Rabinowitsch-Weissenberg correction. Furthermore, calculating the second invariant $\mathrm{II}_{\mathbf{D}_M}$ of the rate-of-deformation tensor yields

$$\mathrm{II}_{\mathbf{D}_M} = -\frac{\dot{\gamma}^2}{4} \tag{7.11}$$

for both experimental applications and hence eq. (7.4) simplifies to

$$\eta = f(d,\dot{\gamma}) = \eta_0(d)g\left(|\dot{\gamma}|\right)^{(h-1)} \quad . \tag{7.12}$$

Eq. (7.12) has now an adequate form for parameter identification routines with respect to the experimental data in sec. 5.6. It should be mentioned here that eq. (7.12) includes a dependency of viscosity on both, dissolution and shear rate, but not on temperature. Of course, a temperature influence is implied indirectly via the temperature dependency of the dissolution. As it is not possible to distinguish within the experimental results in sec. 5.6.3 between a direct temperature influence on viscosity and the temperature influence via dissolution on viscosity, the first influence is consciously disregarded in the constitutive modelling. When more precise experimental data is available, this effect can easily be taken into account within the constitutive equations.

To simplify the parameter identification, the function $\eta_0(d)$ is chosen as $h_\eta d$ in a first approach, whereat h_η is just a proportionality constant. Moreover, h_η is a priori defined as equal to 1 because other values can be allocated to the parameter g for this special structure of the constitutive equation.

In order to obtain appropriate initial values for the optimisation method, the following procedure, similar to that applied for the evolution equation for the degree of cure, has turned out to be helpful. For a constant shear rate (i.e. $10\,s^{-1}$), the parameters K_{d1}, K_{d2}, m, g and h can be determined at different temperatures by separate parameter identification routines. The value

range for the parameter h can already be estimated from the correction slope value n out of the Rabinowitsch-Weissenberg correction (cf. sec. 5.6.2.2),whereas the other parameters might be first adjusted manually. In addition, the initial condition for the progress of dissolution d_0 has to be adjusted in combination with the value of g. Aside, the restriction is imposed, that m is only allowed to take integer values. Having gathered values for K_{di} at different temperatures, initial values of A_{di} and E_{di} are calculated by fitting the Arrhenius behaviour towards the values for K_{di}. These computed values are reasonable initial values for a comprehensive optimisation routine, that takes into account experimental data across different shear rates and temperatures and for both experimental methods, cone-plate rheometry as well as capillary rheometry.
In figs. 7.7(a) to 7.7(d) the results of the parameter identification are plotted in combination with the experimental data of the cone-plate rheometer.

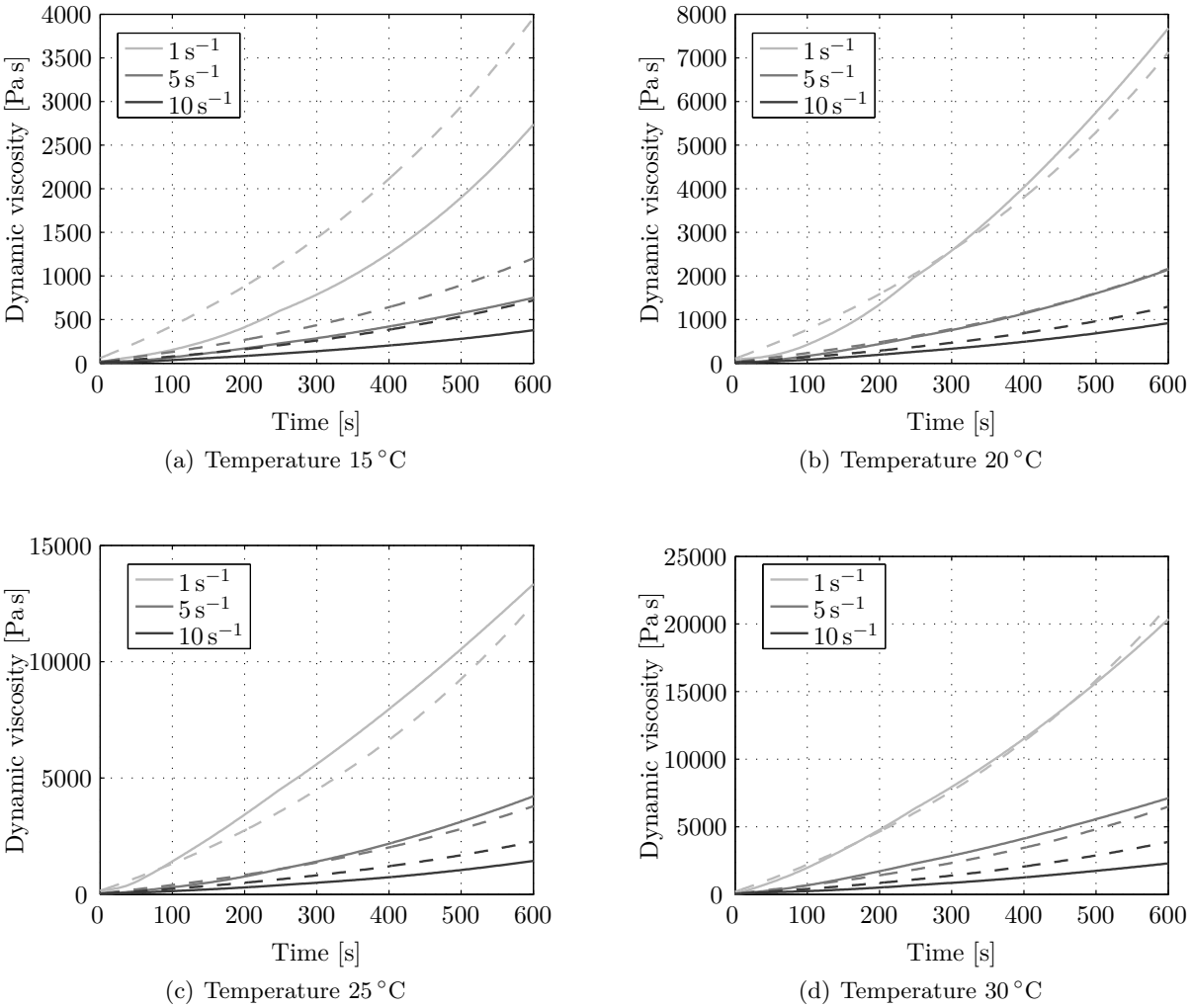

(a) Temperature 15 °C

(b) Temperature 20 °C

(c) Temperature 25 °C

(d) Temperature 30 °C

Figure 7.7.: Dynamic viscosity of acrylic bone cement during main dissolution at different temperatures; Measurement (—) and simulation (- -) with identified parameters

Basically, the model is able to describe the three major effects, governing the rheological behaviour of acrylic bone cement during dissolution. Deviations of more than 50 % can be observed

for the temperature of 15 °C, where the model predicts a higher dynamic viscosity, regardless of the shear rate. The missing direct dependency of viscosity on temperature might be more dominant here than at higher temperatures. By a more detailed mathematical model for the function $\eta_0(d)$, this difference between measurement and model can be minimised. However, deviations may also arise from the measurement as the rheological experiments are difficult to carry out (cf. sec. 5.6.3). Fig. 7.8, showing model data and experimental results at high shear rates, confirms that the model is also able to describe the course of the dynamic viscosity for shear rates beyond $10\,s^{-1}$.

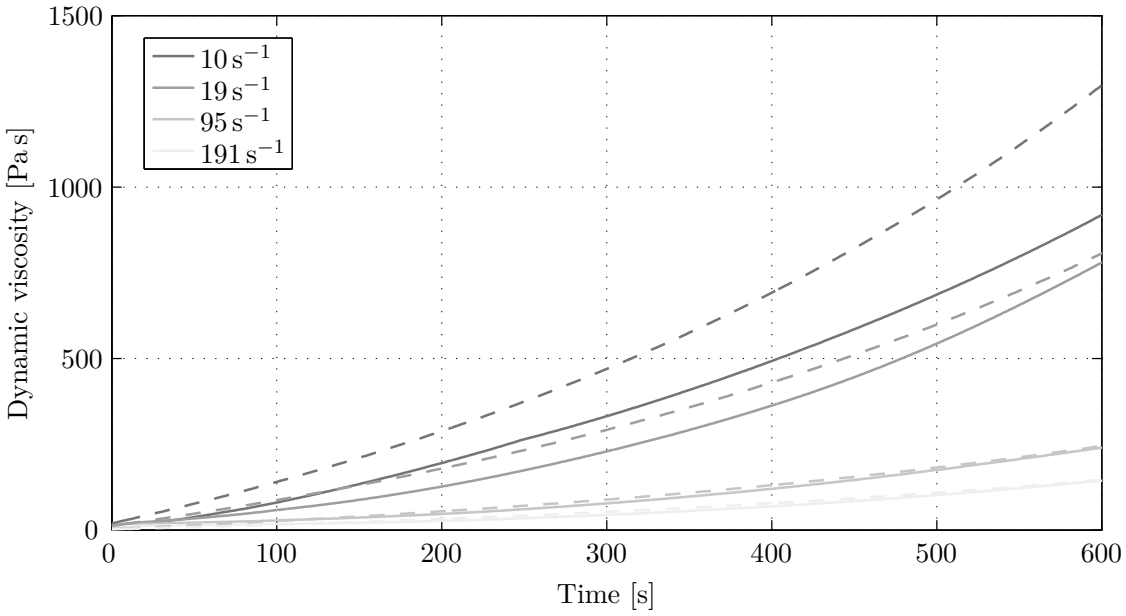

Figure 7.8.: Dynamic viscosity of acrylic bone cement during main dissolution for high shear rates at room temperature; Measurement (—) and simulation (- -) with identified parameters

The parameter values obtained by the identification procedure are listed in tab. 7.7.

Table 7.7.: Material parameters for mechanical behaviour during dissolution

A_{d1}	E_{d1}	A_{d2}	E_{d2}	m	h_η	g	h	d_{max}
s^{-1}	J/mol	s^{-1}	J/mol	-	Pa s	-	-	-
$3.0 \cdot 10^{14}$	$8.232 \cdot 10^4$	0.0023	312.6	1	1	8.996	0.2601	2000

Even if there is still some improvement possible, on the experimental as well as on the modelling side, the results at this stage are satisfactory and promising. With this kind of modelling the rheological behaviour of bone cement, the influences of the described three major effects on the procedure of vertebroplasty can be made accessible.

7.5. Mechanical behaviour during polymerisation

The mechanical behaviour during polymerisation is the last part to complete the parameter identification for the presented model in ch. 6. In detail, eq. (6.87) has to be evaluated for the specific loading of the parallel-plate rheometer experiment. Moreover, an expression for the intrinsic time has to be developed on the basis of the experimental data.
Since the parallel-plate rheometer experiment was performed with small angle amplitudes, it is admissible to linearise the governing material equations (cf. [244]). Therefore the deformation gradient is decomposed additively into a unit tensor and an incremental displacement tensor,

$$\mathbf{F} = \mathbf{1} + \mathbf{h} = \mathbf{1} + \frac{d\,\mathbf{u}}{d\mathbf{X}} \quad , \tag{7.13}$$

whereat

$$\delta = \max_{\substack{\mathbf{X}\in\mathcal{B} \\ -\infty<t<\infty}} \|\mathbf{h}\,(\mathbf{X},t)\| \ll 1 \tag{7.14}$$

holds. In addition, transferring the linearisation onto the multiplicative split of the deformation gradient yields

$$\mathbf{F}_M = \mathbf{1} + \mathbf{h}_M \quad \text{with} \quad \delta_M = \max_{\substack{\mathbf{X}\in\mathcal{B} \\ -\infty<t<\infty}} \|\mathbf{h}_M\,(\mathbf{X}_M,t)\| \ll 1 \tag{7.15}$$

$$\varphi = 1 + \varpi \quad \text{with} \quad |\varpi| \ll 1 \quad . \tag{7.16}$$

Considering the Gateaux-differential, the following expression is obtained for the deformation gradient

$$\mathbf{F} = \varphi^{1/3}\mathbf{F}_M = \mathbf{1} + \frac{1}{3}\varpi\mathbf{1} + \mathbf{h}_M \tag{7.17}$$

and it follows that

$$\mathbf{h} = \frac{1}{3}\varpi\mathbf{1} + \mathbf{h}_M \quad . \tag{7.18}$$

Moreover, the linearised mechanical strain rate tensor $\mathbf{D}_M$ can be calculated, considering the relation $\mathbf{L}_M = \dot{\mathbf{F}}_M\mathbf{F}_M^{-1} \approx \dot{\mathbf{h}}_M$ for the mechanical velocity gradient, as

$$\mathbf{D}_M \approx \dot{\mathbf{E}}_M \approx \frac{1}{2}\left(\dot{\mathbf{h}}_M + \dot{\mathbf{h}}_M^T\right) \quad . \tag{7.19}$$

For small deformations, the displacement field $\mathbf{u}$ within a parallel-plate alignment can be linearly approximated, using cylindrical coordinates (cf. fig. 5.25):

$$\mathbf{u} = \theta\,(t)\,\frac{z}{d}r\mathbf{e}_\theta + \epsilon_z z\mathbf{e}_z \quad . \tag{7.20}$$

Besides a motion in the circumferential direction, an additional motion in the direction of the rotational axis is possible by chemical shrinkage and thermal expansion, as the top plate is normal-force-controlled (cf. sec. 5.7). For calculating the linearised strain rate tensor, it is

necessary to determine the displacement gradient with respect to cylindrical coordinates:

$$\operatorname{grad}\mathbf{u} = \begin{bmatrix} \frac{\partial u_r}{\partial r} & \frac{1}{r}\frac{\partial u_r}{\partial \theta} - \frac{u_\theta}{r} & \frac{\partial u_r}{\partial z} \\ \frac{\partial u_\theta}{\partial r} & \frac{1}{r}\frac{\partial u_\theta}{\partial \theta} - \frac{u_r}{r} & \frac{\partial u_\theta}{\partial z} \\ \frac{\partial u_z}{\partial r} & \frac{1}{r}\frac{\partial u_z}{\partial \theta} & \frac{\partial u_z}{\partial z} \end{bmatrix} = \begin{bmatrix} 0 & -\theta(t)\frac{z}{d} & 0 \\ \theta(t)\frac{z}{d} & 0 & \frac{\partial u_\theta}{\partial z} \\ 0 & 0 & \varepsilon_z \end{bmatrix} \quad . \tag{7.21}$$

With eqs. (7.18) and (7.13)

$$\mathbf{h}_M = \mathbf{h} - \frac{1}{3}\varpi\mathbf{1} = \operatorname{grad}\mathbf{u} - \frac{1}{3}\varpi\mathbf{1} \tag{7.22}$$

holds and the linearised strain rate tensor can be evaluated for the parallel-plate geometry as

$$\mathbf{D}_M = \begin{bmatrix} -\frac{1}{3}\dot{\varpi} & 0 & 0 \\ 0 & -\frac{1}{3}\dot{\varpi} & \frac{1}{2}\theta'(t)\frac{r}{d} \\ 0 & \frac{1}{2}\theta'(t)\frac{r}{d} & \dot{\varepsilon}_z - \frac{1}{3}\dot{\varpi} \end{bmatrix} \quad . \tag{7.23}$$

The Cauchy stress tensor is calculated according to eq. (6.90) and (6.87), which reads as

$$\mathbf{T} = -p\mathbf{1} + \sum_{k=1}^{n}\mathbf{T}_{E,k} = -p\mathbf{1} + 2\int_{-\infty}^{z} G(z-\zeta)\mathbf{D}_M(\zeta)d\zeta \tag{7.24}$$

$$\dot{\mathbf{T}}_{E,k} + \frac{\dot{z}(t)}{\tau_k}\mathbf{T}_{E,k} = 2\rho_{\theta C}\mu_k\mathbf{D}_M \tag{7.25}$$

in the linearised form. It should be noticed that the covariant Oldroyd derivative reduces to the material time derivative in the linearised case. Hence, the Cauchy stress tensor has the following form with respect to the given strain rate tensor for the parallel-plate geometry in eq. (7.23):

$$\mathbf{T} = \begin{bmatrix} \sigma_{rr} & 0 & 0 \\ 0 & \sigma_{\phi\phi} & \sigma_{\theta z} \\ 0 & \sigma_{z\theta} & \sigma_{zz} \end{bmatrix} \qquad \text{with} \qquad \sigma_{\theta z} = \sigma_{z\theta} \quad . \tag{7.26}$$

The external loads, the rheometer torque M_z and the normal force F_z can be calculated with aid of the stress tensor and the geometrical dimensions as follows:

$$F_z = 0 = \int_0^{2\pi}\int_0^{R} r\sigma_{zz}drd\theta \tag{7.27}$$

$$M_z = \int_0^{2\pi}\int_0^{R} r^2\sigma_{\theta z}drd\theta \quad . \tag{7.28}$$

All other cutting loads, including F_z, vanish, when integrated over the specimen geometry. For the purpose of identifying the material parameters τ_k and μ_k, a relationship between them and the measured torque can be established via the stress component $\sigma_{\theta z}$. From eqs. (7.24) and (7.25), it is obvious that the stress component $\sigma_{\theta z}$ results only from the extra stress $\mathbf{T}_E$, but not from the hydrostatic pressure and thus can be calculated as

$$\sigma_{\theta z}(r) = \int_{-\infty}^{z} G(z-\zeta)\theta'(\zeta)\frac{r}{d}d\zeta = \sum_{k=1}^{n}\int_{-\infty}^{z}\mu_k\exp\left(-\frac{z-\zeta}{\tau_k}\right)\theta'(\zeta)\frac{r}{d}d\zeta \quad . \tag{7.29}$$

Inserting the result in eq. (7.28) yields

$$M_z = \sum_{k=1}^{n} \int_{-\infty}^{z} \int_{0}^{2\pi} \int_{0}^{R} \mu_k \exp\left(-\frac{z-\zeta}{\tau_k}\right) \theta'(\zeta) \frac{r^3}{d} dr d\theta d\zeta \quad , \tag{7.30}$$

and can be further evaluated as

$$M_z = \sum_{k=1}^{n} \int_{-\infty}^{z} I_p \mu_k \exp\left(-\frac{z-\zeta}{\tau_k}\right) \frac{\theta'(\zeta)}{d} d\zeta \quad \text{with} \quad I_p = \frac{R^4 \pi}{2} \quad . \tag{7.31}$$

Combining eqs. (7.31) and (7.29), the stress component $\sigma_{\theta z}$ at the plate edge can also be expressed as

$$\sigma_{\theta z}(R) = \frac{M_z}{I_p} R \quad , \tag{7.32}$$

and is in coincidence with eq. (5.23).
In the following, the change in the internal variables and boundary conditions (i.e. the degree of cure and temperature) is supposed to be negligible within one evaluation cycle and therefore, the shifting function $M(t)$ (cf. sec. 6.5.2) is assumed to be constant within this evaluation period. In case of linear viscoelasticity, the stress response can now be written as

$$\sigma_{\theta z} = \sum_{k=1}^{n} \int_{-\infty}^{t} \mu_k \exp\left(-\frac{M(t-s)}{\tau_k}\right) \theta'(s) \frac{r}{d} ds \quad . \tag{7.33}$$

Moreover, assuming the mono frequent, harmonic, angular excitation as explained in sec. 5.7 (cf. eq. (5.21)) and stationary conditions, this stress response is represented by

$$\sigma_{\theta z} = \sum_{k=1}^{n} \gamma_0 \left(\frac{\mu_k \left(\omega \frac{\tau_k}{M}\right)^2}{1 + \left(\omega \frac{\tau_k}{M}\right)^2} \sin(\omega t) + \frac{\mu_k \omega \frac{\tau_k}{M}}{1 + \left(\omega \frac{\tau_k}{M}\right)^2} \cos(\omega t) \right) \quad , \tag{7.34}$$

according to ch. 3 with

$$\gamma_0 = \frac{r \Delta\theta}{d} \quad \text{and} \quad \omega = \frac{2\pi}{T} = 2\pi f \quad , \tag{7.35}$$

whereat

$$G' = \sum_{k=1}^{n} \frac{\mu_k \left(\omega \frac{\tau_k}{M}\right)^2}{1 + \left(\omega \frac{\tau_k}{M}\right)^2} \tag{7.36}$$

and

$$G'' = \sum_{k=1}^{n} \frac{\mu_k \omega \frac{\tau_k}{M}}{1 + \left(\omega \frac{\tau_k}{M}\right)^2} \tag{7.37}$$

can be identified as storage and loss modulus, respectively.
Within the model equations for storage and loss modulus (eqs. (7.36) and (7.37)), the same parameters μ_k, τ_k and the same shift function M appear as in the constitutive stress strain relation in sec. 6.6.1. For an adaptation of the constitutive model towards the material behaviour of acrylic bone cement, the parameters have to be adjusted in a way that the above calculated

storage and loss modulus match the experimentally measured storage and loss modulus as closely as possible. Therefore, a procedure will be presented in the following, which is based on the identification strategies presented by [244] and [245].
The experimental data in sec. 5.7 displays the storage modulus to vary across almost four orders of magnitude during polymerisation, which has to be captured by the model. The basic idea behind the model is to split the range of the storage modulus into n equally spaced subranges δ_μ on a logarithmic scale according to

$$\delta_\mu = \left(\frac{\max(G')}{\min(G')} \right)^{1/n} \quad , \tag{7.38}$$

whereas n corresponds to the number of Maxwell elements. By an appropriate choice of the relaxation times τ_k and the shift function M, which will be discussed later on, it is possible that each Maxwell element is activated one by one and the course of the storage and loss modulus during polymerisation is represented by this kind of modelling. The step by step activation of the Maxwell elements yields to a cumulative stiffness up to the i^{th} Maxwell element of

$$\sum_{k=1}^{i} \mu_k = \min(G')\delta_\mu^i \quad , \tag{7.39}$$

and the stiffness parameter of the i^{th} Maxwell element can be written as

$$\mu_i = \min(G')\delta_\mu^i \left(1 - 1/\delta_\mu\right) \quad . \tag{7.40}$$

This step-by-step activation becomes clearer by considering the exemplary experimental course of the storage modulus in fig. 7.9, which is approximated by a generalised Maxwell model (cf. sec. 3.3) with 4 branches. Within the subrange $\delta_\mu^{i-1} - \delta_\mu^i$, the behaviour of the storage modulus

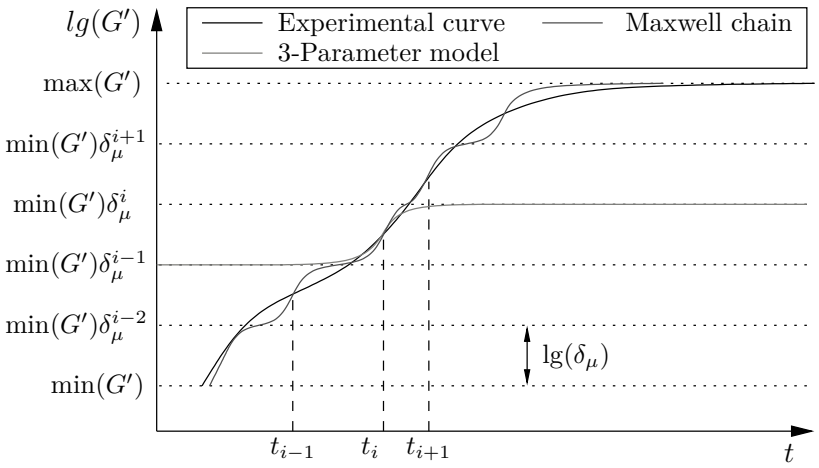

Figure 7.9.: Identification of stiffness and relaxation times by means of the three parameter model

of the generalised Maxwell model can be approximated by

$$G'_{(\delta_\mu^{i-1}-\delta_\mu^i)} = \sum_{k=1}^{i-1}\mu_k + \frac{\mu_i\left(\omega\frac{\tau_i}{M}\right)^2}{1+\left(\omega\frac{\tau_i}{M}\right)^2} = \min(G')\delta_\mu^{i-1} + \min(G')\delta_\mu^i\frac{\left(1-\delta_\mu^{-1}\right)\left(\omega\frac{\tau_i}{M}\right)^2}{1+\left(\omega\frac{\tau_i}{M}\right)^2} \quad , \tag{7.41}$$

which corresponds to a linear viscoelastic three parameter model (cf. [139]). As shown in fig. 7.9, the temporal increase of the storage modulus within the subrange δ_μ^{i-1} – δ_μ^i can be influenced by the relaxation time τ_i in combination with the shift function M. From the approved requirement that the experimental storage modulus and the storage modulus calculated by the model, must temporarily match at $(\min(G')\delta_\mu^{i-1}\min(G')\delta_\mu^i)^{\frac{1}{2}}$, the following constraint can be established:

$$G'_{exp}(t_i) = (\min(G')\delta_\mu^{i-1}\min(G')\delta_\mu^i)^{\frac{1}{2}} = \min(G')\delta_\mu^{i-1} + \min(G')\delta_\mu^{i-1}\frac{(\delta_\mu-1)\left(\omega\frac{\tau_i}{M}\right)^2}{1+\left(\omega\frac{\tau_i}{M}\right)^2} \quad . \tag{7.42}$$

Rearranging and applying the quadratic formula yields

$$\delta_\mu^{\frac{1}{2}} = \left(\omega\frac{\tau_i}{M}\right)^{-2} \quad , \tag{7.43}$$

and the relaxation time can be determined as

$$\tau_i = \frac{M}{\left(\delta_\mu^{\frac{1}{4}}\omega\right)} \quad . \tag{7.44}$$

Until now, the shift function M has been disregarded, but it plays an important role for calculating the relaxation times by eq. (7.44). As indicated in sec. 6.5.2, the shift function M influences the relaxation times τ_i in such a way that the temperature- and polymerisation-dependent viscoelastic behaviour is represented adequately. In order to eliminate temperature influences, the relaxation times are calculated at a reference temperature of 25 °C (here, 25 °C is chosen as reference temperature because no measurements at 37 °C are available and 25 °C is almost in the middle of the experimental temperature range). Since the qualitative form of the shift function has to be determined as well, the calculation of the relaxation times is carried out with the following tentative form of the shift function at the reference temperature

$$M_{ref} = \frac{1}{q^{10}} \quad . \tag{7.45}$$

Herein q is the degree of cure (cf. sec. 6.2.2), which is evaluated at the time t_i by eq. (6.4) and parameters of sec. 7.1. Now, when the relaxation times are determined at the reference temperature, the final form of the shift function can be designed and parametrised. In the case of acrylic bone cement, the following form for the shift function has led to good results:

$$M = \frac{1}{q^r 10^p} \quad , \tag{7.46}$$

whereat the functions r and p are functions of temperature:

$$r(\theta) = a_r(\theta-\theta_0)^2 + b_r(\theta-\theta_0) + c_r \tag{7.47}$$

$$p(\theta) = a_p(\theta-\theta_0) + b_p \quad . \tag{7.48}$$

Fig. 7.10 shows the course of the shift function M during polymerisation for different temperatures. The shift factor increases with increasing temperature, which leads to decreasing relaxation times (cf. eq. (7.36) and (7.37)) and hence to a more thin fluid behaviour. Moreover, for $q \to 0$ the shift factor increases as well. It should be mentioned here that the shift function M is not defined for $q = 0$. However, this has no influence on the application of the model since an initial polymerisation already takes place during the main dissolution phase (cf chs. 5 and 8).

The design of the shift function is more or less a trial and error process. For the temperature dependency, it is often advantageous to use WLF or Arrhenius approaches, however in this study, the Taylor series expansion provides better results. In order to determine the parameters of the temperature-dependent functions r and p a least-square routine is now run to fit the values for r and p separately for each temperature, but for all frequencies. Having gathered the values for r and p for each temperature, the parameters in eqs. (7.47) and (7.48) are fitted by a further least-square routine over all temperatures and frequencies. The previously gathered values from the separate temperature fits serve as starting values and delimit the parameter space for the comprehensive fitting routine.

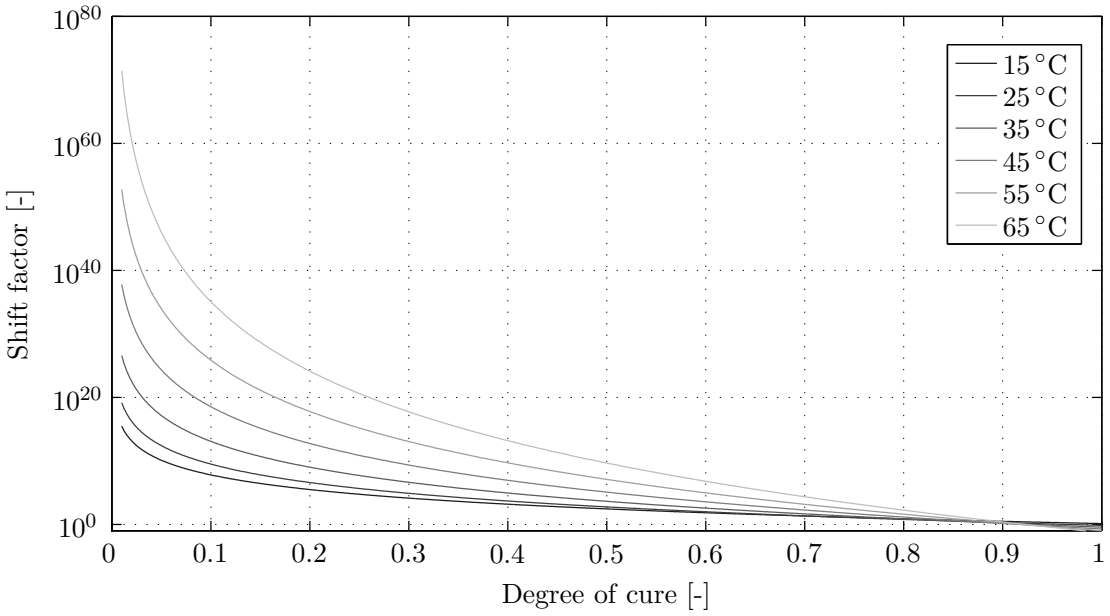

Figure 7.10.: Progress of the shift function M for different temperatures

Exemplary, this procedure is performed for $n = 15$ Maxwell elements. Tab. 7.8 shows the identified stiffness parameters and relaxation times, as well as the parameters of the temperature-dependent functions r and p. The stiffness parameters in tab. 7.8 clearly cover the range of the storage modulus of the experimental data in sec. 5.7. In contrast, the relaxation times do not exhibit a clear physical meaning as they are affected by the shift function M. Furthermore, fig. 7.11 and 7.12 show the experimental data and the numerical results of the model for different

Table 7.8.: Material parameters for mechanical behaviour during polymerisation

μ_1	μ_2	μ_3	μ_4	μ_5
Pa	Pa	Pa	Pa	Pa
$2.3706 \cdot 10^5$	$3.9486 \cdot 10^5$	$6.577 \cdot 10^5$	$1.0955 \cdot 10^6$	$1.8247 \cdot 10^6$
μ_6	μ_7	μ_8	μ_9	μ_{10}
Pa	Pa	Pa	Pa	Pa
$3.0393 \cdot 10^6$	$5.0624 \cdot 10^6$	$8.4322 \cdot 10^6$	$1.4045 \cdot 10^7$	$2.3394 \cdot 10^7$
μ_{11}	μ_{12}	μ_{13}	μ_{14}	μ_{15}
Pa	Pa	Pa	Pa	Pa
$3.8967 \cdot 10^7$	$6.4905 \cdot 10^7$	$1.0811 \cdot 10^8$	$1.8007 \cdot 10^8$	$2.9993 \cdot 10^8$
τ_1	τ_2	τ_3	τ_4	τ_5
1/s	1/s	1/s	1/s	1/s
$6.4449 \cdot 10^{15}$	$4.4695 \cdot 10^{15}$	$1.3558 \cdot 10^{15}$	$1.1444 \cdot 10^{14}$	$2.3704 \cdot 10^{12}$
τ_6	τ_7	τ_8	τ_9	τ_{10}
1/s	1/s	1/s	1/s	1/s
$3.8834 \cdot 10^{10}$	$6.1713 \cdot 10^9$	$1.4555 \cdot 10^9$	$3.8409 \cdot 10^8$	$8.6284 \cdot 10^7$
τ_{11}	τ_{12}	τ_{13}	τ_{14}	τ_{15}
1/s	1/s	1/s	1/s	1/s
$1.0445 \cdot 10^7$	$2.9863 \cdot 10^5$	641.96	2.8897	1.3966
a_r	b_r	c_r	a_p	b_p
$1/K^2$	1/K	-	1/K	-
0.009384	0.5176	14.51	0.02826	0.4961

curing temperatures and an exemplary frequency of 1 Hz. As fig. 7.11 shows, the course of the experimental storage modulus can be adequately described by the model. The temperature specific behaviour at the end of the accelerated curing process (cf. sec. 5.7) is also reproduced correctly by the model, due to the split into two temperature-dependent exponent functions r and p.

Aside, the model also depicts the principal course of the loss modulus, but less accurately than the storage modulus. For a more precise representation of the loss modulus, it has to be incorporated in the least-square-routines as well. The drawback of this incorporation is of course a less accurate representation of the storage modulus. A further increase of the number of Maxwell elements is only partially helpful. Although the oscillations in the course of the storage and loss modulus are reduced and the representation of the experimental storage modulus is improved, the absolute deviations in the loss modulus between experiment and model remain. Here, other formulations of the mechanical free energy or other concepts for viscoelasticity should be addressed, however, this is beyond the scope of this study.

Moreover, it has to be remarked that the identification process also involves the data of the first few minutes in the experiment where the mechanical behaviour is dominated by the dissolution process. Nonetheless, the identified parameters are still valid for the main polymerisation phase, however, it is important to distinguish between the dissolution and polymerisation dominated phase and to restrict the usage of the model to the polymerisation dominated phase, which is not always clearly possible, especially for high temperatures. Once this temperature-

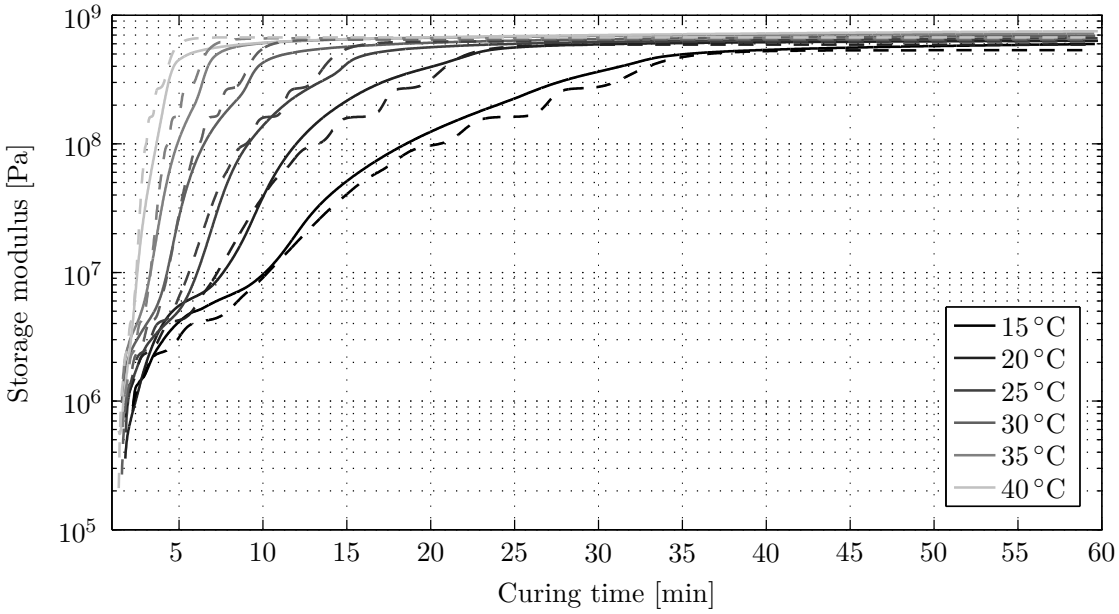

Figure 7.11.: Storage modulus of acrylic bone cement during polymerisation at 1 Hz for different curing temperatures; Measurement (—) and simulation (- -) with identified parameters

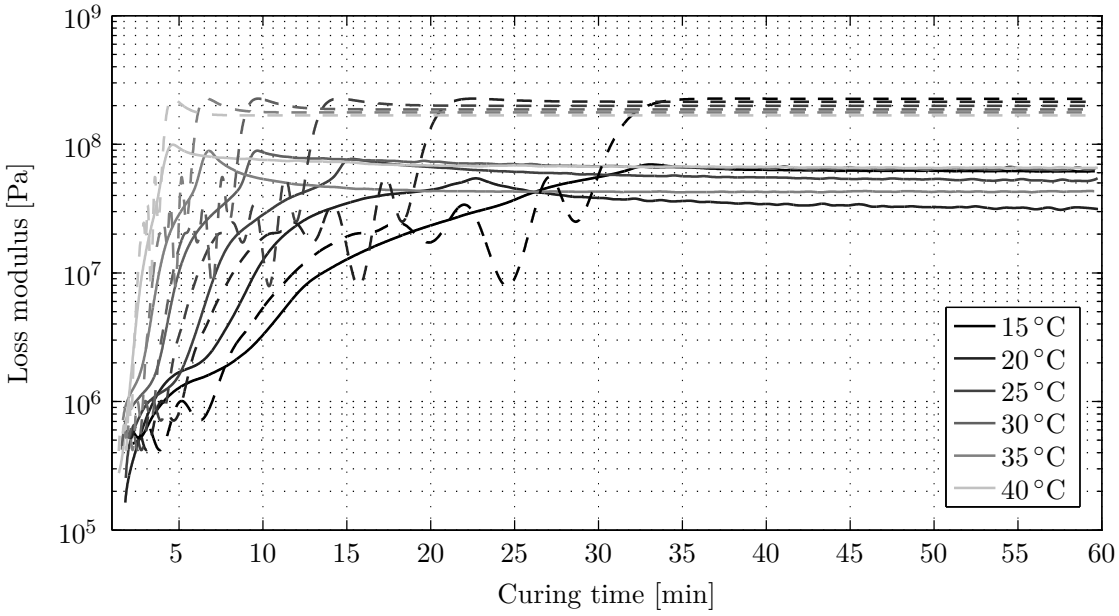

Figure 7.12.: Loss modulus of acrylic bone cement during polymerisation at 1 Hz for different curing temperatures; Measurement (—) and simulation (- -) with identified parameters

history-dependent transition point is known, i.e. the transition point between dissolution and polymerisation dominated phase, the stiffness parameters μ_k can be adjusted to the limited storage modulus range of the main polymerisation phase and a slightly improved correspondence

between experiment and model can be achieved. The collected data during the main dissolution phase can be used for an extension of the non-Newtonian fluid behaviour of sec. 7.4 to viscoelastic effects in a first approach.
At the end of this chapter, a complete set of parameters has been gained for the model presented in ch. 6. The results of the parameter identification process prove, that the structure of the model is suitable to describe the thermomechanical coupled behaviour of curing acrylic bone cement.

8. Finite volume implementation

The model presented in ch. 6 is able to describe the dissolution and polymerisation process of acrylic bone cement in detail. However, analytically, the set of differential equations can, if at all, only be solved for simple geometrical, thermodynamic and mechanical boundary conditions. The numerical implementation and solution of the specific set of equations allows for applying the presented material model to arbitrary geometries with complex boundary and initial conditions, like it is the case in vertebroplasty. Since acrylic bone cement exhibits two main subsequent processes during application, which are also considered by two different parts in the modelling strategy, it is reasonable to continue this differentiation within the implementation of the model in a simulation code and the simulation itself. The injection process of acrylic bone cement is, from an engineering point of view, a fluid mechanics problem and will therefore be treated with methods and tools of computational fluid dynamics (CFD). In contrast, the main curing process can be regarded as a solid mechanics problem and appropriate numerical techniques are applied therefore [119, 121]. As a logical consequence for using two separate simulation tools, the results of the CFD-simulation and the injection process, respectively, serve as initial conditions for the finite-element simulation of the main polymerisation process.

The following chapter will focus on the numerical implementation of the part of the material model that is valid for the main dissolution process of acrylic bone cement. The numerical implementation and simulation of the remaining part of the model, being valid for the main radical polymerisation, is performed in the partner project [119, 121].

Within this work, the CFD toolbox OpenFOAM®, which deploys the finite volume method as a discretisation-method, was chosen as a framework to implement the presented model. The open source code, an extensive range of built-in features and its capability for parallelisation etc. make this tool predestined for such applications.

Before going into details, two challenges should be mentioned in advance that have to be faced while numerically dealing with the injection of bone cement into porous vertebrae. The first one is the complex geometry of osteoporotic bones, which forms the boundaries for the fluid flow. The second one is the fact that the affected vertebra is filled with bone marrow prior to the surgery. In fact, it has to be dealt with an at least two-immiscible-fluids problem. These challenges will be addressed later on in sec. 8.3.

The following of this chapter shall give a short introduction into the finite volume method with a special focus on the volume-of-fluid concept (VoF). Furthermore, the implementation of the thermodynamic coupling, as well as the integration of the evolution equations for dissolution and polymerisation with respect to the volume-of-fluid method will be explained. The remaining

integration of the stress strain relation, i.e. the proposed viscosity model, into the existing solver structure will be illustrated thereafter and an outline of the overall solutions strategy of the governing equations will summarise the numerical implementation of the material model. An overview, how to deal with the complex geometry of a real human vertebra in the scope of the finite volume method, will conclude this chapter.

8.1. Finite volume method

Besides the finite differences and the finite element method, the finite volume method is a popular approach to solve partial differential equations and is most common for fluid mechanics problems. In general, the differential equations that have to be dealt with in fluid mechanics exhibit the following structure:

$$\underbrace{\frac{\partial\,\rho\psi}{\partial t}}_{\text{temporal change}} + \underbrace{\operatorname{div}\left(\rho\mathbf{v}\psi\right)}_{\text{convection}} = \underbrace{\operatorname{div}\left(\Gamma\operatorname{div}\psi\right)}_{\text{diffusion}} + \underbrace{S_\psi}_{\text{source}} \quad . \tag{8.1}$$

Herein, ψ represents any tensorial, vectorial or scalar quantity to be balanced, Γ is the corresponding diffusivity and S_ψ denotes the source of the quantity ψ. Eq. (8.1) is also known as standard transport equation and contains both transport phenomena, convection and diffusion [21, 98, 199]. The idea of the finite volume method is to split the solution domain into a finite number of control volumes, also named cells. Each cell is bordered by several faces, whereas two neighbouring cells are separated by exactly one face. The standard transport equation (eq. (8.1), or any other partial differential equation) is applied on each control volume, namely in an integral formulation with respect to volume and time:

$$\int_t^{t+\Delta t}\left[\int_{V_{CV}}\frac{\partial\,\rho\psi}{\partial t}dV + \int_{V_{CV}}\operatorname{div}\left(\rho\mathbf{v}\psi\right)dV\right]dt = \int_t^{t+\Delta t}\left[\int_{V_{CV}}\operatorname{div}\left(\Gamma\operatorname{div}\psi\right)dV + \int_{V_{CV}}S_\psi dV\right]dt \tag{8.2}$$

Eq. (8.2) includes in addition to the spatial discretisation also the temporal discretisation. There are different numerical techniques available to approximate the volume integrals. Where it is reasonable, Gauss's theorem is applied to convert volume integrals into surface integrals. This discretisation of integrals serves to approximate the exact solution of the differential equation (8.1) with piecewise profiles. For more information on these discretisation practises and the finite volume method in general, the interested reader is referred to Baumann et al., Ferzinger and Peric, Jasak as well as Rusche [21, 58, 98, 199]. Furthermore, the treatment of initial and boundary conditions is discussed as well in the previously mentioned literature.
The result of this temporal and spatial discretisation is a linear algebraic equation for each control volume and a system of linear algebraic equations for the entire computational domain. For solving this system of linear algebraic equations, a variety of efficient numerical algorithms exist [156] so that a solution to a relatively large system (several million equations) can be gained with reasonable computing time.

As a consequence, the obtained values for ψ, by solving the system of linear algebraic equations derived by the finite volume discretisation, do not necessarily satisfy the partial differential equation, e.g. the standard transport equation (8.1), exactly at a given point (e.g. the cell centre or face centre). However, the obtained values rather satisfy the underlying differential equation on average, i.e. the residuum is equal to zero averaged over a control volume.

8.2. Governing equations for incompressible laminar flow

The standard transport equation (8.1) is the most general form of a transport equation. Actually, fluid flows are governed by more specific transport equations, namely the Navier-Stokes equations, and include the conservation of mass (cf. sec. 2.3.1)

$$\frac{\partial \rho}{\partial t} + \operatorname{div}(\rho \mathbf{v}) = 0 \quad , \tag{8.3}$$

also called continuity equation, and the balance of momentum (cf. sec. 2.3.2)

$$\frac{\partial\, \rho \mathbf{v}}{\partial t} + \rho\, (\mathbf{v} \cdot \nabla)\, \mathbf{v} = -\operatorname{grad} p + \operatorname{div} \mathbf{S_E} + \rho \mathbf{k} \quad . \tag{8.4}$$

Herein, the Cauchy stress tensor is decomposed according to eq. (6.90) and the left hand side of eq. (8.4) represents the material time derivative of $\rho\mathbf{v}$. The Navier-Stokes equations have to be complemented at least by a constitutive equation that relates deformation and stress in order to obtain a solvable set of equations. In case of viscous fluids this constitutive equation reads as

$$\mathbf{S_E} = 2\eta \mathbf{D} \quad . \tag{8.5}$$

The viscosity itself can include further dependencies, e.g. as proposed in sec. 7.4. The first law of thermodynamics is omitted here, i.e. isothermal flow is considered first for simplicity (non-isothermal flow will be addressed in sec. 8.4.2).
For numerical simulation purposes in the scope of this thesis, the fluid flow of bone cement into the porous vertebra is supposed to be incompressible and constant in density, i.e. the density does not depend on temperature. According to fig. 5.10, the change in density from 20 °C to 37 °C is less than 2 %, and thus has a minor effect on the fluid flow during the dissolution-dominated phase of a vertebroplastic surgery. These assumptions reduce the continuity equation (8.3) to

$$\operatorname{div}(\mathbf{v}) = 0 \quad , \tag{8.6}$$

and allow for a numerically less expensive computation compared to compressible flow. However, the solution of the incompressible Navier-Stokes equations is still associated with the following issue. The momentum equation exhibits the gradient of the pressure field as part of the source term, whereat there is no additional equation for the pressure. In fact, the pressure field is given indirectly. Calculating the fluxes from the momentum equation by using the correct pressure

field will satisfy the continuity equation [21]. Furthermore, the absolute value of the pressure does not influence the flow, only the change in the absolute pressure value.
In order to overcome this issue and to guarantee a divergence free velocity field (cf. eq. (8.6)), different approaches exist (cf. [58]). The most popular method is a pressure-velocity-correction (i.e. a special algorithm to solve the Navier-Stokes equations), where a pressure corrector equation is derived from the momentum and continuity equations and dealt with in special pressure-velocity-coupling. Commonly used for steady-state solutions, this procedure was first developed by Patankar [178] and is called SIMPLE-algorithm (Semi-Implicit Method for Pressure-Linked Equations). Issa [97] extended the SIMPLE-algorithm for pressure prediction and adapted it to large time step calculations for transient problems. This algorithm is referred to as PISO-algorithm (Pressure Implicit with Splitting of Operator). For more information on pressure-velocity coupling, the interested reader is referred to Ferzinger and Peric [58], as well as to Jasak [98]. In this study the OpenFOAM® built-in algorithm PIMPLE (merged PISO-SIMPLE) is used for pressure-velocity-correction and will be addressed in more detail in sec. 8.5 .
Furthermore, the typical flow rate of bone cement during a vertebroplastic surgery is about a few millimetres per second. In combination with a relatively high viscosity, this guarantees a low Reynolds-number and the flow can be regarded as entirely laminar. Hence, no additional turbulence modelling is required.

8.3. Interface tracking for two immiscible fluids

As bone cement is forced into the porous vertebra and fills out the cavities, it displaces another fluid, bone marrow. Therefore, the numerical simulation of a vertebroplastic surgery has to consider the interaction of both fluids, bone cement and bone marrow, in the flow field. It is assumed for this study that bone cement and bone marrow are immiscible amongst each other and exhibit a sharp interface, also referred to as free surface.
Several techniques exist to numerically treat two-phase flows within the framework of finite volumes, and they can be divided into surface tracking methods, moving mesh methods and volume tracking methods [199]. In contrast to surface tracking methods and moving mesh methods, volume tracking methods also allow to handle highly curved and interacting free surfaces. Amongst volume tracking methods, the level-set approach [172, 217] and the volume-of-fluid method [84] are most popular. In this study, the volume-of-fluid method, which comes along with OpenFOAM® by default, is used to track the interface between bone cement and bone marrow. In the following the physical boundary conditions at the interface are illustrated and the volume-of-fluid method is introduced.

8.3.1. Boundary conditions at the fluid-fluid interface

The position of the free surface between bone cement and bone marrow is only known at the beginning of the injection, i.e. the start of the simulation. The movement and the deformation

of the free surface are part of the solution and have to be calculated along with the fluid flow. Referring to the assumption of immiscibility, a kinematic and a dynamic boundary condition applies to the free surface [55, 58]:

- The kinematic boundary condition states that neither of both fluids can permeate the free surface interface. In other words, the velocity normal to the free surface is the velocity of the free surface itself:

$$\mathbf{v_1} \cdot \hat{\mathbf{n}}_0 = \mathbf{v_2} \cdot \hat{\mathbf{n}}_0 \quad , \tag{8.7}$$

  where $\hat{\mathbf{n}}_0$ is the surface normal vector (cf. fig. 8.1) and $\mathbf{v}_1$ and $\mathbf{v}_2$ are the fluid velocities at the interface of fluid 1 (bone cement) and fluid 2 (bone marrow), respectively.

- The dynamic boundary condition describes the balance of forces at the free surface, where forces of pressure, friction and surface tension have to cancel out each other [30]:

$$p_1 + 2\eta_1 \left(\frac{\partial v_n}{\partial n_0}\right)_1 + \sigma\kappa = p_2 + 2\eta_1 \left(\frac{\partial v_n}{\partial n_0}\right)_2 \tag{8.8}$$

$$\eta_1 \left(\frac{\partial v_t}{\partial n_0} + \frac{\partial v_n}{\partial t_0}\right)_1 - \frac{\partial \sigma}{\partial t_0} = \eta_2 \left(\frac{\partial v_t}{\partial n_0} + \frac{\partial v_n}{\partial t_0}\right)_2 \tag{8.9}$$

$$\eta_1 \left(\frac{\partial v_s}{\partial n_0} + \frac{\partial v_n}{\partial s_0}\right)_1 - \frac{\partial \sigma}{\partial s_0} = \eta_2 \left(\frac{\partial v_s}{\partial n_0} + \frac{\partial v_n}{\partial s_0}\right)_2 \quad . \tag{8.10}$$

  Herein, v_n, v_t and v_s are the velocity components referring to the local orthogonal coordinate system, which is given by the unit vectors $\hat{\mathbf{n}}_0$, $\hat{\mathbf{t}}_0$ and $\hat{\mathbf{s}}_0$ ($\hat{\mathbf{n}}_0$ is perpendicular to the free surface (cf. fig. 8.1)).

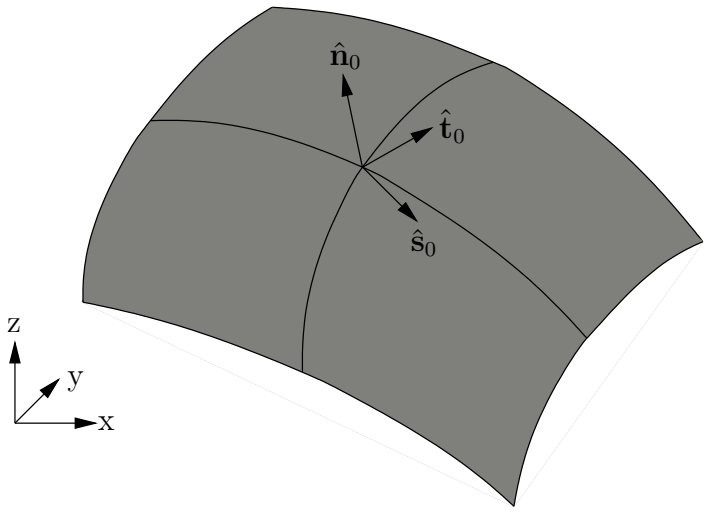

Figure 8.1.: Local coordinate system at free surface

Eq. (8.8) indicates that surface tension σ in combination with the curvature κ of the free surface leads to a force in the normal direction of the free surface. Surface tension is a result of the molecular forces cohesion and adhesion and depends on temperature and the involved fluids. The resulting force leads to a minimisation of the free surface, leading to spherical geometries of a dispersed phase. Furthermore, if a temperature gradient leads

to a gradient of the surface tension across the free surface (cf. eq. (8.9) and eq. (8.10)) an additional shear force on the free surface is acting, which induces additional fluid motion (Marangoni convection). However, for a lot of applications, the shear and normal stress at the free surface are disregarded and the surface tension is assumed to be independent of temperature. With this simplification, the dynamic boundary conditions in the tangential direction (eq. (8.9) and eq. (8.10)) vanish and in the normal direction (eq. (8.8)) it is reduced to the Young-Laplace relation:

$$\Delta p_0 = p_1 - p_2 = \sigma\kappa \quad . \tag{8.11}$$

The Young-Laplace relation (eq. (8.11)) reveals a drop in pressure Δp_0 for a curved free surface. In case of a positive curvature (convex surface) the static pressure rises across the interface and therefore the pressure in the dispersed phase is usually higher than in the surrounding fluid.

8.3.2. Volume-of-fluid method

The idea of the volume-of-fluid method, originally developed by Hirt and Nichols [84], is to introduce an additional internal variable which indicates the volume fraction of bone cement (fluid 1) contained in each control volume (CV). The internal variable, also referred to as phase fraction α_1, is defined as follows:

$$\alpha_1 = \begin{cases} 1 & \text{CV is completely filled with bone cement (fluid 1)} \\ ]0,1[, & \text{bone cement and bone marrow fill the CV in the interface region} \\ 0 & \text{CV is completely filled with bone marrow (fluid 2)} \end{cases} \tag{8.12}$$

Fig. 8.2 points out, how a continuous free surface is represented by the phase fraction on a discretised two-dimensional domain. On the basis of the phase fraction α_1, the physical properties,

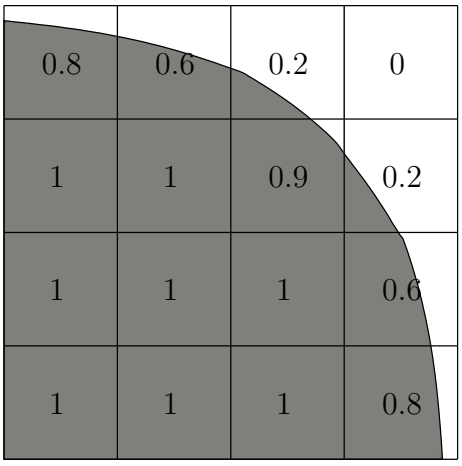

Figure 8.2.: Continuous fluid distribution and discrete assignment of the phase fraction on a rectangular grid

viscosity and density, are calculated for the entire computational domain:

$$\eta = \alpha_1\eta_1 + (1-\alpha_1)\eta_2 \tag{8.13}$$

$$\rho = \alpha_1\rho_1 + (1-\alpha_1)\rho_2 \quad . \tag{8.14}$$

Thus, the volume-of-fluid method considers the different phases by allocation of the appropriate physical properties in a common flow field. It is important to notice that the volume-of-fluid method lacks a sharp interface between the two fluids by linearly interpolating the physical properties. The free surface is rather described by a transition region.
Moreover, a supplementary transport equation is necessary to track the distribution of the phase fraction α_1. Under the constraint that the phase fraction can only be transported by convection, but cannot diffuse, this transport equation reads as follows:

$$\frac{\partial\,\alpha_1}{\partial t} + \operatorname{div}(\alpha_1\mathbf{v}) = 0 \quad . \tag{8.15}$$

Conventional discretisation schemes for the convective term in eq. (8.15) cannot guarantee boundedness of the phase fraction α_1 and usually exhibit numerical diffusion, i.e. the interface region spreads with proceeding simulation time. To overcome this issue, OpenFOAM® uses an artificial compression term in the transport equation for the phase fraction α_1 [199]

$$\frac{\partial\,\alpha_1}{\partial t} + \operatorname{div}(\alpha_1\mathbf{v}) + \operatorname{div}(\alpha_1\mathbf{v}_r\,(1-\alpha_1)) = 0 \quad , \tag{8.16}$$

where $\mathbf{v}_r$ is an appropriate velocity field, which is only active in the interface region, to compress the interface. This artificial velocity field is defined by an artificial flux field $\phi_{r,f}$, evaluated at the control volume faces (indicated by the subscript f):

$$\phi_{r,f} = \mathbf{v}_{r,f}\cdot\mathbf{s}_f = \min\left[C_\alpha\frac{|\phi_f|}{|\mathbf{s}_f|}, \max\left(\frac{|\phi_f|}{|\mathbf{s}_f|}\right)\right](\hat{\mathbf{n}}_{0,f}\cdot\mathbf{s}_f) \quad . \tag{8.17}$$

Herein, $\mathbf{s}_f$ is the cell face area vector (the product of the unit normal outward vector and the surface area of the face) and $\mathbf{v}_{r,f}$ is the artificial velocity field, interpolated at the cell faces. C_α is a user-defined factor, for adjusting the compression of the interface, and is recommended to be set around unity. Greater values for C_α yield an enhanced compression of the interface, but also increase the disturbance of the regular flow field. The face centred interface normal vector $\hat{\mathbf{n}}_{0,f}$ also has to be evaluated at the cell faces and it is common practise to calculate it from the phase fraction α_1:

$$\hat{\mathbf{n}}_{0,f} = \frac{\operatorname{grad}_f(\alpha_1)}{|\operatorname{grad}_f(\alpha_1)| + \delta} \quad , \tag{8.18}$$

where $\delta = 10^{-8}(V_{CV})^{-1/3}$ (V_{CV} is the volume of the corresponding control volumes) for numerical stabilisation purposes outside the transition region ($|\operatorname{grad}_f(\alpha_1)| \to 0$).
To further guarantee the boundedness of the phase fraction α_1, a special solution strategy is applied (referred to as MULES - Multi-dimensional Universal Limiter with Explicit Solution in OpenFOAM®). More information on the topic of the solution of the transport equation for the phase fraction can be found in the work of Rusche [199], Deshpande [47] and in the

OpenFOAM® UserGuide [171].

8.3.3. Continuum-surface-force approach

In the previous subsection, the phase fraction α_1 and its transportation in the flow field have been introduced for the tracking of free surfaces by the volume-of-fluid method. As the interface is rather smeared than a sharp surface, and hence its exact position is unknown, the implementation of the boundary condition, discussed in sec. 8.3.1, has to be performed in a special way, as proposed by Brackbill et al. [30]. This method is known as continuum-surface-force approach (CSF), and describes the implementation of the Young-Laplace relation (eq. (8.11)) for volume-tracking methods, such as the volume-of-fluid method. It should be noticed that the continuum-surface approach disregards additional shear and normal stresses at the interface and possible dependences of surface tension (e.g. on temperature) are neglected.
Since the exact position of the interface between both fluids is unknown, the CSF approach interprets the surface tension force, which acts only at the interface area, as a volume distributed force acting within the transition region. This concept can be expressed as

$$\lim_{h\to 0} \int_V \mathbf{f}_{os}(\mathbf{x}) dV = \int_A \mathbf{b}_{os}(\mathbf{x}_{os}) dA \quad , \tag{8.19}$$

where

$$\mathbf{f}_{os}(\mathbf{x}) = 0 \quad \text{for} \quad h \geq |\hat{\mathbf{n}}_0 \cdot (\mathbf{x} - \mathbf{x}_{os})| \quad . \tag{8.20}$$

Herein, the vector $\mathbf{x}_{os}$ describes the exact position of the free surface and $\mathbf{x}$ indicates an arbitrary point in the computational domain. The expansion of the transitional region is given by h and $\mathbf{b}_{os}$ denotes the surface tension force per unit area, acting normal to the interface and depending on the curvature and surface tension:

$$\mathbf{b}_{os}(\mathbf{x}_{os}) = \sigma\kappa(\mathbf{x}_{os})\hat{\mathbf{n}}_0(\mathbf{x}_{os}) \quad . \tag{8.21}$$

Brackbill et al. [30] derived an explicit formulation for the volume distributed surface tension force $\mathbf{f}_{os}$,

$$\mathbf{f}_{os}(\mathbf{x}) = \sigma\kappa(\mathbf{x}) \operatorname{grad}(\alpha_1(\mathbf{x})) \quad , \tag{8.22}$$

which is in accordance with eq. (8.19) and (8.20). The term $\nabla\alpha_1(\mathbf{x})$ effects the distributed surface tension force to be non-zero only inside the transition region. Additionally, eq. (8.22) needs the evaluation of the curvature of the interface. Using the result in eq. (8.18), the curvature at the cell face is given by

$$\kappa_f = -\operatorname{div}(\hat{\mathbf{n}}_{0,f}) \quad . \tag{8.23}$$

Since OpenFOAM® needs the volume distributed surface tension force being calculated at the cell faces, eq. (8.22) can be rewritten as

$$\mathbf{f}_{os,f} = \sigma \kappa_f \mathrm{grad}_f(\alpha_1(\mathbf{x})) \quad . \tag{8.24}$$

The volume-of-fluid method integrates the volume distributed surface tension force on the right hand side of the momentum equation (8.4) as a part of the volume distributed forces $\mathbf{k}$.

8.4. Adaption and expansion of existing code

So far, the presented methodology comes along with OpenFOAM®, coded in the solver *interFoam*. Due to its open source code, OpenFOAM® offers its users to expand the code and solution strategies. In contrast to many commercial programs, OpenFOAM® does not provide an interface to implement material specific models, but the user has to modify the existing code extracts or rewrite new code and include it into the existing toolbox itself.
Comparing the existing *interFoam* solver with the presented model for the dissolution process in ch. 6 and 7, there is a need for implementing

- the evolution equation for dissolution
- the evolution equation for polymerisation
- the first law of thermodynamics
- the developed viscosity model for dissolution of acrylic bone cement

into the *interFoam* solver framework. The following subsections will briefly discuss the implementation of the equations and will further address the occurring limitations and trade-offs that have to be made.

8.4.1. Evolution equations for dissolution and polymerisation

Both evolution equations, for dissolution and polymerisation, can be interpreted as additional transport equations. Due to the fluid nature of bone cement during dissolution, the progress of dissolution and polymerisation can be transported by convection. Transport by diffusion for both phenomena is assumed to be not existent or at least plays a minor role. Hence, both evolution eqs. (6.1) and (6.3) have to be supplemented by an additional convection term. It should be noted that the convection term has to be treated explicitly within the solution procedure, since the flow field is readily known. Another issue occurs with the volume-of-fluid method, as transport equations are not solved for each phase separately, but holisticly for the entire computational domain. Since the dissolution and polymerisation processes are only valid in the bone cement phase, both transport equations have to be prevented from evolution in the bone marrow phase. This is achieved by multiplying the source term on the right hand side of

eqs. (6.1) and (6.3) with the phase fraction α_1. In the transitional region the multiplication with the phase fraction leads to the correct progress of dissolution and polymerisation averaged over the control volume.
Taking this into account, the evolution equations for dissolution and polymerisation (6.1) and (6.3) can be rewritten in the sense of a finite volume application as

$$\frac{\partial(\rho d)}{\partial t} + \operatorname{div}(\rho \mathbf{v} d) = \begin{cases} \rho\alpha_1 \left(K_{d1} + K_{d2} d^m\right), & \text{if } d < d_{max} \\ 0, & \text{if } d \geq d_{max} \end{cases} \tag{8.25}$$

and

$$\frac{\partial(\rho q)}{\partial t} + \operatorname{div}(\rho \mathbf{v} q) = \rho\alpha_1 (K_{q1} + K_{q2} q^k)(1-q)^l f_D(q) \qquad . \tag{8.26}$$

Regarding the diffusion factor $f_D(q)$, it is admissible to omit it in the finite volume implementation, since it does not perceptibly influence the behaviour of the evolution equation for a degree of cure q smaller than 0.5.
The non-linearities appearing in the source term on the right hand side of eqs. (8.25) and (8.26) cannot be treated by OpenFOAM® implicitly right away. The common way to handle these non-linearities is to derive a linearised form of the source term using Picard's method [178] and to account for the non-linearity in an iterative way. Therefore, the source term S has to be split up in the following manner:

$$S = S_c + S_p z \qquad \text{with} \qquad S_c = S(z^*) - \left.\frac{\partial S}{\partial z}\right|_{z^*} z^* \qquad \text{and} \qquad S_p = \left.\frac{\partial S}{\partial z}\right|_{z^*} \tag{8.27}$$

where z^* is the value of the independent variable z at the previous iteration and $\left.\frac{\partial S}{\partial z}\right|_{z^*}$ is the gradient of S evaluated at z^*. This procedure corresponds to a Taylor series expansion of S about z^*.
The discretisation procedure for each of the terms in eqs. (8.25) and (8.26) can be seen in tab. 8.1

Table 8.1.: Discretisation schemes for dissolution and polymerisation transport

	dissolution	polymerisation
temporal derivative	Euler	Euler
convective term	Total Variational Diminishing Van Leer limiter	Total Variational Diminishing Van Leer limiter $[0, 1]$
source term	implicit/explicit	implicit/explicit

8.4.2. Integration of the first law of thermodynamics

Similar to processes of dissolution and polymerisation, the first law of thermodynamics ((6.116) can also be interpreted as a transport equation and has to be equipped with a convection term

for finite volume purposes:

$$\frac{\partial\, \rho c_p \theta}{\partial t} + \operatorname{div}\left(\rho c_p \theta \mathbf{v}\right) = -\operatorname{div}(\lambda \operatorname{grad}\theta) + \rho\left(\mathbf{T}\cdot\mathbf{D}\right) - \frac{\partial\, \rho h}{\partial q}\dot{q} \quad . \tag{8.28}$$

Herein, c_p denotes the specific heat capacity and λ is the thermal conductivity. $\mathbf{T}\cdot\mathbf{D}$ is the viscous dissipation, given explicitly. Furthermore, the differentiation between thermochemical and mechanical quantities is obsolete here , because of the restriction of incompressible flow (cf. sec. 8.2). Hence, the overall deformation is equal to the mechanical deformation for the finite volume simulation. The second source term $\frac{\partial\, \rho h}{\partial q}\dot{q}$ specifies the heat released by polymerisation and is treated according to eq. (8.27). The last term in eq. (6.116) vanishes due to the constraint of incompressibility ($\frac{\partial \varphi}{\partial \theta} = \frac{\partial \varphi}{\partial q} = 0$). A listing of the discretisation schemes of all terms of eq. (8.28) is provided in tab. 8.2

Table 8.2.: Discretisation schemes for first law of thermodynamics

temporal derivative	Euler
convective term	Total Variational Diminishing Van Leer limiter
source term (heat release due to polymerisation)	implicit/explicit
source term (viscous dissipation)	explicit

8.4.3. Implementation of viscosity model

OpenFOAM® offers separate libraries for modelling different physical phenomena, i.e. there exist separate libraries for e.g. combustion modelling, transport modelling etc. This offers the possibility to use models in combination with different solvers. For example, the Carreau viscosity model can be used in the *interFoam* solver for one of the two fluids, as well as in the *nonNewtonianIcoFoam* solver. Thus the model development is independent of the solver development.

The viscosity model library of OpenFOAM® already contains the most standard non-Newtonian viscosity models, such as the Power-Law or the Herschel-Bulkley model. Based on these built-in viscosity models, a newly derived class of the base class *viscosityModel* can be written, adopted to the needs of eq. (7.12). This structure offers to select the appropriate viscosity model at run time. In contrast to the standard viscosity models, the dissolution field has to be provided to the new derived library member. The viscosity field itself is directly calculated before solving the momentum equation within the PIMPLE-loop, using the actual strain rate field. In contrast to eq. (7.12), OpenFOAM® expects the kinematic viscosity ν instead of the dynamic viscosity η. Due to the constraint of incompressibility the relationship can easily be established by $\nu = \rho\eta$.

8.5. Sequence of solution

Since the governing equations, the transport equation for dissolution and polymerisation, the first law of thermodynamics, the balance of linear momentum and the constraint of a divergence free velocity field are at least weekly coupled amongst each other, a decoupled solution of these equations is not admissible. However, a simultaneous solution of these governing equations is not constructive in terms of memory requirements and computing operations. Instead, OpenFOAM® offers a segregated approach within the PIMPLE-loop (cf. sec. 8.2). In order to outline the solution strategy within the PIMPLE-loop, the derivation of the necessary equations for the pressure-velocity-coupling is explained before. Starting from the balance of linear momentum in a rearranged order

$$\frac{\partial\,\rho\mathbf{v}}{\partial t} + \operatorname{div}(\rho\mathbf{v}\mathbf{v}) - \operatorname{div}\mathbf{S_E} = -\operatorname{grad} p + \rho\mathbf{k} \qquad , \tag{8.29}$$

the volume forces $\rho\mathbf{k}$ can now be split up into a surface tension force $\mathbf{f}_{os} = \sigma\kappa\mathrm{grad}(\alpha_1)$, according to the continuum surface approach (cf. sec. 8.3.3), and a force due to gravity acceleration $\rho\mathbf{g}$. Moreover, a modified pressure $p^* = p - \rho\mathbf{g}\cdot\mathbf{x}$ is introduced to simplify the handling of pressure boundary conditions [199]. For the pressure gradient,

$$\operatorname{grad} p^* = \operatorname{grad} p - \operatorname{grad}(\rho\mathbf{g}\cdot\mathbf{x}) = \operatorname{grad} p - \rho\mathbf{g} - (\mathbf{g}\cdot\mathbf{x})\operatorname{grad}\rho \qquad , \tag{8.30}$$

is valid. The right hand side of eq. (8.29) can be further written in a discretised form

$$\mathcal{A} : \left[\left[\frac{\partial\,\rho\mathbf{v}}{\partial t}\right]\right] + [[\operatorname{div}(\rho\mathbf{v}\mathbf{v})]] = [[\operatorname{div}(\eta\operatorname{grad}\mathbf{v})]] + \operatorname{grad}\mathbf{v}\operatorname{grad}\eta \tag{8.31}$$

whereat the operator [[...]] indicates an appropriate discretisation scheme. Furthermore, the relation

$$\operatorname{div}\mathbf{S_E} = \operatorname{div}(\eta\operatorname{grad}\mathbf{v}) + \operatorname{grad}\mathbf{v}\operatorname{grad}\eta \tag{8.32}$$

under the constraint of a divergence free velocity field is used in eq. (8.31). The set of linear equations, marked by the operator $\mathcal{A}$ can be written as

$$\mathcal{A} : [\mathbf{A}][\mathbf{v}] = [\mathbf{r}] \qquad . \tag{8.33}$$

Herein $[\mathbf{A}]$ represents the coefficient matrix and $[\mathbf{r}]$ is the vector containing sources and boundary conditions. A decomposition of the coefficient matrix $[\mathbf{A}]$ into a diagonal matrix $[\mathbf{D}]$ and an off-diagonal matrix $[\mathbf{N}]$ yields the operators

$$\mathcal{A}_D := [\mathbf{D}] \tag{8.34}$$

$$\mathcal{A}_H := [\mathbf{r}] - [\mathbf{N}][\mathbf{v}] \qquad . \tag{8.35}$$

Using these operators, the balance of linear momentum can be written in a semidiscretised formulation

$$\mathcal{A}_D\mathbf{v} = \mathcal{A}_H - \operatorname{grad} p^* - (\mathbf{g}\cdot\mathbf{x})\operatorname{grad}\rho + \mathbf{f}_{os} \qquad . \tag{8.36}$$

Solving eq. (8.36) for the velocity field $\mathbf{v}$, a momentum corrector equation is obtained:

$$\mathbf{v} = \frac{\mathcal{A}_H}{\mathcal{A}_D} + \frac{1}{\mathcal{A}_D}(-\operatorname{grad} p^* - (\mathbf{g}\cdot\mathbf{x})\operatorname{grad}\rho + \mathbf{f}_{os}) \qquad . \tag{8.37}$$

The face flux is calculated from the cell face velocities $\mathbf{v}_f$ and the cell face area vector $\mathbf{s}_f$ according to

$$\begin{aligned} \phi &= \mathbf{v}_f \cdot \mathbf{s}_f & (8.38)\\ &= \left(\frac{\mathcal{A}_H}{\mathcal{A}_D}\right)_f \cdot \mathbf{s}_f + \left(\frac{1}{\mathcal{A}_D}\right)_f (-\operatorname{grad}_f p^* - (\mathbf{g}\cdot\mathbf{x})_f \operatorname{grad}_f \rho + \mathbf{f}_{os,f}) \cdot \mathbf{s}_f \qquad . & (8.39) \end{aligned}$$

Herein, the subscript f denotes that the corresponding quantities are evaluated at the cell faces. The cell face area vector $\mathbf{s}_f$ is perpendicular to the cell face, points outward and its magnitude represents the cell face area. Neglecting the pressure gradient in eq. (8.39), a flux predictor can be written as

$$\begin{aligned} \tilde{\phi} &= \left(\frac{\mathcal{A}_H}{\mathcal{A}_D}\right)_f \cdot \mathbf{s}_f + \left(\frac{1}{\mathcal{A}_D}\right)_f (-(\mathbf{g}\cdot\mathbf{x})_f \operatorname{grad}_f \rho + \mathbf{f}_{os,f}) \cdot \mathbf{s}_f & (8.40)\\ \phi &= \tilde{\phi} - \left(\frac{1}{\mathcal{A}_D}\right)_f (\operatorname{grad}_f p^*) \cdot \mathbf{s}_f \qquad . & (8.41) \end{aligned}$$

Applying mass continuity (eq. (8.6)) to eq. (8.41) yields a pressure equation

$$\operatorname{div}\left(\left(\frac{1}{\mathcal{A}_D}\right)_f \operatorname{grad}_f p^*\right) = \operatorname{div}\left(\tilde{\phi}\right) \qquad , \tag{8.42}$$

which provides a first estimate of the new pressure field.
So far, all necessary equations for the pressure velocity coupling have been introduced so that the solution procedure within one time step can be outlined in the following. Steps in the solution procedure, which do not deviate from OpenFOAM®'s *interFoam* solver, are not specifically explained, as this would go beyond the scope of this thesis. The interested reader is referred to Rusche [199] and the OpenFOAM® official documentation [61].

1. Adjusting step size Δt for the subsequent time step according to the maximum Courant number and the needs of the phase fraction field α_1
2. Solving the transport equation for the phase fraction α_1 (eq. (8.16)) and subsequent smoothing of the phase fraction field and calculation of the curvature κ (eq. (8.23)
3. PIMPLE-loop
   a) Solution of the balance of linear momentum (eq. (8.29)) in combination with eq. (8.30)), whereas the pressure gradient is calculated using the initial/old pressure field (momentum predictor). A first approximation of the new velocity field is obtained.
   b) PISO-loop
      i. Prediction of the face fluxes based on eq. (8.40). The operator $\mathcal{A}_H$ is assembled, using the velocity field obtained in the momentum predictor step.

ii. Solving for the new pressure field by means of eq. (8.42)

iii. Flux correction, using eq. (8.41)

iv. Explicit reconstruction of the velocity field from face flux field

c) Solution of the transport equation for dissolution (eq. (8.25))

d) Solution of the transport equation for polymerisation (eq. (8.26))

e) Solving the first law of thermodynamics (eq. (8.28))

The number of iteration steps within the PIMPLE-loop can be controlled by the user and establishes a more or less strong coupling between the balance of momentum and the other transport equations. The PISO-loop ensures the pressure-velocity-coupling and is repeated until a predetermined tolerance is reached.

8.6. Computational domain and meshing

The outlined framework above makes it necessary to split the entire computational domain in a number of finite volumes without gaps and overlapping. However, the flow of bone cement through porous vertebral bone is, from a geometric point of view, delicate and specific for each patient. Two problems arise with this meshing task. Firstly, the computational domain has to be identified, which means the cavities, filled with bone marrow, have to be distinguished from the trabecular structure. Secondly, the identified computational domain, i.e. the cavities, have to be split up in a beneficial mesh of finite volumes. To accurately cover the geometrical boundaries, a digital, high-resolution geometrical model of the porous vertebra is necessary. At the moment, such a high resolution can only be generated by a μCT-scan, which, unfortunately, is not applicable to living human tissue. These circumstances are currently limiting the methodology to case studies on non-living tissue.
Although not within the scope of this thesis, the procedure for obtaining high-resolution geometrical models of human vertebra is briefly outlined next. For further information, the interested reader is referred to Landgraf et al. [121]. The basis for this procedure is the established digital output of μCT greyscale scans, the DICOM file format. Using the software package AMIRA® [1], the μCT-scan data is imported, smoothed and grey scale values are analysed. Subsequently, the trabecular structure is segmented by 3D-region growing and 3D-reconstructed by a marching-cube-like algorithm. To further reduce the complexity of the obtained model, an iterative process of smoothing, simplifying, converting to a labelled image stack and reconstructing again is applied. The result of this process is a smooth model with an acceptable level of accuracy without any intersections and non-manifold contacts. In a final step, the obtained model of the trabecular structure is exported in the stereolithography file format (STL), which is the common file format to work with in meshing tools. This file format describes the trabecular bone structure

[1] VSG - Visualization Sciences Group, Berlin, Germany, http://www.amira.com/

as a closed triangulated surface.
On the basis of the stereolithography file format (STL), OpenFOAM® offers a fully automated meshing utility, called *snappyHexMesh*, which is able to create a hexahedral dominant mesh, according to the user's specifications. For this purpose, the first step is to a create a hexahedral base mesh, which includes a part or the complete trabecular structure from a geometrical point of view. The bounding geometry of this base mesh defines also the outer border of the computational domain. The algorithm of *snappyHexMesh* then refines the base mesh in these regions, where cells of the base mesh are intersected by the surface of the trabecular structure, specified by the provided STL-geometry. Following, cells inside the trabecular structure, i.e. the geometrical space which is filled with bone material, are removed. The subsequent stage of the algorithm snaps adjacent or intersected cells to the surface. The resulting mesh includes only the cavity structure within the geometrical region, that was defined by the base mesh. The user is able to define different boundary regions, where different boundary conditions can be applied. Furthermore, the number of cells and the quality of the mesh can be influenced by a control dictionary, a file where the user can control the properties of the meshing procedure and the mesh itself. For more information, the interested reader is referred to the OpenFOAM® official documentation [61].
Having illustrated the meshing process and the relevant components of the finite volume method for implementing the material model for acrylic bone cement during the phase of dissolution in the preceding sections, this framework is now able to calculate the injection process of a vertebroplastic surgery.

9. Computational results

In this chapter, the computational possibilities and results, obtained with the aid of the computational framework introduced in the previous chapter, will be shown and discussed. Therefore, three different geometrical initial and boundary value problems will be considered. The first one is a simple two-dimensional channel flow to show the characteristics of the flow and to give an overview of the different fields, i.e. velocity, pressure, temperature, dissolution and degree of cure. The second case is a cubic extract of a real human cancellous bone, which is virtually penetrated by bone cement. Finally, the last case study is an artificial cancellous bone structure, which is also virtually penetrated by bone cement. However, this structure was also penetrated by bone cement in an experiment after it had been scanned by μCT. Therewith, a comparison between experiment and numerical simulation is possible.

9.1. Flow between parallel plates

The first computational example is a two-dimensional channel flow between two parallel plates, being infinitely perpendicular to the flow direction. The space between the two plates, which is the computational domain, measures 3 mm in height and 6 mm in length (cf. fig. 9.1). Using an equidistant distribution of points in height and length of 0.1 mm results in a total number of 1800 quadratic cells.

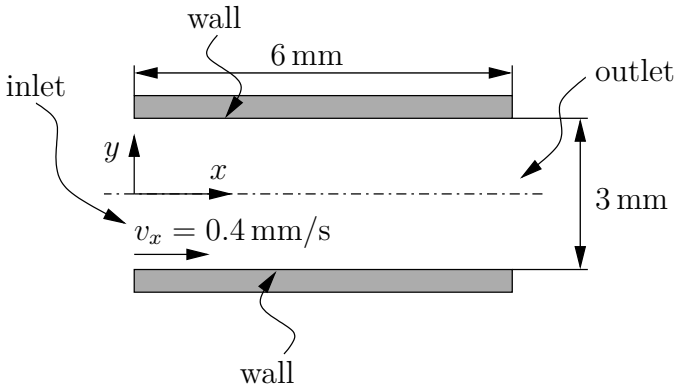

Figure 9.1.: Overview of flow between parallel plates

A certain part of the space between the two parallel plates is initially filled with bone cement,

namely 1 mm from the inlet along the x-direction, to avoid instability at the startup due to a sudden discontinuity in the phase fraction at the inlet. The remaining space in the computational domain is initially covered by bone marrow. Further initial conditions are summarised in tab. 9.1.

Table 9.1.: Flow between parallel plates: Initial conditions

	bone cement	bone marrow
pressure	1 bar	1 bar
velocity	0.4 mm/s	0 mm/s
phase fraction	1	0
temperature	20 °C	37 °C
dissolution	156.7	0
degree of cure	0.02	0

To meet the environmental conditions inside a human body, the pressure field is preset uniformly to 1 bar, as well as the temperature of the bone marrow is initially at 37 °C. For bone cement, it is assumed that the simulation starts 3 minutes after mixing, so that dissolution and polymerisation have already reached the values given in tab. 9.1 as initial condition. Dissolution and polymerisation are not valid in the bone marrow phase and therefore are preset to zero. According to the boundary conditions outlined in tab. 9.2 the flow is expected from the inlet, where bone cement enters with a velocity of $v_x = 0.4\,\mathrm{mm/s}$, to force the remaining bone marrow through the outlet. Within this study, a no-slip condition as a first approach is assumed at the

Table 9.2.: Flow between parallel plates: Boundary conditions

	inlet	outlet	walls
pressure	zero gradient	fixed: 1 bar	zero gradient
velocity	fixed: 0.4 mm/s	zero gradient	fixed: 0 mm/s
phase fraction	fixed: 1	zero gradient	zero gradient
temperature	fixed: 20 °C	zero gradient	fixed: 37 °C
dissolution	fixed: 156.7	zero gradient	zero gradient
degree of cure	fixed: 0.02	zero gradient	zero gradient

wall. However, for high viscous fluids like bone cement, there might also occur slippage at the wall, which makes the boundary conditions more complicated. It is certainly worth investigating this phenomenon more closely, but this is beyond the scope of this study. Moreover, the material properties for the bone marrow phase are given in tab. 9.3. Here, bone marrow is supposed to behave like a Newtonian fluid with constant density, thermal conductivity and heat capacity, whereat the values were taken from literature [73, 78]. Due to the constraint of incompressibility, the density is constant for bone cement and has a value of $1.48\,\mathrm{g/cm^3}$ (density of uncured bone cement at 30 °C). The surface tension between bone cement and bone marrow was estimated as 0.03 N/m in a first approach. Further analysis is necessary here, also including the contact angle between the fluid-fluid interface at the walls. However, this is not captured in this thesis.

Table 9.3.: Material properties of bone cement and bone marrow regarding two phase flow

	bone cement	bone marrow
kinematic viscosity	see sec. 7.4	$4 \cdot 10^{-4}\,\mathrm{m^2/s}$
density	$1.48\,\mathrm{g/cm^3}$	$1.06\,\mathrm{g/cm^3}$
specific heat capacity	see sec. 7.2	$2.67\,\mathrm{kJ/(kgK)}$
thermal conductivity	see sec. 7.2	$0.28\,\mathrm{W/(mK)}$
surface tension		$0.03\,\mathrm{N/m}$

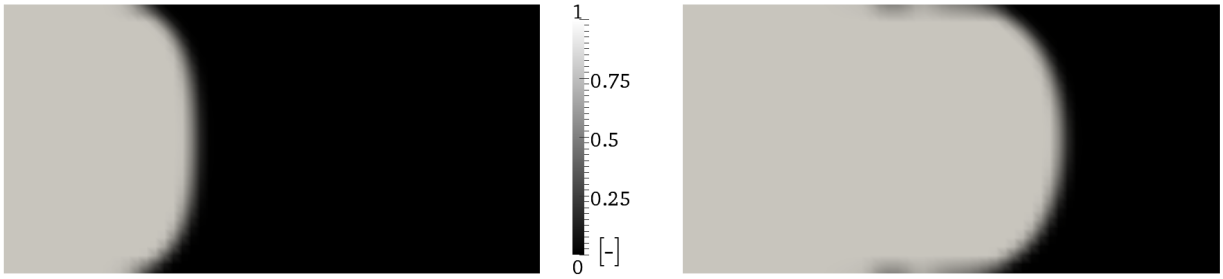

(a) Phase fraction α_1 at 2.5 s

(b) Phase fraction α_1 at 7.5 s

Fig. 9.2 illustrates the most important physical quantities, governing the two-phase flow of bone cement and bone marrow, at 2.5 s and 7.5 s after the start of the simulation. The phase fraction α_1 is displayed in figs. 9.2(a) and 9.2(b). It is noticeable that the flow front is almost fully developed after 2.5 s. In addition, the transition area between bone cement ($\alpha_1 = 1$) and bone marrow ($\alpha_1 = 0$) is very sharp. Close to the wall, bone marrow is not completely displaced by bone cement at once, but forms a kind of boundary layer. This layer disappears with growing distance to the interface and the bone marrow is squeezed out between bone cement and the wall.

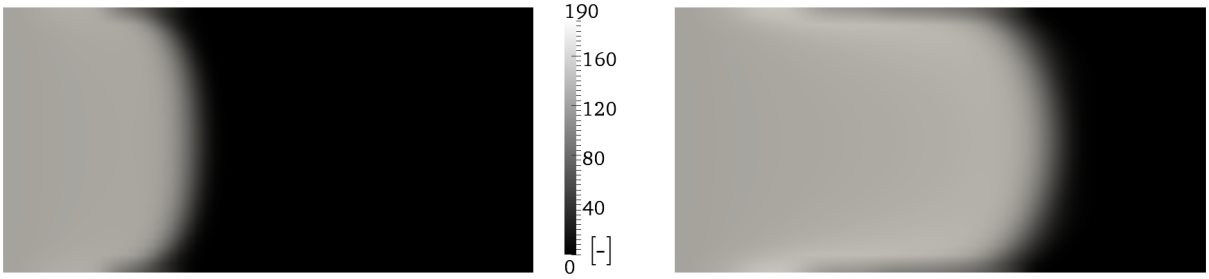

(c) Dissolution d at 2.5 s

(d) Dissolution d at 7.5 s

The fields for dissolution and polymerisation look similar to the phase fraction field (cf. figs 9.2(c) to 9.2(f)). However, the interface between bone cement and bone marrow is not as sharp as for the phase fraction α_1. For the transport equations of dissolution and polymerisation, standard discretisation and solution algorithms have to be applied, which cause more numerical diffusion in contrast to MULES for phase fraction α_1 (cf. sec. 8.3.2). Furthermore, both internal variables, dissolution and degree of cure, show the highest values close to the walls and at the flow front, as the temperature field (cf. figs. 9.2(g) and 9.2(h)) exhibits the highest values there

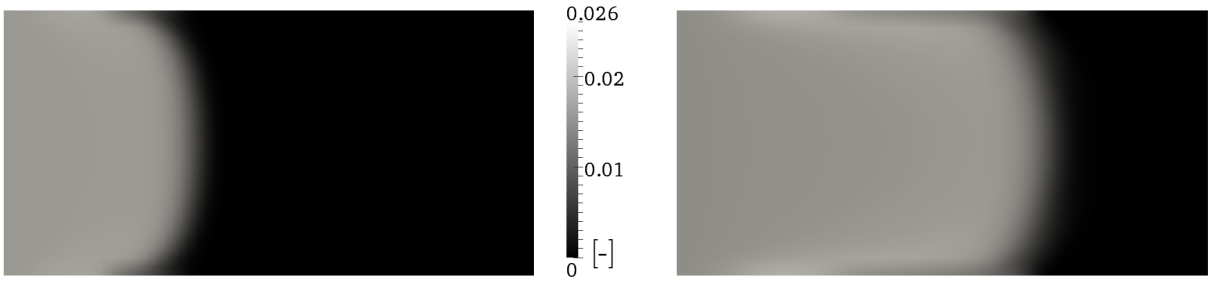

(e) Degree of cure q at 2.5 s

(f) Degree of cure q at 7.5 s

within the bone cement phase. Moreover, the bone cement at the flow front experiences the longest time period for evolution of the internal variables within the computational domain.

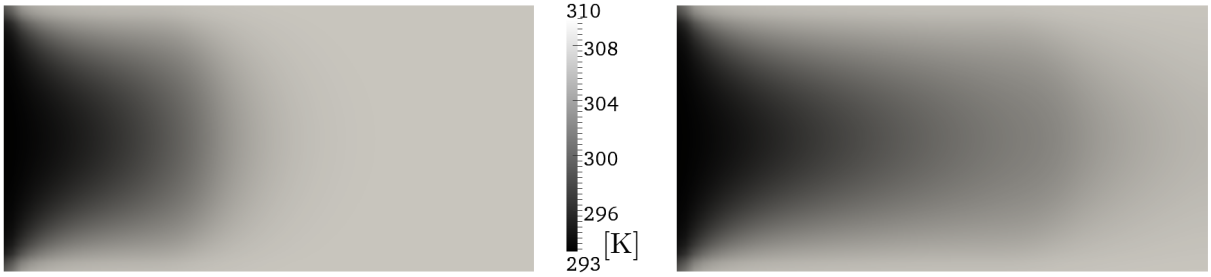

(g) Absolute temperature T at 2.5 s

(h) Absolute temperature T at 7.5 s

The plots of the temperature fields at 2.5 s and 7.5 s demonstrate that the heat transfer phenomena convection and conduction are within the same order of magnitude, taking into account the geometrical dimensions and flow velocity. While bone cement at room temperature enters at the left side of the computational domain, it gets heated up from the walls by more than 10 K within 7.5 s. Closer investigations of the temperature fields yield that viscous heating has almost no effect on the temperature field (not displayed here) and could be neglected in the scope of this thesis, accepting a minor error.

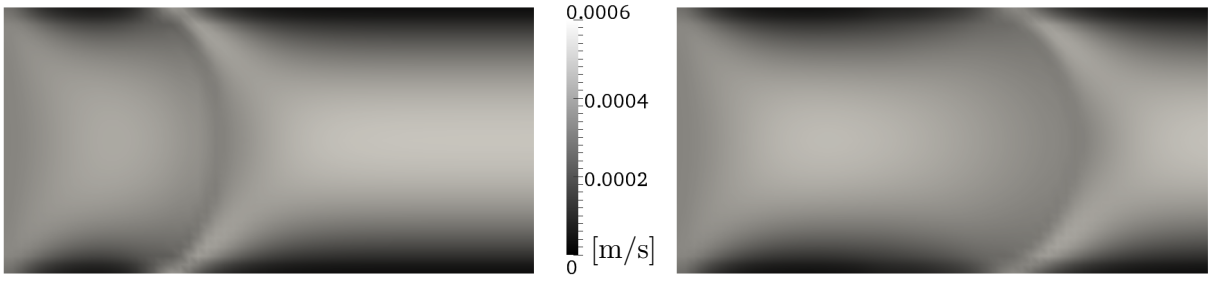

(i) Velocity (magnitude) $|\mathbf{v}|$ at 2.5 s

(j) Velocity (magnitude) $|\mathbf{v}|$ at 7.5 s

Figure 9.2.: Parallel plate flow regarding the bone-cement-bone-marrow interface

Considering the velocity field (cf. figs. 9.2(i) and 9.2(j)), some interesting effects have to be taken into account. Within both fluids, a boundary layer at the walls can be observed, whereas the thickness of the boundary layer is slightly thinner within the bone cement phase. The interface itself does not exhibit a distinctive boundary layer at the wall. In addition, an explicit velocity

gradient is visible at the interface. On the one hand, the bone cement phase has approximately the entrance velocity at the interface, on the other hand, the bone marrow phase has approximately a 50 % higher velocity. This flow in the bone marrow phase at the interface is directed diagonally towards the middle of the two plates and in the direction of the outlet and can interpreted as a form of squeeze effect. Moreover, in the case of a high density ratio between both fluids (not true in this study), the volume-of-fluid method suffers from the existence of spurious currents, which are non-physical, but numerically induced flow patterns, arising from an inaccurate description of the free surface [55, 199].
Having gathered an overview of the flow characteristics, more complex and application-oriented problems can be considered.

9.2. Flow through a μCT-scanned cancellous human bone

This section deals with the flow of bone cement through a cubic sample of trabecular bone structure. Therefore, an osteoporotic thoracic vertebral body (Th10) of a post-mortem preparation of a spinal column (female, 69 years) was scanned with the aid of high resolution μCT technology[1], resulting in an 1804 $\times$ 1824 image matrix with 1353 axial slices at an isotropic voxel size of 19 μm in the x-, y-, and z-direction. The range of grey values varies from approx. -4000 to approx. 7500. This data includes the complete osteoporotic thoracic vertebral body, except the vertebral processes.

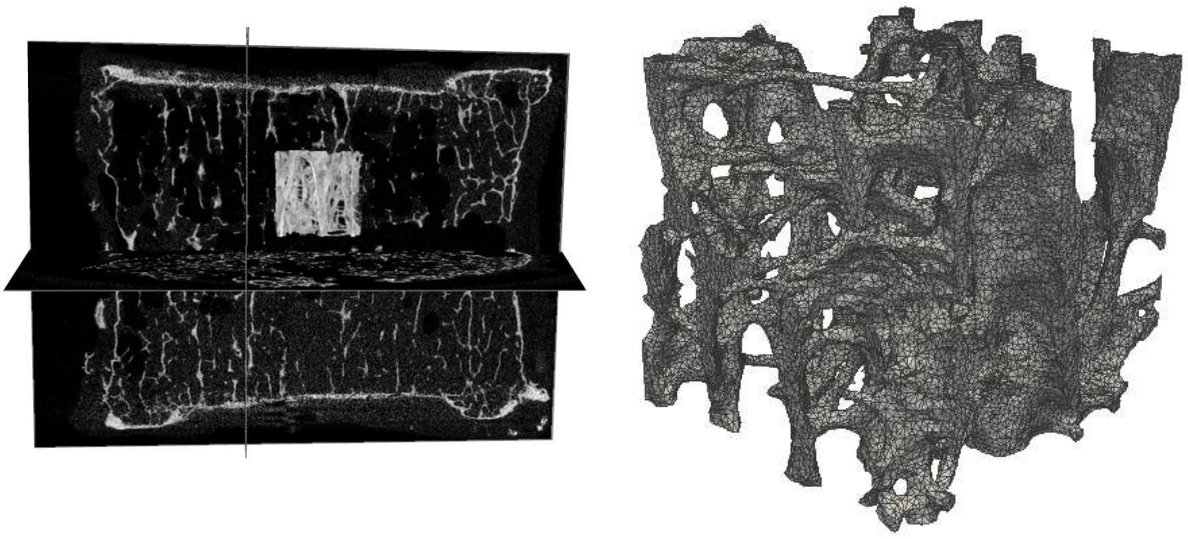

(a) Position of the cubic extract within the vertebra (b) Cubic extract as triangulated surface

Figure 9.3.: Processing of μCT data to triangulated surface data

Subsequently, the procedure described in sec. 8.6 is applied to the obtained data, being existent

[1] vivaCT 40, Scanco Medical AG, Brüttisellen, Switzerland, data acquired at Department of Trauma Surgery/Biomechanics, Medical University Innsbruck, Austria

in DICOM format. The extracted cubic sample of the trabecular structure has a side length of approx. 5 mm, contains about 75,000 triangular faces, which are intersection-free, fully manifold and with suitable element quality. Fig. 9.3(a) shows the position of the cubic extract within the vertebral body and fig. 9.3(b) shows the cubic extract as triangulated surface. This osteoporotic extract shows clearly the typical osteoporotic trabecular structure of cancellous bone. In the direction of the spinal column, the main load direction, relatively thick branches are observable. These thick branches are linked, especially when perpendicular to the main load direction, with delicate trabeculae, which are preferentially weakened by osteoporosis.
On the basis of the digitalised trabecular structure in STL-file format, the computational domain can be meshed. Therefore, the cubic extract is equally enveloped by an underlying cubic base mesh with an edge length of 5.1 mm. Applying the *snappyHexMesh* algorithm, the final mesh, where only the space in between the trabecular structure is meshed, counts about 250,000 cells.

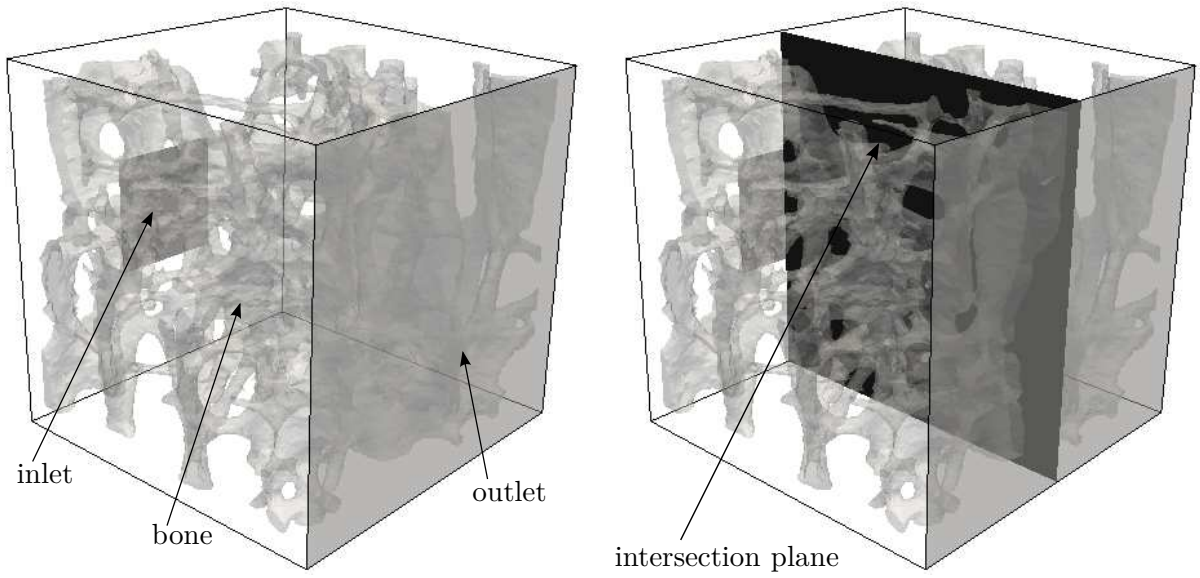

(a) Topology for boundary conditions

(b) Intersection plane for 2D-illustration

Figure 9.4.: Case set up for flow through a μCT-scanned cancellous human bone

For the implementation of the boundary conditions, the topology illustrated in fig 9.4(a) is applied. Bone cement enters the computational domain through the patch named inlet with an initial velocity of 5 mm/s, penetrates the bone structure and displaces bone marrow, which leaves the computational domain through the outlet patch opposite to the inlet. The inlet has quadratic dimensions with an edge length of 1.7 mm, which is in the cross section range of typical biopsy needles. The residual surfaces of the cubic envelope, despite the inlet and outlet, are merged under the patch wall and are allocated with the same boundary conditions. In addition, boundary conditions have to be assigned to the surface of the bone structure as well. The complete set of boundary conditions is summarised in tab. 9.4. It is further assumed that the injection starts three minutes after mixing the cement at an ambient temperature of 20 °C (analogue to sec. 9.1), so that the internal variables for dissolution and polymerisation exhibit

Table 9.4.: Flow through a μCT-scanned cancellous human bone: Boundary conditions

	inlet	outlet	wall, bone
pressure	zero gradient	fixed: 1 bar	zero gradient
velocity	fixed: 5 mm/s	zero gradient	fixed: 0 mm/s
phase fraction	fixed: 1	zero gradient	zero gradient
temperature	fixed: 20 °C	zero gradient	zero gradient
dissolution	fixed: 156.7	zero gradient	zero gradient
degree of cure	fixed: 0.02	zero gradient	zero gradient

the values in tab. 9.4 and 9.5. For numerical stability reasons, part of the computational domain is already filled with bone cement at the beginning of the simulation. This partial volume has prismatic dimensions with the base area being identical to the inlet patch and extending 0.65 mm into the computational domain.
Boundary conditions are straightforward, except for the temperature. In contrast to the fluid flow, heat transfer occurs across the borders of the computational domain. Under these constraints, it is difficult to set realistic boundary conditions for the bone structure and the wall patch. Since the bone structure is delicate, a zero gradient boundary condition is more realistic than a fixed value. Regarding the enveloping walls, neither simple boundary condition (fixed value or fixed gradient) reproduces approximately the real heat transfer behaviour, but in this case a zero gradient condition has been chosen as well.

Table 9.5.: Flow through a μCT-scanned cancellous human bone: Initial conditions

	bone cement	bone marrow
pressure	1 bar	1 bar
velocity	5 mm/s	0 mm/s
phase fraction	1	0
temperature	20 °C	37 °C
dissolution	156.7	0
degree of cure	0.02	0

OpenFOAM® offers the possibility to create more complex and also time-dependent boundary conditions, but to this end, more information on the surrounding heat transfer is needed. The method of conjugate heat transfer enables to get more insight into realistic temperature fields within the bone-cement-bone-marrow-fluid-flow. Applying this method would mean that the volume of bone structure and the surrounding tissue is also discretised and belongs to the computational domain, but only the first law of thermodynamics is solved in this regions, applying correct material properties. OpenFOAM® comes with a basic framework for conjugate heat transfer, which has to be adapted and expanded, but this is beyond the scope of this thesis.
The material behaviour of bone cement and bone marrow is identical to sec. 9.1, applying the values from tab. 9.3 as well. The finite volume calculation was performed on a workstation computer using parallel computing on two cores.

Fig. 9.5 shows the bone cement distribution for 2, 4 and 6 seconds after the start of the cement injection. It is obvious that bone cement flows primarily in the direction of the spinal column,

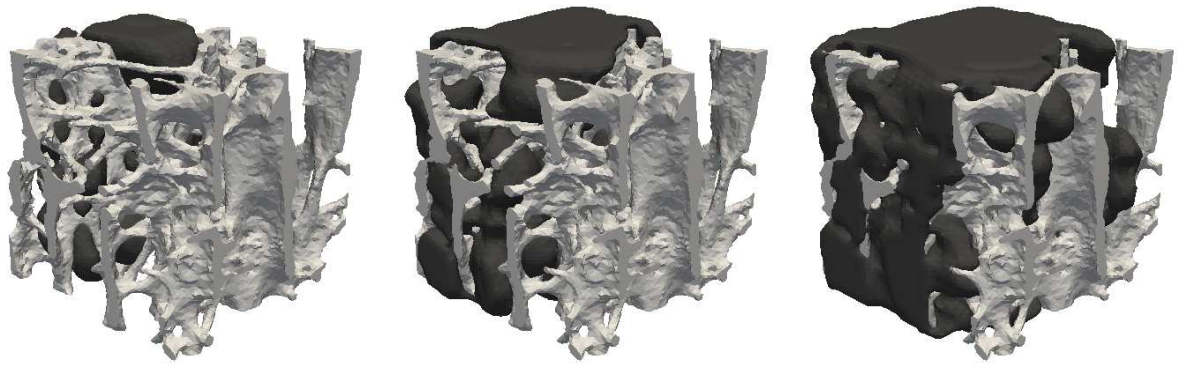

(a) Bone cement distribution after 2 s (b) Bone cement distribution after 4 s (c) Bone cement distribution after 6 s

Figure 9.5.: Bone cement distribution for flow through a μCT-scanned cancellous human bone

as there is less resistance due to the trabecular structure. Only if most of the cavities are filled, bone cement flows also perpendicular to this direction. Furthermore, not all of the bone marrow is displaced by bone cement so that small reservoirs of bone marrow surrounded by bone cement remain. The cement is still low-viscous three minutes after mixing, so that small cavities are also penetrated.
Fig. 9.4(b) shows an intersecting plane through the computational domain, including inlet and outlet. The following fig. 9.6 displays the temperature field on this intersecting plane at the same time steps as in fig. 9.5. Additionally, the bright line marks the bone-cement-bone-marrow-interface as depicted in fig. 9.5.

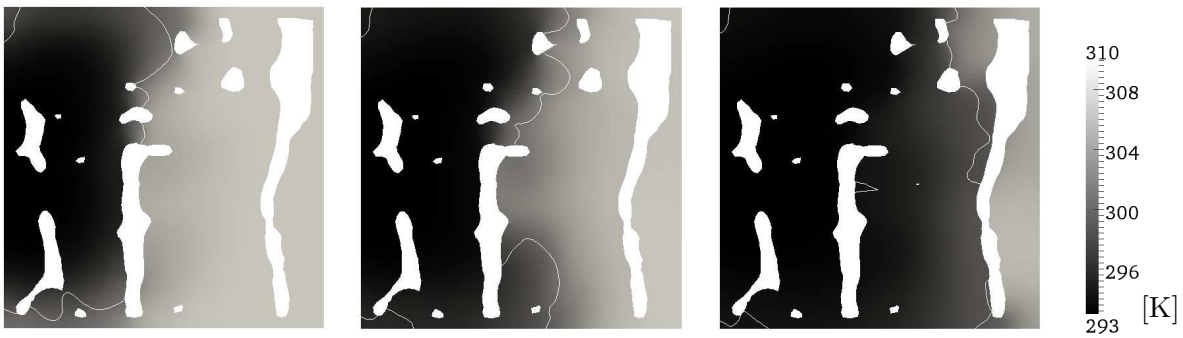

(a) Temperature field after 2 s (b) Temperature field after 4 s (c) Temperature field after 6 s

Figure 9.6.: Temperature field on intersecting plane for flow through a μCT-scanned cancellous human bone

Since the injection velocity is increased by more than one order of magnitude, heat convection is now more dominant than heat conduction. Furthermore, the zero gradient boundary condition on the wall patch and bone patch contribute to the temperature fields shown in figs. 9.6(a) to 9.6(c). Only the flow front experiences a slight heating up. Moreover, figs. 9.6(a) to 9.6(c) demonstrate how the trabecular structure is passed by the bone cement, how small reservoirs

remain filled with bone marrow and how flow fronts recombine after flowing around the trabecular structure.
The associated fields of the dissolution variable at the same time steps as in fig. 9.5 on the intersection plane are illustrated in figs. 9.7(a) to 9.7(c). Compared to sec. 9.1 the internal variable for dissolution evolves more slowly due to the reduced temperature. Numerical diffusion (which is an artefact) is also visible at the flow front, indicated again by the bright line. However, the pale spot in the middle of fig. 9.7(b) is the tip of a flow front of bone cement, which flows perpendicular to the intersection plane here. The streaky area in the middle of fig. 9.7(c) indicates the existence of bone marrow in this zone due to the recombination of two flow fronts. In these cells, there is still bone marrow, resulting in a phase fraction α_1 smaller than 1, but greater than 0.5, so that no clear flow front or interface can be identified.

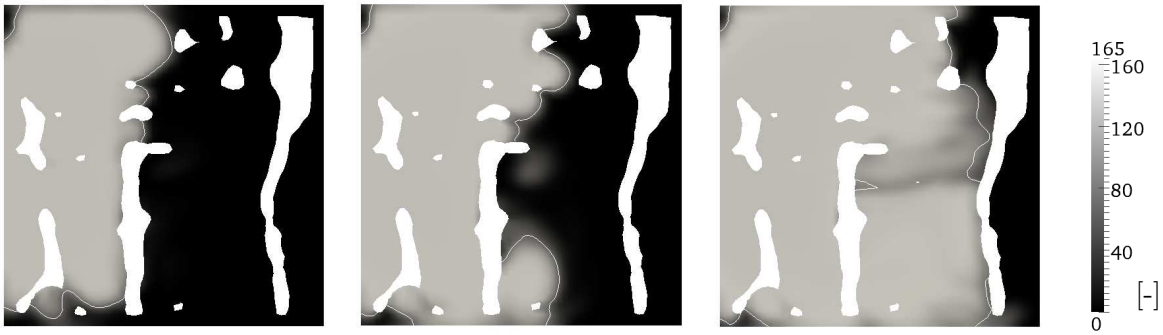

(a) Dissolution field after 2 s (b) Dissolution field after 4 s (c) Dissolution field after 6 s

Figure 9.7.: Dissolution field on intersecting plane for flow through a μCT-scanned cancellous human bone

Of course, other physical variables like pressure and velocity, as well as the empirical variable for the degree of cure have also been stored and could be visualised in a similar manner, but are omitted here due to minor relevance from a clinical point of view.
This computational case study exemplary shows how the cement flow and the temperature field can be visualised with the aid of the prior presented modelling framework throughout the whole injection phase of a vertebral surgery. At a certain point, when the injection is stopped, the relevant field quantities can be transferred to a finite-element analysis, where the curing of the cement is analysed in more detail [119, 121]. How this simulation framework can contribute to enhancements in vertebroplasty and the use of bone cement in general as well as its restrictions will be discussed in the concluding chapter.

9.3. Flow through a μCT-scanned artificial bone structure - experiment and simulation

The preceding computational examples have shown the possibilities of the injection simulation of bone cement. In order to give an estimation of how accurate the modelling and numeri-

cal treatment is, the computational results of the injection simulation are compared with an experiment, having identical initial and boundary conditions.

9.3.1. Experimental setup

The aim of the experimental setup is to establish environmental conditions similar to real vertebroplasty, but still simple enough to treat it with passable effort virtually and numerically. Moreover, data has to be gathered during the injection experiment, which is comparable with the numerical results.
For this purpose, an artificial cubic cancellous bone structure[2] with an edge length of 20 mm is prepared. Prior to the injection experiment, the artificial bone structure is scanned with an industrial μCT-apparatus[3] to digitalise the geometry for the numerical simulation.
In order to guarantee reproducible boundary conditions and a good visibility of the injection process, the bone structure is clamped into a case made out of acrylic glass. The interior dimensions of the case are 60 mm × 50 mm × 25 mm, whereat the bone structure is fixed at the position shown in figs. 9.8(a) and 9.8(b). A hole with a diameter of 3 mm is drilled into the case side wall, where the bone structure is attached to. The position of this hole coincides with the centre of the corresponding side face of the artificial bone structure and serves as an intake for a medical syringe by which the bone cement is injected. The remaining volume of the case is filled with polyethylene glycol as a bone marrow substitute, having a kinematic viscosity of $1.1 \cdot 10^{-4}\,\mathrm{m^2/s}$ at 20 °C. The height of the fluid level is adjusted in such a way that the complete artificial bone structure is covered with polyethylene glycol. Two cameras are installed (cf. fig. 9.9(a)) to capture the injection procedure from the top and from the side, representing the same view as figs. 9.8(a) and 9.8(b).
Although the experiment is not tempered, thermocouples are installed in the positions depicted in figs. 9.8(a) and 9.8(b) in order to record the temperature profile of the subsequent polymerisation. To facilitate the comprehension of the experimental setup, fig. 9.9(a) shows the case with the clamped artificial bone structure, whereat the thermocouples are not aligned and the case has not been filled up with polyethylene glycol yet. The artificial bone structure is surrounded almost completely with PMMA-walls for transparency, apart from the right side face (from a injection direction point of view). So bone cement enters the artificial bone structure through the hole in the side wall, penetrates it and both fluids, bone cement and polyethylene glycol, can exit the structure through the right side face. Next to the side wall, including the hole, a mount is installed for a medical syringe. To ensure a constant injection rate, the syringe is operated by a linear actuator. Additionally, a load cell is applied to the tip of the linear actuator to record the force necessary to press the bone cement into the artificial bone structure. The complete test stand with all actuators and sensors is controlled using the *National Instruments*™software *LabVIEW*. For the conduction of the injection experiment, polymerising bone cement has been

[2] Open Cell Block 7.5 PCF, manufactured by Sawbones®, Malmö, Sweden
[3] phoenix v|tome|x L 300, General Electrics Measurement and Control, data acquired at Wehrwissenschaftliches Institut für Werk- und Betriebsstoffe (WIWeB), Erding, Germany

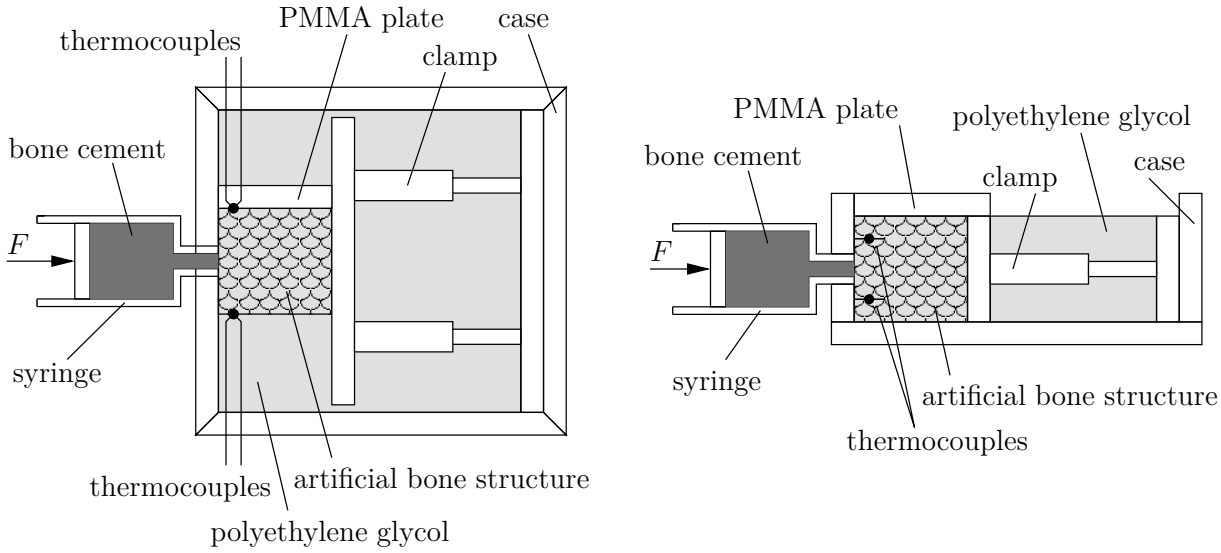

(a) Top view (b) Side view

Figure 9.8.: Schematic overview of the experimental setup of bone cement injection into an artificial bone structure

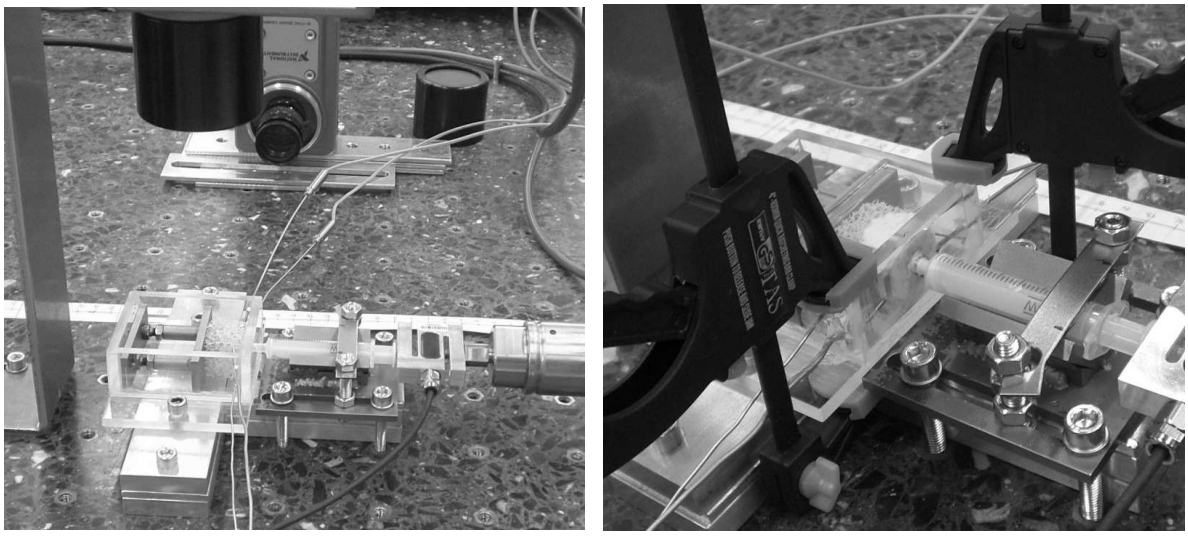

(a) Clamped artificial bone structure (b) Experimental setup with injected bone cement

Figure 9.9.: Experimental setup with clamped bone structure and after cement injection

mixed according to sec. 5.1 and filled into the syringe. The injection and data recording are started approximately 261 s after both components have been stirred together. Temperature values and pictures are recorded every 0.65 s and force values, as well as the position of the linear actuator are stored every 20 ms.

9.3.2. Numerical setup

The numerical setup is aimed to reproduce the experimental initial and boundary conditions as best as possible. Basically, the procedure is similar to that described in sec. 9.2. The scanned artificial structure has a 2024 × 2024 image matrix with 1440 axial slices at an isotropic voxel size of 18.5 μm in the x-, y-, and z-direction. Using the open source software *Slicer 3*, the original bitmap data is converted into a DICOM image stack. The stl-file itself is generated with the aid of the medical image processing and visualisation tool *MeVisLab*© [4]. The digitalised, triangulated artificial bone structure has a side length of approx. 20 mm, contains about 175,000 triangular faces, which are intersection-free, fully manifold and with suitable element quality. Equivalent to sec. 9.2, the stl-file is the basis for meshing the computational domain. To represent the boundary conditions at its best, the underlying rectangular base mesh envelopes the bone structure according to the PMMA case in the experimental setup. Applying the *snappyHexMesh* algorithm, the final mesh counts about 800,000 cells. Fig. 9.10 shows the triangulated artificial bone structure and illustrates the topology for the boundary conditions.

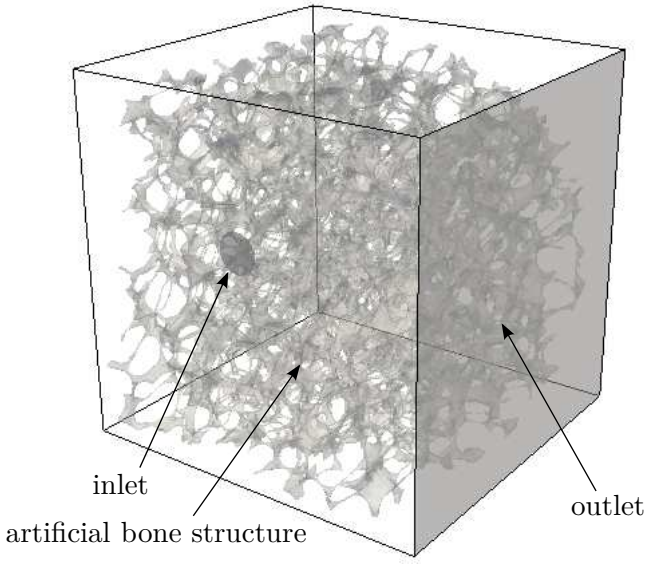

Figure 9.10.: Topology for boundary conditions for flow through a μCT-scanned artificial bone structure

Bone cement enters the computational domain through the circular inlet, penetrates the artificial bone structure and displaces the secondary fluid, polyethylene glycol. Both fluids can exit the computational domain through the right side face, marked as outlet in fig. 9.10.
The overall set of boundary conditions is summarised in tab. 9.6 and reflects the boundary conditions in the experimental setup.
In tab. 9.7 the material properties of both fluids as input for the numerical simulation are listed. The values for the specific heat capacity and the thermal conductivity of polyethylene glycol

[4] Image processing and triangulation of the artificial bone structure was performed at the Department of Solid Mechanics, Faculty of Mechanical Engineering, Technische Universität Chemnitz, Chemnitz, Germany

Table 9.6.: Flow through a μCT-scanned artificial bone structure: Boundary conditions

	inlet	outlet	wall, bone
pressure	zero gradient	fixed: 1 bar	zero gradient
velocity	fixed: 5 mm/s	zero gradient	fixed: 0 mm/s
phase fraction	fixed: 1	zero gradient	zero gradient
temperature	fixed: 20 °C	zero gradient	zero gradient
dissolution	fixed: 158	zero gradient	zero gradient
degree of cure	fixed: 0.021	zero gradient	zero gradient

are estimated values due to the lack of data. However, as the experiment and the simulation are isothermal, these values are less important for this case study. The initial conditions for the

Table 9.7.: Material properties of bone cement and polyethylene glycol regarding two phase flow

	bone cement	polyethylene glycol
kinematic viscosity	see sec. 7.4	$1.1 \cdot 10^{-4}\,\mathrm{m^2/s}$
density	$1.48\,\mathrm{g/cm^3}$	$1.120\,\mathrm{g/cm^3}$
specific heat capacity	see sec. 7.2	1.2 kJ/(kgK)
thermal conductivity	see sec. 7.2	0.25 W/(mK)
surface tension	0.03 N/m	

numerical simulation can be found in tab. 9.8. Basically, these values are similar to the ones in the previous case in tab. 9.5, only the initial values in the bone cement phase for dissolution and degree of cure are adapted to the time period between mixing both components together and the start of injection, assuming a uniform room temperature of 20 °C. Furthermore, the initial temperature of the polyethylene glycol phase is identical to room temperature. The calculation

Table 9.8.: Flow through a μCT-scanned artificial bone structure: Initial conditions

	bone cement	polyethylene glycol
pressure	1 bar	1 bar
velocity	5 mm/s	0 mm/s
phase fraction	1	0
temperature	20 °C	20 °C
dissolution	156.7	0
degree of cure	0.02	0

was carried out on a *SGI Altix UV 1000* cluster using 24 cores and took 96 hours to calculate a physical time of 60 seconds of the injection process.

9.3.3. Comparison of experiment and simulation

Having established identical geometrical and process boundary conditions, the experiment can be conducted and the calculations can be run to gather the data. However, it is quite difficult to collect data in a fluid flow experiment, like the velocity field, temperature field, pressure field or the fields of the internal variables, dissolution and degree of cure, without disturbing the experiment itself. That is why in the injection experiment, the focus was laid on the acquisition of data regarding the phase fraction, i.e. the cement distribution. With a particular attention to the actual application of vertebroplasty, the cement distribution is in fact the most interesting field.
Figs. 9.11(a) to 9.11(c) depict the cement distribution within the artificial bone structure for 10 s, 27 s and 50 s after the beginning of the injection, for the experiment (top) and CFD-simulation (bottom), each viewed from the top.

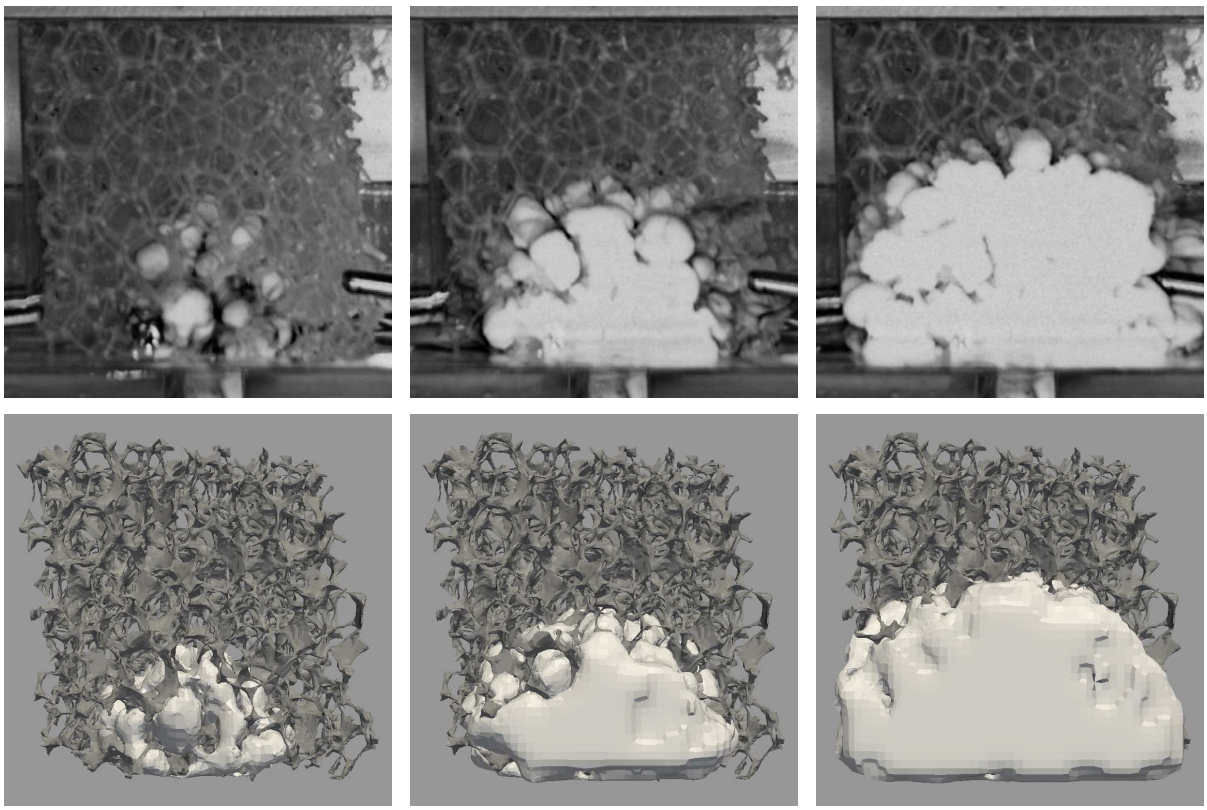

(a) Cement distribution after 10 s (b) Cement distribution after 27 s (c) Cement distribution after 50 s

Figure 9.11.: Bone cement distribution for flow through a μCT-scanned artificial bone structure: Experiment and simulation (view from top)

The side view is illustrated in fig. 9.12(a) to 9.12(c) (the blurred regions on the left side in the experiments pictures arise from the sealing of the thermocouple holes in the case wall).
Comparing the artificial bone structure in the experiment and its digitalised image in the simulation result, they seem to differ at first sight. This is partly owed to the slight transparency of the artificial bone structure, which is not visible in the digitalised form. Of course, there is a

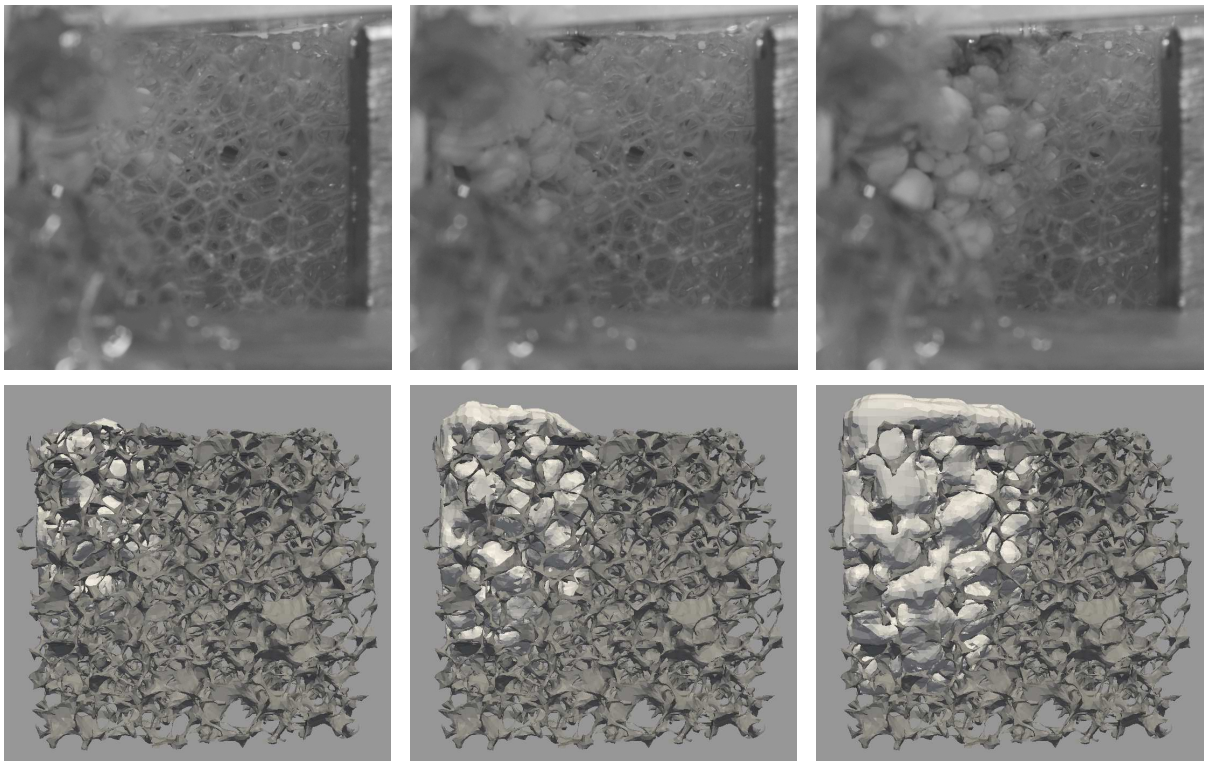

(a) Cement distribution after 10 s (b) Cement distribution after 27 s (c) Cement distribution after 50 s

Figure 9.12.: Bone cement distribution for flow through a μCT-scanned artificial bone structure: Experiment and simulation (view from side)

potential source of error in the digitalisation process, described in subsec. 9.3.2, and no validation procedure, e.g. by a volume check, has been set up yet. A visual inspection shows that the structure of the artificial bone is well reproduced by the digitalised image, only some trabecular branches appear to be too bulky. Furthermore, the clamping in the experimental setup leads to a small deformation of the artificial bone structure in the peripheral zones adjacent to the clamp and opposite at the inlet side.

Comparing the cement distributions of the experiment with the simulation results, a generally good accordance can be noticed. Both, the amount and the shape of the cement cloud coincide well. The penetration of the trabecular structure and the development of cement bubbles at the flow front, as visible in the experiment, is reproduced clearly in the numerical simulation. Deviations that are obvious between experiment and simulation can be ascribed to different reasons. In both views, from the top (fig. 9.11) and the side (fig. 9.12), the bubbles at the flow front appear bigger in the experiment than in the numerical simulation. This is obvious, as viscoelastic effects have been omitted in the rheological modelling of the dissolution process. In the experiment, cement gets compressed when it flows through constrictions in the artificial bone structure and expands again as cavities offer more space again. This behaviour is similar to die swelling in the capillary rheometer experiment (cf. sec. 5.6.2). However, the numerical simulation does not reproduce this phenomenon and the cement bubble formed after a constriction in the artificial bone structure does not expand. A further issue that causes differences between

experiment and simulation, is the interference, i.e. the mutual influence, and reunification of flow fronts. In the numerical simulation, this phenomenon is just controlled by the distribution of the phase fraction α_1 and the surface tension modelling, as outlined in sec. 8.3. In fact, bone cement forms a film over its surface at a sufficient time after mixing, which complicates the reunification of flow fronts in the experiment (cf. sec. 5.6.3.1 and [31, 114]). This is particularly visible in figs. 9.11(b) and 9.12(c).

Aside from slight geometrical deviations and the differences mentioned above, there exist further sources of error, whose influence is difficult to allocate. Although the experimental investigations in ch. 5 have been carried out with utmost care, there is no statistical basis for these measurements because of the great range of different experiments. Moreover, the proposed constitutive material functions describe the material behaviour very well, but not exactly (cf. ch. 7). At least, there are potential numerical errors, regarding discretisation, mesh quality, whose quantity requires an appropriate analysis.

Nevertheless, this first comparison of an injection experiment with the numerical simulation, performed with the proposed material modelling, yields results which are very satisfactory.

10. Conclusion

Osteoporosis is among the ten most frequent and important diseases world wide. In addition to its economic impact, the persons concerned are likely to suffer from lowered self-esteem, disfigurement, reduction or loss of mobility, and reduced independence [181]. In order to prevent and overcome osteoporosis, conservative methods like proper nutrition and physical activity, as well as selective medicinal treatment is essential. However, osteoporosis is mainly detected after fractures occur, as this is the first noticeable indication being obvious for the patient. In the majority of cases, an exclusively conservative treatment is not beneficial and a surgical intervention is required. Vertebroplasty is among the most popular intervention techniques that have proofed to be successful to effect a direct pain relief within the last 25 years. Nevertheless, vertebroplastic interventions are still challenging even for experienced surgeons and are not seldom accompanied by complications (cf. ch. 1). A major reason for this situation is the complex behaviour of the involved material bone cement.

The aim of this study was to investigate in detail the behaviour of acrylic bone cement during its phase transition from liquid to solid and to contribute to a better understanding of the complex processes that take place inside the human body during a vertebroplasty. For a comprehensive inspection of acrylic bone cement, detailed thermodynamic and thermomechanic experiments have been carried out (cf. ch. 5). The thermodynamic experiments consist of the determination of the reaction kinetics as well as the temperature-dependent heat of reaction including the effect of vitrification and, hence, uncomplete curing. Furthermore, the specific heat capacity and the density were examined with respect to temperature and the progress of polymerisation, using temperature modulated differential scanning calorimetry and volumetric dilatometry. Preliminary mechanical experiments by means of a parallel-plate rheometer and an in-house developed pan-indenter device for a universal testing machine have given insight into the general mechanical behaviour of acrylic bone cement during the phase transition from liquid to solid. The impact of the two processes, dissolution and polymerisation, on the mechanical behaviour has been carved out and it was ascertained that they can be treated independently in a first approach from a modelling point of view. Subsequently, an advanced analysis has been performed with the aid of appropriate rheological techniques in order to characterise independently the mechanical behaviour during dissolution and polymerisation. The test conditions were varied with respect to temperature and rate of deformation in a range relevant for vertebroplasty. The determination of the viscoelastic behaviour of the cured material with respect to water uptake, as well as the creep behaviour provided additional information for modelling purposes and concluded the experiments.

Based on the experimental results, a thermomechanically coupled material model has been developed in ch. 6, capable to describe all effects discovered during dissolution and polymerisation of an acrylic bone cement. Starting from a multiplicative split of the deformation gradient and an additive split of the free energy into a thermochemical and a pure mechanical part, a special focus was laid on the accurate description of reaction kinetics including the effect of vitrification, as well as the interdependence between specific heat capacity and enthalpy of reaction. The modelling of the mechanical behaviour distinguishes between a dissolution and polymerisation dominated phase, motivated by the experimental findings. Additionally, with respect to the clinical application, the dissolution dominated phase is rather a fluid dynamics problem, whereas the polymerisation dominated phase can be considered as a solid mechanics problem. These circumstances support the introduction of two model stages from a mechanical point of view. For the dissolution dominated phase, a non-Newtonian, shear-thinning fluid behaviour is applied, and for the polymerisation dominated phase, a functional viscoelastic approach is chosen. An evaluation of the Clausius-Duhem inequality, taking into account the constitutive material equations, proofed the model to be thermodynamically consistent.
In ch. 7, the material parameters of the constitutive equations are identified by numerical methods so that the model is able to depict the experimentally analysed material behaviour at its best.
Within the scope of this thesis, the first model stage, corresponding to the dissolution dominated phase, has been implemented into the open source CFD toolbox OpenFOAM® (cf. ch. 8). Since bone cement displaces bone marrow in the cancellous bone of an affected vertebra during the application phase, an interface-tracking-method based on the volume-of-fluid approach was utilised to describe the free surface between bone cement and bone marrow. Furthermore, μCT-scanning, digital image processing and automated meshing tools were employed to reconstruct the geometrical boundary conditions for simulation purposes as they appear in real human vertebral bones.
The simulation examples in ch. 9 give a review of the capabilities of the modelling framework introduced. By means of the computational results it is possible to track the flow pattern of bone cement through cancellous human bone and the cement distribution inside the vertebra at the end of the injection. When using vertebral bodies affected by osteoporosis and differing in their intensity, the influence of the geometrical boundary conditions, i.e. different porosity and the influence of fractures on the cement distribution can be studied numerically. An additional variation of the initial state of dissolution will also influence the cement distribution so that guidelines can be developed for surgeons on how and when to inject the cement for specific osteoporotic affected vertebrae. The aim of such guidelines is, of course, to attain an optimal cement distribution and to avoid unfavourable cement leakage outside the vertebra. Furthermore, taking into account the second model stage, which was implemented into a finite element code by the partner project (cf. [119, 121]), additional information can be gained to evaluate the cement distribution. Knowing the temporal course of the temperature field, areas with potential risk for heat necrosis can be identified. The analysis of the degree of cure gives evidence on how much residual monomer is remaining in the vitrified cement bulk and may diffuse into

the surrounding tissue. A further issue to be observed is the chemical shrinkage and the associated stresses. The investigation of the computational results can identify areas with stresses at the failure limit and therewith, consequential damages in the trabecular structure during or after curing. This knowledge can help to find cement distributions numerically that omit high stresses in the trabecular structure. Another benefit that can be obtained from this simulation framework is the information on the altered mechanical behaviour of the cement filled vertebra with respect to the loadings occurring in the spinal column.
The comparison of experiment and simulation for a flow through a μCT-scanned artificial bone structure in ch. 9 proves that mechanical phenomena are represented well by the simulation framework. Moreover, the results of ch. 9 encourage that the developed simulation framework is a promising approach for gaining a deeper insight into the complex processes during a vertebroplasty. However, throughout the preceding chapters, different, and to some extent unexpected issues occurred that could not be addressed within the scope of this thesis. These issues are discussed in the following as a prospect on future research activities, which are recommended to improve and expand the possibilities of the developed simulation framework.

- Starting from an experimental point of view, the thermal conductivity was not measured in the uncured, liquid phase. These measurements should be carried out on an appropriate device, as the chain growth might have a rather strong impact on thermal conductivity.

- A further point to discuss is the fact that wall slippage was disregarded for the capillary and the cone-plate rheometer. As mentioned in the previous chapters, it is likely that wall slippage is evident and has to be taken into account. To identify this phenomenon experimentally, an opaque capillary filled with a cement which is partly dyed or includes a few marker particles might be helpful. There exist approaches, like the Mooney correction, for adjusting the measured viscosity. Additionally, proper boundary conditions have to be applied for the numerical calculation to reproduce the experimental findings.

- In this context it has to be mentioned that the viscoelastic nature of acrylic bone cement has been omitted for the dissolution dominated phase, although the rheological analysis and the injection experiment clearly exhibit viscoelastic phenomena. The comparison of experiment and simulation in sec. 9.3 clearly indicates that the simulation currently lacks viscoelastic properties in the flow pattern. In order to obtain a further improvement in the simulation quality it is reasonable to include viscoelasticity in the dissolution dominated phase, too. However, it has to be taken into account that difficulties exist in capturing viscoelastic material properties in a capillary rheometer experiment and that the computational effort significantly increases compared to a pure viscous fluid simulation. In addition, appropriate constitutive equations have to be implemented since OpenFOAM® offers no standard viscoelastic constitutive law.

- Within the scope of this thesis, acrylic bone cement has been treated mechanically incompressible for simplicity. In literature, the Poisson's ratio for PMMA in the glassy state is indicated from 0.35 to 0.4 and rises up to 0.5 for temperatures beyond the glass transition

(cf. sec. 5.8.1). Future research should take up this issue and analyse it from an experimental and modelling point of view, especially with respect to the main polymerisation phase. Regarding the main dissolution phase, mechanically incompressible flow behaviour is fairly admissible. However, it has to be mentioned that compressible fluid flow has to be applied if thermochemically volume changes shall be considered in the finite volume method to satisfy the balance laws (cf. sec. 8.2).

- The direct influence of temperature on viscosity in the main dissolution phase has not been covered by the modelling yet (cf secs. 5.6.3 and 7.4). With the aid of more sophisticated experiments and parameter identification routines for adapted constitutive equations, the impact of temperature on viscosity and dissolution can be separated and this is likely to improve the model quality.

- The constitutive equations, representing the viscoelastic material behaviour during the main polymerisation, describe the experimental data very well, regarding the storage modulus. In order to achieve also a good agreement in the experimental and modelled loss modulus, the constitutive equations need to be developed further, and the data for the loss modulus has to be incorporated into the optimisation routine.

- Only the cavities in between the trabecular structure are used as computational domain in the current simulation framework. This is sufficient for fluid flow but not for heat transfer. To gain a more realistic course of the temperature field, a conjugate heat transfer approach should be consulted (cf. sec. 9.2). This allows for solving the equation of heat conduction also inside the trabecular structure and in the surrounding tissue, whereat appropriate boundary conditions have to be defined at the interfaces.

- Further research is also required in the process for obtaining digital geometrical data of human vertebral bodies. μCT-scanning offers a sufficient resolution of the vertebral body and the described image processing (cf. sec. 8.6) yields automatically a triangulated surface. However, some manual finishing work is currently still required to eliminate triangles with acute angles, which have an adverse effect on the meshing process, and thus on the stability of the numerical solution. This manual correction is feasible for small extracts, but not for a complete vertebral body. Furthermore, a validation for the digital imaging process is missing in the current study, ensuring a precise geometrical accordance between the trabecular structure of the real human vertebral body and the digital image. This geometrical accordance is essential for obtaining reliable computational results.

The above listing illustrates that the research in the field of vertebroplasty offers a variety of improvements. Thereby, the scientific benefit and the experimental as well as computational effort have to be carefully balanced, since the current simulation framework will reach its limits even on mainframe computers, when considering an entire vertebral body.
Nonetheless, the current study presents one of the first approaches that allow for capturing and tracking of the thermomechanical processes during a vertebroplastic surgery in a scientific

depth which is novel. With the aid of this simulation framework, open clinical problems can be answered, which contributes to enhancements in vertebroplasty.

A. Explanatory calculations

Leibniz rule for taking the derivative of parameter integrals

$$\frac{d}{dt}\int\limits_{\varpi(t)}^{\varphi(t)} f(x,t)dx = \int\limits_{\varpi(t)}^{\varphi(t)} \frac{d}{dt}f(x,t)dx + f(\varphi(t),t)\frac{d\,\varphi(t)}{dt} - f(\varpi(t),t)\frac{d\,\varpi(t)}{dt} \quad . \tag{A.1}$$

Velocity profile within a fully developed pipe flow for a power law fluid

This derivation of the velocity profile within a fully developed pipe flow for a power law fluid follows the argumentation of [9] and [192].
From eq. (7.2) and (7.7), it follows that the only non zero components of the extra stress tensor are

$$\sigma_{rz} = \sigma_{zr} = -\eta(-4\mathrm{II}_{\mathbf{D}_M})\dot{\gamma} = g|-4\mathrm{II}_{\mathbf{D}_M}|^{(h-1)/2}\dot{\gamma} \quad \text{with} \quad -4\mathrm{II}_{\mathbf{D}_M} = \dot{\gamma}^2 \quad . \tag{A.2}$$

Using the above results in the equation of linear momentum with respect to cylindrical coordinates, yields

$$\begin{aligned} \frac{\partial\, p}{\partial r} &= 0 \\ \frac{\partial\, p}{\partial \theta} &= 0 \\ \frac{\partial\, p}{\partial z} &= \frac{1}{r}\frac{\partial\,(r\sigma_{rz})}{\partial r} \quad . \end{aligned} \tag{A.3}$$

This evaluation shows that the pressure p is independent of r and θ and that $\partial p/\partial z$ is constant and will be denoted as $-k$ in the following. Integration of eq. $(\mathrm{A}.3)_3$ with respect to r and considering that σ_{rz} is bounded at $r = 0$, results in

$$\sigma_{rz} = -\frac{kr}{2} \quad . \tag{A.4}$$

Moreover, by merging eqs. (A.2) and (A.4), the following expression for the viscosity is obtained:

$$g\dot{\gamma}^h = \frac{kr}{2} \quad . \tag{A.5}$$

Again, integration (whereat $-dw(r)/dr = \dot{\gamma}$ holds) and the use of no-slip boundary conditions at the pipe wall lead to an expression for the axial velocity profile in the form of

$$w(r) = \left(\frac{kR}{2g}\right)^{1/h} \left(\frac{Rh}{h+1}\right) \left[1 - \left(\frac{r}{R}\right)^{(1+1/h)}\right] \quad . \tag{A.6}$$

Now the volumetric flow rate $\dot{V}$ computes as

$$\dot{V} = 2\pi \int_0^R r w(r) dr = \left(\frac{kR}{2g}\right)^{1/h} \frac{R^3 \pi h}{3h+1} \quad . \tag{A.7}$$

Inserting eq. (A.7) into eq. (A.6) provides the final form of the axial velocity profile

$$w(r) = \frac{\dot{V}}{\pi R^3} \frac{3h+1}{h+1} \left[1 - \left(\frac{r}{R}\right)^{(1+1/h)}\right] \quad . \tag{A.8}$$

Deriving the axial velocity profile of eq. (A.8) with respect to r and taking into account $-dw(r)/dr = \dot{\gamma}$ yields the final form for the shear rate

$$\dot{\gamma} = \frac{\dot{V}}{\pi R^3} \frac{3h+1}{h+1} \left(\left(1 + \frac{1}{h}\right) \left(\frac{r}{R}\right)^{\frac{1}{h}}\right) \quad . \tag{A.9}$$

Small angle approximation of the shear profile for a cone-plate rheometer

The expression (7.6) can also be written as

$$\dot{\gamma} = \sin\phi \frac{\partial}{\partial\phi} \left(\frac{\omega(\phi)}{\sin\phi}\right) = \frac{\partial\,\omega(\phi)}{\partial\phi} - \omega(\phi)\cot\phi \quad . \tag{A.10}$$

By using the relation $\beta = \pi/2 - \phi$, $\cot\phi = \tan\beta$ holds and for small angles $0 < \beta < \alpha$, with α being the cone angle (cf. fig. 5.17), $\tan\beta$ is approximately 0. Hence, eq. (A.10) simplifies to

$$\dot{\gamma} \approx \frac{\partial\,\omega(\phi)}{\partial\phi} \approx \frac{\omega(\pi/2-\alpha) - \omega(\pi/2)}{\alpha} \quad . \tag{A.11}$$

Assuming further a linear flow profile between plate and cone as well as no slip boundary conditions at plate and cone

$$\omega(\pi/2) = 0 \quad \text{and} \quad \omega(\pi/2-\alpha) = \Omega \sin(\pi/2-\alpha) \approx \Omega \quad , \tag{A.12}$$

yields finally

$$\dot{\gamma} \approx \frac{\Omega}{\alpha} \quad . \tag{A.13}$$

By specifying a constitutive viscosity function, the tangential flow profile with respect to ϕ can be calculated and a more precise solution can be obtained (cf. [192]). However, in case of small cone angles ($\alpha < 5°$), the error of the small angle approximation derived above is less than 5 %.

Bibliography

[1] http://heraeus-medical.com/media/webmedia_local/dc/int/bro_osteopal_v_int.pdf, 04. March 2013.

[2] Consensus development conference: Prophylaxis and treatment of osteoporosis. *The American Journal of Medicine*, 90:107 – 110, 1991.

[3] D.B. Adolf and R.S. Chambers. A thermodynamically consistent, nonlinear viscoelastic approach for modeling thermosets during cure. *Journal of Rheology*, 51(1):23–50, 2007.

[4] D.B. Adolf and J.E. Martin. Time-cure superposition during crosslinking. *Macromolecules*, 23(15):3700–3704, 1990.

[5] D.B. Adolf and J.E. Martin. Calculation of stresses in crosslinking polymers. *Journal of Composite Materials*, 30(1):13–34, 1996.

[6] N. Aebli, J. Krebs, D. Schwenke, G. Davis, and J.-C. Theis. Pressurization of vertebral bodies during vertebroplasty causes cardiovascular complications: An experimental study in sheep. *Spine*, 28(14):1513–1519, 2003.

[7] J Altenbach and H. Altenbach. *Einführung in die Kontinuums-Mechanik*. Teubner Verlag, Stuttgart, 1994.

[8] A. J. Ambard and L.eonard Mueninghoff. Calcium phosphate cement: Review of mechanical and biological properties. *Journal of Prosthodontics*, 15(5):321–328, 2006.

[9] G. Astarita and G. Marrucci. *Principles of Non-Newtonian Fluid Mechanics*. McGraw-Hill Book Company (UK) Limited, 1974.

[10] J.L. Bailleul, G. Guyonvarch, B. Garnier, Y. Jarny, and D. Delaunay. Identification des propriétés thermiques de composites fibres de verre/résines thermodurcissables: Application à l'optimisation des procédés de moulage. *Revue Générale de Thermique*, 35(409):65–76, 1996.

[11] J. Ball, J.D. Barr, S.M. Belkoff, M. Bellantoni, B. Boszczyck, J. Chiras, A. Cotten, A. Curcin, H. Deramond, T. Franz, P.F. Heini, R. Henrys, J. Kim, K. Kortman, J.M. Mathis, R. Orler, A.O. Ortiz, M.J.B. Stallmeyer, and G.H. Zoarski. *Percutaneous Vertebroplasty and Kyphoplasty*. Springer, 2006.

[12] G. Baroud, M. Bohner, P. Heini, and T. Steffen. Injection biomechanics of bone cements

used in vertebroplasty. *Bio-Medical Materials and Engineering*, 14(4):487–504, 2004.

[13] G. Baroud, M. Crookshank, and M. Bohner. High-viscosity cement significantly enhances uniformity of cement filling in vertebroplasty: An experimental model and study on cement leakage. *Spine*, 31(22):2562–2568, 2006.

[14] G. Baroud, J. Nemes, P. Heini, and T. Steffen. Load shift of the intervertebral disc after a vertebroplasty: A finite-element study. *European Spine Journal*, 12(4):421–426, 2003.

[15] G. Baroud, M. Samara, and T. Steffen. Influence of mixing method on the cement temperature-mixing time history and doughing time of three acrylic cements for vertebroplasty. *Journal of Biomedical Materials Research*, 68B(1):112–116, 2004.

[16] G. Baroud, C. Vant, D. Giannitsios, M. Bohner, and T. Steffen. Effect of vertebral shell on injection pressure and intravertebral pressure in vertebroplasty. *Spine*, 30(1):68–74, 2005.

[17] G. Baroud, C. Vant, and R. Wilcox. Long-term effects of vertebroplasty: adjacent vertebral fractures. *Journal of Long-Term Effects on Medical Implants*, 16(4):265–280, 2006.

[18] G. Baroud, J.Z. Wu, M. Bohner, S. Sponagel, and T. Steffen. How to determine the permeability for cement infiltration of osteoporotic cancellous bone. *Medical Engineering & Physics*, 25(4):283–288, 2003.

[19] G. Baroud and F.B. Yahia. A finite element rheological model for polymethylmethacrylate flow: Analysis of the cement delivery in vertebroplasty. *Proceedings of the Institution of Mechanical Engineers, Part H: Journal of Engineering in Medicine*, 218(5):331–338, 2004.

[20] R. Bartl and W. Buchberger. *Der große Patientenratgeber Osteoporose.* Zuckschwerdt, München, Germering, 2011.

[21] W.W. Baumann, U. Bunge, O. Frederich, M. Schatz, and F. Thiele. Finite–Volumen–Methode in der Numerischen Thermofluiddynamik - Manuskript zur Vorlesung im Fachgebiet Numerische Methoden der Thermofluiddynamik. Technical report, Technische Universität Berlin, 2006.

[22] A.J. Beaudoin, W.M. Mihalko, and W.R. Krause. Finite element modelling of polymethylmethacrylate flow through cancellous bone. *Journal of Biomechanics*, 24(2):127–136, 1991.

[23] S. Becker, J. Meissner, A. Tuschel, A. Chavanne, and M. Ogon. Cement leakage into the posterior spinal canal during balloon kyphoplasty: A case report. *Journal of Orthopaedic Surgery*, 15:222–225, 2007.

[24] S.M. Belkoff, J.M. Mathis, L.E. Jasper, and H. Deramond. The biomechanics of vertebroplasty: The effect of cement volume on mechanical behavior. *Spine*, 26(14):1537–1541, 2001.

[25] P. Benisch. *Molekulare Analysen zur Knochenregeneration im Alter und bei Osteoporose.*

PhD thesis, Julius-Maximilians-Universität Würzburg, 2011.

[26] S.A. Bidstrup and C.W. Macosko. Chemorheology relations for epoxy-amine crosslinking. *Journal of Polymer Science Part B: Polymer Physics*, 28(5):691–709, 1990.

[27] T. Blumenstock. *Analyse der Eigenspannungen während der Aushärtung von Epoxidharzmassen*. PhD thesis, Universität Stuttgart, 2003.

[28] M. Bohner, B. Gasser, G. Baroud, and P. Heini. Theoretical and experimental model to describe the injection of a polymethylmethacrylate cement into a porous structure. *Biomaterials*, 24(16):2721–2730, 2003.

[29] A. Borzacchiello, L. Ambrosio, L. Nicolais, E.J. Harper, K.E. Tanner, and W. Bonfield. Isothermal and non-isothermal polymerization of a new bone cement. *Journal of Materials Science: Materials in Medicine*, 9(6):317–324, 1998.

[30] J.U. Brackbill, D.B. Kothe, and C. Zemach. A continuum method for modeling surface tension. *Journal of Computational Physics*, 100(2):335–354, 1992.

[31] S.J. Breusch and K.-D. Kühn. Knochenzemente auf Basis von Polymethylmethacrylat. *Der Orthopäde*, 32(1):41–50, 2003.

[32] A. Briscoe. *Characterisation and computational modelling of acrylic bone cement polymerisation*. PhD thesis, University of Southampton, 2006.

[33] A. Briscoe and A. New. Polymerisation stress modelling in acrylic bone cement. *Journal of Biomechanics*, 43(5):978–983, 2010.

[34] J.A. Cape and G.W. Lehman. Temperature and finite pulse-time effects in the flash method for measuring thermal diffusivity. *Journal of Applied Physics*, 34(7):1909–1913, 1963.

[35] D. Carnelli, E. Bianchi, T. Villa, F. Galbusera, and G. Pennati. Design of a 'driven cylinder' viscometer for bone cement rheological characterization. *Proceedings of the Institution of Mechanical Engineers, Part H: Journal of Engineering in Medicine*, 225(4):353–363, 2011.

[36] J. Charnley. Anchorage of the femoral head prothesis to the shaft of the femur. *The Journal of Bone and Joint Surgery*, 42B:28–30, 1960.

[37] H.-L. Chen, C.-S. Wong, S.-T. Ho, F.-L. Chang, C.-H. Hsu, and C.-T. Wu. A lethal pulmonary embolism during percutaneous vertebroplasty. *Anesthesia & Analgesia*, 95(4):1060–1062, 2002.

[38] D.H. Choe, E.M. Marom, K. Ahrar, M.T. Truong, and J.E. Madewell. Pulmonary embolism of polymethyl methacrylate during percutaneous vertebroplasty and kyphoplasty. *American Journal of Roentgenology*, 183(4):1097–1102, 2004.

[39] B.D. Coleman and M.E. Gurtin. Thermodynamics with internal state variables. *Journal of Chemical Physics*, 47(2):597–613, 1967.

[40] B.D. Coleman and W. Noll. Foundations of linear viscoelasticity. *Reviews of Modern Physics*, 33(2):239–249, 1961.

[41] B.D. Coleman and W. Noll. The thermodynamics of elastic materials with heat conduction and viscosity. *Archive for Rational Mechanics and Analysis*, 13(1):167–178, 1963.

[42] T.F. Coleman and Y. Li. On the convergence of interior-reflective newton methods for nonlinear minimization subject to bounds. *Mathematical Programming*, 67(1-3):189–224, 1994.

[43] T.F. Coleman and Y. Li. An interior trust region approach for nonlinear minimization subject to bounds. *SIAM Journal on Optimization*, 6(2):418–445, 1996.

[44] A. Collyer and D. Clegg. *Rheological Measurement*. Elsevier Applied Science, 1988.

[45] O.E. Dahl, L.J. Garvik, and T. Lyberg. Toxic effects of methylmethacrylate monomer on leukocytes and endothelial cells in vitro. *Acta Orthopaedica*, 65(2):147–153, 1994.

[46] H. Deramond, N.T. Wright, and S.M. Belkoff. Temperature elevation caused by bone cement polymerization during vertebroplasty. *Bone*, 25(2, Supplement 1):17S–21S, 1999.

[47] S.S. Deshpande, L. Anumolu, and M.F. Trujillo. Evaluating the performance of the two-phase flow solver interfoam. *Computational Science & Discovery*, 5(1):014016, 2012.

[48] A.T. DiBenedetto. Prediction of the glass transition temperature of polymers: A model based on the principle of corresponding states. *Journal of Polymer Science Part B: Polymer Physics*, 25(9):1949–1969, 1987.

[49] F.R. DiMaio. The science of bone cement: A historical review. *Orthopedics*, 25:1399–1407, 2002.

[50] W.N. dos Santos, J.A. de Sousa, and R. Gregorio Jr. Thermal conductivity behaviour of polymers around glass transition and crystalline melting temperatures. *Polymer Testing*, 32(5):987–994, August 2013.

[51] N.J. Dunne and J.F. Orr. Curing characteristics of acrylic bone cement. *Journal of Materials Science: Materials in Medicine*, 13(1):17–22, 2002.

[52] P. Eyerer. Kunststoffe in der Gelenkendoprothetik. *Materialwissenschaft und Werkstofftechnik*, 17(12):444–448, 1986.

[53] S. Faller. Untersuchung der mechanischen Eigenschaften des Knochenzements während der Aushärtung. Technical report, Universität der Bundeswehr München, 2009.

[54] S. Faller. Beiträge zur Materialtheorie - Bestimmung der temperatur- und aushärtegrad-

abhängigen Wärmeleitfähigkeit mit Hilfe finiter Volumen gestützter inverser Methoden. Technical report, Universität der Bundeswehr München, 2011.

[55] S. Faller. Reduktion der parasitärern Strömung an freien Oberflächen bei der Berechnung von Mehrphasenströmungen mit der Volume-of-Fluid Methode. Master's thesis, Universität der Bundeswehr München, 2012.

[56] D.F. Farrar and J. Rose. Rheological properties of PMMA bone cements during curing. *Biomaterials*, 22(22):3005–3013, 2001.

[57] J.D. Ferry. *Viscoelastic properties of polymers*. John Wiley & Sons, New York, 1980.

[58] J.H. Ferziger and M. Perić. *Numerische Strömungsmechanik*. Springer-Verlag, 2008.

[59] P.J. Flory. Thermodynamic relations for high elastic materials. *Transactions of the Faraday Society*, 57:829–838, 1961.

[60] J. H. Flynn and L. A. Wall. A quick, direct method for the determination of activation energy from thermogravimetric data. *Journal of Polymer Science Part B: Polymer Letters*, 4(5):323–328, 1966.

[61] The OpenFOAM Foundation. OpenFOAM® Documentation, 28. March 2015.

[62] J. Fournier, G. Williams, C. Duch, and G.A. Aldridge. Changes in molecular dynamics during bulk polymerization of an epoxide - amine system as studied by dielectric relaxation spectroscopy. *Macromolecules*, 29(22):7097–7107, 1996.

[63] S. Freynik. *Ballonkyphoplastie von pathologischen Frakturen der Wirbelkörper bei vertebralen Tumormetastasen. Prospektive Studie mit 65 Patienten über zwei Jahre Nachuntersuchungszeitraum*. PhD thesis, Charité - Universitätsmedizin Berlin, 2009.

[64] P. Galibert, H. Deramond, P. Rosat, and D. Le Gars. Preliminary note on the treatment of vertebral angioma by percutaneous acrylic vertebroplasty. *Neurochirurgie*, 33:166–168, 1987.

[65] S. Garcia, B. Garnier, and Y. Jarny. Simultaneous estimation of kinetic parameters using genetic algorithms. *Inverse Problems in Engineering: Theory and Practice: 3rd Int. Conference on Inverse Problems in Engineering*, 3:1–8, 1999.

[66] J.L. Gilbert, J.M. Hasenwinkel, R.L. Wixson, and E.P. Lautenschlager. A theoretical and experimental analysis of polymerization shrinkage of bone cement: A potential major source of porosity. *Journal of Biomedical Materials Research*, 52(1):210–218, 2000.

[67] M.P. Ginebra, L. Albuixech, E. Fernández-Barragán, C. Aparicio, F.J. Gil, J. San Román, B. Vázquez, and J.A. Planell. Mechanical performance of acrylic bone cements containing different radiopacifying agents. *Biomaterials*, 23(8):1873–1882, 2002.

[68] Y.K. Godovsky. *Thermophysical Properties of Polymers*. Springer, 1992.

[69] C. Gracia-Fernandez, J. Tarrio-Saavedra, J. Lopez-Beceiro, S. Gomez-Barreiro, S. Naya, and R. Artiaga. Temperature modulation in PDSC for monitoring the curing under pressure. *Journal of Thermal Analysis and Calorimetry*, 106(1):101–107, 2011.

[70] G. N. Greaves, A. L. Greer, R. S. Lakes, and T. Rouxel. Poisson's ratio and modern materials. *Nature Materials*, 10(11):823–837, 2011.

[71] J.G. Grohs. Minimal-invasive Stabilisierung osteoporotischer Wirbelkörpereinbrüche. *Journal für Mineralstoffwechsel*, 10:7–12, 2003.

[72] T. Grupp. *Entwicklung eines neuartigen Verfahrens zur sekundären Fixierung eines Hüftendoprothesenschaftes*. PhD thesis, Universität Stuttgart, 2002.

[73] U.A. Gurkan and O. Akkus. The mechanical environment of bone marrow: A review. *Annals of Biomedical Engineering*, 36(12):1978–1991, 2008.

[74] S.S. Haas, G.M. Brauer, and G. Dickson. A characterization of polymethylmethacrylate bone cement. *The Journal of Bone & Joint Surgery*, 57:380–391, 1975.

[75] M. Habib, G. Baroud, F. Gitzhofer, and M. Bohner. Mechanisms underlying the limited injectability of hydraulic calcium phosphate paste. *Acta Biomaterialia*, 4(5):1465–1471, 2008.

[76] M. Habib, G. Baroud, F. Gitzhofer, and M. Bohner. Mechanisms underlying the limited injectability of hydraulic calcium phosphate paste. Part II: Particle separation study. *Acta Biomaterialia*, 6(1):250–256, 2010.

[77] E. Hansen. Modelling heat transfer in a bone-cement-prosthesis system. *Journal of Biomechanics*, 36(6):787–795, 2003.

[78] P. Hasgall, E. Neufeld, M. Gosselin, A. Klingenböck, and N. Kuster. It'is database for thermal and electromagnetic parameters of biological tissues, 30. July 2013. Version 2.4.

[79] P. Haupt. *Continuum Mechanics and Theory of Materials*. Springer, Berlin, 2002.

[80] P. Haupt and A. Lion. On finite linear viscoelasticity of incompressible isotropic materials. *Acta Mechanica*, 159:87–124, 2002.

[81] P. Haupt and C. Tsakmakis. On the application of dual variables in continuum mechanics. *Continuum Mechanics and Thermodynamics*, 1(3):165–196, 1989.

[82] T. Heimes. *Finite Thermoviskoelastizität*. PhD thesis, Universität der Bundeswehr München, 2005.

[83] P.F. Heini, B. Wälchli, and U. Berlemann. Percutaneous transpedicular vertebroplasty with PMMA: Operative technique and early results. *European Spine Journal*, 9:445–450, 2000.

[84] C.W. Hirt and B.D. Nichols. Volume of fluid (VOF) method for the dynamics of free boundaries. *Journal of Computational Physics*, 39(1):201–225, 1981.

[85] M. Holst. *Reaktionsschwindung von Epoxidharz-Systemen*. PhD thesis, Technische Universität Darmstadt, 2001.

[86] G.A. Holzapfel. *Nonlinear Solid Mechanics - A Continuum Approach for Engineering*. John Wiley & Sons, LTD, 2000.

[87] M. Hossain. *Modelling and Computation of Polymer Curing*. PhD thesis, Friedrich-Alexander-Universität Erlangen-Nürnberg, 2010.

[88] M. Hossain, G. Possart, and P. Steinmann. A finite strain framework for the simulation of polymer curing. Part I: Elasticity. *Computational Mechanics*, 44(5):621–630, 2009.

[89] M. Hossain, G. Possart, and P. Steinmann. A small-strain model to simulate the curing of thermosets. *Computational Mechanics*, 43(6):769–779, 2009.

[90] M. Hossain, G. Possart, and P. Steinmann. A finite strain framework for the simulation of polymer curing. Part II: Viscoelasticity and shrinkage. *Computational Mechanics*, 46(3):363–375, 2010.

[91] T.H. Hsieh and A.C. Su. Cure behavior of an epoxy–novolac molding compound. *Journal of Applied Polymer Science*, 44(1):165–172, 1992.

[92] H.W.J. Huiskes. *Some fundamental aspects of human joint replacement - Analyses of stresses and heat conduction in bone-prosthesis structures*. PhD thesis, University of Nijmegen, 1979.

[93] K. Hutter. The foundations of thermodynamics, its basic postulates and implications. A review of modern thermodynamics. *Acta Mechanica*, 27(1-4):1–54, 1977.

[94] P. Höfer. *Dynamische Eigenschaften technischer Gummiwerkstoffe - Experimente, thermomechanische Materialmodellierung & Implementierung in die FEM*. PhD thesis, Universität der Bundeswehr München, 2009.

[95] G. Höhne, W. Hemminger, and H.-J. Flammersheim. *Differential Scanning Calorimetry–An Introduction for Practitioners*. Springer, Berlin, 2nd edition, 2003.

[96] J. Ihlemann. *Beobachterkonzepte und Darstellungsformen der nichtlinearen Kontinuumsmechanik*. VDI Düsseldorf, 2014.

[97] R.I. Issa. Solution of the implicitly discretized fluid flow equations by operator-splitting. *Journal of Computational Physics*, 62:40–65, 1986.

[98] H. Jasak. *Error analysis and estimation for the finite volume method with applications to fluid flow*. PhD thesis, Imperial College of Science, Technology and Medicine London, 1996.

[99] C.D. Jefferiss, A.J.C. Lee, and R.S.M. Ling. Thermal aspects of selfcuring polymethylmethacrylate. *Journal of Bone & Joint Surgery, British Volume*, 57-B(4):511–518, 1975.

[100] M.E. Jensen, A.J. Evans, J.M. Mathis, D.F. Kallmes, H.J. Cloft, and J.E. Dion. Percutaneous polymethylmethacrylate vertebroplasty in the treatment of osteoporotic vertebral body compression fractures: Technical aspects. *American Journal of Neuroradiology*, 18:1897–1904, 1997.

[101] M. Johlitz. *Experimentelle Untersuchung und Modellierung von Maßstabseffekten in Klebungen*. PhD thesis, Universität des Saarlandes, 2008.

[102] A.C. Jones, V.N. Wijayathunga, S. Rehman, and R.K. Wilcox. Subject-specific models of the spine for the analysis of vertebroplasty. In *Studies in Mechanobiology, Tissue Engineering and Biomaterials*, volume 09, pages 133–154. Springer Berlin Heidelberg, 2012.

[103] M. Kaliske and H. Rothert. Formulation and implementation of three-dimensional viscoelasticity at small and finite strains. *Computational Mechanics*, 19(3):228–239, 1997.

[104] D.F. Kallmes, M.E. Jensen, and J.K. McGraw. Percutaneous vertebroplasty. In *Interventional Radiology of the Spine*, pages 197–215. Humana Press, 2004.

[105] M.R. Kamal and S. Sourour. Kinetics and thermal characterization of thermoset cure. *Polymer Engineering & Science*, 13(1):59–64, 1973.

[106] M.S. Kiasat. *Curing shrinkage and residual stresses in viscoelastic thermosetting resins and composites*. PhD thesis, Delft University of Technology, 2000.

[107] S. Kolmeder and A. Lion. On the thermomechanical-chemically coupled behavior of acrylic bone cements: Experimental characterization of material behavior and modeling approach. *Technische Mechanik*, 30(1-3):195–202, 2010.

[108] S. Kolmeder and A. Lion. Characterisation and modelling rheological properties of acrylic bone cement during application. *Mechanics Research Communications*, 48(0):93–99, 2013.

[109] S. Kolmeder, A. Lion, R. Landgraf, and J. Ihlemann. Thermophysical properties and material modelling of acrylic bone cements used in vertebroplasty. *Journal of Thermal Analysis and Calorimetry*, 105(2):705–718, 2011.

[110] S. Konno, K. Olmarker, G. Byröd, C. Nordborg, B. Strömqvist, and B. Rydevik. Acute thermal nerve root injury. *European Spine Journal*, 3(6):299–302, 1994.

[111] R. Kono. The dynamic bulk viscosity of polystyrene and polymethyl methacrylate. *Journal of the Physical Society of Japan*, 15(4):718–725, 1960.

[112] W.R. Krause, J. Miller, and P. Ng. The viscosity of acrylic bone cements. *Journal of Biomedical Materials Research*, 16(3):219–243, 1982.

[113] A. Krawietz. *Materialtheorie*. Springer, Berlin, 1986.

[114] K.-D. Kuehn, W. Ege, and U. Gopp. Acrylic bone cements: Composition and properties. *Orthopedic Clinics of North America*, 36(1):17–28, 2005.

[115] K.-D. Kuehn, W. Ege, and U. Gopp. Acrylic bone cements: Mechanical and physical properties. *Orthopedic Clinics of North America*, 36(1):29–39, 2005.

[116] N.M.G. Kurdy, J.P. Hodgkinson, and R. Haynes. Acrylic bone cement: Influence of mixer design and unmixed powder. *The Journal of Arthroplasty*, 11(7):813–819, 1996.

[117] P. Kurzweil and P. Scheipers. *Chemie Grundlagen, Aufbauwissen, Anwendungen und Experimente*. Vieweg und Teubner Verlag, 2012.

[118] R.S. Lakes and A. Wineman. On Poisson's ratio in linearly viscoelastic solids. *Journal of Elasticity*, 85(1):45–63, 2006.

[119] R. Landgraf. *Modellierung und Simulation der Aushärtung polymerer Werkstoffe*. PhD thesis, Technische Universität Chemnitz, 2015.

[120] R. Landgraf, J. Ihlemann, S. Kolmeder, and A. Lion. Thermo-mechanically coupled curing processes of acrylic bone cements used in vertebroplasty: Material modelling and finite-element-simulation. In *Proceedings of the 10th International Symposium on Computational Methods in Biomechanics and Biomedical Engineering, Berlin, Germany, April 7th - 11th*, pages 19–24. ARUP, 2012.

[121] R. Landgraf, J. Ihlemann, S. Kolmeder, A. Lion, H. Lebsack, and C. Kober. Modelling and simulation of acrylic bone cement injection and curing within the framework of vertebroplasty. *ZAMM - Journal of Applied Mathematics and Mechanics / Zeitschrift für Angewandte Mathematik und Mechanik*, 95(12):1530–1547, 2015.

[122] R. Landgraf, M. Rudolph, R. Scherzer, and J. Ihlemann. Modelling and simulation of adhesive curing processes in bonded piezo metal composites. *Computational Mechanics*, 54(2):547–565, 2014.

[123] R. Lenk. *Polymer Rheology*. Applied Science Publishers, London, 1978.

[124] A.B. Lennon and P.J. Prendergast. Residual stress due to curing can initiate damage in porous bone cement: Experimental and theoretical evidence. *Journal of Biomechanics*, 35(3):311–321, 2002.

[125] G. Lewis. Properties of acrylic bone cement: State of the art review. *Journal of Biomedical Materials Research*, 38(2):155–182, 1997.

[126] G. Lewis and M. Carroll. Rheological properties of acrylic bone cement during curing and the role of the size of the powder particles. *Journal of Biomedical Materials Research*, 63(2):191–199, 2002.

[127] G. Lewis and S. Mladsi. Effect of sterilization method on properties of Palacos® R acrylic bone cement. *Biomaterials*, 19(1-3):117–124, 1998.

[128] L. Lidgren, B. Bodelind, and J. Möller. Bone cement improved by vacuum mixing and chilling. *Acta Orthopaedica*, 58(1):27–32, 1987.

[129] I.H. Lieberman, D. Togawa, and M.M. Kayanja. Vertebroplasty and kyphoplasty: Filler materials. *The Spine Journal*, 5(6, Supplement):S305–S316, 2005.

[130] C. Liebl. *Viskoelastisch-viskoplastische Modellierung von Strukturklebstoffen während der Aushärtung*. PhD thesis, Universität der Bundeswehr München, 2014.

[131] C. Liebl, M. Johlitz, B. Yagimli, and A. Lion. Simulation of curing-induced viscoplastic deformation: A new approach considering chemo-thermomechanical coupling. *Archive of Applied Mechanics*, 82(8):1133–1144, 2012.

[132] C. Liebl, M. Johlitz, B. Yagimli, and A. Lion. Three-dimensional chemo-thermomechanically coupled simulation of curing adhesives including viscoplasticity and chemical shrinkage. *Computational Mechanics*, 49(5):603–615, 2012.

[133] M.A.K. Liebschner, W.S. Rosenberg, and T.M. Keaveny. Effects of bone cement volume and distribution on vertebral stiffness after vertebroplasty. *Spine*, 26(14):1547–1554, 2001.

[134] T.-H. Lim, G.T. Brebach, S.M. Renner, W.-J. Kim, J.G. Kim, R.E. Lee, G.B.J. Andersson, and H.S. An. Biomechanical evaluation of an injectable calcium phosphate cement for vertebroplasty. *Spine*, 27(12):1297–1302, 2002.

[135] E.P. Lin, S. Ekholm, A. Hiwatashi, and P.-L. Westesson. Vertebroplasty: Cement leakage into the disc increases the risk of new fracture of adjacent vertebral body. *American Journal of Neuroradiology*, 25(2):175–180, 2004.

[136] P. Lingois, L. Berglund, A. Greco, and A. Maffezoli. Chemically induced residual stresses in dental composites. *Journal of Materials Science*, 38(6):1321–1331, 2003.

[137] A. Lion. On the large deformation behaviour of reinforced rubber at different temperatures. *Journal of the Mechanics and Physics of Solids*, 45:1805–1834, 1997.

[138] A. Lion. *Thermomechanik von Elastomeren - Experimente und Materialtheorie*. Habilitation, Institut für Mechanik, Fachbereich Maschinenbau der Universität Gesamthochschule Kassel, 2000.

[139] A. Lion. Beiträge zur Materialtheorie - Einführung in die lineare Viskoelastizität. Technical report, Univeristät der Bundeswehr München, 2007.

[140] A. Lion, B. Dippel, and C. Liebl. Thermomechanical material modelling based on a hybrid free energy density depending on pressure, isochoric deformation and temperature. *International Journal of Solids and Structures*, 51(3–4):729–739, 2014.

[141] A. Lion and P. Höfer. On the phenomenological representation of curing phenomena in continuum mechanics. *Archives of Mechanics*, 59:59–89, 2007.

[142] A. Lion and C. Kardelky. The payne effect in finite viscoelasticity: Constitutive modelling based on fractional derivatives and intrinsic time scales. *International Journal of Plasticity*, 20(7):1313–1345, 2004.

[143] A. Lion, C. Liebl, S. Kolmeder, and J. Peters. Representation of the glass-transition in mechanical and thermal properties of glass-forming materials: A three-dimensional theory based on thermodynamics with internal state variables. *Journal of the Mechanics and Physics of Solids*, 58(9):1338–1360, 2010.

[144] A. Lion and J. Peters. Coupling effects in dynamic calorimetry: Frequency-dependent relations for specific heat and thermomechanical responses – a one-dimensional approach based on thermodynamics with internal state variables. *Thermochimica Acta*, 500(1-2):76–87, 2010.

[145] A. Lion and B. Yagimli. Differential scanning calorimetry - continuum mechanical considerations with focus to the polymerisation of adhesives. *ZAMM - Journal of Applied Mathematics and Mechanics / Zeitschrift für Angewandte Mathematik und Mechanik*, 88(5):388–402, 2008.

[146] A. Lion and B. Yagimli. On the frequency-dependent specific heat and TMDSC: Constitutive modelling based on thermodynamics with internal state variables. *Thermochimica Acta*, 490(1-2):64–74, 2009.

[147] A. Lion, B. Yagimli, G. Baroud, and U. Goerke. Constitutive modelling of PMMA-based bone cement: A functional model of viscoelasticity and its approximation for time domain investigations. *Archives of Mechanics*, 60:221–242, 2008.

[148] H. Lu, X. Zhang, and W. G. Knauss. Uniaxial, shear, and poisson relaxation and their conversion to bulk relaxation: Studies on poly(methyl methacrylate). *Polymer Engineering & Science*, 37(6):1053–1064, 1997.

[149] J. Lubliner. A model of rubber viscoelasticity. *Mechanics Research Communications*, 12(2):93–99, 1985.

[150] A. Maffezzoli. Polymerization kinetics of acrylic bone cements by differential scanning calorimetry. *Journal of Thermal Analysis*, 47(1):35–49, 1996.

[151] A. Maffezzoli, D. Ronca, G. Guida, I. Pochini, and L. Nicolais. In-situ polymerization behaviour of bone cements. *Journal of Materials Science: Materials in Medicine*, 8(2):75–83, 1997.

[152] R. Mahnken. Thermodynamic consistent modeling of polymer curing coupled to visco–elasticity at large strains. *International Journal of Solids and Structures*,

50(13):2003–2021, 2013.

[153] R. Mahnken and M. Schlimmer. Simulation of strength difference in elasto-plasticity for adhesive materials. *International Journal for Numerical Methods in Engineering*, 63(10):1461–1477, 2005.

[154] J.M. Mathis, J.D. Barr, S.M. Belkoff, M.S. Barr, M.E. Jensen, and H. Deramond. Percutaneous vertebroplasty: A developing standard of care for vertebral compression fractures. *American Journal of Neuroradiology*, 22(2):373–381, 2001.

[155] S. Mazzullo, M. Paolini, and C. Verdi. Numerical simulation of thermal bone necrosis during cementation of femoral prostheses. *Journal of Mathematical Biology*, 29(5):475–494, 1991.

[156] A. Meister. *Numerik linearer Gleichungssysteme - Eine Einführung in moderne Verfahren*. Vieweg Verlag, 2008.

[157] K.P. Menard. *Dynamic Mechanical Analysis - A Practiacl Introduction*. CRC Press LLC, 1999.

[158] T. Mezger. *Das Rheologie-Handbuch*. Curt R. Vincentz Verlag, Hannover, 2000.

[159] C. Migliaresi, L. Fambri, and J. Kolarik. Polymerization kinetics, glass transition temperature and creep of acrylic bone cements. *Biomaterials*, 15(11):875–881, 1994.

[160] S. Molloy, J.M. Mathis, and S.M. Belkoff. The effect of vertebral body percentage fill on mechanical behavior during percutaneous vertebroplasty. *Spine*, 28(14):1549–1554, 2003.

[161] J.J. Moré. The Levenberg-Marquardt algorithm: Implementation and theory. In *Lecture Notes in Mathematics*, volume 630, pages 105–116. Springer Berlin Heidelberg, 1978.

[162] S.D. Muller, S.M. Green, and A.W. McCaskie. The dynamic volume changes of polymerising polymethyl methacrylate bone cement. *Acta Orthopaedica*, 73(6):684–687, 2002.

[163] A.J.M.-L. Mühlhoff. *Charakterisierung der Osteoporose in einer Rehabilitationsklinik in den Jahren 1993 - 2002*. PhD thesis, Julius-Maximilians-Universität Würzburg, 2006.

[164] M. Müller. *Thermoplastische Elastomere als neuartige Additive für die Kunststoffverarbeitung*. PhD thesis, Technische Universität Berlin, 2009.

[165] D.A. Nussbaum, P. Gailloud, and K. Murphy. The chemistry of acrylic bone cements and implications for clinical use in image-guided therapy. *Journal of Vascular and Interventional Radiology*, 15(2, Part 1):121–126, 2004.

[166] A. Nzihou, L. Attias, P. Sharrock, and A. Ricard. A rheological, thermal and mechanical study of bone cement–from a suspension to a solid biomaterial. *Powder Technology*, 99(1):60–69, 1998.

[167] A. Nzihou, P. Sharrock, and A. Ricard. Reaction kinetics and heat transfer studies in thermoset resins. *Chemical Engineering Journal*, 72(1):53–61, 1999.

[168] D.J. O'Brien, P.T. Mather, and S.R. White. Viscoelastic properties of an epoxy resin during cure. *Journal of Composite Materials*, 35(10):883–904, 2001.

[169] C. Oeser. Experimentelle Untersuchung der rheologischen Eigenschaften von Knochenzement während des Quellvorgangs. Master's thesis, Universität der Bundeswehr München, 2011.

[170] M.J. O'Neill. Measurement of specific heat functions by differential scanning calorimetry. *Analytical Chemistry*, 38(10):1331–1336, 1966.

[171] OpenFOAM. *UserGuide*. (The OpenFOAM Foundation 2012), Version 2.1.1 edition, 2012.

[172] S. Osher and J. A. Sethian. Fronts propagating with curvature-dependent speed: Algorithms based on Hamilton-Jacobi formulations. *Journal of Computational Physics*, 79(1):12–49, 1988.

[173] D.J. O'Brien, N.R. Sottos, and S.R. White. Cure-dependent viscoelastic Poisson's ratio of epoxy. *Experimental Mechanics*, 47(2):237–249, 2007.

[174] B. Padovani, O. Kasriel, P. Brunner, and P. Peretti-Viton. Pulmonary embolism caused by acrylic cement: A rare complication of percutaneous vertebroplasty. *American Journal of Neuroradiology*, 20(3):375–377, 1999.

[175] R.L. Pagano, V.M.A. Calado, F.W. Tavares, and E.C. Biscaia. Parameter estimation of kinetic cure using DSC non-isothermal data. *Journal of Thermal Analysis and Calorimetry*, 103(2):495–499, 2011.

[176] M. Pahl, W. Gleissle, and H.-M. Laun. *Praktische Rheologie der Kunststoffe und Elastomere*. VDI-Gesellschaft Kunststofftechnik, Düsseldorf, 1995.

[177] W.J. Parker, R.J. Jenkins, C.P. Butler, and G.L. Abbott. Flash method of determining thermal diffusivity, heat capacity, and thermal conductivity. *Journal of Applied Physics*, 32(9):1679–1684, 1961.

[178] S.V. Patankar. *Numerical heat transfer and fluid flow*. Hemisphere Publishing Corporation, 1980.

[179] M. A. Pérez, N. Nuño, A. Madrala, J. M. García-Aznar, and M. Doblaré. Computational modelling of bone cement polymerization: Temperature and residual stresses. *Computers in Biology and Medicine*, 39(9):751–759, 2009.

[180] F.M. Phillips, T.F. Wetzel, I. Lieberman, and M. Campbell-Hupp. An in vivo comparison of the potential for extravertebral cement leak after vertebroplasty and kyphoplasty. *Spine*, 27(19):2173–2178, 2002.

[181] J. Plant and G. Tidey. *Understanding, Preventing and Overcoming Osteoporosis*. Virgin Books Ltd, London, 2004.

[182] M. J. Provenzano, M.P.J. Kieran, and L.H. Riley. Bone cements: Review of their physiochemical and biochemical properties in percutaneous vertebroplasty. *American Journal of Neuroradiology*, 25(7):1286–1290, 2004.

[183] T. Ranz. *Viskoelastisches Materialmodell für Holz - Experimente, Modellierung und Simulation*. PhD thesis, Universität der Bundeswehr München, 2008.

[184] S. Reese and S. Govindjee. A theory of finite viscoelasticity and numerical aspects. *International Journal of Solids and Structures*, 35(26-27):3455–3482, 1998.

[185] M. Rendek. *Transient Effects of Filler Reinforced Rubber with respect to the Payne Effect: Experiments, Constitutive Modelling and FEM Implementation*. PhD thesis, Universität der Bundeswehr München, 2011.

[186] D.K. Resnick and S.R. Grafin. *Vertebroplasty and Kyphoplasty*. Thieme, New York, 2005.

[187] J. Retka. *Vibroakustisches Verhalten von viskoelastischen Strukturen unter finiter Vordeformation*. PhD thesis, Universität der Bundeswehr München, 2012.

[188] J. Retka and P. Höfer. Numerische Simulation aushärtender Klebstoffe. Master's thesis, Univeristät der Bundeswehr München, 2007.

[189] A. P. Reverberi, P. Bagnerini, L. Maga, and A. G. Bruzzone. On the non-linear Maxwell–Cattaneo equation with non-constant diffusivity: Shock and discontinuity waves. *International Journal of Heat and Mass Transfer*, 51(21–22):5327–5332, 2008.

[190] R. Risen and J. Schawe. Die Glasübergangstemperatur gemessen mit verschiedenen TA-Techniken, Teil 1: Übersicht. *UserCom*, 1:1–4, 2003.

[191] R. Risen and J. Schawe. Die Glasübergangstemperatur gemessen mit verschiedenen TA-Techniken, Teil 2: Ermittlung der Glasübergangstemperatur. *UserCom*, 2:1–5, 2003.

[192] A.M. Robertson. Lecture Notes on Non-Newtonian Fluids - Part I: Inelastic Fluids. Technical report, University of Pittsburgh, 2005.

[193] A. Rohlmann, H.N. Boustani, G. Bergmann, and T. Zander. A probabilistic finite element analysis of the stresses in the augmented vertebral body after vertebroplasty. *European Spine Journal*, 19(9):1585–1595, 2010.

[194] A. Rohlmann, U. Gabel, F. Graichen, A. Bender, and G. Bergmann. An instrumented implant for vertebral body replacement that measures loads in the anterior spinal column. *Medical Engineering & Physics*, 29(5):580–585, 2007.

[195] A. Rohlmann, T. Zander, and G. Bergmann. Spinal loads after osteoporotic vertebral fractures treated by vertebroplasty or kyphoplasty. *European Spine Journal*, 15(8):1255–

1264, 2006.

[196] A. Rohlmann, T. Zander, T. Jony, U. Weber, and G. Bergmann. Einfluss der Wirbelkörpersteifigkeit vor und nach Vertebroplastik auf den intradiskalen Druck. *Biomedizinische Technik (Biomedical Engineering)*, 50:148–152, 2005.

[197] D. Rosu, C.N. Cascaval, F. Mustatat, and C. Ciobanu. Cure kinetics of epoxy resins studied by non-isothermal DSC data. *Thermochimica Acta*, 383(1-2):119–127, 2002.

[198] M. Rudolph, M. Stockmann, R. Landgraf, and J. Ihlemann. Experimental determination and modelling of volume shrinkage in curing thermosets. *arXiv*, Preprint arXiv:1404.0310, 2014.

[199] H. Rusche. *Computational fluid dynamics of dispersed two-phase flows at high phase fractions*. PhD thesis, Imperial College of Science, Technology and Medicine London, 2002.

[200] M.E. Ryan and A. Dutta. Kinetics of epoxy cure: a rapid technique for kinetic parameter estimation. *Polymer*, 20(2):203–206, 1979.

[201] S. Saha and S. Pal. Mechanical properties of bone cement: A review. *Journal of Biomedical Materials Research*, 18(4):435–462, 1984.

[202] S. Sarda, E. Fernández, J. Llorens, S. Martínez, M. Nilsson, and J.A. Planell. Rheological properties of an apatitic bone cement during initial setting. *Journal of Materials Science: Materials in Medicine*, 12(10-12):905–909, 2001.

[203] J.E.K. Schawe. A comparison of different evaluation methods in modulated temperature DSC. *Thermochimica Acta*, 260(0):1–16, 1995.

[204] J.E.K. Schawe. Modulated temperature DSC measurements: The influence of the experimental conditions. *Thermochimica Acta*, 271(0):127–140, 1996.

[205] J.E.K. Schawe. A description of chemical and diffusion control in isothermal kinetics of cure kinetics. *Thermochimica Acta*, 388(1-2):299–312, 2002.

[206] M. Schlimmer. *Fliessverhalten plastisch kompressibler Werkstoffe*. PhD thesis, Rheinisch-Westfälische Technische Hochschule Aachen, 1974.

[207] F. Schmidt. Rheologische Charakterisierung von akrylischem Knochenzement vor dem Hintergrund seiner Verwendung in der Vertebroplastik. Master's thesis, Fachhochschule Aachen, 2006.

[208] R. Schmidt, B. Cakir, T. Mattes, M. Wegener, W. Puhl, and M. Richter. Cement leakage during vertebroplasty: An underestimated problem? *European Spine Journal*, 14(5):466–473, 2005.

[209] F.R. Schwarzl. *Polymermechanik - Struktur und mechanisches Verhalten von Polymeren*.

Springer, 1990.

[210] G. Schütze. Perkuntane Vertebroplastie. *Schmerztherapie - Deutsche Gesellschaft für Schmerztherapie e.V. – DGS*, 3:15f, 2004.

[211] J.C. Simo. On a fully three-dimensional finite-strain viscoelastic damage model: Formulation and computational aspects. *Computer Methods in Applied Mechanics and Engineering*, 60(2):153–173, 1987.

[212] S. Sourour and M.R. Kamal. Differential scanning calorimetry of epoxy cure: Isothermal cure kinetics. *Thermochimica Acta*, 14(1–2):41–59, 1976.

[213] S. Srimongkol, B. Wiwatanapataphee, and Y. H. Wu. Computer simulation of polymethylmethacrylate bone cement flow through femoral canal and cancellous bone. *Australian & New Zealand Industrial and Applied Mathematics Journal*, 47:C404–C418, 2006.

[214] M. Stańczyk. Study on modelling of PMMA bone cement polymerisation. *Journal of Biomechanics*, 38(7):1397–1403, 2005.

[215] M. Stańczyk and J.J. Telega. Modelling of heat transfer in biomechanics - a review. Part II. Orthopaedics. *Acta of Bioengineering and Biomechanics*, 4:31–61, 2002.

[216] M. Stańczyk and B. van Rietbergen. Thermal analysis of bone cement polymerisation at the cement-bone interface. *Journal of Biomechanics*, 37(12):1803–1810, 2004.

[217] M. Sussman, P. Smereka, and S. Osher. A level set approach for computing solutions to incompressible two-phase flow. *Journal of Computational Physics*, 114(1):146–159, 1994.

[218] M.I. Syed, N.A. Patel, S. Jan, M. S. Harron, K. Morar, and A. Shaikh. New symptomatic vertebral compression fractures within a year following vertebroplasty in osteoporotic women. *American Journal of Neuroradiology*, 26(6):1601–1604, 2005.

[219] M.M.H. Teng, H. Cheng, D.M.-T. Ho, and C.-Y. Chang. Intraspinal leakage of bone cement after vertebroplasty: A report of 3 cases. *American Journal of Neuroradiology*, 27(1):224–229, 2006.

[220] J.C.M. Teo. *Patient specific finite volume modeling for intraosseous PMMA cement flow simulation in vertebral cancellous bone.* PhD thesis, National University of Singapore, 2007.

[221] J.C.M. Teo and S.H. Teoh. Permeability study of vertebral cancellous bone using micro-computational fluid dynamics. *Computer Methods in Biomechanics and Biomedical Engineering*, 15(4):417–423, 2011.

[222] J.C.M. Teo, S.C. Wang, and S.H. Teoh. Preliminary study on biomechanics of vertebroplasty: A computational fluid dynamics and solid mechanics combined approach. *Spine*, 32(12):1320–1328, 2007.

[223] A.V. Tobolsky. *Mechanische Eigenschaften und Struktur von Polymeren*. Berliner Union, Stuttgart, 1967.

[224] A.G. Tohmeh, J.M. Mathis, D.C. Fenton, A.M. Levine, and S.M. Belkoff. Biomechanical efficacy of unipedicular versus bipedicular vertebroplasty for the management of osteoporotic compression fractures. *Spine*, 24:1772–1776, 1999.

[225] N.W. Tschoegl. *The phenomenological theory of linear viscoelastic behavior - an introduction*. Springer, Berlin, 1989.

[226] N.W. Tschoegl, W.G. Knauss, and I. Emri. Poisson's ratio in linear viscoelasticity – a critical review. *Mechanics of Time-Dependent Materials*, 6(1):3–51, 2002.

[227] R.C. Turner, P.E. Atkins, M.A. Ackley, and J.B. Park. Molecular and macroscopic properties of PMMA bone cement: Free-radical generation and temperature change versus mixing ratio. *Journal of Biomedical Materials Research*, 15(3):425–432, 1981.

[228] A.A. Uppin, J.A. Hirsch, L.V. Centenera, B.A. Pfiefer, A.G. Pazianos, and I.S. Choi. Occurrence of new vertebral body fracture after percutaneous vertebroplasty in patients with osteoporosis. *Radiology*, 226(1):119–124, 2003.

[229] C.I. Vallo. Residual monomer content in bone cements based on poly(methyl methacrylate). *Polymer International*, 49(8):831–838, 2000.

[230] G. Van Assche, A. Van Hemelrijck, H. Rahier, and B. Van Mele. Modulated differential scanning calorimetry: Isothermal cure and vitrification of thermosetting systems. *Thermochimica Acta*, 268(0):121–142, 1995.

[231] A. Venmans, C.A.H. Klazen, P.N.M. Lohle, W.J. van Rooij, H.J.J. Verhaar, J. de Vries, and W.P.Th.M. Mali. Percutaneous vertebroplasty and pulmonary cement embolism: Results from VERTOS II. *American Journal of Neuroradiology*, 31(8):1451–1453, 2010.

[232] N. Verdonschot and H.W.J. Huiskes. Dynamic creep behavior of acrylic bone cement. *Journal of Biomedical Materials Research*, 29(5):575–581, 1995.

[233] J.-J. Verlaan, F.C. Oner, A. J. Verbout, and W.J.A. Dhert. Temperature elevation after vertebroplasty with polymethyl-methacrylate in the goat spine. *Journal of Biomedical Materials Research Part B: Applied Biomaterials*, 67B(1):581–585, 2003.

[234] J.C.J. Webb and R.F. Spencer. The role of polymethylmethacrylate bone cement in modern orthopaedic surgery. *Journal of Bone & Joint Surgery, British Volume*, 89-B(7):851–857, 2007.

[235] M. Wenzel. *Spannungsbildung und Relaxationsverhalten bei der Aushärtung von Epoxidharzen*. PhD thesis, Technischen Universität Darmstadt, 2005.

[236] S.R. White and H.T. Hahn. Process modeling of composite materials: Residual stress

development during cure. Part I. Model formulation. *Journal of Composite Materials*, 26(16):2402–2422, 1992.

[237] WHO Scientific Group Meeting on Prevention and Management of Osteoporosis. Prevention and management of osteoporosis. Technical report, World Health Organization, 2003.

[238] R.P. Widmer and S.J. Ferguson. On the interrelationship of permeability and structural parameters of vertebral trabecular bone: A parametric computational study. *Computer Methods in Biomechanics and Biomedical Engineering*, 15:1–15, January 2012.

[239] P. Wiedemann. Wärmeausbreitung in der Mikroskala und numerische Analyse mittels der Methode der diskontinuierlichen finiten Elemente. Master's thesis, Technische Universität Berlin, 2012.

[240] R.K. Wilcox. The biomechanical effect of vertebroplasty on the adjacent vertebral body: A finite element study. *Proceedings of the Institution of Mechanical Engineers, Part H: Journal of Engineering in Medicine*, 220(4):565–572, 2006.

[241] R.A. Wilkes, J.G. Mackinnon, and W.G. Thomas. Neurological deterioration after cement injection into a vertebral body. *Journal of Bone & Joint Surgery, British Volume*, 76-B(1):155–155, 1994.

[242] R.L. Wixson, E.P. Lautenschalager, and M.A. Novak. Vacuum mixing of acrylic bone cement. *The Journal of Arthroplasty*, 2(2):141–149, 1987.

[243] B. Wunderlich, A. Boller, I. Okazaki, K. Ishikiriyama, W. Chen, M. Pyda, J. Pak, I. Moon, and R. Androsch. Temperature-modulated differential scanning calorimetry of reversible and irreversible first-order transitions. *Thermochimica Acta*, 330(1-2):21–38, 1999.

[244] B. Yagimli. *Kontinuumsmechanische Betrachtung von Aushärtevorgängen - Experimente, thermomechanische Materialmodellierung und numerische Umsetzung*. PhD thesis, Universität der Bundeswehr München, 2013.

[245] B. Yagimli and A. Lion. Experimental investigations and material modelling of curing processes under small deformations. *ZAMM - Journal of Applied Mathematics and Mechanics / Zeitschrift für Angewandte Mathematik und Mechanik*, 91(5):342–359, 2011.

[246] J. S. Yeom, W. J. Kim, W. S. Choy, C. K. Lee, B. S. Chang, and J. W. Kang. Leakage of cement in percutaneous transpedicular vertebroplasty for painful osteoporotic compression fractures. *Journal of Bone & Joint Surgery, British Volume*, 85-B(1):83–89, 2003.

[247] T. Zeiser, M. Bashoor-Zadeh, A. Darabi, and G. Baroud. Pore-scale analysis of newtonian flow in the explicit geometry of vertebral trabecular bones using Lattice Boltzmann simulation. *Proceedings of the Institution of Mechanical Engineers, Part H: Journal of Engineering in Medicine*, 222(2):185–194, 2008.

[248] N. Zolyniak. *Einfluss der Polymerisationstemperatur von Knochenzement auf den Spinalkanal bei der perkutanen Vertebroplastie.* PhD thesis, Ludwig-Maximilians-Universität München, 2009.